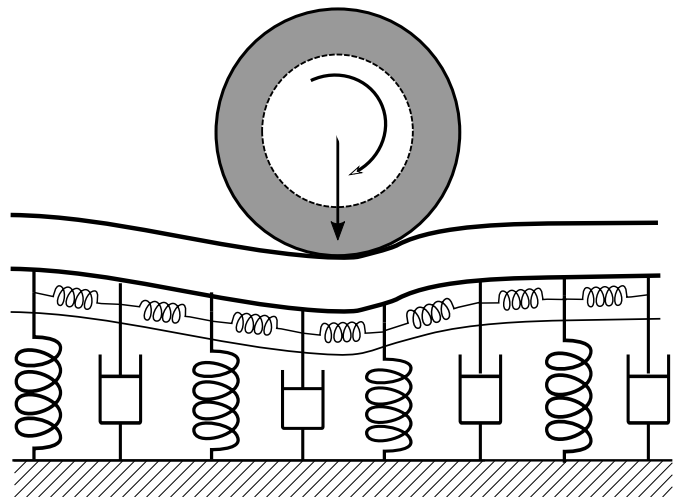


# Investigating pavement response to a moving vehicle

Characterisation of structural properties and direct measurement of structural rolling resistance



**Natasja Ringsing Nielsen**

PhD thesis  
December 2020

Supervised by  
Associate Professor Tina Hecksher  
Associate Professor Poul Hjorth  
Christoffer Nielsen, PhD

This thesis has been submitted to the Doctoral School of Science and Environment,  
Roskilde University



**GREENWOOD  
ENGINEERING**

**RUC**  
Roskilde University

PhD thesis  
"Investigating pavement response to a moving vehicle: *Characterisation of structural properties and direct measurement of structural rolling resistance*"

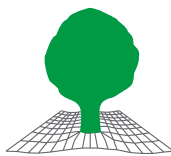
by Natasja Ringsing Nielsen

Submitted to  
the Doctoral School of Science and environment  
Roskilde University  
14 December 2020

Supervised by  
Associate Professor Tina Hecksher  
IMFUFA, Roskilde University

Co-supervised by  
Christoffer Nielsen, PhD  
Greenwood Engineering A/S

and  
Associate Professor Poul Hjorth  
DTU Compute



**GREENWOOD  
ENGINEERING**



Cover: Sketch of a moving tire on top of a two layered beam model derived in this thesis. In this model, the asphalt layer is modelled as a viscoelastic Euler-Bernoulli beam resting on a damped Pasternak foundation. The Pasternak foundation models the soil by a set of continuously-distributed springs and dashpots with an in-compressible layer connecting the elements at the top.

# Abstract

In this thesis, we use measurements of the pavement deflection slope, obtained with the Traffic speed deflectometer (TSD) technology, to analyze two road sections. We show, that the structural rolling resistance (SRR) is given by the deflection slope directly under the moving load. Furthermore, a simple pavement response model is developed and fitted to data. Based on the model fitting results, structural characteristics about the pavement are obtained. Overall, the thesis is split into four main parts:

**I** The aim was to develop a new method for measuring rolling resistance. The idea is that the longitudinal deformation of the non-driven, rear-end tire axle is directly related to the rolling resistance. This deformation can in principle be measured using strain gauges. In practice, due to temperature effects in the axle, these measurements were not producing consistent results and the method needs further development to be brought to a routinely functioning state.

**II** SRR for two road sections is found by estimating the deflection slope directly under the load through a linear interpolation between the two closest data points. The method gives highly reproducible results (standard deviations from three repeated measurements between 4 and 10%) with a high spatial resolution. The influence of temperature is tested on a  $\sim 10$ km road segment, where the measured SRR coefficient values varies from 0.01%-0.03% of the load for 18°C and 0.01%-0.05% for 35°C. These values are small compared to typical tire rolling resistance values. The validity of the linear interpolation method was investigated by comparing to results from simulated curves using a continuum pavement model, and it was found to provide a valid estimate of SRR.

**III** A simple one-dimensional pavement response model consisting of a viscoelastic Euler-Bernoulli beam resting on a Pasternak foundation is developed. A theoretical study of the model is performed, including a sensitivity analysis. It is found that only the behavior of the asphalt complex modulus within some range of wave numbers influence the modelled pavement response. Consequently, a simple viscoelastic model is used to describe top layer behavior and furthermore, the influence of velocity and temperature on the beam response is described.

**IV** The simple pavement response model is fitted to TSD data and is found to fit data very well. By analyzing the resulting best estimated parameter values, a connection between observed changes in the deflection slope data and changing structural characteristics of the pavement is derived. Surprisingly, the dominating source of damping is found to be the foundation damping. In fact, the top layer acts almost elastic in a majority of data. The ratio of maximum and minimum deflection slope amplitudes is shown to identify the dominating source of damping in a pavement within the model framework. Lastly, a pilot study for determining asphalt complex modulus master curves based on TSD data at different temperatures and driving velocities is presented. The study illustrates that it is possible to create master curves describing the viscoelastic behaviour of the asphalt layer

by applying the Time-Temperature Superposition principle to TSD data in conjunction with a sufficiently advanced road model. The presented method has the advantage that it uses a non-destructive measuring method and is easy to apply on large road sections. For future work, we recommend a study involving numerous different temperatures in order to cover a larger range of frequencies.

# Resumé

I denne afhandling analyseres to vejstrækninger ved målinger for vejafbøjningshældning indsamlet med *Traffic Speed Deflectometer* (TSD) -teknologien. Vi viser at den strukturelle rullemodstand (SRR) er givet ved afbøjningshældningen direkte under det kørende hjul. Derudover udvikles en simpel vejrespons model og denne fittes til data. Baseret på resultaterne fra model-fittet er strukturelle egenskaber omkring vejen udtrukket. Afhandlingen er inddelt i fire hoveddele:

**I** Vi havde til mål at udvikle en ny målemetode til måling af rullemodstand. Ideen bag metoden er, at den tværgående deformation af en ikke-dreven hjulaksel er direkte relateret til rullemodstanden. Denne deformation kan, i princippet, måles ved hjælp af strain gauges. Grundet temperatureffekter i akslen var disse målinger dog ikke konsistente i praksis og målemetoden bør derfor videreudvikles før den kan bruges rutinemæssigt.

**II** SRR er fundet for to vejstrækninger ved at estimere afbøjningshældningen direkte under belastningen gennem en lineær interpolation imellem de to nærmeste datapunkter. Metoden giver meget reproducerbare resultater (standard afvigelser fra tre gentaget kørsler på 4-10%) med en god rumlig opløsning. Indflydelsen af temperatur er undersøgt på en omtrent 10km vejsektion, hvor de målte SRR koefficient værdier variere imellem 0,01% og 0,03% af belastningen ved 18°C og mellem 0,01% og 0,05% for 35°C. De fundne værdier er lave sammenlignet med typiske værdier for dæk rullemodstand. Gyldigheden af den lineær interpolationsmetode blev undersøgt ved at sammenligne med resultater hvor simulerede kurver fra en kontinuumsmodel er brugt. Vi vurderer at metoden giver valide estimater for SRR.

**III** Der udvikles en simpel en-dimensionel vejrespons model bestående af en viskoelastisk Euler-Bernoulli bjælke på toppen af et Pasternak fundament. En teoretisk undersøgelse af modellen udføres, herunder en sensitivitsanalyse. Det viser sig at kun opførelsen af asfaltens kompleks modul inde for et område af bølgetal har en påvirkning på det modellerede vejrespons. Dermed kan vi bruge en simple viskoelastisk model til at karakteriserer bjælken, samt beskrive dets påvirkning af hastighed og temperatur.

**IV** Den simple vejrespons model er fittes til TSD data. Vi vurderer at denne giver et godt fit. Ved at analysere de resulterende bedst estimerede parameterværdier findes en forbindelse imellem observerede ændringer i afbøjningshældnings data og ændringer i vejens strukturelle egenskaber. Overraskende viser det sig, at den dominerende kilde til dæmpning er undergrunden. Det viser sig at top-laget opfører sig næsten elastisk for størstedelen af data. Vi viser at ratioen imellem amplituden på maksimummet og minimummet i afbøjningshældningen kan identificere hvor den mest dominerende kilde til dæmpning findes, inde for rammerne af modellen. Endeligt præsenteres en pilotundersøgelse til bestemmelse af masterkurver for asfalt kompleks modul baseret på TSD data målt ved forskellige kørehastigheder og temperaturer. Undersøgelsen viser at det

er muligt at udvikle masterkurver der beskriver den viskoelastiske opførsel af asfalten ved at bruge princippet for tid-temperatur superposition TSD data, samt en tilstrækkelig avanceret vejmodel. Til fremtidigt arbejde anbefaler vi en undersøgelse, der involverer mange forskellige vejtemperaturer for at dække et større frekvensområde.

# Preface

This doctoral thesis describes the work done by the author from November 2017 to December 2020. In this period, I have had the pleasure of being part of the Glass and Time group at IMFUFA, Roskilde University. The project is a cooperation between Roskilde University and Greenwood Engineering, and as a result, I have had my everyday life both places. Working in this intersection between the academic and the cooperate world has been a learning, and sometimes frustrating, experience and I'm sure that it has contributed positively to the project and my personal development. During the project, I have had the pleasure to visit Professor Karim Chatti at the department of Civil Engineering, Michigan State University for five months in the spring 2019. I much appreciated my stay there as it was very educational to experience the work environment outside of Denmark.

The subject dealt with in this thesis is rolling resistance of heavy traffic. This subject is traditionally a pavement engineering problem, and thus it is often approached using engineering solutions. However, the work in this thesis has been made in the interdisciplinary field of physics, mathematics and engineering, with input and guidance from all three fields. Working in this cross section of subjects, all with different ways to view problems and to come up with solutions, has been a challenge at times but also a rewarding and educational experience. As I have a background in mathematics and is not a trained pavement engineer, some of the approaches to problems in this thesis might be different than what traditionally would have been done. It is my hope and believe that the variety of backgrounds of the people contributing to the project, as well as my atypical background, have resulted in some new and interesting insight into the subject of rolling resistance.

Throughout the thesis, I will use the first person point of view pronoun "we" to refer to both work and reflections which are my own and made in collaboration with my supervisors.

## Acknowledgement

This thesis would not have been possible if it was not for the existence of the lovely people surrounding me the last three years. Firstly, I would like to thank my three supervisors. Tina Hecksher, for guiding me through the last three years, both in good and bad times. You have taught me to question everything I think I know and not to settle with a simple and superficial understanding. I appreciate the informal relationship we have developed, where supervision can take place at the office or over a beer, and where there is room for both personal and academic talks. Christoffer Nielsen, for your joyful personality and for introducing this brand new field of pavement engineering to me in an understandable and manageable way. I am grateful for all the many hours of supervision and your tireless effort to teach until I finally understood it myself. Finally to Poul Hjorth, for sharing

his inexhaustible amount of knowledge and humorous anecdotes. It has been a great experience to work with you all.

A major part of the thesis work has been to develop an experimental method. For this, I owe the technical staff at Greenwood a great thanks for all their help and guiding. Furthermore, a great thanks to all of my coworkers at Greenwood for including me in a great work environment.

To my coworkers at Roskilde University and IMFUFA, I owe a special thanks. I have had the pleasure of being a part of RUC the last nine years and in the last three, as a part of a group of PhD students among whom I have developed long lasting friendships. To have such a great and diverse group of people to lighten the everyday life makes the hard times easier and the good times amazing. In particular, I should thank Lisa and Rasmus for being my longtime partners in crime. I have been so lucky to share an office with Rasmus the last three years and I have absolutely loved it, with all of our talks about work, personal life and everything in between.

Last but not least, a big thanks to my family and friends. For supporting me all the way through and for listening to all my stories about asphalt and pavement layers. I really appreciate your patience and interest in my work and without your support the last three years, this would not have been possible.



# Contents

<b>I</b>	<b>Introduction</b>	<b>1</b>
<b>1</b>	<b>Rolling resistance for heavy vehicles</b>	<b>3</b>
1.1	Thesis aim and reading guide . . . . .	5
1.2	List of publications . . . . .	7
<b>II</b>	<b>Measuring the total rolling resistance of a truck</b>	<b>9</b>
<b>2</b>	<b>Background</b>	<b>11</b>
2.1	Existing techniques for measuring rolling resistance . . . . .	11
2.2	Physical measures representing rolling resistance . . . . .	14
<b>3</b>	<b>New method for measuring the total rolling resistance - in theory</b>	<b>15</b>
3.1	Force and momentum balance in the axle system . . . . .	15
<b>4</b>	<b>New method for measuring the total rolling resistance - in practice</b>	<b>19</b>
4.1	Strain gauges . . . . .	19
4.2	The measurement setup . . . . .	21
4.3	Calibration procedure for strain gauges . . . . .	23
<b>5</b>	<b>Axle deformation data</b>	<b>29</b>
5.1	Preliminary measurements . . . . .	29
5.2	Temperature effects in the system . . . . .	32
5.3	Test of simple temperature compensation . . . . .	37
<b>6</b>	<b>Summarizing conclusion</b>	<b>41</b>
<b>III</b>	<b>Measuring Structural Rolling resistance</b>	<b>45</b>
<b>7</b>	<b>Structural rolling resistance</b>	<b>47</b>
7.1	State of the art . . . . .	47
<b>8</b>	<b>Traffic Speed Deflectometer</b>	<b>51</b>
8.1	The TSD principle . . . . .	51

<b>9</b>	<b>Traffic Speed deflectometer data</b>	<b>57</b>
9.1	Spatial variations and temperature dependence (Måløv data) . . . . .	57
9.2	Temperature and driving velocity dependence (Finland data) . . . . .	69
<b>10</b>	<b>Estimating structural rolling resistance from TSD data</b>	<b>73</b>
10.1	The simple approach . . . . .	73
10.2	Structural rolling resistance from data . . . . .	75
10.3	Extension of simple approach . . . . .	78
10.4	Investigating validity of the simple approach through simulated pavement responses . . . . .	81
10.5	Investigating dual tires vs a single load . . . . .	90
<b>11</b>	<b>Partial conclusion on the simple approach</b>	<b>93</b>
<b>IV</b>	<b>Modelling the pavement deflection underneath a moving load</b>	<b>95</b>
<b>12</b>	<b>Pavement response models</b>	<b>97</b>
<b>13</b>	<b>Elasticity and Viscoelasticity</b>	<b>101</b>
13.1	Mechanics of continuous matter . . . . .	101
13.2	Viscoelastic materials . . . . .	103
13.3	Response models . . . . .	110
<b>14</b>	<b>Beam theory</b>	<b>115</b>
14.1	Elastic beam theory . . . . .	115
14.2	Governing equation for deflection of a viscoelastic beam . . . . .	127
<b>15</b>	<b>Viscoelastic beam on a damped Pasternak foundation</b>	<b>129</b>
15.1	The simple Winkler model . . . . .	129
15.2	The Pasternak foundation . . . . .	130
15.3	Viscoelastic beam on damped Pasternak foundation model . . . . .	132
15.4	Layer dimensions in a 1D model . . . . .	135
<b>16</b>	<b>Numerical study of the pavement response model</b>	<b>139</b>
16.1	Choice of viscoelastic model for the beam . . . . .	139
16.2	Choice of parameters . . . . .	139
16.3	Simulated pavement deflection basin and slope . . . . .	142
16.4	Influence of asphalt thickness . . . . .	142
<b>17</b>	<b>Influence of complex modulus</b>	<b>147</b>
<b>18</b>	<b>Sensitivity analysis of the model</b>	<b>153</b>
18.1	Local sensitivity analysis . . . . .	154
18.2	Global sensitivity analysis . . . . .	157

<b>V</b>	<b>Comparing pavement response model with TSD data</b>	<b>161</b>
<b>19</b>	<b>Structural rolling resistance from model fit</b>	<b>163</b>
<b>20</b>	<b>Analysis of pavement characteristics based on model fit to TSD data</b>	<b>167</b>
20.1	Goodness of fit . . . . .	167
20.2	Estimated parameter values . . . . .	168
20.3	Interpreting data groups based on model results . . . . .	169
20.4	Comparison of different simplified models . . . . .	175
20.5	Effect of increased road temperature . . . . .	177
20.6	The models limitations to fit data . . . . .	182
20.7	Summarising discussion . . . . .	184
<b>21</b>	<b>Characterising pavement damping based on TSD data</b>	<b>185</b>
21.1	How velocity and temperature influence the pavement deflection . . . . .	185
21.2	Asphalt complex modulus master curves from TSD data . . . . .	189
21.3	Characterising foundation damping . . . . .	196
<b>22</b>	<b>Manifestation of viscoelastic effects</b>	<b>199</b>
22.1	Formulation of hypothesis . . . . .	199
22.2	Investigation through pavement model study . . . . .	201
22.3	Study of hypothesis using Viscowave II-M . . . . .	217
22.4	$\Omega$ in TSD data . . . . .	221
<b>VI</b>	<b>Summary</b>	<b>225</b>
<b>23</b>	<b>Summarising discussion and outlook</b>	<b>227</b>
23.1	Measuring total and structural rolling resistance . . . . .	227
23.2	Characterising structural properties based on model fit to TSD data . . . . .	230
23.3	Conclusive remarks . . . . .	234
	<b>Bibliography</b>	<b>235</b>
<b>VII</b>	<b>Appendix</b>	<b>243</b>
<b>A</b>	<b>Reprints of articles</b>	<b>245</b>
A.1	Method for Direct Measurement of Structural Rolling Resistance for Heavy Vehicles . . . . .	245
A.2	Measurement of structural rolling resistance at two temperatures . . . . .	256
A.3	Impact of viscous damping in asphalt and foundation - part 1: Theoretical investigation of a viscoelastic beam on a damped Pasternak foundation . . .	261

<b>B</b>	<b>Viscowave</b>	<b>285</b>
B.1	Overview over the solution . . . . .	285
B.2	Modifications of the program to match TSD setup . . . . .	286
<b>C</b>	<b>Metropolis Monte Carlo algorithm</b>	<b>289</b>

## **Part I**

# **Introduction**



## Chapter 1

# Rolling resistance for heavy vehicles

The world face a global climate crisis, which affects our way of living. One of the main reasons is our extensive emission of greenhouse gases such as carbon dioxide ( $\text{CO}_2$ ), methane ( $\text{CH}_4$ ) and nitrous oxide ( $\text{N}_2\text{O}$ ) (USDOT, 2010). The traffic sector is a significant contributor to the world's emission of  $\text{CO}_2$ . It is estimated that 13.5% of the total  $\text{CO}_2$  emission in the European Union (in 2016) was due to fuel consumption within the transport sector (Eurostat, 2016). For the United states this number is estimated to be 29% (in 2010) and growing steadily (USDOT, 2010). Within the European transport sector, 72% of the emission comes from road traffic, with 59% associated with light vehicles (such as passenger cars) and 19 % associated with heavy vehicles (fig. 1.1) (European Environment Agency, 2018). Consequently, there are both economic and environmental incentives to reduce fuel consumption of motor vehicles.

Vehicles consume fuel and emit  $\text{CO}_2$  as a consequence, in order to overcome an overall *driving resistance*. The driving resistance consists of several different components that all resist vehicle movement, with the majority being the energy consumption in the engine, which is estimated to account for 60% of the energy used (estimated for a truck driving 105 km/h) (Sharpe et al., 2014). The remaining 40% is distributed over; air drag (21%), rolling resistance (13%), drivetrain (2%) and the auxiliary loads (4%), which includes components driven by the engine such as cooling fans, AC etc (see fig. 1.1). All components of the driving resistance can be optimized to minimize the total vehicle energy use. In this thesis, we focus on the *rolling resistance*.

Rolling resistance is the force resisting motion of an object (such as a tire) rolling on a surface. It is created by the interaction between object and surface, and the predominant source of rolling resistance for vehicles are viscoelastic effects in both tires and pavement. The viscoelastic effects means that when e.g. the tire is deformed, the deformation is not purely elastic and thus it does not fully recover, but some of the energy is dissipated as heat (Sandberg et al., 2011b). This mechanism is taking place in both the tire and the pavement.

Overall, the components that contribute to the total rolling resistance are; deformation of the tire, structural response of the pavement and losses in the bearings and aerodynamic resistances (Sandberg et al., 2011b). Note that the loss in the suspension system in some studies is included in the total rolling resistance (as in fig. 1.1) and in some it is an

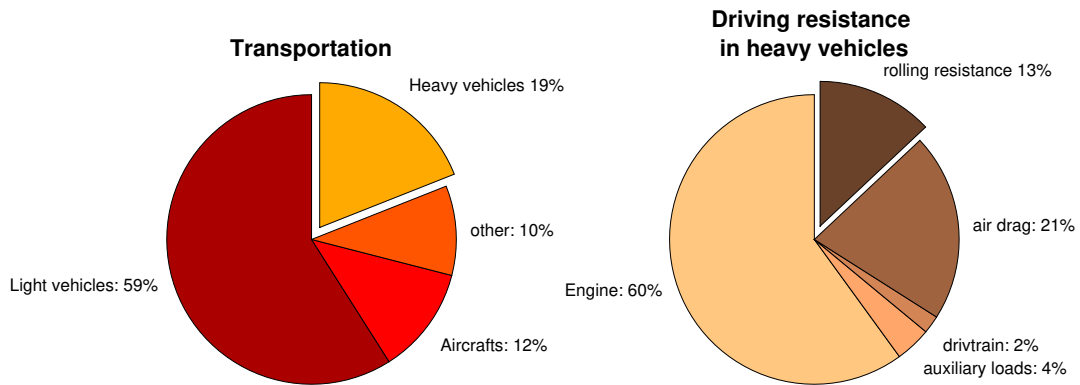


FIGURE 1.1: Left pie chart showing the distribution of CO<sub>2</sub> emission within the transportation sector. 19% of this is due to heavy traffic. Within this category, the driving resistance forces are distributed as shown in the right panel. Source: (Sharpe et al., 2014) and (USDOT, 2010)

independent part of the driving resistance. In this study, we do not include losses in the suspension system in the definition of rolling resistance.

Deformation of the tires is the component that contributes the most to the rolling resistance (Pouget et al., 2012). It is caused by features associated with the tire itself and the road surface. When the tire is traveling on top of a surface, different kinds of deformations and vibrations within the tire occur. The main source is the load, which flattens the tire and creates a contact area between the tire and surface, where the tire is flat. Furthermore, deformations and vibrations also occur in the tire tread elements. This includes effects such as tangent motions in the tread elements known as stick-slip and breaking of the molecular bonds when they leave the surface, known as stick-snap.

The road surface influences the tire deformation by creating local tire deformations and by introducing vibrations into the tire/wheel/suspension system. This results in an energy loss in both the tire and the suspension. In practice, it can be difficult to separate the two energy losses which is the reason why some studies include losses in the suspension system into the total rolling resistance loss.

The road surface texture is divided based on the characteristic length scale, and a systematic review of this can be found in Sandberg et al. (2011b). Overall the surface texture can be divided into the following four groups:

- Unevenness of the road ( $\lambda = 0.5\text{-}50\text{ m}$ )  
 Unevenness covers texture on the biggest length scale which affects the entirety of the vehicle. The vibration due to unevenness is mainly captured in the shock absorber and in the large tire deformation. It is described through international roughness index (IRI). This is thought to be the biggest contribution to the vehicle fuel consumption (Harvey et al., 2016; Pouget et al., 2012)



- Mega texture ( $\lambda = 50 - 500$  mm)  
Mega texture includes sand, pebbles etc. on the road which creates local deformations of the tire. Like unevenness, it is known to have a huge influence on the rolling resistance (Pouget et al., 2012).
- Macro texture ( $\lambda = 0.5 - 50$  mm)  
Macro texture is described by use of mean texture depth (MTD) or mean profile depth (MPD). It is found to have a much smaller influence on the fuel consumption than unevenness and mega texture (Harvey et al., 2016).
- Micro texture ( $\lambda < 0.5$  mm)  
So far no studies has shown that microtexture has a significantly effect on the rolling resistance and not much literature exist about this (Sandberg et al., 2011a).

Another component of the rolling resistance loss is losses related to the pavement deformation underneath the load. When the vehicle drives on a pavement, it will deform underneath the tire. If the pavement is viscoelastic, the deformation will result in energy dissipating into the pavement structure. In order to maintain a constant driving velocity, the lost energy has to be compensated. The amount of additional energy the vehicle engine has to produce to overcome this energy loss is called the *structural rolling resistance loss* (SRR). How big an influence structural rolling resistance has on the overall rolling resistance loss is still unclear. It is widely accepted that the effects from the pavement deformation are smaller than the ones arising from tire deformations, but whether they are insignificant or big enough to be considered important in the total rolling resistance are still debated (Pouget et al., 2012; Bazi et al., 2018; Shakiba et al., 2016; Haider et al., 2011; Sandberg et al., 2012).

We hypothesise that there are two main reasons why there is no clear consensus about the importance of pavement deflection. Firstly, the structural response is found to be highly dependent on external variables like temperature (even daily fluctuations), vehicle speed, the pavement structure, age of the asphalt materials, etc. This makes it difficult to compare result across studies (Harvey et al., 2016). Secondly, it has proven very difficult to devise accurate and robust ways of measuring it (Akbarian et al., 2012). Despite the uncertainties, there seems to be a consensus in the literature that for light and fast vehicles and/or cold road conditions, the structural effects can be neglected. On the other hand, for heavy vehicles driving at low speed and/or under high road-temperatures, the contribution to the rolling resistance from the structural response should not be neglected (Zaabar and Chatti, 2014; Sandberg et al., 2011a). Harvey et al. (2016) stated that the influence has not been comprehensively validated with experimental methods, and research into this field is necessary.

## 1.1 Thesis aim and reading guide

The starting point of this PhD project was to develop a method for measuring the total and structural rolling resistance simultaneously. Based on this, we aimed to evaluate, not

only the total rolling resistance of a given pavement section, but also how big a contribution the structural rolling resistance was to the overall rolling resistance loss. However, due to experimental difficulties, no reproducible values of the total rolling resistance were obtained. Instead, the focus was shifted to the method for measuring structural rolling resistance based on deflection slope measurements obtained using a Traffic Speed Deflectometer. The method provided highly reproducible results and using this, we have investigated the effects of temperature and driving velocity on SRR. Furthermore, spatial variations in SRR and general trends were studied on a  $\sim 10$ km road segment. For estimating SRR accurately, a simple pavement response model was developed. This was used to fit to TSD data and obtain the pavement deflection underneath the load. Furthermore, as this model was founded in physical elements structural characteristics about the pavement measured on were deduced based on the model fitting results.

The thesis is structured into six parts. First, the method for measuring total rolling resistance is presented in part II. Here the work with making the measurements reproducible is presented and discussed, and a way to move forward with the method is proposed. As no useful measurements of the total rolling resistance were obtained, this subject is not discussed further in the rest of the thesis.

In parallel with developing the method for measuring total rolling resistance, a method for measuring the structural rolling resistance (SRR) was developed. This is presented in part III. A discussion about the validity of the simple approach to measuring SRR is made, and a comparison study with an extended method is made using a sophisticated pavement response model. Furthermore, the simple approach for calculating SRR is used on three sets of measurements, studying the influence of temperature and velocity on SRR.

In part IV, a simple pavement deflection model is presented, consisting of a viscoelastic beam on top of a viscoelastic foundation. Before deriving the model, the basic theory about bending of a beam and viscoelastic materials is introduced. Subsequently to deriving the model, a numerical study is presented which includes a discussion of model limits and sensitivity analysis. Furthermore, the influence of the beam complex modulus on the pavement response and considerations about this is presented.

The results from fitting the simple pavement response model to data is presented in part V. In addition to calculating the SRR, these results are used to derive how empirical observations in data can be related to structural changes of the pavement. Furthermore, a pilot study showing how to develop complex modulus master curves for the asphalt is presented here.

The thesis ends with a summarizing discussion in part VI. Here the most important results from the thesis work is summarized and discussed, and ideas for future work is proposed.

## 1.2 List of publications

During the period of the PhD project, the author has participated in the work and preparation of two published papers and one paper draft. All three are attached in Appendix A. Throughout the thesis, the draft paper is referred to by referring to its location in appendix.

- I Nielsen, N. R., Chatti, K., Nielsen, C. P., Zaabar, I., Hjorth, P. G., and Hecksher, T. (2020b). Method for Direct Measurement of Structural Rolling Resistance for Heavy Vehicles. *Transportation Research Record: Journal of the Transportation Research Board*, 2674(5):371–380.
- II Nielsen, N. R., Nielsen, C. P., Hjorth, P. G., and Hecksher, T. (2020a). Measurements of structural rolling resistance at two temperatures. In *Proceedings for Advances in Material and Pavement Performance Prediction II*, pages 220-223.
- III Nielsen, N. R., Nielsen, C. P., Hjorth, P. G., and Hecksher, T. (Draft). Impact of viscous damping in asphalt and foundation - part 1: Theoretical investigation of a viscoelastic beam on a damped Pasternak foundation.



## **Part II**

# **Measuring the total rolling resistance of a truck**



## Chapter 2

# Background

The interest in rolling resistance began in the 1970s where, among other things, the high oil prices motivated investigations into the phenomenon and how to lower it (Sandberg et al., 2012). Initially, the focus of these investigations was mainly on the tires and the materials of which they are made. Big improvements in this area have been made, and from 1980 to 2000 the rolling resistance index of Michelin tires was reduced by approximately 50% (Hall and Moreland, 2001). Later, the focus widened as the significance of pavement and surface texture became clear. Since then, there has been extensive research into the influence of surface texture on rolling resistance (Haider et al., 2011; Lédée, 2016). Currently, inclusion of rolling resistance into the road construction planning process is highly desired, as this could lead to advantages both from an environmental and economic point of view (Zoller, 2014). In order to include rolling resistance as a parameter in asset management systems, it is necessary to have methods that reliably measure rolling resistance properties, allowing for a comparison of different types of pavements. These methods should also be practical for large road networks.

Measuring rolling resistance is not an easy task as the magnitude of rolling resistance force is only about 1% of the tire load and *in-situ* measurements are often influenced by a series of external factors (Sandberg et al., 2012; Zoller, 2014). There are currently multiple approaches to determine rolling resistance, some of which focus on measuring pure tire rolling resistance in a laboratory setting, while other focuses on measuring rolling resistance on real roads.

In the following, a brief overview of the different existing techniques is given. This will not be an in-depth review but it will provide some context to the following chapters. For a systematic in-depth review of the different techniques for measuring rolling resistance see; Sandberg et al. (2012), Zoller (2014) or Andersen et al. (2014).

## 2.1 Existing techniques for measuring rolling resistance

The existing techniques for measuring rolling resistance can be divided into laboratory tests and in-situ test, as they are either conducted on test tracks or regular public roads. Each method has advantages and disadvantages. The choice of method should be based

on the underlying motivation for making the measurements as well as which effects that are studied.

As a in-situ test is performed in "the real world", one can get a much better picture of the real rolling resistance. However, the number of external parameters that can influence the experiment is high and unpredictable. Conversely for laboratory measurements, these uncertainties are removed or controlled when conducting the test.

### 2.1.1 Drum test

The drum test is the most simplified method of the ones presented here and is used for measuring the rolling resistance of tires (Andersen et al., 2014). The basic idea is to have a test tire running on either a smooth steel drum, or on a drum with a custom-made surface. The tire is pressed down with a known applied load, and the energy it takes to maintain a constant velocity is measured. This is then related to the rolling resistance of the tire. The specifics of how the energy is measured depends on the individual setup used.

As the method takes place in a controlled environment, it can also be used to test the influence of surface textures, curvature or air temperature on the tire rolling resistance (Andersen et al., 2014).

The advantage of the technique is that it eliminates many external factors that influences the tire rolling resistance and can thus be used to compare tire rolling resistance across tires. To do so several ISO standards (International Organization for Standardization) are published (Andersen et al., 2014). For an overview of these standards the reader is referred to Sandberg et al. (2011b).

The disadvantage of this method is that it does not take the influence of road properties and potential pavement deflection into account. This limits the applicability of the method when it comes to measuring overall rolling resistance, especially for heavy traffic where pavement deflection is suspected to have a significant effect.

### 2.1.2 Trailer method

A trailer test is a measurement performed with a custom-made trailer hauled by a vehicle. The trailer is equipped with a test tire where the resistance to rolling is measured (Andersen et al., 2014; Sandberg et al., 2011b). The measurements are often performed on test tracks or public roads, and thus gives a more realistic picture of the rolling resistance than the drum measurements.

There exists a variety of trailer methods, each with an individual measurement concept. One of the first systematic reviews of existing measurement techniques was conducted in the MIRIAM project in 2014 (Sandberg et al., 2012; Zoller, 2014). In a follow-up study from 2016, the repeatability of a series of different methods was investigated (Lédée, 2016). One of the main conclusions was that the methods showed an acceptable ability to repeat results obtained within the same day, but a poor ability to repeat results across different days (7-25 % deviation). Severe inconsistencies were found when comparing across methods (up to 40 % difference) (Sandberg et al., 2012; Lédée, 2016). The results of



the study emphasizes the difficulty of in-situ measurement of rolling resistance.

All trailers included in the study measure rolling resistance for passenger cars. Only a few methods for in-situ measurements of heavy vehicle rolling resistance exist and are presented in Zoller (2014). This includes the IPW rolling resistance trailer developed by IPW Automotive GmbH. Here an external trailer is loaded with weights to have approximately 9 t on the front and rear axle respectively and is towed behind the truck. The overall longitudinal force between the truck and the trailer is measured and from this, the rolling resistance is calculated. Another approach is to install a test wheel in the center of a semitrailer. This is done in the IPW rolling resistance semitrailer and the IKA (Institute for Automotive Engineering, RWTH Aachen University) semitrailer "FaReP". The desired test tire can be placed in the specialised holder and the horizontal and vertical forces are measured using a non-rotation force transducer.

Common for all trailer methods is that the influence of air drag and possible longitudinal gradient of the road have to be eliminated. The air drag is often dealt with by making the measurements at low speed ( $< 25 - 30$  km/h).

### 2.1.3 Coast down

In a coast down measurement, a vehicle is accelerated to some speed and then put into neutral gear after which it will decelerate. During the deceleration different parameters such as speed, time and surface texture are monitored. By fitting these to a mathematical model, the rolling resistance can be calculated (Sandberg et al., 2011b; Andersen et al., 2014). The advantage of this method is that it does not require a lot of specialized equipment, like the trailer methods described above. However, there is a lot of uncertainties involved and what is measured is not just the rolling resistance, but rather the overall driving resistance.

### 2.1.4 Fuel consumption test

In a fuel consumption test, the overall fuel consumption of the vehicle is measured while driving. This is then used to compare rigid and flexible pavements, under the assumption that for the flexible pavement there will be an energy loss due to the viscoelastic behaviour of the asphalt layer. Whereas for the rigid pavement, which consists of concrete slabs, it is assumed elastic and thus there is no energy loss due to deformation of the pavement (Balzarini et al., 2018). This means that, assuming all external parameters are the same, the difference between the two surfaces is the contribution from the structural rolling resistance loss. Similar to the coast down method, this method has the advantage that it is easy to perform, as it does not demand a lot of specialized equipment (Sandberg et al., 2011b). However, they are both very general measurements that does not directly say anything about rolling resistance, but provide information about all forces resisting motion of the vehicle. In order to calculate the rolling resistance, either a mathematical model or some physical assumptions have to be used. And these could involve a lot of unknown parameters, resulting in uncertainties. On the other hand, the interest is in

some situations not in the specific rolling resistance, but in the overall energy cost of the vehicles. In these cases, the methods might be sufficient.

## 2.2 Physical measures representing rolling resistance

Rolling resistance can be expressed as the rolling resistance force  $F_{RR}$  or the dissipated energy due to rolling resistance  $P_{RR}$  depending on the situation. The two are connected through the relation:

$$P_{RR} = vF_{RR}, \quad (2.1)$$

where  $v$  is the driving velocity in [m/s]. In the following, we will use the term rolling resistance loss about  $P_{RR}$  and rolling resistance force about  $F_{RR}$ .

Studies suggest that an approximately linear relationship exists between rolling resistance force and the wheel load  $F_L$  (Sandberg et al., 2011b). This has given rise to the dimensionless rolling resistance coefficient, given as

$$C_{RR} = \frac{F_{RR}}{F_L}. \quad (2.2)$$

## Chapter 3

# New method for measuring the total rolling resistance - in theory

We aim to develop a method for measuring the overall rolling resistance of a truck while driving. The method is based on measuring the longitudinal deformation of the tire axle and subsequently correlate this to the overall rolling resistance. In this chapter, the theoretical considerations about how longitudinal axle deformation is correlated with rolling resistance is given. In chapter 4, the experimental design for measuring the longitudinal axle deformation is described as well as the calibration procedure developed for the setup. Through a set of systematic measurements presented in chapter 5, a temperature dependence in the setup was found and an improved setup was developed. The improved setup revealed the need for further understanding of the temperature dynamic in the axle during driving before reproducible measurements of the rolling resistance can be made.

### 3.1 Force and momentum balance in the axle system

In the the ideal case of pure rolling, a stiff tire is driving on a stiff pavement in the  $x$  direction (fig. 3.1a). The wheel has two movements; translational velocity ( $v$ ) and rotational velocity ( $\omega$ ). In this case, the rolling condition states that

$$v = r\omega \quad (3.1)$$

where  $r$  is radius of the tire.

For the tire to move in the  $x$  direction, there has to be a force in the opposite direction at the point where the tire and surface are in contact. This is called the skid resistance and if this is not present, the tire will slide on the surface instead of move forward.

If a tire and a pavement are subject to an external load ( $F_L$ ), both elements will be deformed and the interaction between tire and pavement is not happening in a point but over a surface. As a result, the normal force acting opposite the load is not a point force, but distributed over the contact area. For a stationary tire (fig. 3.1b), the normal force profile is symmetric around the center of mass of the tire, since there is no movement in the vertical direction,  $|F_L| = |F_n|$ .

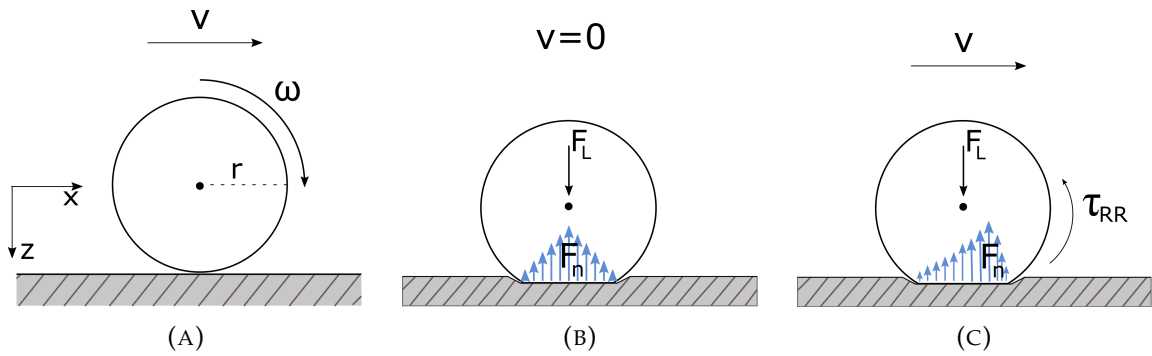


FIGURE 3.1: A) Ideal rolling of a stiff tire on a stiff pavement. B) Deformed stationary tire on a deformed pavement. When there is no motion, the normal force profile  $F_n$  is symmetric around center of mass. C) When the tire is moving, the normal force profile becomes asymmetric and a moment is created around the  $y$  axis,  $\tau_{RR}$ .

For a tire in motion however, the normal force profile is shifted and act asymmetric around the center of mass (fig. 3.1c). This results in a situation where  $F_L$  and the  $z$  component of the normal force  $F_n$  is not located at the same  $x$  position, and consequently a moment around the  $y$ -axis,  $\tau_{rr}$ , are created.  $\tau_{rr}$  acts in the opposite direction of  $\omega$  and is called the rolling resistance, as it resists rotation of the tire.

We now consider the forces in the tire-axle-suspension system for which we aim to measure the rolling resistance. In the experimental setup, the longitudinal deformation of the rear-end tire axle is measured. The rear-end tires is freely rotating, which simplifies the situation as input from the engine does not affect the rotation but only pulls in the tire axle. The tires are attached to the rear-end axle, which is then attached to the trailer through the suspension system (fig. 3.2a). The tire axle bends when the vehicle is in motion as the trailer is pulling it forwards through the suspension system, while the rolling resistance makes the tires oppose movement.

The force at which the trailer is pulling the axle (in the  $x$ -direction) is denoted  $F_{pull}$ . If we assume that the vehicle is driving at constant velocity  $v$ , no acceleration is present and as a result,  $F_{pull}$  is counterbalanced by an opposite directed longitudinal force,  $F_{long}$  (fig. 3.2b). This opposing force is often used to illustrate the rolling resistance force as it counteracts movement of the vehicle. However, when observing the system from the side (fig. 3.2c), it is not trivial at which point the force should be originating, as it is a sum of various contributions. Rather than considering the rolling resistance through this longitudinal force, we consider the moments created in the tire.

As sketched on figure 3.2c,  $F_{pull}$  is acting in the  $z$  location equal to the axle. In addition, the horizontal component of the skid resistance is acting in the  $z$  location corresponding to the place where the tire touches the pavement, located a distance  $h$  from the axle. As a result, a moment around the  $y$  axis  $\tau_{pull}$  is created, making it move forward. The moment

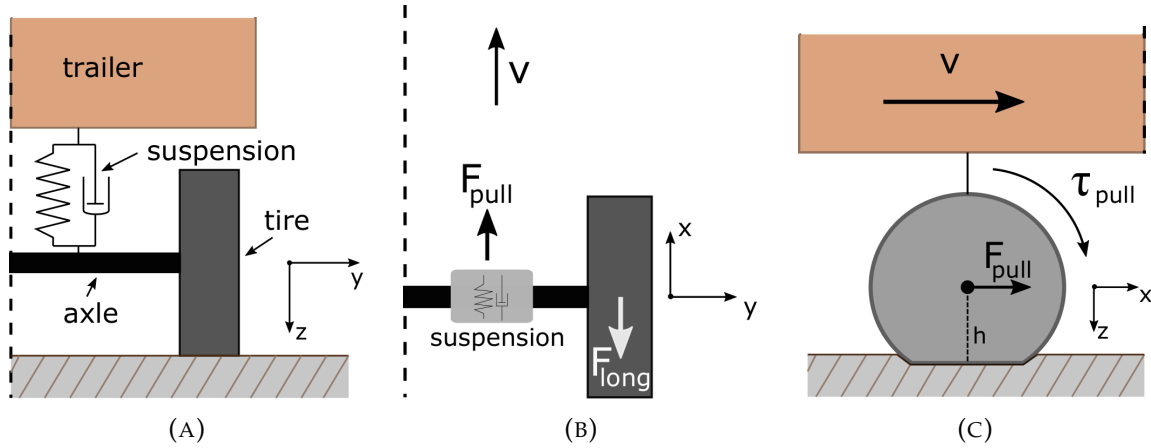


FIGURE 3.2: Sketch of the tire-axle-suspension system of a vehicle seen from different angles. In the vehicle used for the measurements, the trailer is connected to the axle through a suspension system, here illustrated as a spring-damper system. The vehicle is driving in the positive  $x$  direction. A) The system seen from behind the trailer. B) The system seen from above. C) The system seen from the side.

can be expressed as a function of the pulling force and distance  $h$ ,

$$\tau_{pull} = F_{pull}h. \quad (3.2)$$

Assuming constant speed, and thus constant angular velocity, the sum of moments around the  $y$ -axis must equal zero. In the clockwise direction, only the moment  $\tau_{pull}$  acts. In the counterclockwise direction, all moments resisting rotation of the tire acts. We divide the counterclockwise moments into the rolling resistance  $\tau_{RR}$  and all other possible moments acting counterclockwise denoted by  $\tau_b$ .

$$\tau_{pull} = \tau_{rr} + \tau_b. \quad (3.3)$$

In an experimental setup, such moments could originate from the bearings inside the wheel.

The dissipated energy in a rotating system is given by the moment and angular velocity, and thus we can find the rolling resistance loss as

$$P_{RR} = \tau_{RR}\omega = (\tau_{pull} - \tau_b)\omega. \quad (3.4)$$

Using equation (3.2) and (3.1) gives

$$P_{RR} = F_{pull}h\frac{v}{r} - \tau_b\omega. \quad (3.5)$$

If we assume that the deformation of the tire is small, then  $h = r$  and we get

$$P_{RR} = F_{pull}v - \tau_b\omega. \quad (3.6)$$

Neglecting the energy loss in the bearings, the rolling resistance loss can be found as

$$P_{RR} = F_{pull}v.$$

### 3.1.1 Measuring $F_{pull}$ through strain gauges

Above we derived how the rolling resistance loss  $P_{RR}$  can be found from the pulling force acting on the axle,  $F_{pull}$ . When the vehicle pulls in the tire axle, it results in a bending of the axle which can be measured by use of *strain gauges*.

A strain gauge is a measuring device that explores the strain-resistance relationship of electrical conductors (Hoffmann, 2017). The gauge is a small electric conductor which is glued to an object. When the object is deformed, so is the gauge. When the object, and thus the gauge, is stretched the resistance in the gauge will increase and when it is compressed, the resistance will decrease. The technical details about the strain gauges used in the experimental setup is described in detail in section 4.1.

The strain gauges are mounted such that they measure the longitudinal strain of the axle close to the tires. This means that losses in the suspension are not included in the measurements. Through a calibration process (explained in section 4.3), the measured deformation of the axle is correlated with the applied force  $F_{pull}$  and from this  $P_{RR}$  is calculated.

### 3.1.2 Moment in the axle - how we measure $\tau_b$

In order to get the best estimate of the rolling resistance loss, any contribution from unrelated counterclockwise moments should be removed. We speculate that the biggest contribution to the term  $\tau_b$  is energy losses in the bearings. The contribution from the bearings is accounted for by measuring the twisting of the tire axle.

As we measure on a freely rotating tire, any twisting of the axle will be due to resistance in the bearing. This creates a moment around the  $y$ -axis (thus the axle direction) and the axle is twisted. This effect is measured using a set of strain gauges mounted perpendicular to the axle direction.

## Chapter 4

# New method for measuring the total rolling resistance - in practice

In the previous chapter, we described how the rolling resistance loss of a non-driven wheel on a truck can be correlated with the longitudinal pulling force on the axle. The longitudinal pulling force is measured by use of strain gauges. In this chapter, background information about strain gauges and the technical information about the measurement setup are presented, followed by the calibration routine of the equipment.

### 4.1 Strain gauges

The following section is based on information from Hoffmann (2017).

The strain gauges used to measure the deformation of the tire axle are *electrical resistance* strain gauges. These types of strain gauges are used to measure the applied stress on an object based on its deformation. They exploit the relation between electrical resistance and strain in an electrical conductor, which means that the deformation of the conductor can be found by measuring the change in electrical resistance. If the gauge is mounted on top of an object, and we assume that any deformation of the object is transferred to the gauge, then the measured change in resistance in the strain gauge can be converted to strain of the object. Assuming small deformations and an elastic material, the measured strain  $\varepsilon$  of the object is related to the applied stress  $\sigma$  on the object by use of Hooke's law,

$$\sigma = E\varepsilon. \quad (4.1)$$

Where  $E$  is the Young's modulus of the object material.

This type of strain gauge was invented in the late 1930's by Arthur Claude Ruge and quickly became popular as they are light and thin, allowing them to be glued on to the measured object. This ensures that the strain is transferred without loss.

On figure 4.1 a sketch of a strain gauge is shown. It consist of a carrier metal with a measuring grid of conducting material on top. The measuring grid ends in two connections where wires can be connected. When exposed to mechanical stress, such as tensile or compression forces, the resistance of the electrical conductor used for the measuring grid will change.

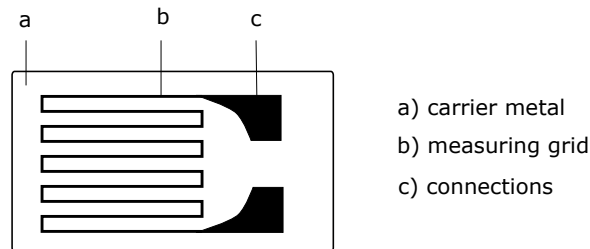


FIGURE 4.1: Strain gauge. It consists of a carrier metal with a measuring grid of conducting material on top. The measuring grid starts and ends in connections where wires can be connected.

### Temperature effects

When choosing a material for the strain gauges, a metal that exhibits a low or no temperature dependence in the electrical resistance is typically chosen in order to reduce temperature effects. However, there will still be some. Temperature effects on the strain gauges can be divided into three categories;

- 1) effects due to high temperature level,
- 2) effects due to variations in temperature during the measurement,
- 3) thermal drift.

High temperature levels can affect the materials used for mounting of the strain gauges to the object, and thus how well it binds to the object measured on. This might influence how well strain of the object is transferred to strain of the gauge and result in a measurement error.

Fluctuating temperatures during the measurement mainly affect the offset of the strain gauge, which is the signal that the strain gauge gives when there is no deformation. The offset is determined through a calibration process, however if it changes as a function of temperature during the measurement it can give rise to a systematic measurement error. Thermal drift is a non-reversible process primarily caused by micro-structural changes or oxidation of the measuring grid. This affects the offset measurements.

There are different actions one can use to counteract the temperature effects. One is to make frequent calibrations of the system. This will compensate for potential thermal drift. Another way the temperature effects can be compensated is through the structure of the measuring circuit.

When the strain gauges are mounted on an object, it is placed in a measuring circuit. For accurate measurements a *Wheatstone* bridge circuit is used. Such a circuit is illustrated on figure 4.2.

The fundamental idea of a Wheatstone bridge circuit is that four resistances  $R_1 - R_4$  are placed with two on each side of the object. The resistances are connected through leads and in points 2 and 3, the bridge excitation voltage  $V_s$  is connected. This is where the voltage is applied to the system. In points 1 and 4, the bridge output voltage  $V_0$  is placed



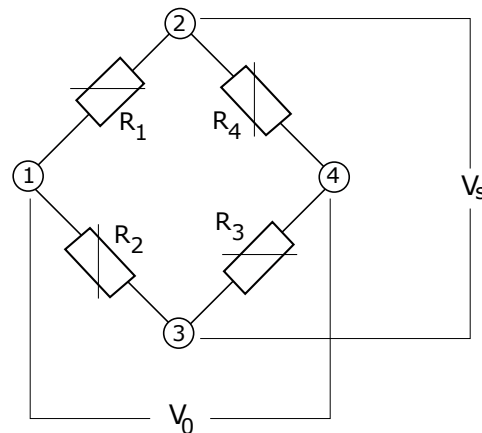


FIGURE 4.2: Wheatstone bridge circuit. The resistances  $R_1$ - $R_4$  is connected through leads. In points 2 and 3 the bridge excitation voltage  $V_s$  is connected. In points 1 and 4, the bridge output voltage  $V_0$  is placed and thus the measurement signal is recorded here.

and hence the measurement signal is recorded here. When no deformation is present, the bridge is in balance which means that  $\frac{R_1}{R_2} = \frac{R_3}{R_4}$  and  $V_0 = 0$ . But when the object on which the bridge is mounted is deformed, the bridge will be unbalanced due to the difference in voltage from the different resistances  $R_n$ .

The Wheatstone bridge circuit design exists in various versions, where one or more of the active strain gauges are replaced with bridge completion resistances. This is known as a quarter bridge (only  $R_1$  is an active strain gauge), a half bridge ( $R_1$  and  $R_2$  is active strain gauges), a diagonal bridges ( $R_1$  and  $R_3$  is active strain gauges) or a full bridge (all resistances are active strain gauges).

The advantage of a full bridge with respect to temperature effect is that the strain gauges are placed in close distance of each other, which means the thermal effects on connecting leads are very small. Furthermore, the temperature effect from the object in the form of thermal strain is affecting all four strain gauges in the same way, and the influence on the bridge unbalance will be small. Thus, it is said to have a good temperature compensation. However, if both sides of the bridge is not subject to the same thermal effect, e.g. if there is a temperature difference in the object measured on, this can create an difference in resistance and result in measurement error.

## 4.2 The measurement setup

The measurements are conducted using a full size truck trailer, shown on figure 4.3. Inside the trailer, around the rear-end axle, a beam with Doppler lasers is mounted to measure the pavement deflection underneath the right rear-end tire during driving. This technology is used in part III of this thesis to measure the structural rolling resistance and is

explained in details in chapter 8. The measurement trailer will be referred to as the TSD trailer in the following.

In addition to the Doppler lasers, the trailer is equipped to measure the following other quantities (only equipment related to this project are listed):

- The driving velocity is measured using an odometer located behind the rear-end tire.
- Air and road temperature is measured continuously. The road temperature is measured using infrared lasers mounted close to the right tire, and thus this measures the road surface temperature.
- The driving velocity is controlled by cruise control in order to maintain a constant driving velocity.
- Adjustable loads.  
The trailer has an external weight system such that two external weights on  $\sim 6$  and  $\sim 1$  tonnes can be added to the undercarriage. By using these, we can obtain four different axle load configurations ranging 6-10 tonnes (3-5 tonnes on each tire). The absolute weight of the truck may vary from day to day, as equipment inside the trailer is moved in and out of the trailer. Furthermore, the tire load on the left and right tire is not the same, as equipment inside the trailer is located on top of the right tire. The exact axle load in both sides is measured continuously during measurements by use of vertical strain gauges.
- Temperature of the rear-end axle.  
Through systematic analysis of the initial data, we found indications that the temperature of the axle changes during the measurements, to a degree where it affects the measurements. To account for temperature differences a temperature sensor was mounted on the right hand side of the axle close to the strain gauges. The temperature sensor measures the axle temperature with a frequency of 384 Hz and thus provides a well resolved signal of axle temperature as a function of time.

### 4.2.1 Strain gauge setup

For this project, we have mounted three measuring circuits in each side of the rear-end tire axle. Using these we measure vertical bending strain, horizontal bending strain and torsion strain. On figure 4.4, a schematic sketch of the tire axle is shown with the location of the strain gauges inserted. As seen they are placed close to the tires, in between the tire and suspension attachment.

The system of strain gauges for vertical bending strain are mounted on top and bottom of the axle, and the system of strain gauges for the longitudinal bending strain are mounted in front and behind the axle compared to driving direction. Both are oriented such that they measure bending along the axial direction. The system of strain gauges that measures the torsion strain are oriented such that the active direction of the strain



FIGURE 4.3: The Traffic Speed Deflectometer vehicle used in this study. Strain gauges are mounted on the rear-end axle.

gauges are perpendicular to the axle direction. As a result, when the beam experiences torsion, they will be stretched or compressed.

Each strain gauge circuit is placed in a full Wheatstone bridge configuration with two strain gauges on each side of the axle. The strain gauges are glued to the axle and then covered with a coat consistent of several layers in order to protect them from both water and mechanical damage. The full Wheatstone bridge circuit ensures a high sensitivity to strain as well as it minimizes effect of temperature.

When reporting raw strain gauge signals, we use the unit *least significant bit*, lsb. This is the output when transforming the analog strain gauge signal into a digital one.

More in depth details about the measurement system, the mounting of the strain gauges to the axle and the considerations that has been involved in this process is not within the scope of this thesis and will not be covered here.

### 4.3 Calibration procedure for strain gauges

In order to convert the measured electrical resistance in the strain gauges to applied load on the axle, a calibration process has been developed for each type of strain. Calibration procedure for the vertical strain gauges were established before this project started, whereas procedures for longitudinal and torsion strain gauges were developed in this project. The procedures depend on each other and described below.

#### 4.3.1 Vertical strain gauges

The vertical strain gauges are calibrated using the adjustable loads and a specialized weight which can measure the weight underneath the tires.

A series of different loads is applied to the axle and the vertical strain signal is measured simultaneously. An example of the calibration procedure is seen on figure 4.5a. On figure 4.5b, a plot of the measured strain signal as a function of the applied load is shown.

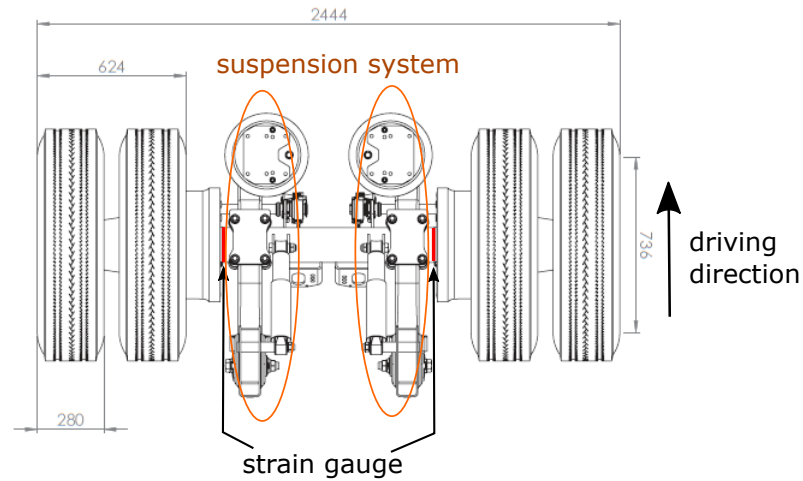


FIGURE 4.4: Rear-end tire axle seen from above. The strain gauges are located in between the tires and the suspension system, marked with red. Each strain gauge circuit is placed in a full Wheatstone bridge configuration with two strain gauges on each side of the axle. This ensures a high sensitivity to strain and minimizes the effect of temperature.

A linear relation between load  $F_L$  and vertical strain gauge signal  $G_v$  is found,

$$G_v = \alpha F_L + \beta. \quad (4.2)$$

$\alpha$  and  $\beta$  will vary over time due to drift in the system, and consequently, this procedure is conducted regularly to get a proper calibration of the equipment.

### 4.3.2 Longitudinal strain gauges

For the longitudinal strain gauges, a linear relation between strain and load is assumed. As a result, a linear relationship between the measured strain gauge signal  $G_l$  and the applied pulling force is assumed.

$$G_l = \alpha F_{pull} + \gamma \quad (4.3)$$

The slope  $\alpha$  is assumed to be the same as for the vertical strain gauges, and thus is reused from the vertical calibration process.

The offset  $\gamma$  is found by measuring the strain signal when the pulling force is zero. This is done by having the stationary TSD trailer on level ground with no brakes pulled. On figure 4.6, a plot of the longitudinal strain vs time for the calibration procedure is shown. The truck starts in a stationary position, is then moved a few meters forward, stopped and backed up. The procedure is repeated 2-3 times. In figure 4.6, the stationary

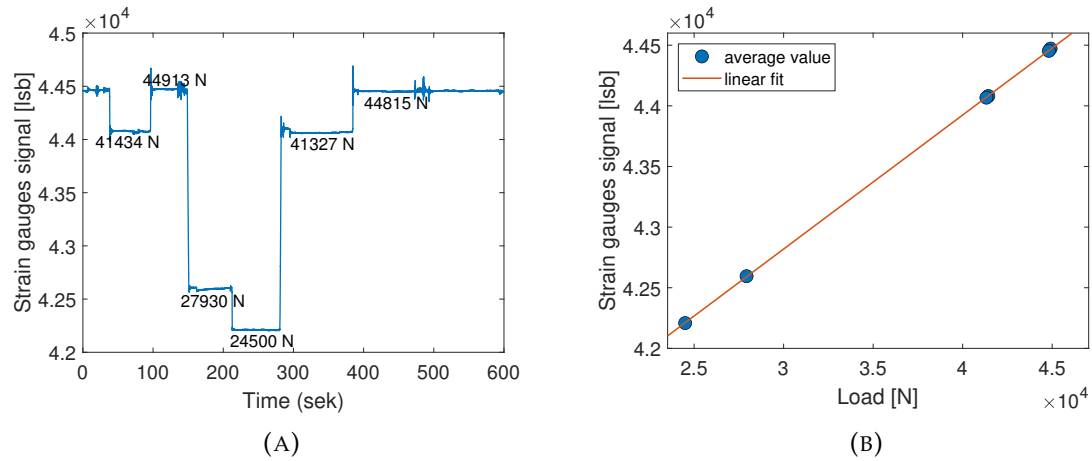


FIGURE 4.5: The vertical strain gauges are calibrated using the adjustable loads and a specialized weight which can measure the weight underneath the tires. A) The vertical strain gauge signal  $G_v$  is measured while changing the axle load. B) A linear relationship between  $G_v$  and the axle load  $F_L$ .

positions corresponds to the marked areas with constant signal and  $\gamma$  is determined as the average value of these.

### 4.3.3 Torsion strain gauges

The torsion strain gauges requires calibration to correlate a given torsion in the axle  $\tau$  with the corresponding strain gauge signal  $G_T$ . In order to do so, we exploit that when the suspension is pulling in the axle, it creates a moment as it is not attached directly on the horizontal plane. This moment can be written as

$$\tau = \bar{F}_{pull} \times r_{axle}, \quad (4.4)$$

where  $r_{axle}$  is the radius of the tire axle. Assuming that the pulling force acts perpendicular to the axle this becomes

$$\tau = F_{pull} r_{axle}. \quad (4.5)$$

We conduct a measurement where the axle is forced to twist. This is done by having the rear brakes pulled and moving the truck forwards and backwards. This means that the trailer/suspension system will be pushing and pulling the axle, forcing a twisting of the axle. The corresponding pulling force is measured using the longitudinal strain gauges. A linear relation between  $F_{pull}$  and the torsion strain gauge signal  $G_T$  is found (figure 4.7).

$$F_{pull} = aG_T + b, \quad (4.6)$$

$$\tau = r_{axle}(aG_T + b). \quad (4.7)$$

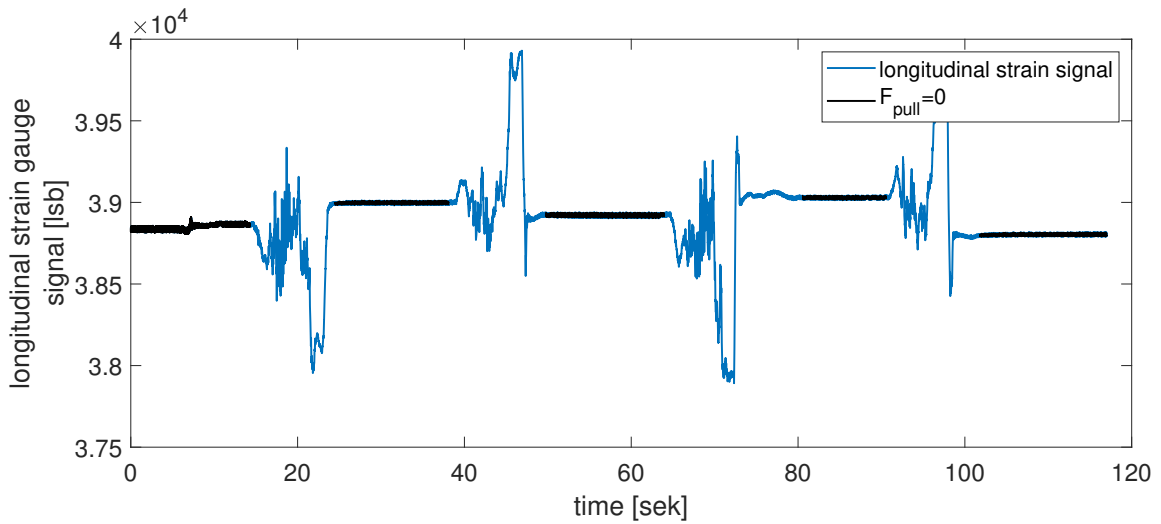


FIGURE 4.6: A linear relation between strain and load is assumed for the longitudinal strain gauges. The offset value is found based on a measurement of the strain gauge signal when no pulling force is applied (black lines). This measurements was made several times with the truck moved forwards and backwards in between in order to find a stable offset signal.

Note that both positive and negative  $F_{pull}$  present on figure 4.7 as the twisting was made in both directions.

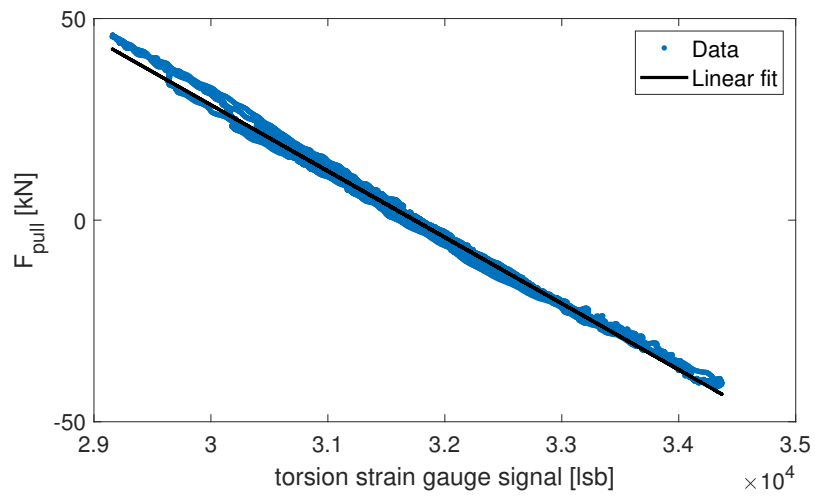


FIGURE 4.7: A linear relation between measured torsion strain gauge signal  $G_T$  and pulling force is found. Using this, the torsion in the axle  $\tau$  is correlated with  $G_T$  using  $\tau = F_{pull}r_{axle}$ , where  $r_{axle}$  is the radius of the tire axle.





## Chapter 5

# Axle deformation data

### 5.1 Preliminary measurements

Four series of preliminary measurements was made at Kystholmen, Copenhagen. For each series, measurements was made at 30, 45 and 60 km/h and each measurement was repeated three times in order to test reproducibility. The order of driving velocities is mixed between the different series in order to avoid systematic biases (see tab. 5.1 for an overview).

For each measurement in the series, a time series of  $P_{RR}$  is obtained over approximately 2 km. A vital assumption in the derivation of  $P_{RR}$  is that the measurements were conducted under constant driving velocity. For this reason, the measurements are cut-off such that only data under constant driving velocity was used (fig. 5.1a). The different measurements can be compared, either within a measurement series or across measurement series, in the form of time series (fig. 5.1b) or using an average value (fig. 5.1c). Using the three repeated measurements at same driving velocity, one average value for the particular driving velocity was obtained. The standard deviation of the three repeated measurements are illustrated through error bars (fig. 5.1c).

#### 5.1.1 Reproducibility of the method

Before the method can be used to state anything conclusive about the rolling resistance, reproducible values of  $P_{RR}$  have to be obtained. There are two types of reproducibility to consider; reproducible results between measurements conducted on the same day, and between measurements conducted over several days. The latter has been found difficult for other methods (Sandberg et al., 2012).

Initial analysis of data shows poor reproducible for the three repeated measurements at same driving velocity, conducted in the same data. This was seen for data in series B, C and D. These measurement series are characterised by not having subsequent measurements of the same driving velocity, but alternate between velocities. The effect of the order at which measurements is collected is investigated by plotting the average value for each data set as a function of time from the first measurement (fig. 5.2a).

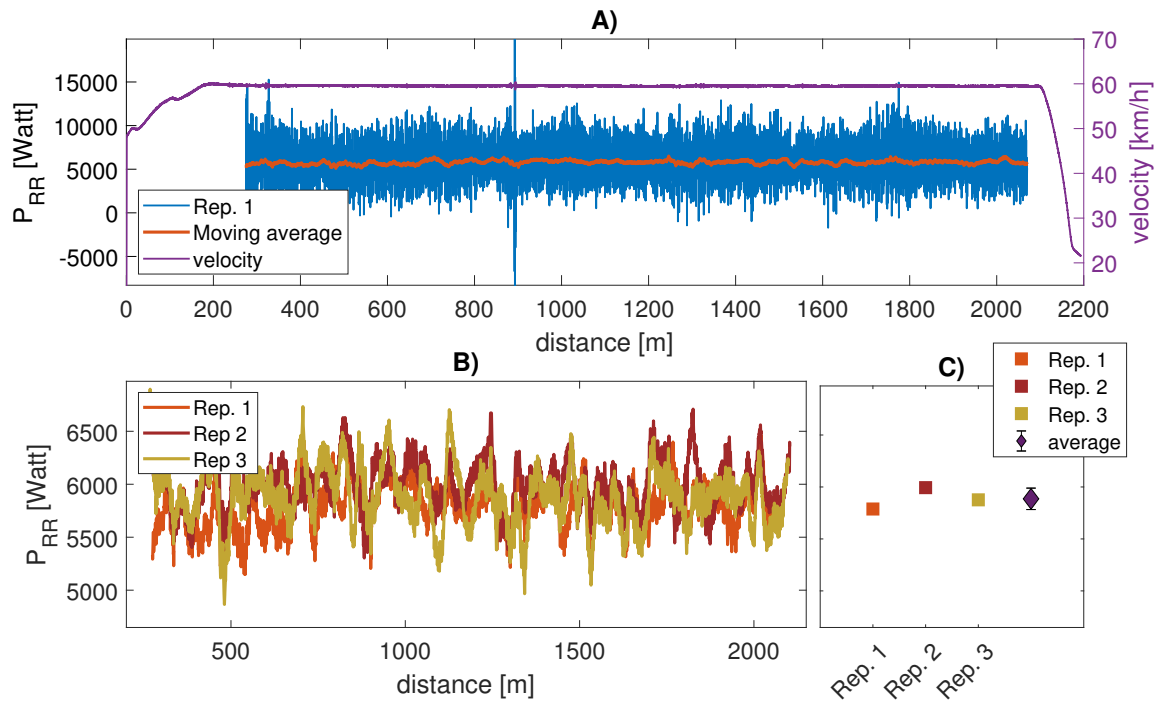


FIGURE 5.1: A) For each given driving velocity a time series of  $P_{RR}$  is obtained. The series is cut-off to ensure constant driving velocity. In order to better evaluate the underlying behaviour, we use a moving average filter with cut-off frequency 1 Hz. Moving average is a lowpass filter which removes the high frequency part of the signal, and thus only shows low frequency behaviour. B) The three repeated measurements at same driving velocity are compared using the moving average filtered signal. C) In order to compare across different measurement series, an average of the time series is obtained for each measurement. Furthermore, an average across the three repeated measurement sets can be found, with the standard deviations illustrated through error bars.

TABLE 5.1: Four preliminary measurement series was conducted with changing order of driving velocity. The order for each measurement A-D is listed here.

# Measurement	A	B	C	D
1	60 km/h	60 km/h	60 km/h	30 km/h
2	60 km/h	45 km/h	45 km/h	45 km/h
3	60 km/h	30 km/h	30 km/h	60 km/h
4	45 km/h	60 km/h	60 km/h	30 km/h
5	45 km/h	45 km/h	45 km/h	45 km/h
6	45 km/h	30 km/h	30 km/h	60 km/h
7	30 km/h	60 km/h	60 km/h	30 km/h
8	30 km/h	45 km/h	45 km/h	45 km/h
9	30 km/h	30 km/h	30 km/h	60 km/h

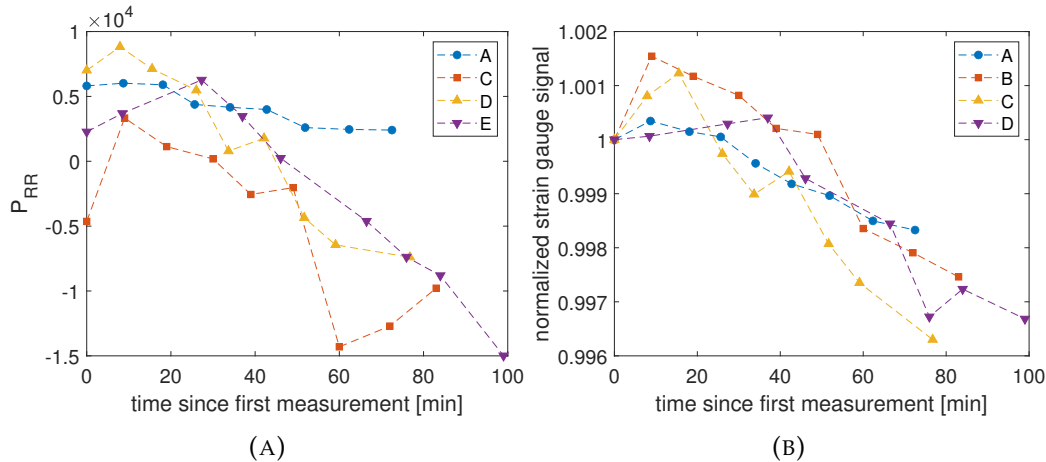


FIGURE 5.2: Four preliminary measurement series of the rolling resistance loss  $P_{RR}$  were made in order to study the reproducibility of the method. A)  $P_{RR}$  as a function of time from first measurement. A clear underlying systematic trend was seen in data. B) Data is shown in form of longitudinal strain gauge signal normalized with the first value. This was done in order to compare data without introducing errors from the calibration process.

Figure 5.2a reveals an underlying systematic trend in data, in which the signal is decreasing over time. The trend seems to be similar for measurement B, C and D. Furthermore, we find that the calibration procedure is not sufficient, as we get negative values which is non physical. The calibration procedure is performed before starting the measurements,  $t < 0$ , and thus it does not capture the time dependent features found in data. In order to study the phenomenon without any influence of the calibration process, the raw Strain gauge signal is plotted as a function of time from the first measurement (fig. 5.2b). The signal is normalized with the value of the first measurements to enabling comparison across measurement series. A clear decreasing trend in the strain gauge signal is found.

The preliminary analysis of data indicates an underlying systematic measurement error. The origin of this error is speculated to arise from the following sources:

- Drift in the strain gauge system.  
This is investigated through static measurements where the sensors is turned on over a long period of time ( $\sim 16$  hours). Some drift was found in the system, but not in the order of magnitude as seen in figure 5.2b and we hypothesize that frequent calibration of the strain gauges could eliminate this.
- Losses associated with the suspension system.  
As the suspension system is located above the axle, we assume that effects in this do not affect the measured axle deflection. This assumption might not be valid and the influence of the suspension system was investigated by Fourier analysis of the vertical strain gauge signals. Furthermore, an analysis of the behaviour of the suspension system was made using simple spring-dashpot models. No obvious time dependent behaviour was found in the vertical data or by the modelling. However, we found that a thorough analysis of the suspension system required more elaborate modelling with nonlinear springs and dashpots. This approach was not pursued further.
- Temperature effects in the system.  
Temperature effects could arise from a number of places such as heating of the tires while driving, effects in the bearings, increased axle temperature etc. The strain gauge circuits were arranged in a full Wheatstone bridge which in theory should minimize the effects of temperature. However, if the influence of temperature is unevenly distributed across the bridge or large temperature fluctuations is appearing, this might influence the measurements. An experiment was constructed to investigate the effects of temperature.

## 5.2 Temperature effects in the system

A preliminary study was made investigating how the temperature of the tire axle changes during a set of measurements. The hypothesis is that when the truck decelerate, the brake disks heat up and since these are mounted in extension of the end of the axle, this leads to diffusing of heat into the axle. To investigate this hypothesis we measured the axle

temperature manually with an infrared thermometer during series D (tab. 5.1). A consequence of this is that the truck has to hold still while measuring and thus the axle temperature is measured in between the data sets. However, this gives us an idea whether any temperature changes is occurring in the axle and if so, an estimate of how big a temperature change is happening during the measurements.

On figure 5.3, a plot of the axle temperature as a function of time since first measurement is shown, together with the longitudinal force. The temperature was measured both in front and behind of the axle, in order to investigate if wind cooling effect on the axle creates a temperature gradient through the axle. Furthermore, the temperature of the brake drum was measured as well as the air and road temperature for each measurement.

A large increase in the axle temperature was found, with an increase of approximately  $30^{\circ}\text{C}$ . The measurement was performed a cold October morning, with an initial axle temperature of approximately  $4^{\circ}\text{C}$  ( $t=-2400$  s) and thus the axle was expected to heat up while driving from the Greenwood Engineering parking lot to the road section measured on. However, a converging axle temperature was not seen as this increased monotonically during the measurements. No big temperature change between the front and back of the axle was observed.

Based on the preliminary investigation of axle temperature, we concluded that this should be investigated further and a systematic experiment was designed to measure the temperature dependence of the strain gauges.

### 5.2.1 Temperature dependence of the strain gauge signals

An experiment was made in order to establish if the strain gauges are temperature dependent. In this, the tire-axle was heated as much as possible and afterwards the truck was parked in a garage to cool down. The axle was heated up by doing a lot of acceleration and braking with the vehicle, thus heating the brake disks. The axle temperature was monitored while the axle cooled down. For this purpose, a temperature sensor was mounted on the right side of the axle near the strain gauges, measuring the axle temperature continuously.

As the parked truck was stationary and no external forces were applied upon it, the strain gauge signal was expected to be constant as a function of time. On figure 5.4a-c, the strain gauge signal from the longitudinal, vertical and torsion strain gauges is seen respectively. A clear non-constant behaviour was found. On figure 5.4d, the axle temperature is shown as a function of time. The temperature started at an initial temperature of  $42^{\circ}\text{C}$  and end at  $20^{\circ}\text{C}$ .

The relationship between longitudinal strain gauge signal at no applied force  $G_l(F_{pull} = 0, T)$  and temperature were investigated and results are showed on figure 5.5. A second order polynomial was found to fit the correlation well, giving the relation

$$G_l(F_{pull} = 0, T) = \alpha T^2 + \beta T + \gamma \quad (5.1)$$

$$= -1.14T^2 + 22.71T + 33976 \quad (5.2)$$

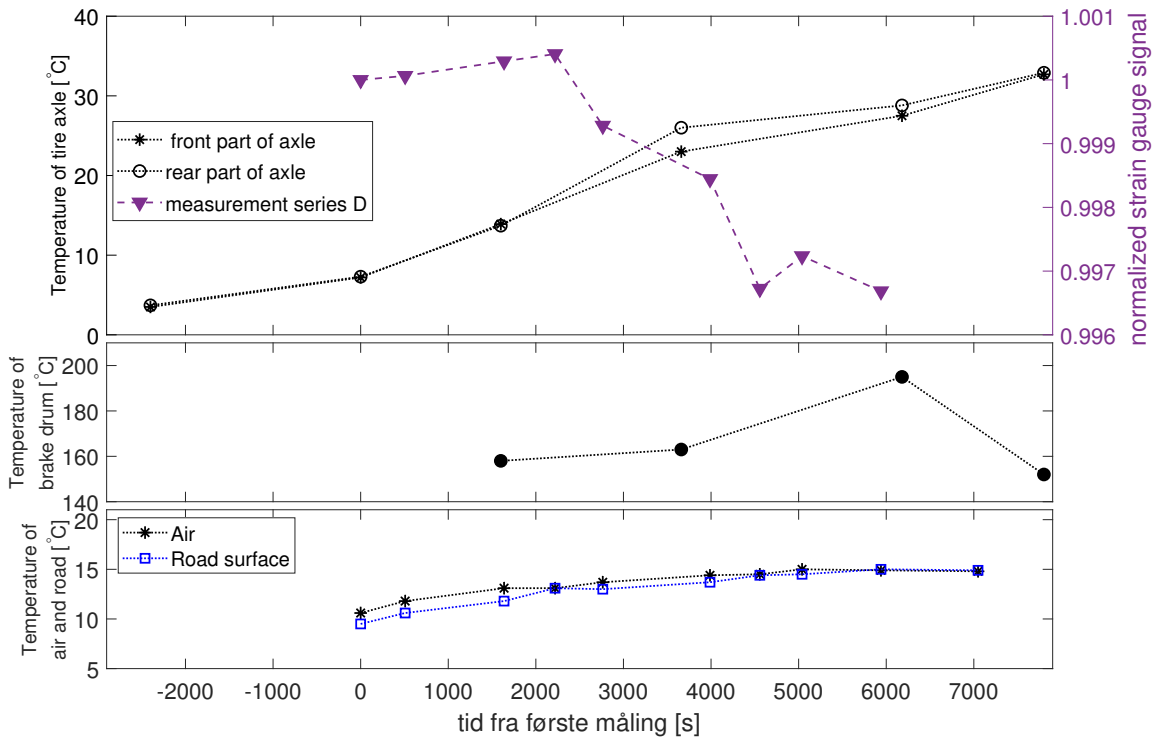


FIGURE 5.3: During measurement series D, the temperature of the tire axle (top) and brake drum (middle) were measured manually in order to investigate potential change. We find a large increase in the axle temperature, with an increase of  $\sim 30^{\circ}\text{C}$ . No big change between front and back is observed. Measurements at  $t < 0$  are performed before the truck leaves the parking lot and the last measurement at  $t = 7800\text{s}$  is made at the arrival in the same parking lot. Air and road temperature is measured simultaneously with the strain gauge signals and an average value for each measurement set is shown (bottom).

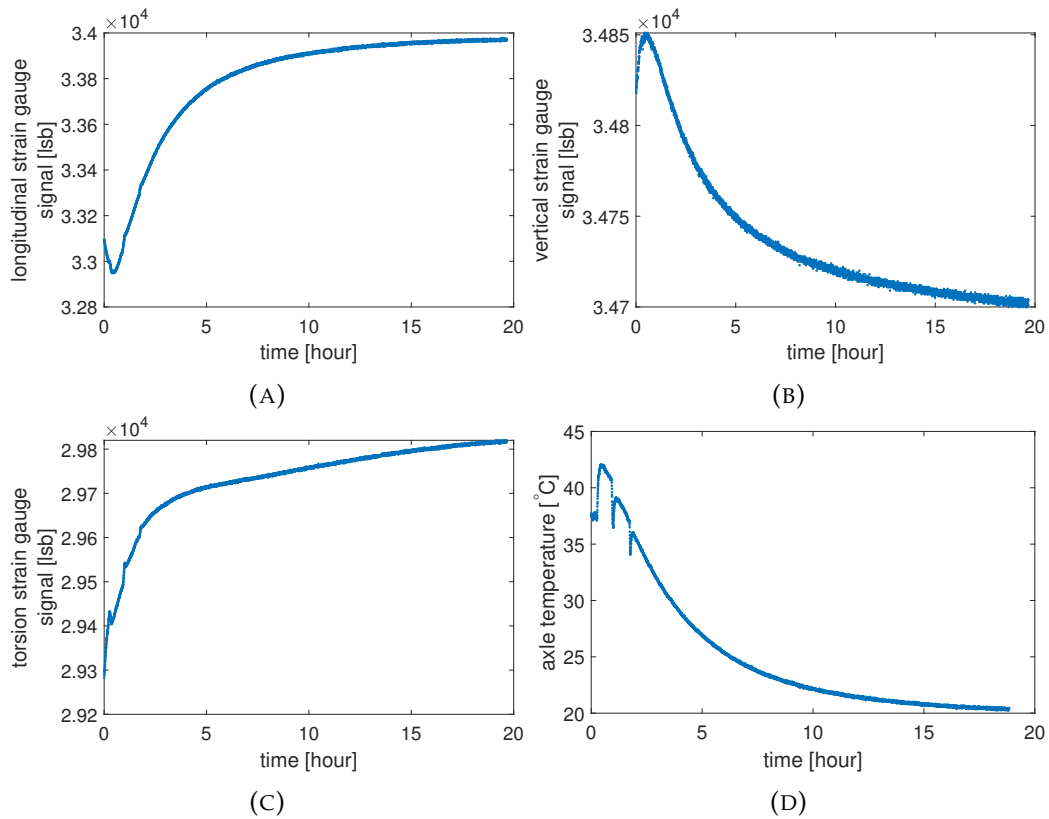


FIGURE 5.4: An experiment was conducted where the axle is heated and subsequently left to cool while the A) longitudinal bending strain, B) vertical bending strain, C) torsion strain and D) axle temperature is measured. As all other parameters is hold constant (no applied load) the dependence in strain signal is due to temperature effects.

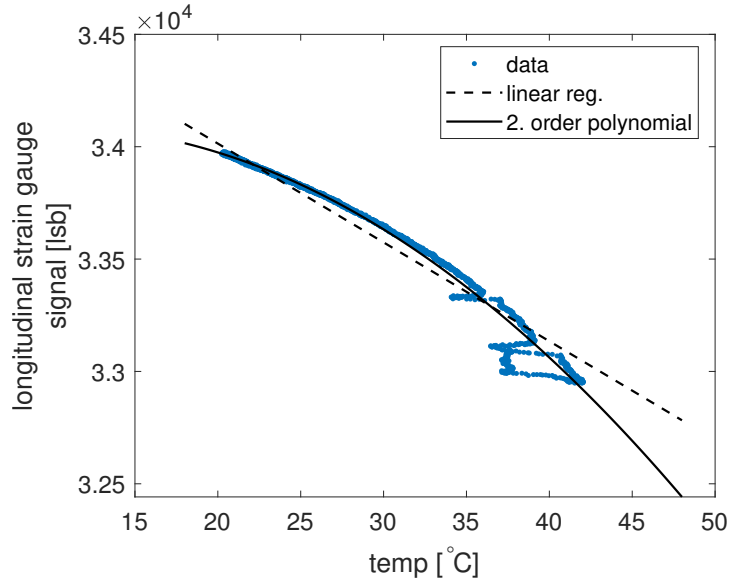


FIGURE 5.5: A second order dependence between longitudinal strain gauge signal  $G_l(F_{pull}, T)$  and axle temperature  $T$  is found when no pulling force is applied.

In section 4.3.2, a linear relation between pulling force and strain gauge signal was assumed, using coefficients that were not temperature dependent. However, this experiment clearly illustrates that the offset is in fact are temperature dependent, and thus the relation is

$$G_l(F_{pull}, T) = aF_{pull} + G_l(F_{pull} = 0, T). \quad (5.3)$$

A temperature increase from 7°C to 32°C, as seen on figure 5.3, results in a decrease in offset value on  $\Delta G_l(F_{pull} = 0, T) = -543$  lsb. This is  $\sim 1.5\%$  of an average offsets calculated using the standard calibration procedure. Relating this to force (using a typical scaling factor  $a = 0.12$  lsb/N) gives

$$\Delta F_{pull} = \left( \frac{G_l(F_{pull}, T) - 1.14 \cdot 32^2 + 22.71 \cdot 32 + 33976}{0.12} \right) - \quad (5.4)$$

$$\left( \frac{G_l(F_{pull}, T) - 1.14 \cdot 7^2 + 22.71 \cdot 7 + 33976}{0.12} \right) \quad (5.5)$$

$$= 4220N \quad (5.6)$$

If we assume that the total rolling resistance is 1% of the load ( $\sim 5$  tonnes), this corresponds to  $F_{RR} = 490N$ . Thus, the errors introduced into the measured rolling resistance due to temperature effects was almost 10 times as large as the quantity we aimed to measure. This result depended on the specific calibration values obtained, but it clearly



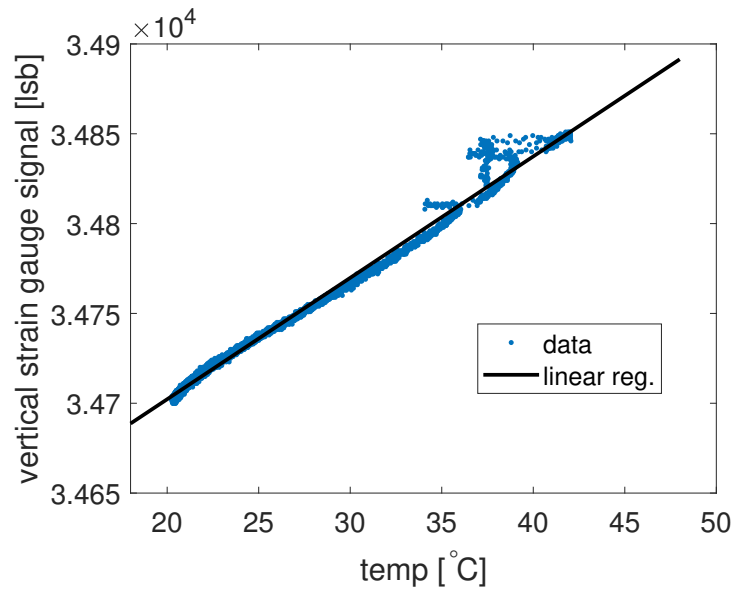


FIGURE 5.6: A linear correlation between vertical strain gauge signal and temperature is found, given by  $G_v(F_L = 0, T) = 6.8T + 34567$ .

showed that the temperature dependence was bigger than the rolling resistance signal we were trying to measure, and thus can not be neglected in the described setup.

A similar analysis can be made of the vertical strain gauges. The relation between strain signal and temperature is shown on figure 5.6. The axle was lifted from the ground by several jacks such that the vertical load on the axle, in the end near the tires, during the measurement was approximately 0 N. Thus, the temperature dependence found in figure 5.6 applies to the offset  $G_v(F_L = 0, T)$ ,

$$G_v(F_L = 0, T) = 6.8T + 34567 \quad (5.7)$$

A change in temperature from  $7^\circ\text{C}$  to  $32^\circ\text{C}$  thus leads to a change in vertical force on

$$\Delta F_L = -1416\text{N}. \quad (5.8)$$

The vertical strain gauges are used to measure the dynamical or stationary load of the truck. For the maximum load, the steady axle-load is approximately 49000 N, and thus the influence of a jump in temperature of  $25^\circ\text{C}$  is  $\sim 2\%$  of this quantity. Consequently, the influence of temperature on the vertical strain gauge sensors is small.

### 5.3 Test of simple temperature compensation

We aimed to test if the simple relation between strain gauge offset and temperature found in equation (5.3) would be enough to compensate the measured  $P_{RR}$  value for temperature

effects. To do so, a set of measurements were made with the new setup on a highway making three repeated repetitions at constant velocity of 80 km/t.

The axle temperature was found to increase steadily from 23°C to 27°C during the measurements (fig. 5.7a). The measured longitudinal strain gauge signal is plotted on figure 5.7b using a moving average filter. A clear difference between the first signal at  $\sim 24^\circ\text{C}$  and the two subsequent signals was observed. Using the temperature dependent relation between pulling force and strain gauge signal in equation (5.3), the strain gauge signal was converted into pulling force and subsequently  $P_{RR}$ . We chose to find  $P_{RR}$  with respect to a reference temperature  $T_{ref}=25^\circ\text{C}$ . In this case, the offset was given by

$$G_l(T, 0) - G_l(T_{ref}, 0) = \alpha(T^2 - T_{ref}^2) + \beta(T - T_{ref}), \quad (5.9)$$

$$\Downarrow$$

$$G_l(T, 0) = G_l(T_{ref}, 0) + \alpha(T^2 - T_{ref}^2) + \beta(T - T_{ref}). \quad (5.10)$$

Consequently the temperature compensated rolling resistance power was found by

$$P_{RR} = \frac{G_l(T, F_{pull}) - G_l(T_{ref}, 0) - \alpha(T^2 - T_{ref}^2) - \beta(T - T_{ref})}{a} v \quad (5.11)$$

The resulting  $P_{RR}$  is plotted on figure 5.8, with the average value of the three signals plotted to the right. We found that using a temperature compensated offset resulted in better reproducibility. Taking the average of the three measurements yielded  $P_{RR} = -198.740 \pm 2347 \text{ W}$ .

The absolute value of  $P_{RR}$  was clearly off, as this was found to be negative. This is expected to be due to the fact that there was six month between the temperature dependence measurement (fig. 5.5) and this measurements. As a result, drift in the system had occurred and thus some unknown amount should be added or subtracted to the offset. This error can be removed by making both calibration procedures close to the time of measurement.

The standard deviation of the signal on the other hand, was not affected by a potential underlying drift in the signal and thus this could be used to evaluate the reproducibility of the method when we applied the simple temperature compensation. If the rolling resistance was assumed to be 1% of the load, this would correspond to  $P_{RR} = 10.889 \text{ W}$  under assumption of an driving velocity 80km/h and a load of 5 tonnes. Hence, the found deviation in data was about 20% of the desired measured value. This means that the deviation found in the signal across measurements was smaller than the desired quantity we aimed to measure, and thus an improvement of the method. However, a standard deviation of 20% was believed to be bigger than the introduced changes in RR across different pavements and thus further work on minimizing this is required.

The procedure was made for the vertical strain gauge signal as well, in order to investigate what effect temperature compensation had on the calibrated signal. The temperature

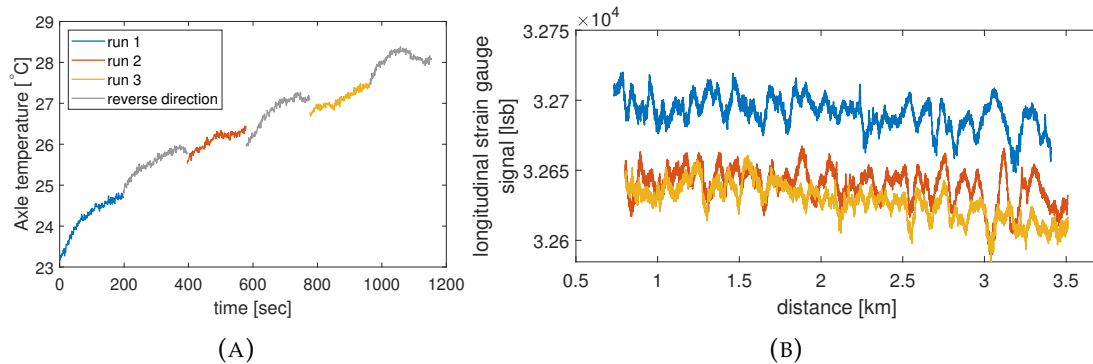


FIGURE 5.7: A) a set of measurements was made with the new setup on a highway making three repeated repetitions at constant velocity of 80 km/t. The axle temperature is monitored during the measurements and show a steady increase. Grey lines show the axle temperature of the measurements made in the reverse direction. B) The measured longitudinal strain gauge signal as a function of distance for the three repeated measurements. A moving average filter is applied to the signals in order to better compare across measurements.

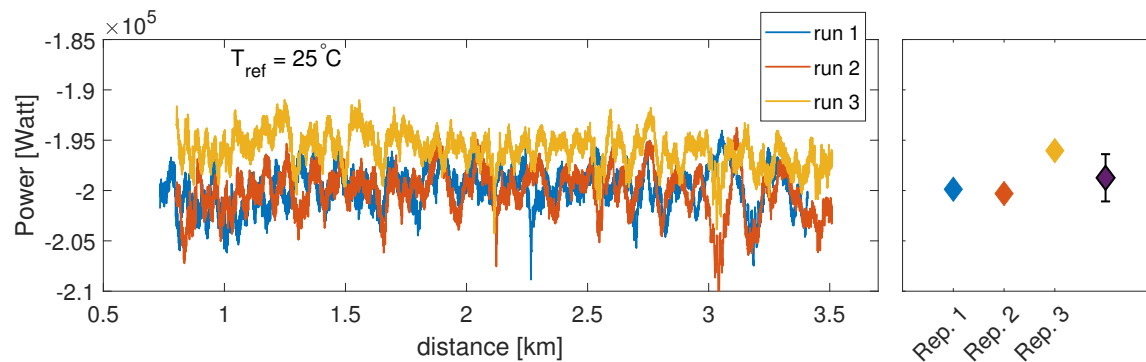


FIGURE 5.8: The rolling resistance loss was calculated for a reference temperature  $T_{ref} = 25^\circ\text{C}$  using the new temperature compensated offset in equation (5.3). To the right, the average value of each signal and an average of all three signal is shown. The absolute value of  $P_{RR}$  was clearly off as this was found to be negative and cannot be used as a measure of the rolling resistance. The standard deviation of the signal, on the other hand, was not affected by a potential underlying drift in the signal and thus this can be used to evaluate the reproducibility of the method when we applied the simple temperature compensation.

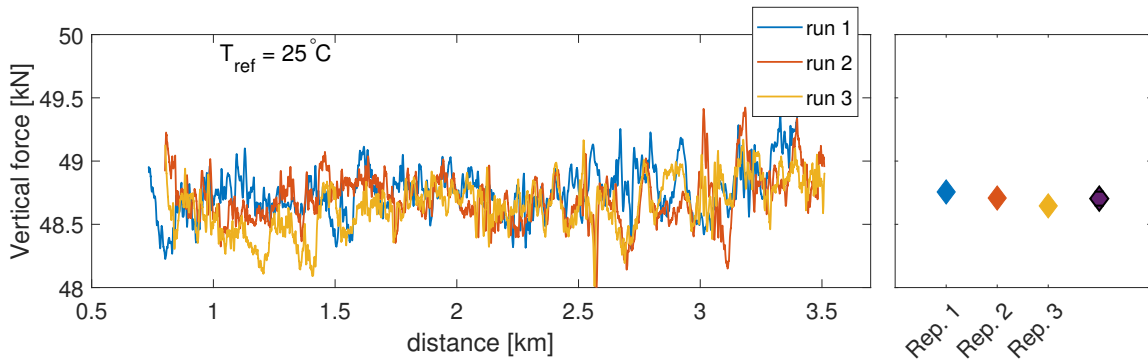


FIGURE 5.9: The vertical strain gauge signal was converted to vertical force using the temperature compensated offset found in equation (5.7). This was done with respect to a reference temperature  $T_{ref} = 25^{\circ}\text{C}$ . To the right, an average of the three signals and an overall average is shown. Compared to the non temperature compensated method, a difference of  $-1.6\%$  was found. This indicated that temperature had no significant influence on the method used to measure the vertical load.

compensated signal for the vertical force is seen on figure 5.9 and the average value is  $F_L = 48.672 \pm 1.155 \text{ N}$ . The difference between this and using the old calibration method, which do not take into account temperature effects, is  $\Delta F_L = -758 \text{ N}$ . Thus including temperature effects gives a decrease in measured vertical force of  $-1.6\%$ . From this we concluded that temperature effects on the vertical strain gauge signal does not have a significant influence on the method used for measuring the vertical load.

## Chapter 6

# Summarizing conclusion

We set out to develop a new way to measure the total rolling of a truck. This was done by using the correlation between deformation of the tire axle and the rolling resistance loss. More specifically, we used the relationship between the force at which the trailer pulls the axle (at constant velocity)  $F_{pull}$  and the dissipated energy due to rolling resistance  $P_{RR}$  given by

$$P_{RR} = F_{pull}v. \quad (6.1)$$

The pulling force  $F_{pull}$  was determined by measuring the deformation of the axle using strain gauges. A measurement setup was developed in which we measured the vertical bending strain, horizontal bending strain and torsion strain simultaneously. Furthermore, a calibration procedure was developed for correlating the measured axle deformations to the vertical force  $F_L$ , the pulling force  $F_{pull}$  and the axle torsion  $\tau$  respectively.

A set of four preliminary measurement series was conducted in order to evaluate the reproducibility of the method. By analysing these, an underlying systematic measurement error was found which decreased the longitudinal strain gauge signal in a similar manner across the four measurement series. It was concluded that this was due to temperature effects in the system due to heating of the tire axle. An improved version of the setup was developed including a temperature sensor measuring the axle temperature near the strain gauges.

The influence of temperature on the strain gauges was studied by heating the axle and then measure the strain gauge signals as well as the temperature over time. This study showed that the gauges are highly dependent on temperature. For the longitudinal strain gauges, a second order polynomial dependence was observed between strain gauge signal and temperature. Based on this, a simple temperature compensation method was derived and applied to a set of measurements. We found that applying this simple temperature correction results better reproducibility, however we measure an absolute value which can not be used. Thus, if this has to be applied, a temperature calibration should be made shortly before or after the measurements in order to counteract for drift in the system. Furthermore the standard deviation of the measurements was found to be approximately 20% of the desired signal and hence a change in rolling resistance will be impossible to measure accurately.

The conclusions about the simple temperature compensation method was made based on three repeated measurements conducted within a short time frame ( $\sim 20$  min) and as a consequence, the temperature difference were only around  $4^\circ\text{C}$ . The preliminary measurements had a time frame of hours, resulting in a temperature increase of  $25^\circ\text{C}$ . Thus the longer a measurement series, the bigger a temperature change is seen. and hence the simple method should be tested for such large temperature changes as well.

It was hypothesised that the increased temperature of the axle originates from the tire brakes which where found to become very hot (around  $200^\circ\text{C}$ ) during the measurements. As a consequence, we suspected that the increase in axle temperature was not uniformly distributed over the axle, but a temperature gradient in the axle exists. This was believed to arise not only from the sides and inwards, but also from the front of the axle to behind. The latter was due to cooling of the front of the axle due to aerodynamic effects. If a temperature gradient was present in the axle, this would introduce an error in the strain gauge signal as the Wheatstone bridge only compensates for uniformly distributed temperature effects (all strain gauges in the circuit would experienced the same temperature). A way to study the temperature dynamics in the axle is to apply several temperature sensors located both in the front and behind of the axle as well as close to and far away from the brake drums.

In conclusion, a proper understanding of the temperature effects in the axle system is needed in order to make reproducible and applicable measurements of the rolling resistance. For future work, the temperature effects should be studied in more depth in order to develop a better temperature compensation method. As the effects due to rolling resistance we aimed to measure are very small, the method needs to be able to reproduce measurements accurately before any conclusions are made. The experimental setup also includes measurements of the torsion in the axle which in the long term can be used to subtract contribution from the bearings and thus make the estimate of  $P_{RR}$  more accurate. However, these measurements are also affected by temperature and thus this problem should be solved first.

A practical method for reducing temperature gradients within the axle, is to coat it in an isolating material. This could create a more uniform temperature distribution within the axle. Furthermore, initial heating of the axle and tires is recommended before beginning the measurements. For measurements presented here, the truck had driven at least 10 km before and thus we would expect the tires and other components to have reached some equilibrium temperature value. However, as seen on figure 5.7a, the axle temperature was steadily increasing and did not reach an equilibrium value within the time frame of the presented measurements.

Lastly, we investigated the effects of temperature in the strain gauges measuring vertical deformation. As the vertical load is a much larger quantity than the rolling resistance, we hypothesised that the effects of temperature would be smaller. Using the correlation between strain gauge signal and temperature, a calibration method including temperature effects was developed. We found that the difference in calculated vertical force, between

applying the original calibration method and the one which take into account temperature effects was 1.6%. Thus, we conclude that temperature effects did not have a significant effect on the measured vertical load.





## **Part III**

# **Measuring Structural Rolling resistance**



## Chapter 7

# Structural rolling resistance

A pavement subject to a moving load will deform underneath it. If the pavement is viscoelastic, this deformation will result in energy dissipating into the pavement structure. In order to maintain a constant driving velocity, the lost energy has to be compensated through additional work from the vehicle engine (Louhghalam et al., 2014). The amount of additional energy needed depends on the structure of the pavement and is called the structural rolling resistance (SRR) loss.

Viscoelastic materials are materials which behaves both elastic and viscous at the same time. They are characterized by having a time dependent relationship between stress and strain. This means that the resulting strain to an applied load will depend on the loading history and the frequency at which the loading is applied. Asphalt consist of bituminous materials, which are known to be highly viscoelastic (Chupin et al., 2010). In fact, most engineering materials behave viscoelastic to some extend, but they are often represented as elastic for the sake of simplicity. The viscoelastic properties of a pavement subject to a moving load are expressed through an asymmetric pavement deflection basin. A simulated pavement deflection basin for a viscoelastic and purely elastic pavement is seen on figure 7.1a. The center of the load is at  $x = 0$  and due to the time delay in the viscoelastic pavement response, the maximum deflection appears behind the load. As a result, the tire is always driving on a uphill slope. This is illustrated by looking at the pavement deflection slope (fig. 7.1b) in  $x = 0$ . As a result, the tire has to do work in order to maintain a constant driving speed when driving on an viscoelastic pavement (Flügge, 1975). Using this uphill slope notion, the SRR can be calculated directly from the asymmetric deflection basin (Chupin et al., 2010; Balzarini et al., 2018; Chupin et al., 2013).

In this part of the thesis, we will present a newly developed method for direct measurement of the structural rolling resistance. This method uses an already existing measuring technology explained in section 8. Three sets of data has been collected through the period of the project on which the newly proposed method is applied to calculate SRR. The method was first proposed in Nielsen et al. (2020b) and it will be described in detail in chapter 10.

### 7.1 State of the art

The subject of structural rolling resistance is investigated in the literature through indirect measurements and numerical/analytical model studies.

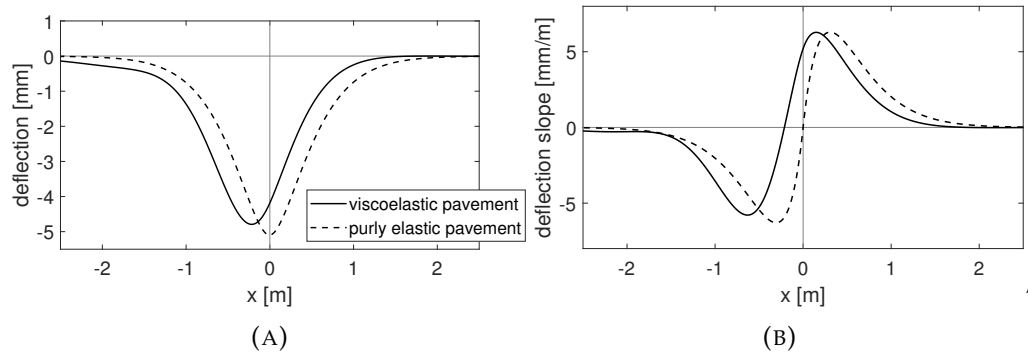


FIGURE 7.1: (a) Simulated deflection basin underneath a moving load for an elastic (dashed line) and viscoelastic (solid line) pavement, and (b) associated deflection slope for the elastic and viscoelastic pavement. The basin is obtained using a numerical simulation explained later in this thesis.

Although SRR has been studied for decades, it has proven difficult to devise accurate and robust ways of measuring it (Akbarian et al., 2012). There are two main reasons for this. First of all, it is a very small quantity to measure. The viscous effects are manifested through the asymmetric pavement deflection underneath the tire, which is of the order of magnitude millimeters to micrometers. This is a small quantity compared to other dimensions of a standard truck and is, as a result, difficult to measure with high enough accuracy and reproducibility. Secondly, the effect from pavement structure is found to be highly dependent on external parameters such as road temperature, vehicle speed, pavement conditions, and so forth (Harvey et al., 2016). This makes it difficult to compare measurements across studies.

Akbarian et al. (2012) gives a review of studies evaluating the correlation between pavement deflection and fuel consumption. These types of studies compare fuel consumption measurements on flexible (asphalt) and rigid (concrete) pavements. The underlying assumption is that rigid pavements have little or no viscous losses and thus the difference in fuel consumption between these types of pavements can be ascribed to the viscous behavior of the asphalt (Balzarini et al., 2018; Zaabar and Chatti, 2014; Balzarini et al., 2017a). Overall, the studies concludes that there are a difference in fuel consumption between the two pavement types. However, the measured fuel consumption is quite small and a high variability in the resulting change in fuel consumption was found. Furthermore, the measurements are performed under different external conditions and thus it is difficult to get a clear conclusion based on the measurements (Akbarian et al., 2012).

This illustrates very well the challenges that come with these types of measurements, as external parameters such as temperature, wind etc can change from pavement to pavement and in the end introduce errors when change in fuel consumption is calculated and different pavements are compared. Nevertheless, these kind of measurements have the advantage that they are easy to perform and give some kind of qualitatively insight into the problem.

As it is not possible to measure SRR directly, estimates of SRR typically involves some kind of modelling process. Some studies are purely numerically/analytical, whereas others use empirical results to calibrate the models or compare their numerical results. Data used for calibration of models are often obtained using *Falling Weight Deflectometer* (FWD) measurements. FWD is a non-destructive technology that is widely used to evaluate structural properties of asphalt pavements (Zhao et al., 2015). In short, the principle behind the technology is to apply a stationary impulse load and then measure the resulting surface deflection at different locations around the load (Gopalakrishnam et al., 2014). Through a *backcalculation* procedure, characteristic structural parameter values can be estimated and used to either calculate the given stress and strains in the pavement structure for analysis purposes or as a basis for simulating pavement responses.

Another modelling approach is to develop a mechanistic founded model and through this correlate material and structural parameters with the pavement deflection, and in the end fuel consumption (Akbarian et al., 2012). In these studies, empirical results from rheological measurements of bitumen mixes are used to gain information about the viscoelastic behaviour of asphalt.

There exist other measurement techniques with the purpose of assessing structural pavement response. This includes e.g. in-ground sensors which can measure the deformation, stress, temperature etc. (Di Graziano et al., 2020). To our knowledge, these have not been used to evaluate the dissipated energy due to pavement deformation, and thus we will not touch upon this further.

Theoretical analysis of the deflection of a structure subject to a moving load has been reported in the literature since the 1960s. A pioneering study was made in Flügge (1975), where the viscoelastic response of a Kelvin beam is analyzed, and the viscoelastic effects reported to manifest themselves through an asymmetric deflection basin. When modelling pavement response to a moving load, there are two overall frameworks in which this can be done; a fixed or moving reference frame.

- The fixed reference frame is also called *dissipation-induced pavement-vehicle interaction*. In this, the energy dissipation is evaluated as a function of time in a finite pavement segment as a load is moving by (Louhghalam et al., 2013). Thus the pavement deflection is calculated for one (or more) observation points on the pavement as the load moves past. This is illustrated on figure 7.2a. Examples on models in this framework is Pouget et al. (2012); Coleri and Harvey (2017); Lee (2014). Here the dissipated energy is calculated based on finite-element modelling of the pavement segment.
- The moving reference frame is also called *deflection-induced pavement-vehicle interaction* (Louhghalam et al., 2013). In this framework, a steady-state is assumed (constant driving velocity) and the tire is considered to stay in the same place while the pavement "moves" underneath it. In order to go from fixed to moving reference frame the following coordinate change is applied,  $x = x' - vt$ . The uphill slope analogy explained above is set in a moving reference frame. Studies made in this framework includes Flügge (1975); Akbarian et al. (2012); Akbarian and Ulm (2012).

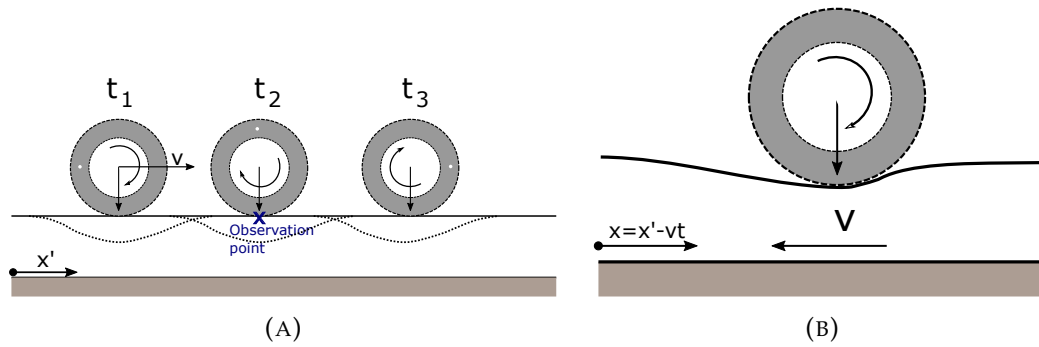


FIGURE 7.2: Interaction between a moving tire and the pavement surface for A) fixed reference frame and B) moving reference frame. The figure is inspired by figure 1 in Louhghalam et al. (2013).

The two methods are equal from a thermodynamic point of view, thus the predicted dissipated energy is the same (Louhghalam et al., 2013). A comparison of the two methods is found in Lee et al. (2018). In this thesis, we will focus on studies made in a moving reference frame, as this can be compared directly to measurements made with the *Traffic Speed Deflectometer*.

## Chapter 8

# Traffic Speed Deflectometer

In this thesis, we used the Traffic Speed Deflectometer (TSD) technology to study the pavement response underneath a moving load and to calculate the structural rolling resistance. The TSD measuring principle was developed by Greenwood Engineering in 2004 and is a nondestructive measuring method, meaning that it can be used to determine structural characteristics of a pavement without damaging it. Essentially, it provides measurements of the pavement deflection slope underneath the right rear-end tire while driving.

TSD measurements are conventionally used for continuous bearing capacity measurements of the pavement, which are used within pavement management and currently 16 TSD's exist around the world (Ferne et al., 2009; Nasimifar et al., 2020; Engineering, 2020). Each of them have different features as they are continuously developed and refined. The vehicle used for data collection in this thesis was the TSD 7 (fig. 8.1a), which belongs to Greenwood Engineering and all technical details written here regards this specific vehicle. In this chapter, the fundamental principle behind the measurement technology is described. In the next chapter, the three main data sets which is the foundation for the later analysis is presented.

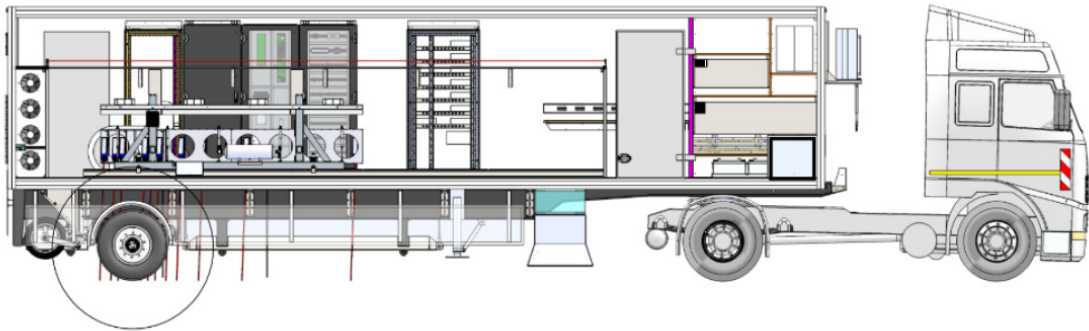
### 8.1 The TSD principle

The main principle behind the TSD is to use Doppler lasers to measure the vertical pavement velocity around the tire as the vehicle moves. From this, the pavement deflection slope can be found and subsequently the pavement deflection. The TSD is a full size customised truck and as a result, it can operate under realistic axle loads (10 tonnes) and driving speeds. The trailer is the same as the one used in the experimental setup for measuring total rolling resistance in part II of this thesis. Inside the trailer, a series of *Laser Doppler vibrometers* are mounted on a rigid steel beam, pointing downwards towards the pavement (Nielsen, 2019; Ferne et al., 2009). This is illustrated on figure 8.1b where a sketch of the inside of the trailer is seen with the sensor beam arranged around the right rear-end tire.

A Laser Doppler vibrometer measures the velocity of an object moving away or towards it using the Doppler effect. Thus, it measures the frequency shift in the reflected light beam that arise due to the instant velocity of the object. Using this, the lasers are capable of measuring the instant velocity of the pavement while the truck is driving.



(A)



(B)

FIGURE 8.1: A) Picture of the TSD 7 used to conduct all measurements in this thesis. B) Technical sketch of the TSD trailer. Inside the trailer a series of Doppler lasers are mounted on a rigid steel beam, pointing downwards towards the pavement. Using these the pavement deflection slope is measured around the right rear-end tire.



In order to remove effects from the vertical movement of the truck, a reference laser is mounted 3.1 meters from the rear-end axle, where the deflection of the pavement is assumed to be zero (red sensor on figure 8.2a).

In practice, it is not possible to mount the sensors without some angle with respect to the beam. As this angle differs for the different sensors, a calibration procedure is applied in order to subtract related effects from the measured signal. This procedure, as well as more in depth technical details will not be described here as it is not within the scope of this thesis.

The Doppler sensors are located in a line going through the right rear-end tire pair, as illustrated on figure 8.2a. Note that the distance between the two tires on the sketch is exaggerated compared to the real distance (64 mm). Having this location of the sensors makes it possible to measure close to the center of the load. However, due to the presence of the tire axle, it is not possible to measure directly underneath the load. We assume that the two tires are so close together that they can be considered as one, and that we measure in the center-axis of the load (meaning that the load on the left and right side of the center-axis is symmetric). How valid this assumption is, and if it affects the resulting conclusions, is discussed in section 10.5.

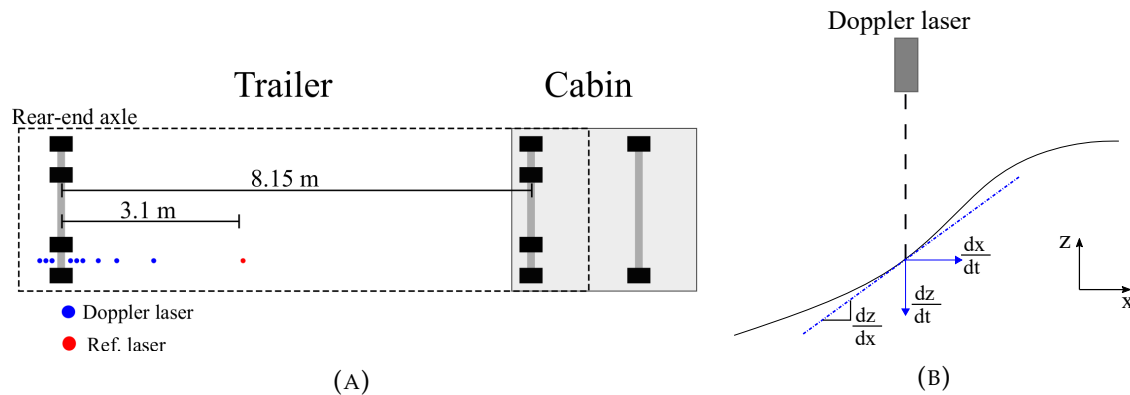


FIGURE 8.2: (A) Top view sketch of the TSD. Nine Doppler sensors are located in between the right rear-end tire pair indicated with blue dots. The measured vertical pavement velocity is adjusted for vertical movement of the truck due to, e.g., unevenness in the road, by a reference sensor located 3.1 m from the rear-end axle and indicated with a red dot. Note that the tires in the tire-pairs appear further from each other on the sketch than they, in fact, are (64 mm). (A) The vertical pavement velocity ( $\frac{dz}{dt}$ ) in a given point is measured using a Doppler laser. The deflection slope in that point ( $\frac{dz}{dx}$ ) corresponds to the slope of the tangent going through the point (grey dotted line) and can be found by dividing  $\frac{dz}{dt}$  with the horizontal driving speed,  $\frac{dx}{dt}$ .

Figure is taken from Nielsen et al. (2020b).

From the measured vertical pavement velocity, the pavement deflection slope,  $\frac{dz}{dx}$ , at the sensor point can be calculated. This is done by dividing the vertical pavement velocity ( $\frac{dz}{dt}$ ) with the driving velocity ( $\frac{dx}{dt}$ )

$$\frac{\partial z}{\partial x} = \frac{\frac{\partial z}{\partial t}}{\frac{\partial x}{\partial t}}, \quad (8.1)$$

as illustrated in figure 8.2b. The driving speed,  $\frac{dx}{dt}$ , is measured using a odometer located behind the right rear-end tire pair.

Thereby the measurements obtained from the TSD are measures of the pavement deflection slope around the load. The associated pavement deflection basin can be found by use of a model (fig. 8.3).

The TSD is equipped with Doppler lasers both in front and behind of the right rear-end tire, see figure 8.2a. This enables us to capture the viscoelastic effects in form of the asymmetric deflection basin (fig. 8.3), which is not captured when pavement deflection only is measured in front of the load. As this specific TSD vehicle is used continuously for research and development, the number of sensors and their locations is not the same for all measurements used in this thesis. The specific sensor locations are listed together with data.

The sensors in the TSD collect data at a sampling frequency of 250.000 samples per second, thus we obtain almost continuously measurements of the pavement deflection slope as a function of time or distant driven. In our case, such a high resolution in data is not needed and thus data used here is averaged over 10 meter unless it is stated otherwise.

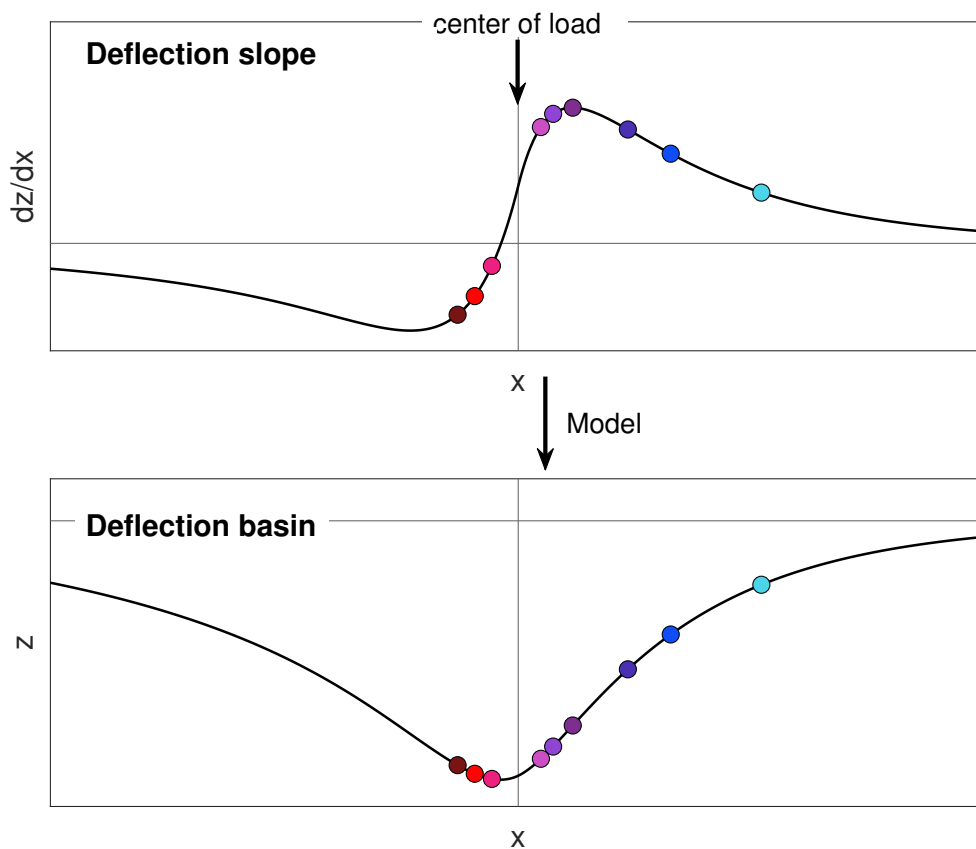


FIGURE 8.3: From the measured vertical pavement velocity the pavement deflection slope,  $\frac{\partial z}{\partial x}$ , at the sensor point can be calculated. The associated pavement deflection basin can be found by use of a model. As the TSD is equipped with Doppler lasers both in front and behind of the right rear-end tire, the asymmetric behaviour of the deflection basin caused by viscoelastic effects can be measured.



## Chapter 9

# Traffic Speed deflectometer data

In this chapter, data used for analysis in the remaining part of the thesis will be presented. Overall, three series of TSD measurements have been collected during the project. Two of these are measured on the same road segment in Måløv, Denmark, approximately 1 year apart and the last is measured in Muonio, Finland. For simplicity, they will be referred to as Måløv data and Finland data.

The underlying aim behind the measurements in the two locations was different, and thus the data series and treatment of these are also different. For data in Måløv, the aim was to look at the pavement deflection over a longer distance and at different temperatures. This enabled us to investigate spatial variations in the pavement deflection and have enough data sets to say something general about underlying trends. Furthermore, having a spatial resolution in the signal at two temperatures gave us the possibility to investigate the impact of temperature as a function of pavement structure. The two data series measured in Måløv are presented in the section *Spatial variations and temperature dependence (Måløv data)* (sec. 9.1).

The Finland data, on the other hand, was collected in order to study pavement properties at different velocities and temperatures. Thus, we investigate a specific pavement structure over a wide range of velocities and temperatures. These data are presented in *Temperature and driving velocity dependence (Finland data)* (sec. 9.2).

The different measurements was collected in different steadies of the project and consequently, they have been processed in different amount. Data presented in 9.1.1 was obtained within the first year of the project and as a result this data has been the base of a thorough sensitivity analysis and model study. The result of which is included in Nielsen et al. (2020b) and Nielsen et al. (2020a).

### 9.1 Spatial variations and temperature dependence (Måløv data)

Two series of TSD measurements were conducted on a road segment in Måløv, Denmark. The first in spring 2018 with a road temperature of  $\sim 18^{\circ}\text{C}$  and the latter in the summer of 2019 with a road temperature of  $\sim 35^{\circ}\text{C}$ . Both measurements were made on a 9.7 km road segment and three subsequent measurements were conducted in order to evaluate the reproducibility. The axle load was 10 tonnes, approximately 5 tonnes in each side.

### 9.1.1 Measurements at 18°C

For this data series, the sensor position relative to the center of the tire axle (in meters) was

$$\text{Sensor position} = [-0.366, -0.269, -0.167, 0.163, 0.260, 0.362, 0.662, 0.964, 1.559]. \quad (9.1)$$

As the TSD follows the traffic flow, the exact driving speed changes during the measurements. On average it was between 50-60 km/h, with the exact driving speed being recorded during all measurements. The velocity profile is seen on figure 9.1a. The measurements were conducted under almost constant air temperature of  $\sim 14^\circ\text{C}$  and road temperature of  $\sim 18^\circ\text{C}$ . The temperature profiles are seen on figure 9.1b and 9.1c respectively.

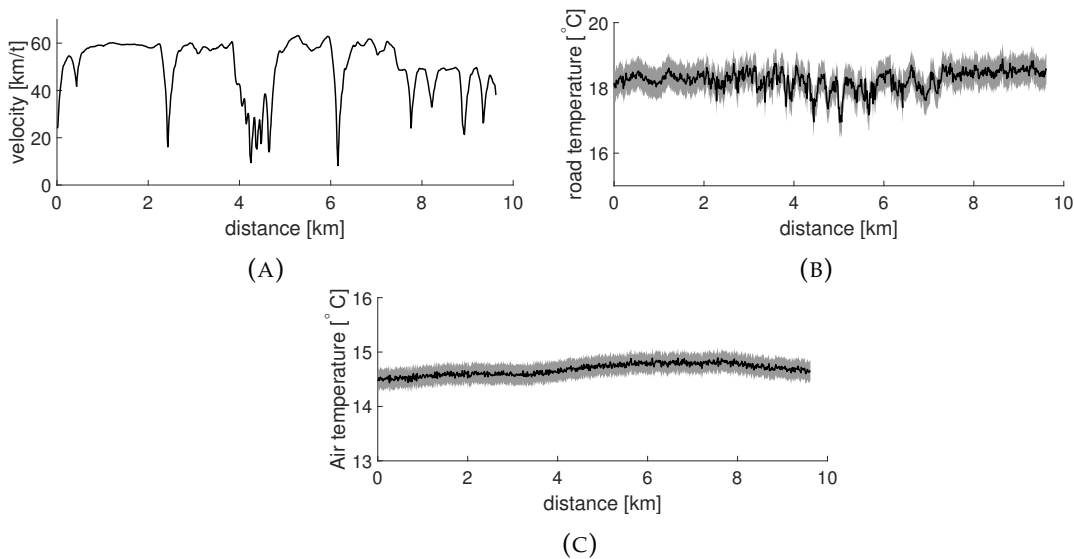


FIGURE 9.1: A) The driving velocity is measured using an odometer located behind the right rear-end tire pair. As the TSD follows the traffic flow, the driving velocity varies during the measurement. B) The road surface temperature is measured using an inferred laser and is found to be stable  $\sim 18^\circ\text{C}$  during the three repeated measurements. The standard deviation based on the three repeated measurements are illustrated with a gray shaded area. C) Air temperature is measured during the measurements and is found to be constant at  $14 - 15^\circ\text{C}$ .

On figure 9.2, a plot of the mean value for each sensors is seen as a function of distance. The measured deflection slope for each sensor varied significantly throughout the measured distance. These variations were however highly reproducible, with average standard deviation for the sensors, found from the three measurement runs, in the interval  $12\text{-}26 \mu\text{m}/\text{m}$ , which corresponded to 4-10% of the measured slope. This means that the observed variations was not due to noise, but an artifact of the changing pavement structure.

A change in amplitude of the slope signals was seen around 2.5 km, with a significantly lower slope signal seen before this limit. This could indicate that there was a structural difference between the road segment before and after 2.5 km. No visible changes in the asphalt layer was seen on the road in this area, and thus this was expected to be a feature of one of the underlying layers.

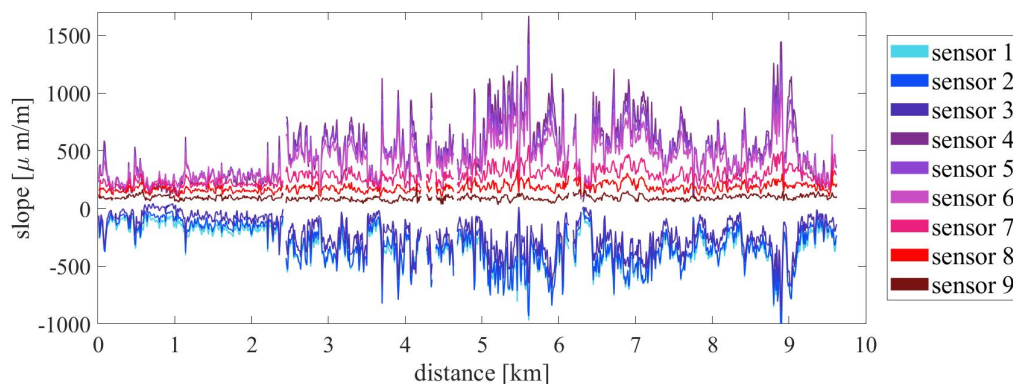


FIGURE 9.2: Measured pavement deflection slope at 18°C . The sensors 1,2 and 3 are located behind the load and the sensors 4-9 are located in front of the load.

On figure 9.3a, an example of measured deflection slope as a function of sensor position is shown for measurement at 2 km. The center of the load is located at  $x=0$ . The standard deviation found from the three repeated runs is illustrated with error bar. Note that for some data points the standard deviation was so small that the resulting error bars were smaller than the markers.

The deflection slope curve was characterised by having a maximum in front of the load and a minimum behind the load. We chose to divide the data sets within the series into groups based on the behaviour of the maximum deflection slope peak. This yielded a qualitatively way to group data and later these groups will be correlated with different structural characteristics.

### Group division based on the x-position of maximum deflection slope

In table 9.1, an overview of the criteria on which data was divided into group 1, 2 and 3 is presented. In group 1, the maximum deflection peak must be closer than, or exactly at, sensor 4 (counted from the left). In group 2, the maximum occurs around sensor 5 and finally for group 3, the maximum deflection slope is around sensor 6 or further away from the load. Thus, the x-position of the maximum deflection slope peak moved further away from the center of the load when going from group 1 to 3. In terms of the deflection basin, this means that the basing got broader. Three exemplary data sets are shown on figure 9.3b illustrating the difference on the three groups.

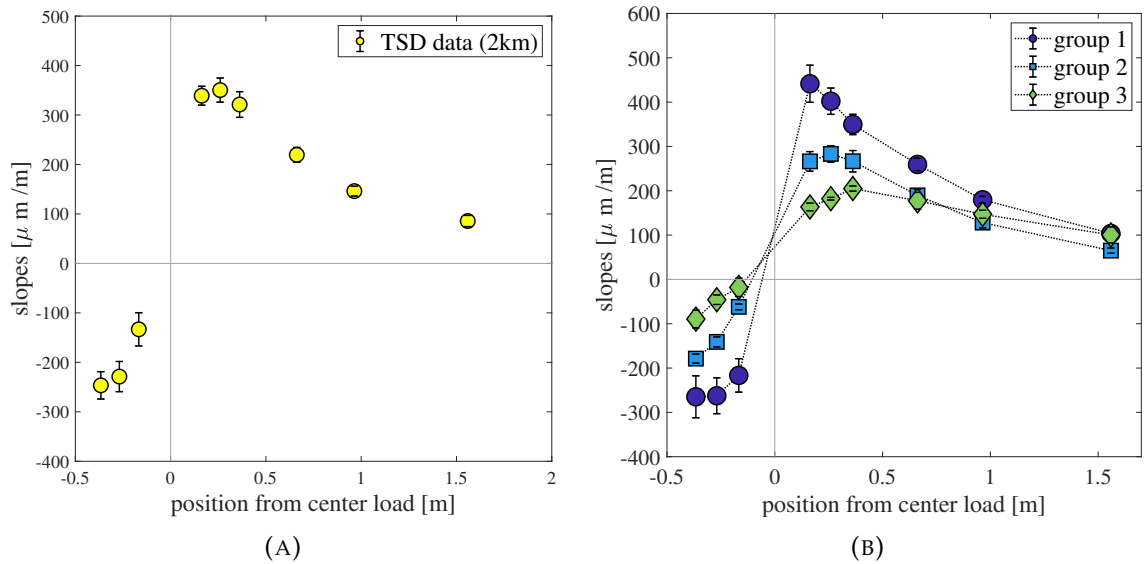


FIGURE 9.3: A) Example of pavement deflection slope data measured with the TSD. The deflection slope curve is characterised by having a minimum behind the load and a maximum in front of the load. B) Examples of group 1, 2 and 3. The division is based on the x-position of the maximum and the criterias are listed in table 9.1.

A high amplitude of the maximum was often correlated with a x-position close to the load (group 1) and thus it was often the case that the amplitude in group 1 was higher than in group 2 and 3. However, this correlation was not consistent, and thus we chose to divide data independently based on x-position and amplitude.

TABLE 9.1: Table explaining the criteria on which the groups are divided.

x-placing of maximum deflection slope	
	Behaviour of the measured signal in $n$ 'th sensor
Group 1	sensor 4 > sensor 5 and sensor 5 > sensor 6
Group 2	sensor 4 $\leq$ sensor 5 and sensor 5 > sensor 6
Group 3	sensor 4 < sensor 5 and sensor 5 < sensor 6

### Group division based on amplitude of maximum deflection slope

Data was divided based on the amplitude of the maximum deflection slope. The criteria of division is listed in table 9.2 and is illustrated on figure 9.4. Here a plot of all data sets is seen on the left, and on the right these are divided into group A, B and C.

As seen, data in group A had the smallest amplitude and data in group C had the largest. The general trend was that when the amplitude of the maximum decreased, so



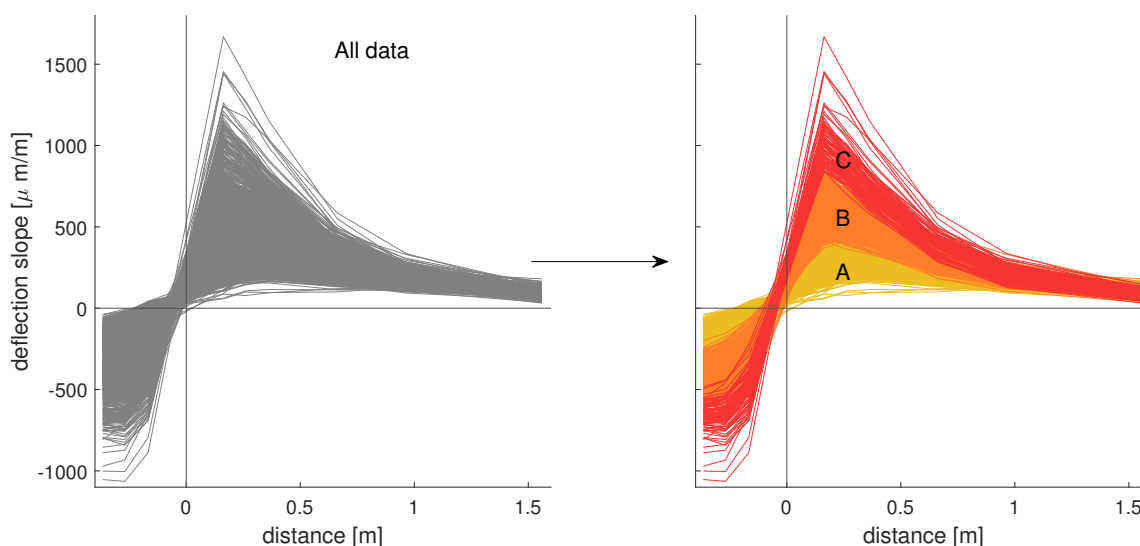


FIGURE 9.4: Division of data into group A, B and C. On the left all measurement sets in the data series is plotted and on the right these are divided into groups based on the amplitude of the maximum.

did the minimum. However, the minimum was often not fully resolved within the three sensor points and thus the division was only done based on the maximum.

TABLE 9.2: Table explaining the criteria on which the groups are divided based on the amplitude of the maximum.

Amplitude of maximum deflection slope	
The maximum measured signal in sensors in front of load	
Group A	Underneath $\frac{1}{4}$ of total maximum amplitude for the data series
Group B	In between $\frac{1}{4}$ and $\frac{2}{4}$ of total maximum amplitude for the data series
Group C	Above $\frac{2}{4}$ of total maximum amplitude for the data series

### Groups as a function of distance

On figure 9.5, the distribution of the different groups over the measured distance is shown. We find a clustering of data with group 1 and B and C data primarily located after 2.5 km and opposite, data in group 3 and A are primarily located before 2.5 km.

A physical interpretation of the underlying structural changes which causes these changes in deflection slope behaviour is made in section 20.3 using a pavement response model derived in section 15.

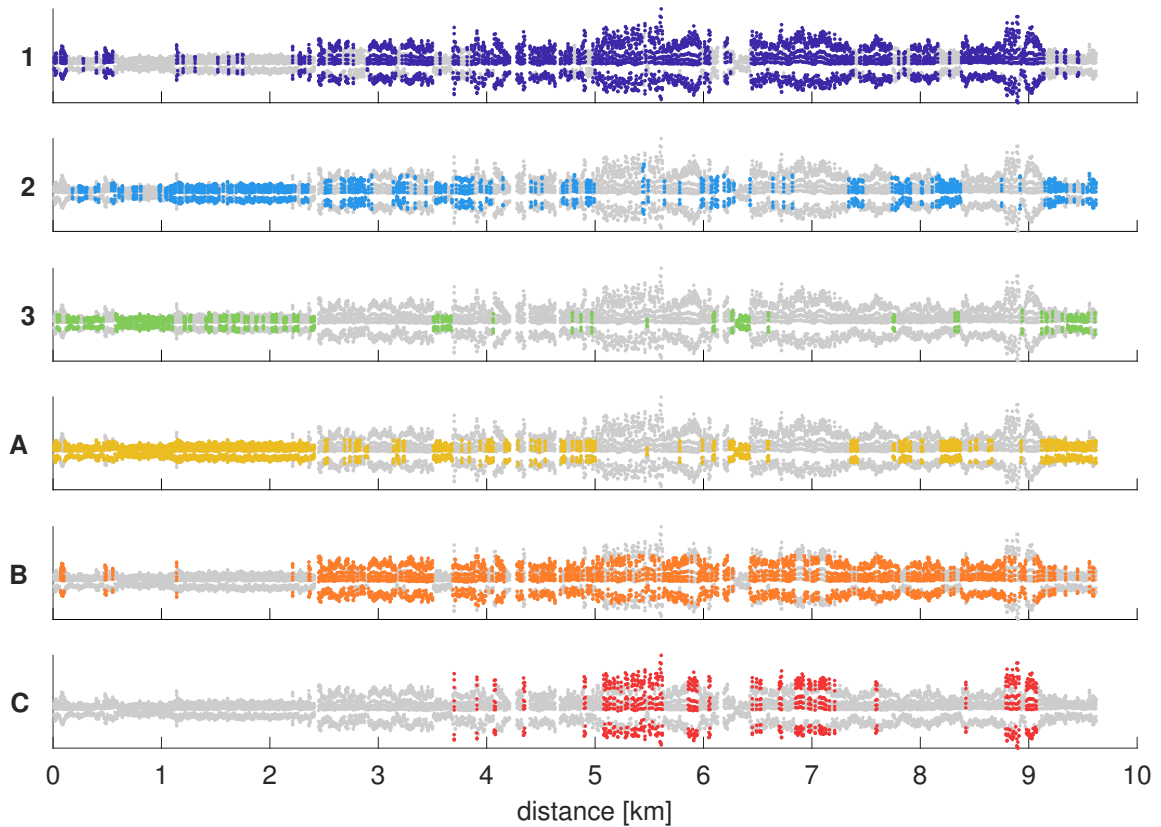


FIGURE 9.5: Plot showing in which area of the road the different groups of data belongs. With gray is the full data series, with 9 points on the y-axis representing the slope values in each sensor for the given distance. Since the data points are averages over 10 meters, it jumps between groups from one data set to another. This is why it in some places looks like two of the same type of groups are represented in one data set. However when zooming in, this is not the case as each data set only belongs to one of group 1, 2, 3 and one of group A, B, C.

### 9.1.2 Measurements at 35°C

Due to maintenance of the equipment, the sensor position is slightly different compared to the measurements in 9.1.1. The sensor position with respect to the center of the axle is:

$$\text{Sensor position} = [-0.424, -0.324, -0.224, 0.11, 0.21, 0.31, 0.61, 0.91, 1.51] \quad (9.2)$$

As before, the driving velocity, road and air temperature were monitored during the measurements. These are plotted on figure 9.6a, 9.6b and 9.6c respectively. The driving velocity was seen to vary since we follow the traffic flow, with a top velocity at 60 km/h. The road temperature is found to be approximately 35°C and the air temperature approximately 30°C.

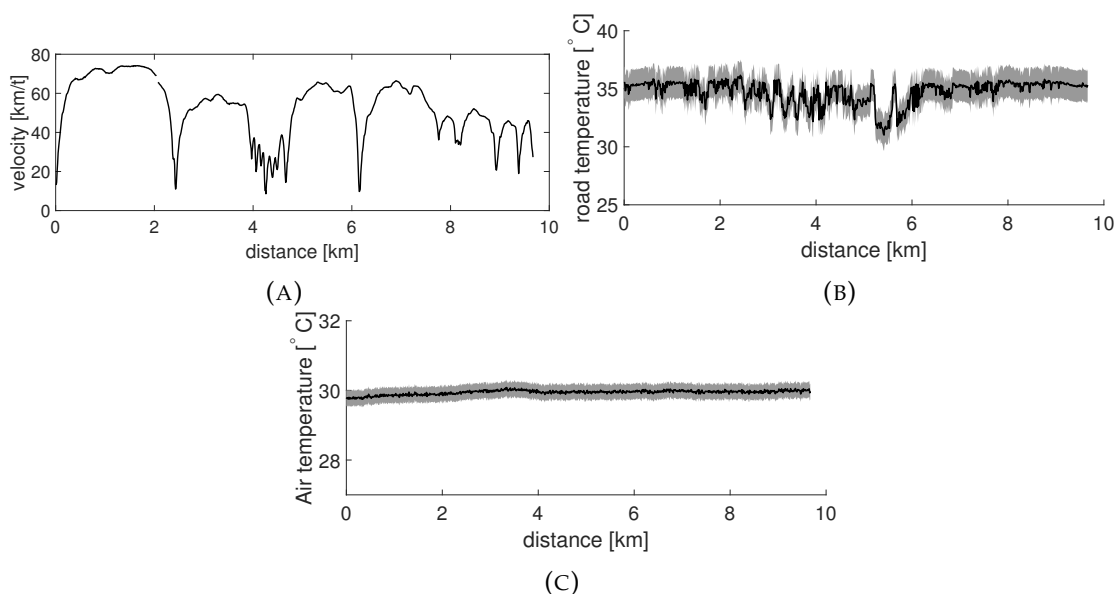


FIGURE 9.6: A) Velocity profile for measurements in Måløv at 35 degrees. B) The road surface temperature is measured using an inferred laser and is found to be stable  $\sim 35^\circ\text{C}$  during the three repeated measurements. The standard deviation based on the three repeated measurements are illustrated with a gray shaded area. C) Air temperature is measured during the measurements and is found to be constant at  $30^\circ\text{C}$ .

A plot of the measured deflection slope signal as a function of distance is seen on figure 9.7. As for measurements in section 9.1.1, spatial fluctuations due to changing structural conditions is seen. The average standard deviations based on the three measurements lay in the interval 15-35  $\mu\text{m}/\text{m}$  (6-9%). An exception was for sensor 9, which measures values close to zero and thus had high percentage derivation (24%).

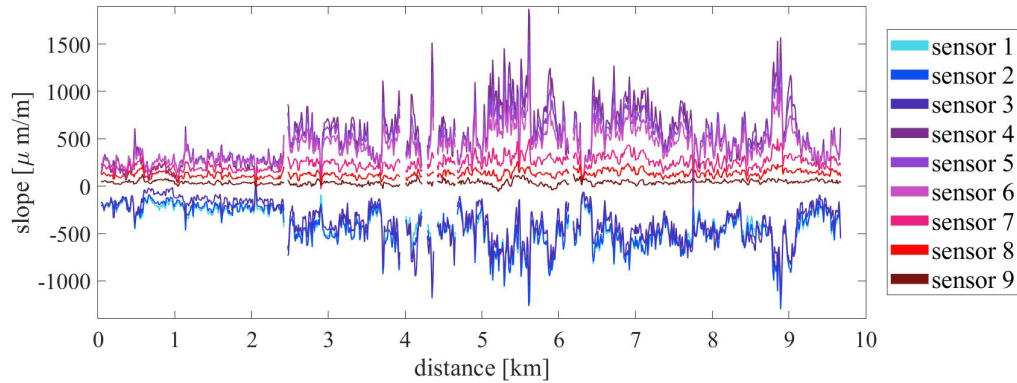


FIGURE 9.7: Measured pavement deflection slope as a function of distance for road temperature of  $35^{\circ}\text{C}$ . Sensor 1-3 is located behind the load and 4-9 in front of the load.

### Division into groups

In section 9.1.1, data were divided into groups based on their behaviour in front of the load. This was done for data at  $35^{\circ}\text{C}$  as well. On figure 9.8, the distribution of the different groups over the measured distance was shown. We found that a large proportion of the data sets belong to group 1 and that almost none belonged to group 3. Thus, the maximum peak location was in general close to the load. Furthermore, we observe that before 2.5 km there was almost exclusive data belonging to group A, thus with low amplitude of the maximum, relative to the average maximum amplitude.

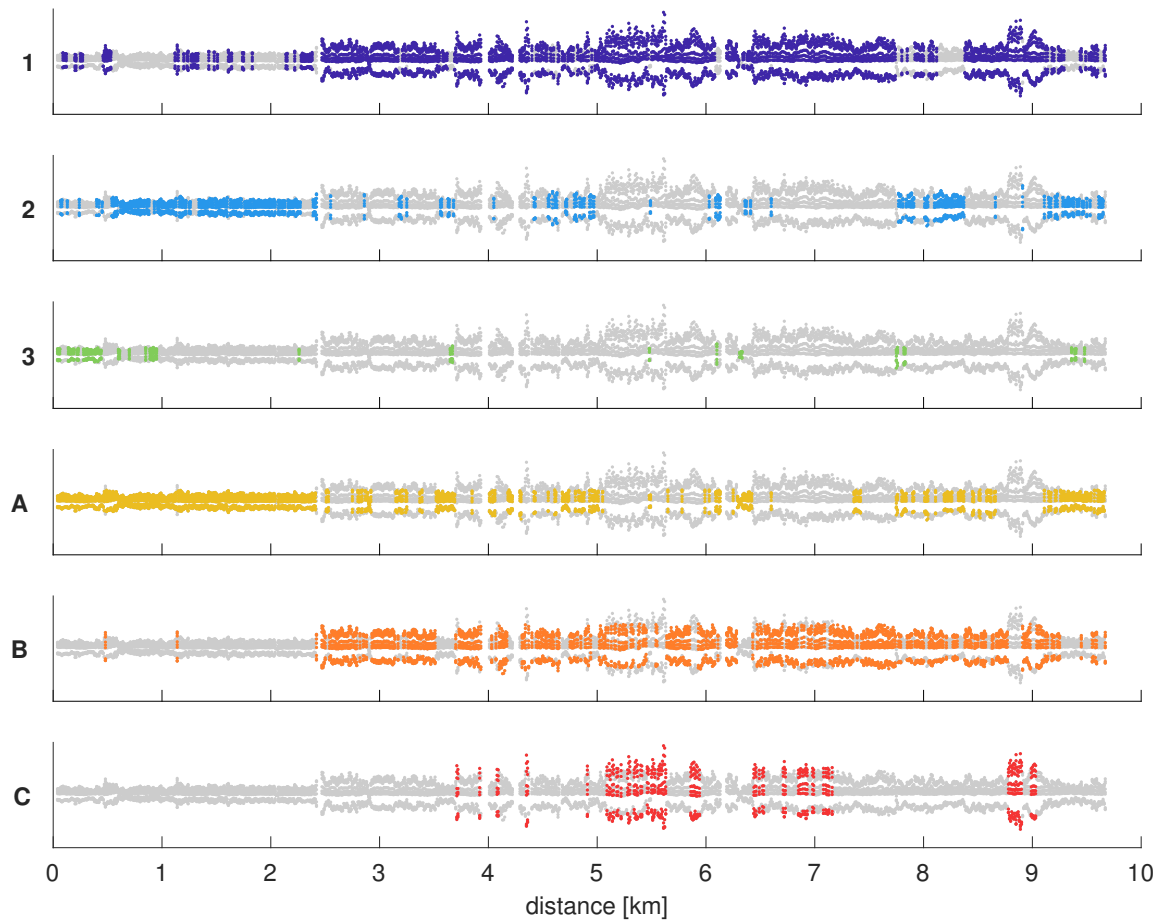


FIGURE 9.8: Distribution of the different groups over the measured distance. We find that data in the section before 2.5 km belong mainly to group 2/3 and A, whereas data after 2.5 km mainly belong to group 1 and B/C.

### 9.1.3 Qualitatively comparison of the measured deflection slope at 18°C and 35°C

Based on the presented data here, we could make a preliminary analysis of the effect increased temperature have on the measured pavement deflection slope.

Firstly, by comparing the measured pavement deflection slopes in figure 9.2 and 9.7, we found that in general the amplitude of the deflection slope is higher for measurements at 35 °C . On figure 9.9, a plot of all data sets for 18°C and 35°C respectively is seen, divided into groups. As the groups were divided relative to the maximum and minimum amplitude within the specific data series, a comparison across data series was not possible. Instead a comparison of some characteristic values of the maximum amplitudes is seen in table 9.3. This, together with visual inspection of figure 9.9, lead to the conclusion that the average amplitude of the maximum deflection slope increased when temperature was increased.

	18°C	35°C
Maximum amplitude in data series [ $\frac{\mu\text{m}}{\text{m}}$ ]	1668	1873
Spread in amplitudes [ $\frac{\mu\text{m}}{\text{m}}$ ]	1610	2089
Average amplitude [ $\frac{\mu\text{m}}{\text{m}}$ ]	494	530

TABLE 9.3: Comparison of characteristic values of the maximum amplitudes for measurements at 18°C and 35°C .

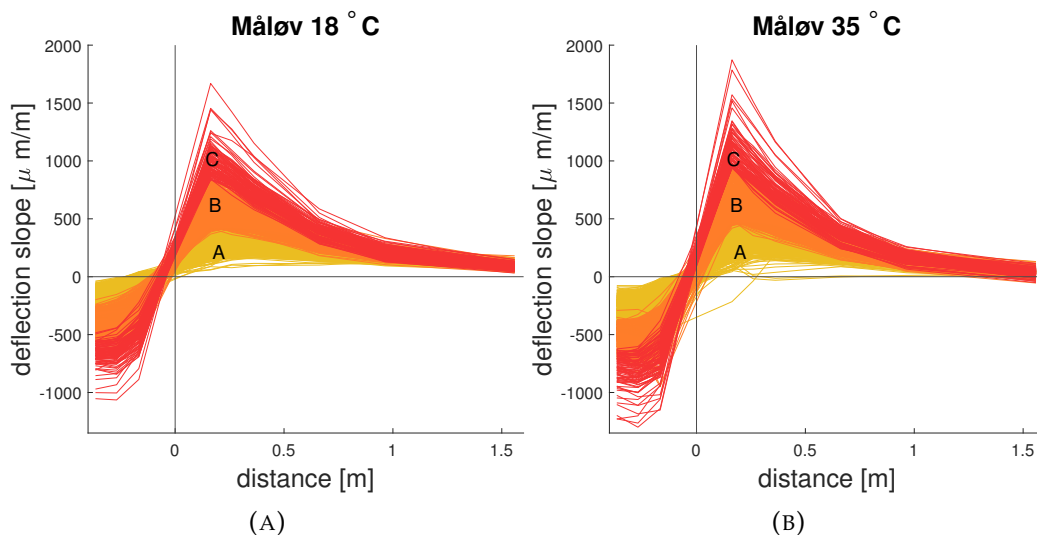


FIGURE 9.9: All data sets divided into groups based on the amplitude of the maximum for data measured at a) 18°C and b) 35°C .

The amount of data sets belonging to group 1, 2 and 3 can be compared across the two different data series and gives an indication if the maximum deflection placing is affected

by temperature. In table 9.4, the amount of data set belonging to each group is listed. We found that there was a clear shift as more data sets belong to group 1 at 35 °C . In figure 9.10a, a plot of two measurements measured at the same location at 18 and 35 °C is seen. Here it was clearly illustrated how the amplitude was increased in the 35 °C measurements and also how the maximum peak placing was moved closer to the load ( $x=0$ ).

	number of measurements (18 °C )	number of measurements (35 °C )
Group 1	506	620
Group 2	270	261
Group 3	161	53

TABLE 9.4: Number of data sets within each group for measurements at 18°C and 35 °C .

Another feature which changed a lot with temperature was the behaviour of the minimum peak. For measurements at 18°C , this was almost always unresolved within the sensors as it was located far away from the load. However, in data measured at 35 °C the behaviour seemed to have changed. In order to investigate this, the two data series were divided into groups based on the  $x$ -placing of the minimum. We call these groups group 4, 5 and 6 and illustrative data sets from each group is seen on figure 9.10b.

In table 9.5, the amount of data sets belonging to each group is listed. It was observed that for measurements at 18°C almost all data sets had the minimum peak location further away from the load than sensors were located (group 6). A significantly shift was seen for measurements at 35°C , where approximately half of the measurements had the  $x$ -position of the minimum within the reach of sensors or even closer to the load than the sensor location (group 4 and 5). We must keep in mind that the location of the sensors had changed between the two measurements, but this alone can not explain the observed change in behaviour.

In conclusion, we have found that both amplitude and peak position of the maximum and minimum deflection slope curves were affected by temperature. The general trend was that the  $x$ -position of the peaks moves closer to the load and their amplitude was increased when going from 18°C to 35°C . This indicated that the deflection basin gets more narrow and steeper. A physical interpretation of this was that the top layer got softer and deform around the load under high road temperatures.

	number of measurements (18 °C )	number of measurements (35 °C )
Group 4	1	100
Group 5	80	313
Group 6	835	494

TABLE 9.5: Number of data sets within group 4, 5 and 6 for measurements at 18°C and 35°C .

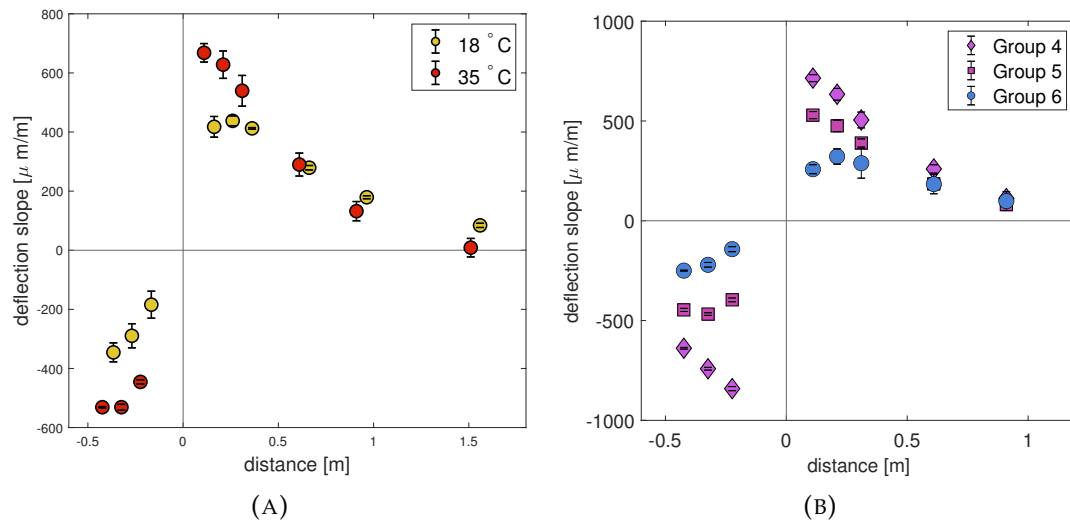


FIGURE 9.10: A) Measured pavement deflection slope at 2.56 km at 18°C and 35°C . B) Illustrative data sets representing group 4, 5 and 6 which is divided based on the x-position of the minimum.



## 9.2 Temperature and driving velocity dependence (Finland data)

A series of measurements was conducted in Muonio, Finland. These measurements was a part of a larger study where in-ground sensors was compared to TSD measurements of the pavement deflection. In this thesis, only the TSD sensor data will be included. The aim of the study was to measure the pavement response under different velocity and temperature conditions. Measurements was made under 5 different driving velocities and 2 road temperatures, at two different locations on the road approximately 800m apart.

Changes in the pavement surface were obtained by conducting measurements at day ( $\sim 22^{\circ}\text{C}$ ) and night ( $\sim 14^{\circ}\text{C}$ ). In table 9.6, the velocity-temperature configurations measured is seen. Each velocity-temperature configuration was measured three times in order to investigate reproducibility. The exception was 5 km/h at  $14^{\circ}\text{C}$ , which was only measured ones due to logistical reasons.

TABLE 9.6: Velocity-temperature configurations and how many repetitions was made. Each configuration was repeated three times with the exception of 5 km/h due to logistical reasons.

Day T $\sim 23^{\circ}\text{C}$		Night T $\sim 14^{\circ}\text{C}$	
speed	rep.	speed	rep.
10	3	5	1
20	3	20	3
40	3	40	3
80	3	80	3

### 9.2.1 Driving velocity dependence

On figure 9.11, a plot of the pavement deflection slope as a function of distance to the axle is shown, for each location at the two temperatures. The mean deflection slope for each velocity was found from the three repetitions and illustrated with a marker and the corresponding standard deviation is illustrated with an error bar. We find that the measurements were highly reproducible with low error bars for all velocity-temperature configurations and locations. Often the standard deviations were so small that the error bars were smaller than the markers.

A common trend for all location and temperature variations was that the magnitude of the maximum and minimum deflection slope decreased when the velocity increased. This indicated a shallow deflection basin, thus the pavement behaved more stiff. Furthermore, we observe that the x-position of the maximum was unchanged when driving velocity changes. The x-position of the minimum on the other hand, was moved closer to the load when driving velocity was decreased. This behaviour was mostly evident for location 1 data and was observed for both temperatures. An increased amplitude of the minimum combined with a x-position closer to the load indicated that the pavement deflection basin

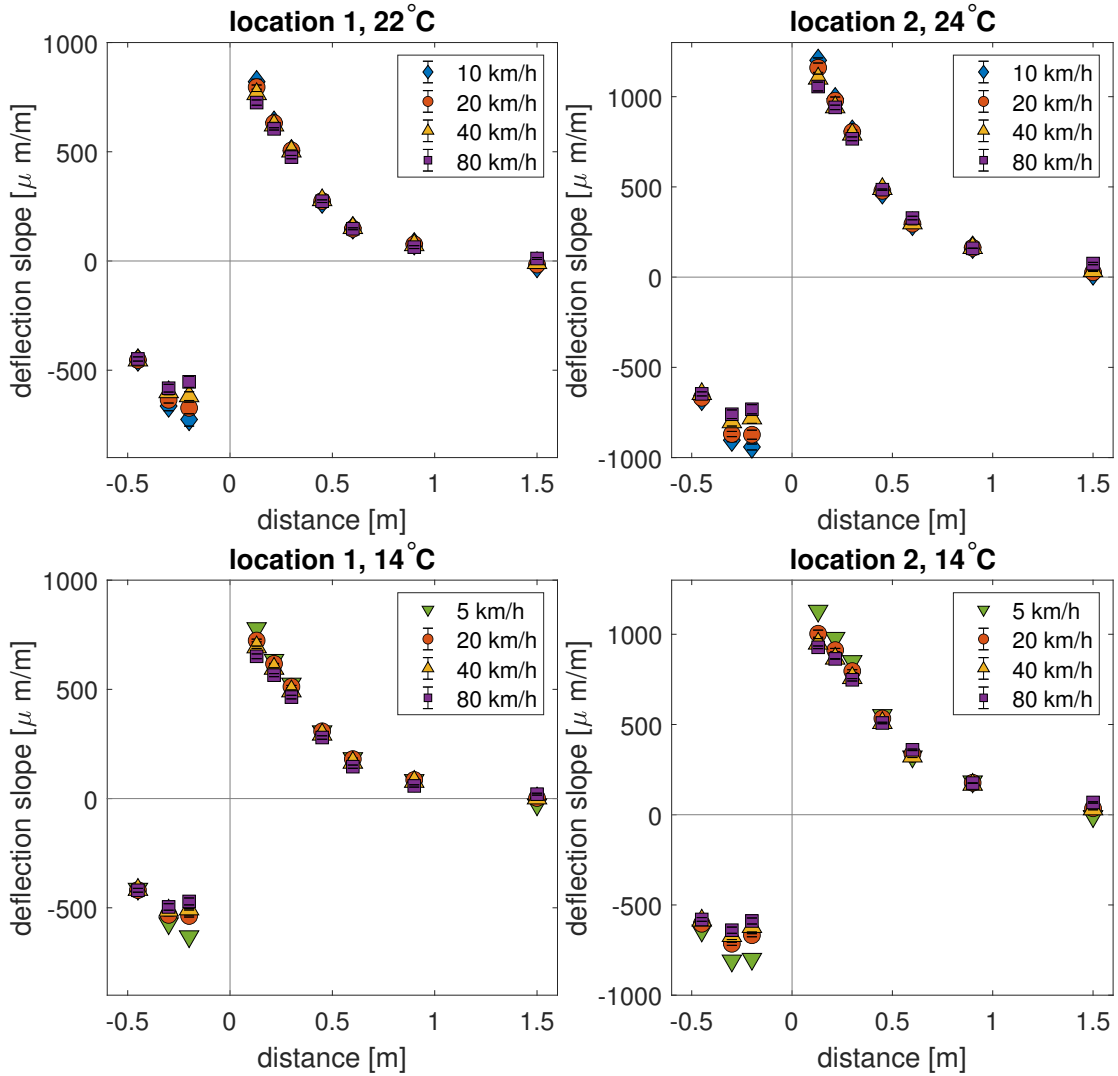


FIGURE 9.11: Mean pavement deflection slope signals for different driving velocities, road temperatures and locations. Overall a decrease in the amplitudes of both maximum and minimum is seen when driving velocity increases. Furthermore a change in the x-position of the minimum is seen when changing the driving velocity. Standard deviations found from the three repeated measurements is illustrated with error bars and shows a good reproducibility in data.

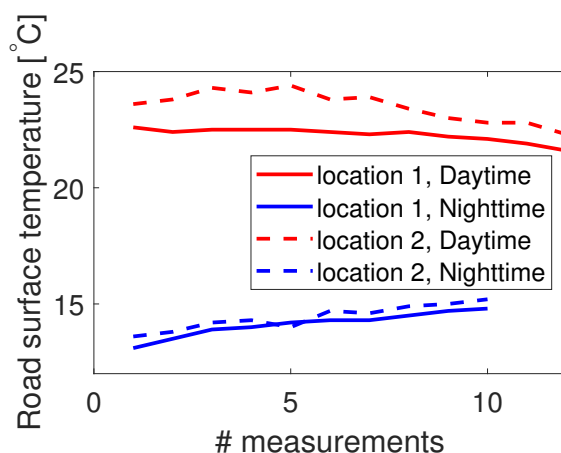


FIGURE 9.12: Temperature profile of the surface temperature during measurements.

behind the load was getting more steep and deep. Thus, we observe a softer behaviour of the pavement when velocity was decreased.

Finally, an interesting observation in location 1 data was that the range of which velocity influence the sensor signals changed. For 22°C, a change was seen in sensor 2-6 ( $\pm 0.5\text{m}$ ), whereas for 14°C a change in the sensor signal in front of the load was also seen in sensor 7 and 8. Even though this was not a large difference, it indicated that the influence of velocity became increasingly centered around the load when temperature increased and the outer parts of the deflection basin in this case were unaffected of velocity changes.

### 9.2.2 Temperature dependence

In order to study the effect of temperature, measurements was conducted at daytime and nighttime. The temperature profile is plotted on figure 9.12 and showed reasonable stable road temperatures during the measurements.

On figure 9.13, a plot of the deflection slope for comparable velocities at different temperatures is seen. The temperature indicated in the legend is the average road surface temperature over the three measurements. Overall, it was found that the maximum and minimum amplitudes was higher for the daytime measurements than nighttime, with the largest change seen in the minimum. Furthermore, for 20 km/h (and in some degree for 40 km/h) the x-position of the minimum moved closer to the load when temperature was increased. These changes in the pavement deflection slope indicated that an increase in the road temperature resulted in a softer pavement.

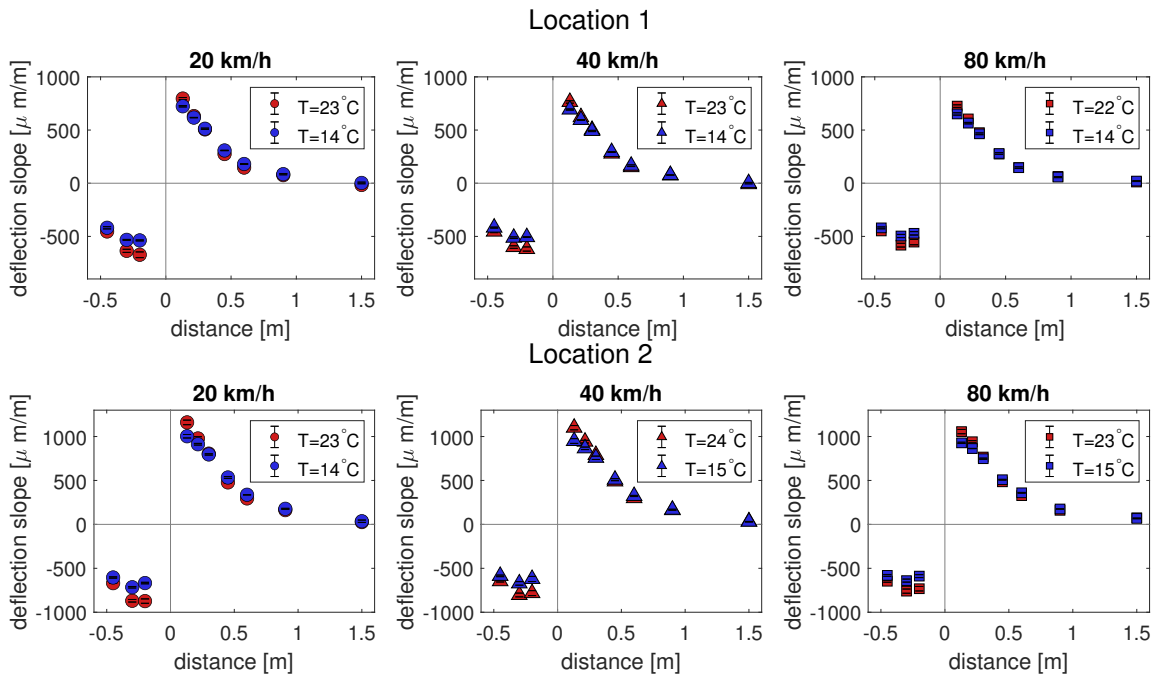


FIGURE 9.13: Deflection slope signals at different temperatures. We find that increasing the road temperature makes the amplitude of the maximum and minimum deflection slope increase. Furthermore it affects the x-location of the minimum.

## Chapter 10

# Estimating structural rolling resistance from TSD data

In this chapter, a simple approach for calculate the structural rolling resistance based on measured pavement deflection slopes using the TSD was presented. Subsequently, the method was applied to calculate the structural rolling resistance for the TSD data series presented in section 9. The proposed method aimed to be simple and easy applicable, and as a result no modelling procedure of data was involved. As a consequence, a linear interpolation between data points was used to estimate the deflection slope underneath the load. An extension of the method was derived in section 10.3, where a simulated pavement response underneath the load could be used instead. Using a set of simulated pavement responses, the two approaches were compared with the aim of determine when the linear interpolation methods provided a valid estimate of SRR, and when the extended method should be used.

The method was presented in Nielsen et al. (2020b) and thus some of the details here will overlap with details given in the paper. However, in this chapter a more elaborate and detailed description of the method will be given, as well as a thorough discussion of the underlying assumptions and its validity.

### 10.1 The simple approach

A pavement subjected to a moving load will deform underneath it. In the following, we assume that the applied load is a point load at the center of the tire, corresponding to  $x = 0$ , with the magnitude  $F_L$  (fig. 10.1). The dissipated power in  $x=0$  can be found from the applied load and the pavement velocity at this point ( $\frac{\partial z(x=0)}{\partial t}$ ) and is noted  $P_{SRR}$ ,

$$P_{SRR} = F_L \frac{\partial z(x = 0)}{\partial t}. \quad (10.1)$$

The vertical pavement velocity can be rewritten in terms of pavement deflection slope ( $\frac{dz(x=0)}{dx}$ ) by using the horizontal driving velocity  $\frac{dx}{dt}$  and the chain rule. Thereby, the dissipated energy can be written as

$$P_{SRR} = F_L \frac{\partial z(x = 0)}{\partial x} \frac{dx}{dt}. \quad (10.2)$$

For simplicity, was the horizontal driving velocity denoted  $v$  in the rest of the thesis.

In the case of a perfectly elastic pavement, the maximum deflection will occur directly under the load, making the deflection slope at this point zero and thus  $P_{SRR} = 0$ . For a viscoelastic pavement however, the maximum deflection occurs behind the load and there is an uphill slope underneath the load, thus  $P_{SRR} > 0$ .

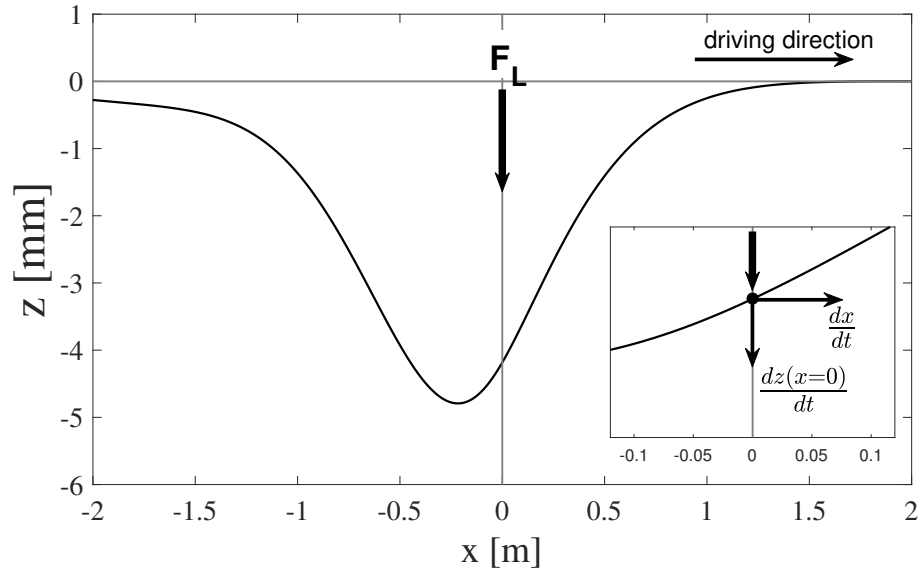


FIGURE 10.1: Sketch of pavement deflection underneath a moving load for a viscoelastic pavement. The applied load is assumed to be a point load at the center of the tire, marked with a black arrow. The dissipated power in that point ( $x=0$ ) can be found from the vertical velocity of the pavement, given by  $\frac{dz(x=0)}{dt}$  and the magnitude of the load  $F_L$ .

The TSD setup measures the deflection slope in between the two right rear-end tires and as a consequence, the tire axle prevents measurements directly underneath the load. In order to obtain information about this, it has to be estimated from sounding data points. If the slope underneath the load is assumed to behave linearly, it can be estimated through linear interpolation between the measured deflection slope in the two sensors located closest to the center of the load (sensor 3 and 4), see figure 10.2.

When using a linear interpolation, the dissipated energy can be written as follows

$$P_{SRR} = F_L v b, \quad (10.3)$$

where  $b$  is the intersection of the linear interpolation  $\frac{\partial z}{\partial x}(x) = ax + b$  with the  $z$ -axis,  $\frac{\partial z}{\partial x}(x = 0)$ . From the dissipated power we can define the rolling resistance force as  $F_{SRR} = \frac{P_{SRR}}{v} = F_L b$ . Using the standard definition of rolling resistance coefficient as the ratio between rolling resistance force and the load, this leads to the following simple relation between deflection slope at  $x = 0$  and the SRR coefficient

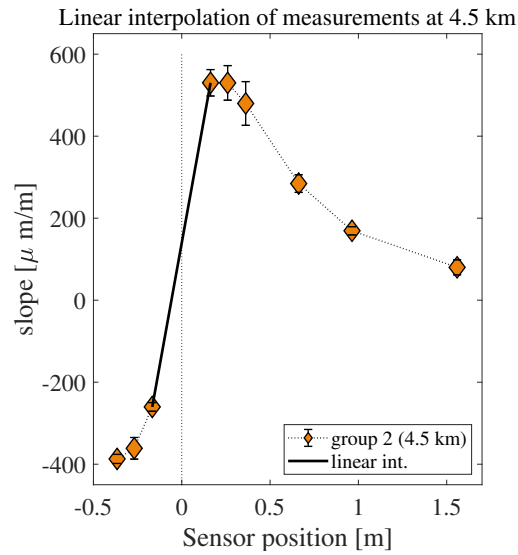


FIGURE 10.2: The deflection slope directly underneath the load is estimated by use of a linear interpolation between sensor 3 and 4 (counted from the left). Here seen done for a data set measured in Måløv at 18°C .

$$C_{SRR} = \frac{F_{SRR}}{F_L} = b. \quad (10.4)$$

## 10.2 Structural rolling resistance from data

The simple method for calculating structural rolling resistance was applied to the TSD measurements, and the results were presented here.

### 10.2.1 Måløv data

Data from the TSD measured at Måløv was presented in section 9.1.1 and 9.1.2. Using the simple method presented above, the structural rolling resistance was calculated for pavement response measured at two temperatures. These results are also discussed in Nielsen et al. (2020b) and Nielsen et al. (2020a) (see appendix A).

In figure 10.3, the calculated structural rolling resistance coefficient is plotted as a function of distance for the two temperatures. Below the difference between the two signals was calculated as

$$\text{Change in } C_{SRR} = \frac{C_{SRR}^{35} - C_{SRR}^{18}}{C_{SRR}^{18}}. \quad (10.5)$$

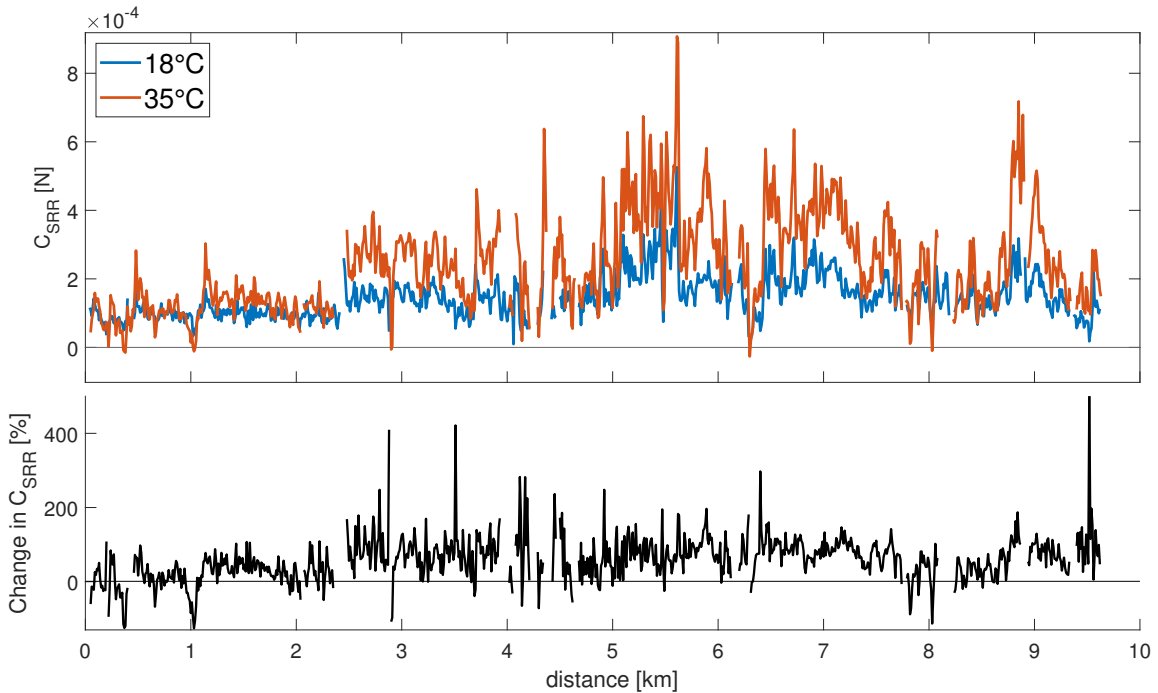


FIGURE 10.3: Calculated structural rolling resistance coefficient plotted as a function of distance for the two temperatures 18°C and 35°C. The difference between the two signals is seen below, calculated as  $(C_{srr}^{35} - C_{srr}^{18}) / C_{srr}^{18}$ .

The calculated structural rolling resistance coefficient is shown in the form of a histogram on figure 10.4.

On figure 10.3, we found that the  $C_{SRR}$  values for both temperatures varied considerably over the traveled distance, reflecting the spatial variation in the measured pavement deflection slope. These variations occurred since the structural properties of the road segments varied as a function of distance. The variations were completely reproducible with median standard deviation on 9% for 18°C and 5.5% for 35°C. This emphasised the robustness of the method and its ability to measure  $C_{SRR}$  with a high spacial resolution.

Furthermore, a clear change in  $C_{SRR}$  was observed at 2.5km, with significantly higher  $C_{SRR}$  after this point. This trend was seen for both temperatures.

When comparing  $C_{SRR}$  for the two temperatures we found an overall, systematic increase in  $C_{SRR}$  when temperature increased, with the average value increasing from 0.014% of the load to 0.024% of the load (fig. 10.4).

The distribution of 10.4 became broader when temperature increased. This was related to the fact that we are not looking at a homogeneous road section, but a section which most likely has a changing structural characteristics. Thus, the effect of increasing temperature varied across the different areas of the road. This is clearly seen in figure 10.3, where the difference in  $F_{SRR}$  varied from 50-150% with some outliers going as high as 400-500%.



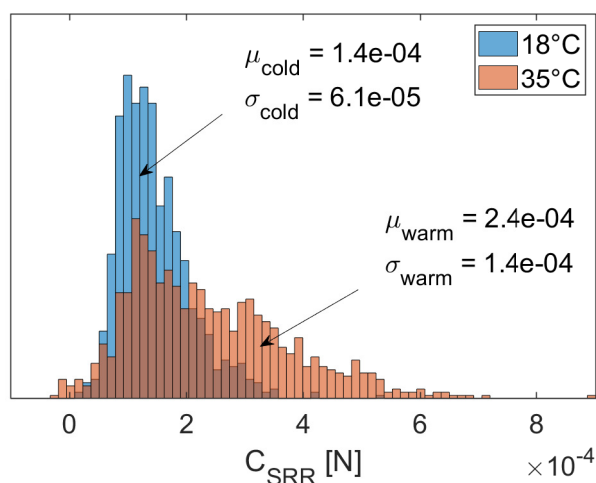


FIGURE 10.4: Histogram of measured structural rolling resistance for road temperature 18°C and 35°C. We see an increase in the mean ( $\mu$ )  $C_{SRR}$  value, when the road temperature is increased. Furthermore the distribution of measured values is broadening under warm conditions (increased  $\sigma$ ).

In table 10.1, the average SRR values were listed for the group division based on the x-position of the maximum deflection slope (group 1, 2 and 3). The SRR values were given in form of  $C_{SRR}$ ,  $P_{SRR}$  and  $F_{SRR}$ . Looking within the same road temperature, we found that there was a clear difference on SRR within the different groups, with the highest value in group 1 and the lowest value in group 3. If we compared across the two different road temperatures, SRR was increasing within group 1 and 2, similarly to the overall trends. For group 3 data, however, we find that the average SRR was decreased when going from 18°C to 35°C. On figure 10.3, these data sets have a difference below 0.

The behaviour in data sets having a difference below 0 was qualitatively investigated by visual inspection of the associated pavement deflection slope plots. Figure 10.5a illustrated the most commonly behaviour in cases where the SRR was decreased when temperature was increased, namely that only a small difference was seen in the maximum but a large difference was seen in the amplitudes of the minimum. Since this simple method used to calculate SRR used an interpolation between sensor 3 and 4, it was highly affected by this change of behaviour in the minimum.

Recall from the data presentation, that when temperature increased we found a significant change in the minimum, moving closer to the load. If the movement of the minimum is combined with no or a small decrease in maximum amplitude, it can result in a negative calculated SRR value (fig. 10.5b). From figure 10.3, we found that this situation happend a few times during the 9.5 km road segment measured. Having a negative SRR is unphysical, as it would mean that energy is led into the system. Instead, it is an artifact of the linear interpolation used in the simple method. Thus, we can conclude that when the

TABLE 10.1: Average values for  $F_{SRR}$ ,  $P_{SRR}$  and  $C_{SRR}$  divided into group 1, 2 and 3 for 18°C and 35°C. The standard deviation indicates the spread of SRR values within each group.

	$C_{SRR}$		$P_{SRR}$		$F_{SRR}$	
	18°C	35°C	18°C	35°C	18°C	35°C
Group 1	$1.7 \cdot 10^{-4} \pm 6 \cdot 10^{-5}$	$2.9 \cdot 10^{-4} \pm 1.3 \cdot 10^{-4}$	$124.2 \pm 57$	$212.2 \pm 112$	$8.6 \pm 3.0$	$14.4 \pm 6$
Group 2	$1.2 \cdot 10^{-4} \pm 4 \cdot 10^{-5}$	$1.3 \cdot 10^{-4} \pm 4.9 \cdot 10^{-5}$	$84.9 \pm 30$	$97.5 \pm 52$	$5.9 \pm 1.8$	$6.4 \pm 2$
Group 3	$0.9 \cdot 10^{-4} \pm 3 \cdot 10^{-5}$	$6.7 \cdot 10^{-5} \pm 4.0 \cdot 10^{-5}$	$61.7 \pm 21$	$46.8 \pm 32$	$4.2 \pm 1.3$	$3.3 \pm 2$

pavement became warm, using a simple linear interpolation may not be sufficient and a more sophisticated method should be used to estimate the deflection slope underneath the load.

### 10.2.2 Finland data

The simple approach was applied to Finland data presented in section 9.2 and the impact of temperature and velocity on SRR was studied. The calculated values for  $F_{SRR}$  and  $P_{SRR}$  is seen on figure 10.6 for the two locations studied.

With respect to velocity, we found that this had no influence on  $C_{SRR}$  in location 1, whereas a small decrease in  $C_{SRR}$  was seen at increased driving velocity for location 2 14°C. This trend was not seen for 22°C.

With respect to temperature, we found that in location 2 when comparing  $C_{SRR}$  for same driving velocities, it was increased with temperature. This was consistent with trends seen in Måløv data. For location 1, no significant trend was found, as the difference in  $C_{SRR}$  within the two temperatures was not larger than the standard deviations.

## 10.3 Extension of simple approach

The simple approach presented above uses a linear interpolation to estimate the pavement deflection underneath the load. In the following, an approach using a simulated deflection slope instead was derived. In this, the assumption that the tire load can be seen as a point load was no longer needed, as the extended approach used the integral over the area where the tire and pavement interacts, the *contact area*.

In order to calculate the structural rolling resistance using a simulated deflection slope we adopted an expression for the structural-induced power dissipation due to the rolling of a wheel derived in Chupin et al. (2013). This expression take into account that the tire load on the pavement surface is a distribution of vertical pressures  $p$  over the contact area  $S$ . A uniform pressure distribution was chosen over a more complicated distribution, as this simplification do not affect the resulting dissipated energy (Chupin et al., 2013).

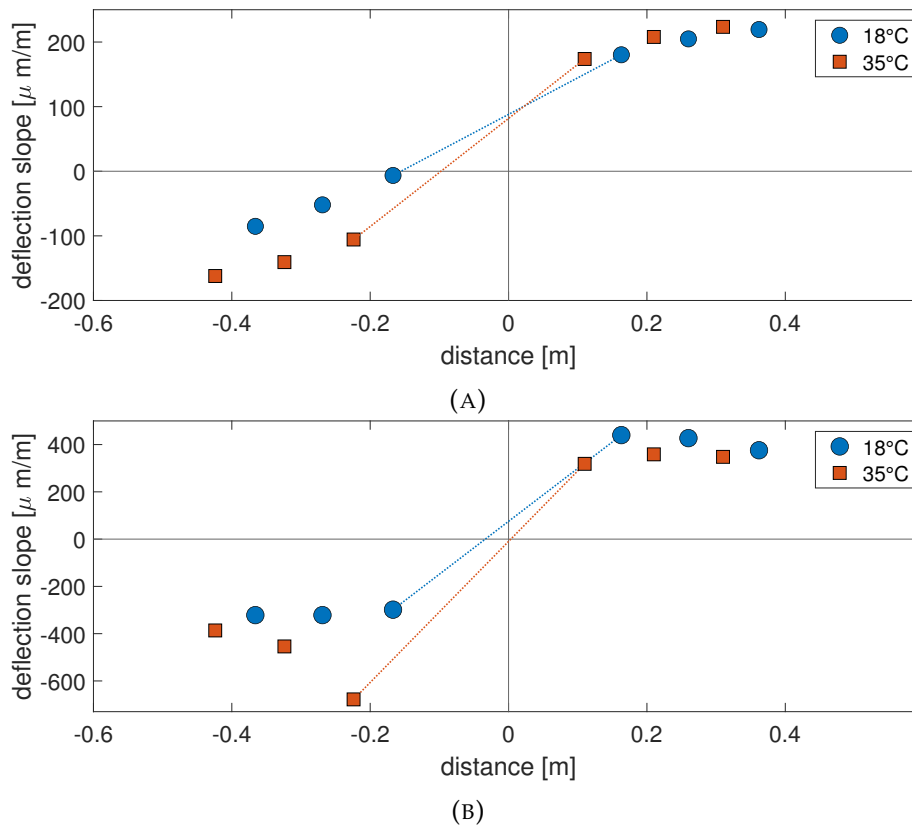


FIGURE 10.5: A) Representative data set where SRR is higher for  $18^\circ\text{C}$  ( $8.8 \cdot 10^{-5}$ ) than for  $35^\circ\text{C}$  ( $8.2 \cdot 10^{-5}$ ). The reason for the negative difference in  $C_{SRR}$  is that only a small difference is seen in the maximum but a big difference is seen in the amplitudes of the minimum. Data points in front of the load was cut of in order to enlarge the intersection with the  $y$ -axis. B) Example on a data set where SRR calculated for  $35^\circ\text{C}$  is negative. The reason is the big change in the minimum deflection, where the peak moves closer to the load and its amplitude increases. In this case, a simple liner interpolation is not sufficient to estimate the deflection slope underneath the load, but a more complex approach should be used.

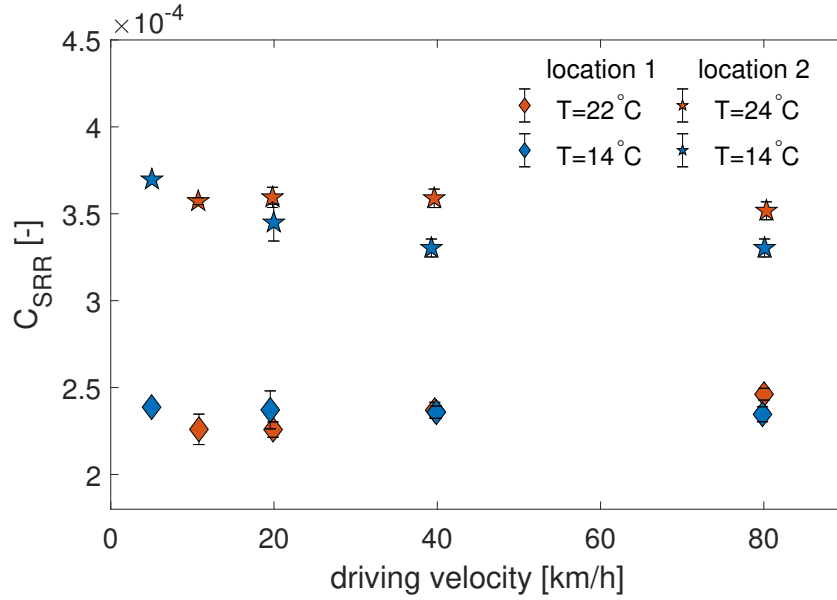


FIGURE 10.6: Structural rolling resistance calculated for Finland data. Here the effect of driving velocity and temperature is studied on two different locations.

The power dissipation due to structural effects can be written as follows,

$$P_{SRR}^{contact\ area} = pv \int_S \frac{\partial z(x, y, z)}{\partial x} dS. \quad (10.6)$$

Here  $v$  is the driving speed,  $z$  is the vertical component of the displacement field of the pavement surface, and  $\frac{\partial z(x, y, z)}{\partial x}$  is the derivative with respect to the driving direction  $x$  (Chupin et al., 2013).

The expression in (10.6) is written in a moving reference frame (hence assuming constant velocity) and thus is comparable with the framework used in the simple method derived in this thesis. In the derivations of equation (10.6), it was assumed that the tire is non-dissipative, that there is a constant load (thus no dynamic loading effects) and that the power dissipation arising due to horizontal forces can be neglected (Chupin et al., 2013).

Note that the two approaches are equal if the the pavement deflection slope within the contact area is assumed linear and the contact area is circular in the  $x$ - $y$  plane.

$$\begin{aligned} P_{SRR}^{contact\ area} &= pv \int_S \frac{\partial z(x, y, z)}{\partial x} dS = pv \int_{-r}^r \int_{-\sqrt{r^2-x^2}}^{\sqrt{r^2-x^2}} (ax + b) dy dx \\ &= pvb\pi r^2 = Fvb = P_{SRR}^{point\ load}. \end{aligned} \quad (10.7)$$

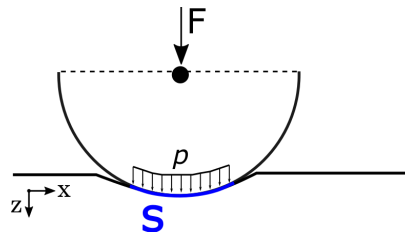


FIGURE 10.7: Sketch of the tire-pavement interaction. The tire is applied with an axle load  $F$ , which is applied to the contact surface  $S$  in form of the distributed vertical pressures  $p$ . The sketch is inspired by figure 2 in Chupin et al. (2013).

Here we use that  $F = pA$ , where the area of a circle is  $A = \pi r^2$ .

Thus, for a linearly varying deflection slope the calculated dissipated power using the simple approach is the same as using the extended approach with a contact area. However, if the pavement deflection slope deviates from a linear behaviour the two approaches will give different SRR estimates.

## 10.4 Investigating validity of the simple approach through simulated pavement responses

We aimed to investigate under which circumstances the simple approach which assumes a linear pavement deflection provided valid estimates of SRR and when the extended method should be used instead. This was done by analysing different simulated pavement responses and comparing the estimated SRR values.

In section 9, it was observed that the TSD data could be divided into groups according to the behaviour of the maximum deflection slope. We aimed to simulate pavement sections which has pavement responses matching these general trends. Note that the aim here was not to reproduce the behaviour seen in TSD data with respect to absolute amplitude and peak position, but rather to simulate responses following the general trends. Using the simulated pavements, a general statement about the validity of the simple approach can be derived.

### 10.4.1 ViscoWave II-M

For simulating the pavement responses used in the following analysis, we used the time-domain based viscoelastic solver ViscoWave II-M, developed at Michigan State University (Lee, 2013; Balzarini et al., 2017b). ViscoWave II-M employs the so-called spectral element method, where each element is defined as one layer of the pavement, to solve the wave propagation problem in a pavement structure and thereby calculate the pavement response to an arbitrary loading. The model can simulate the time-dependent responses and allows each pavement layer to be either elastic or viscoelastic (Lee et al., 2018).

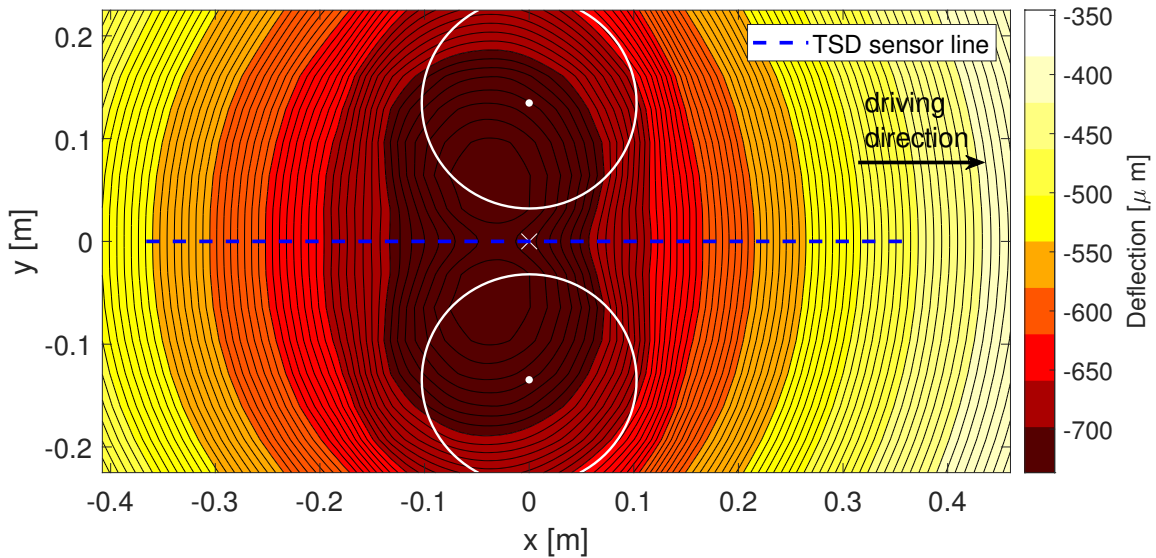


FIGURE 10.8: The loading configuration in ViscoWave II-M was modified to be used in this study such that the response to two dual tires with 6.4 cm spacing is calculated. This configuration matches the TSD setup. Here the pavement deflection underneath a dual tire is simulated and illustrated with contour lines. This shows that the pavement deflection is manifested as one deflection basin located symmetric around  $y=0$  (seen by closed contour circles) and with two local maximum deflection points on each side of  $y=0$ . Due to the viscous effects in the asphalt, the maximum deflections is located behind the center of the load with respect to the driving direction.

As developing the program was not a part of this thesis, it will not be discussed in detail here. A brief overview of the fundamental principle used within the solver is given in appendix B. For more information, we refer to Lee (2013) or appendix C in Chatti et al. (2017).

The output of the program was slightly modified to be used in this study. First of all, the simulation output was changed such that the simulated conditions were similar to the TSD setup. The original solution calculated the pavement deflection under a tire in a steady reference frame. A coordinate shift was made such that the model output was in a moving reference frame. Furthermore, the loading configuration had been modified such that the response was calculated in between two dual tires with 6.4 cm spacing, matching the distance at the TSD. This is illustrated on figure 10.8, where a contour plot of simulated pavement deflection is shown together with the location of the two tire contact areas (assumed circular with a load of 2.5 tonnes each). To mimic the TSD setup, the pavement response used for the analysis was obtained through the line at  $y=0$  (fig. 10.8).

Secondly, numerically differentiation was used to obtain the deflection slope as ViscoWave provides the pavement deflection. As a consequence, some numerical noise was introduced to the signal. A filtering procedure was developed, which removed numeric

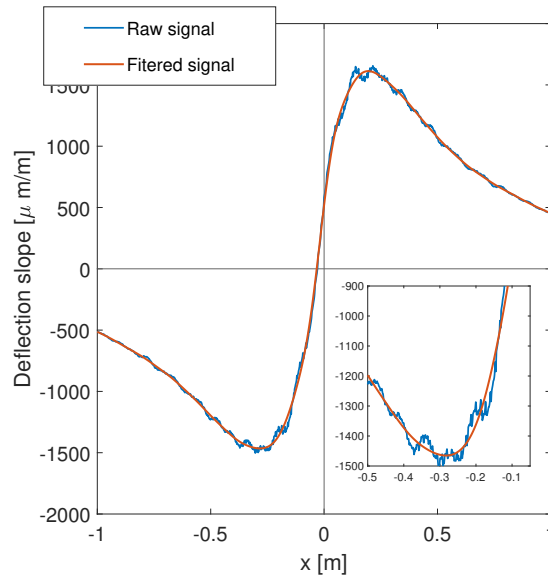


FIGURE 10.9: Example on pavement deflection slope simulated using ViscoWave II-M. The raw signal (blue line) has both high and low frequency noise, seen as fast and more slow oscillations in the signal. The noise is an artifact related to numerical differentiation and is removed by use of filtering process explained in appendix B (red line).

noise from the system but left any physical related features in the slope signal (fig. 10.9). The procedure is described in more detail in appendix B.

### 10.4.2 Simulated pavement sections

The pavements used in this analysis all consist of three layers, representing an asphalt layer, a base layer, and a subgrade layer. The parameters for the structure (height, elastic moduli, Poisson's ratio and density) were chosen to be typical values for these kinds of pavement layers, and they are listed in table 10.2. The base and subgrade was assumed semi-elastic as some damping need to be present in order to stabilise the numerical solution. The asphalt layer was assumed viscoelastic and its viscoelastic properties were described by the relaxation modulus  $E(t)$ .

We chose to simulate four pavements with the same mechanical characteristics in the base and subgrade layer, and different viscoelastic properties of the asphalt layer. The viscoelastic properties of the asphalt layer are described through the relaxation function  $E(t)$ , given by

$$\log(E(t)) = c_1 + \frac{c_2}{1 + e^{(-c_3 - c_4 \log(t_R))}}, \quad (10.8)$$

$$\log(t_R) = \log(t) - \log(a_T), \quad (10.9)$$

TABLE 10.2: Mechanical characteristics for the simulated pavement. All pavement structures are made of three layers, each characterized by their Poisson's ratio ( $\nu$ ), mass density ( $\rho$ ), average thickness ( $h$ ) and the relaxation modulus ( $E$ ). The relaxation modulus for the asphalt layer is given by equation (22.38).

Asphalt
$E(t)$ $\nu = 0.35$ $\rho = 2322.7 \frac{\text{kg}}{\text{m}^3}$ $h = 0.15 \text{ m}$
Base
$E_2 = 124.3 \text{ MPa}$ $\nu = 0.35$ $\rho = 2082.4 \frac{\text{kg}}{\text{m}^3}$ $h = 0.3 \text{ m}$
Subgrade
$E_3 = 65.4 \text{ MPa}$ $\nu = 0.45$ $\rho = 1762 \frac{\text{kg}}{\text{m}^3}$ $h = \infty$

where  $c_1, \dots, c_4$  are the sigmoid coefficients,  $t_R$  is the reduced time and  $a_T$  is the shift factor (Balzarini et al., 2019).

In order to ensure realistic  $E(t)$  curves, the parameters for the relaxation modulus were taken from backcalculated falling weight deflectometer tests on road segments located in California (Balzarini et al., 2019) (fig. 10.10). The characteristics of these moduli ranged from very stiff with high damping to very soft with little damping, see table 10.3.

Using the parameter values listed in table 10.2 and 10.3, four different pavement responses to a moving road was simulated. The deflection basin and associated deflection slopes are shown on figure 10.11.

In the simulated deflection curves, the stiff pavement with large damping (PAV4) resulted in a shallow deflection basin, and consequently the deflection slope maximum and minimum has a low amplitude and is located far from the load. The soft pavement with little damping (PAV1) results, on the other hand, in a steep deflection basin, and have a deflection slope maximum with a big amplitudes and x-location close to the load.

In Figure 10.12, a zoom of the contact region for each of the simulated deflection slope curves is shown. By assuming that the contact surface is circular with center in  $x=0$ , the contact region is given by the radius  $r$  which can be calculated from the tire pressure ( $p$ ) and load ( $F$ ),  $r = \sqrt{\frac{F}{p\pi}}$ . Using standard values from the TSD vehicle we found  $r = 14.5$  cm.



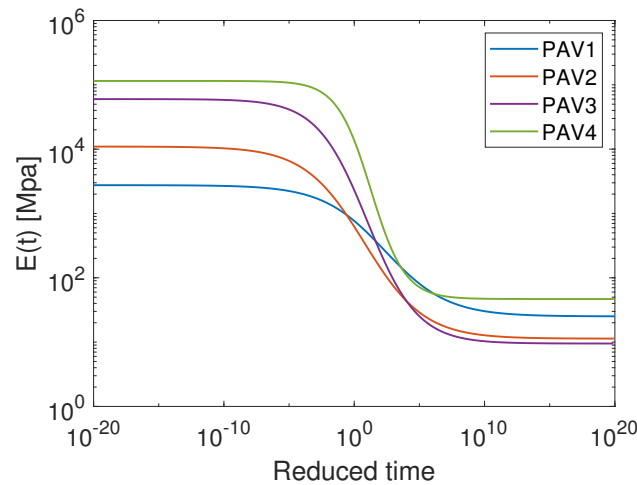


FIGURE 10.10: The asphalt layer is assumed viscoelastic and its viscoelastic properties are described by the relaxation modulus  $E(t)$  given by equation 22.38. In order to ensure realistic  $E(t)$  curves, the parameters for the relaxation modulus are taken from backcalculated falling weight deflectometer tests on road segments located in California (Balzarini et al., 2019).

TABLE 10.3: For the study, four different  $E(t)$  were used and their properties are listed here. The relaxation modulus are taken from backcalculated falling weight deflectometer tests on road segments located in California (Balzarini et al., 2019) and is plotted on figure 10.10.

	Pavements			
	PAV1	PAV2	PAV3	PAV4
<u>Sigmoid coefficients</u>				
$c_1$	1.4	1.054	0.978	1.67
$c_2$	2.04	2.986	3.8	3.39
$c_3$	0.944	0.335	0.521	0.981
$c_4$	-0.417	-0.436	-0.519	-0.767
Shift factor $\log(a_T)$	0.37	0.32	0.49	0.34
<u><math>E(t)</math> characteristics</u>				
$E_0$ [Mpa]	2,753	10,956	59,970	114,820
$E_0 - E_\infty$ [Mpa]	2,728	10,945	59,960	114,770
Stiffness	—————>			
Amount of damping	—————>			

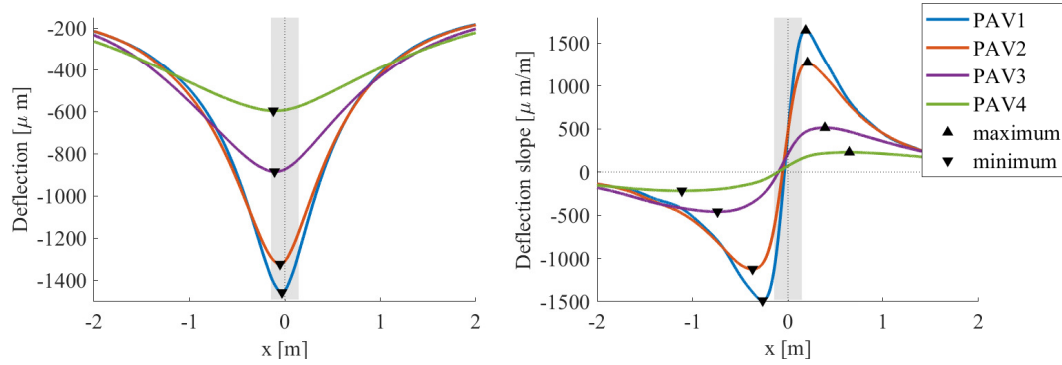


FIGURE 10.11: Simulated pavement response using the parameter values listed in table 10.2 and 10.3. The contact area between the tire and pavement is assumed circular with radius ( $r$ ). The interval  $[-r;r]$  is marked with a gray color.

### 10.4.3 Structural rolling resistance using simple and extended approach

Using the simulated pavement sections, we could calculate the structural rolling resistance using the simple and extended method and subsequently compare the estimated values.

When using the extended approach (eq. 10.6), the surface integral was taken over the contact area  $S$ . Thus, it required knowledge about both the shape of  $S$  and the pavement deflection in the  $x$ - $y$  plane. If we assume the contact area is circular with radius  $r$ , equation (10.6) can be rewritten as

$$P_{SRR} = -pv \int_{-r}^r \int_{-\sqrt{r^2-x^2}}^{\sqrt{r^2-x^2}} \frac{\partial w(x,y)}{\partial x} dy dx. \quad (10.10)$$

Through Viscowave, it was possible to simulate deflection underneath the contact area and obtain information in both  $x$  and  $y$  direction (fig. 10.8). However, as we aimed to mimic the TSD setup, only information about the deflection obtained in-between the tires was used. Consequently, in order to integrate over  $S$ , we assumed that the deflection slope  $\frac{\partial w(x,y)}{\partial x}$  was constant in the  $y$  direction. In this case, the integral with respect to  $y$  could be evaluated as

$$\int_{-\sqrt{r^2-x^2}}^{\sqrt{r^2-x^2}} \frac{\partial w(x,y)}{\partial x} dy = 2 \frac{\partial w(x,y)}{\partial x} \sqrt{r^2 - x^2}. \quad (10.11)$$

And thus, equation (10.10) becomes

$$P_{SRR} = -pv \int_{-r}^r 2\sqrt{r^2 - x^2} \frac{\partial w(x,y)}{\partial x} dx. \quad (10.12)$$

Equation (10.12) enables calculation of SRR based on simulated deflection slope behaviour underneath a load with a finite size.

A comparison study of calculated SRR values using the simple and extended approach were made. In total, four different methods for calculating SRR will be compared.

**Method 1** This uses the simple approach given by equation (10.3), where a point load is assumed and a linear interpolation is used to estimate the pavement deflection slope underneath the load. The linear interpolation was made from the simulated deflection slopes values in the x-positions corresponding to sensor 3 and 4 (according to Måløv 18°C data). This is marked on figure 10.12 by a black line.

**Method 2** This uses the simple approach in equation (10.3), but includes a more elaborate interpolation method instead of the linear. We chose to use a cubic spline interpolation which is seen with dotted line on figure 10.12. In this, a 3rd order polynomial was used to find the values in-between the two interpolation points instead of a linear function, and thus this yielded a smoother interpolation curve. As this method has more unknown parameters to fit than the linear, we needed all nine simulation points to make the interpolation. The deflection slopes corresponding to these points were found in x-positions corresponding to the TSD sensors (according to Måløv 18°C data). Using a spline interpolation includes no modelling of the pavement, and thus remains an easy and fast evaluation method of the SRR value. However, as it used a 3rd order polynomial to find values in between two interpolation points, more unknown parameters were included and it will mimic the shape of the used data points to a higher degree.

**Method 3** This uses the simple approach where a point load is assumed, but uses the simulated deflection slope intersection with the y-axis,  $\frac{\partial z(x=0)}{\partial x}$ . This method is a combination between the simple and extended approach, as it used a simulated deflection slope but no assumptions about the shape of the contact area was made.

**Method 4** This uses the extended approach given by equation 10.12, where a simulated pavement deflection over a finite contact area was used to estimate the SRR value.

In table 10.4, the dissipated energy due to structural effects calculated using the four methods are listed. As the extended approach (method 4) uses both the simulated pavement deflection and a finite contact area, we assumed that this provide the closest estimate to *the real* SRR value as possible. The relative difference between the extended approach and another method, e.g. method 1, was found as

$$\Delta P^{\text{method 1}} = \frac{P_{SRR}^{\text{method 4}} - P_{SRR}^{\text{method 1}}}{P_{SRR}^{\text{method 4}}}. \quad (10.13)$$

The analysis showed that the difference between the simple approach (method 1) and the extended approach (method 4) indeed depends on the shape of the deflection slope curve. For PAV4, where the deflection maximum and minimum were far apart, a difference on 9% was seen. Decreasing stiffness of the pavement result in the maximum and minimum moving closer to the load and consequently, the relative difference increase,

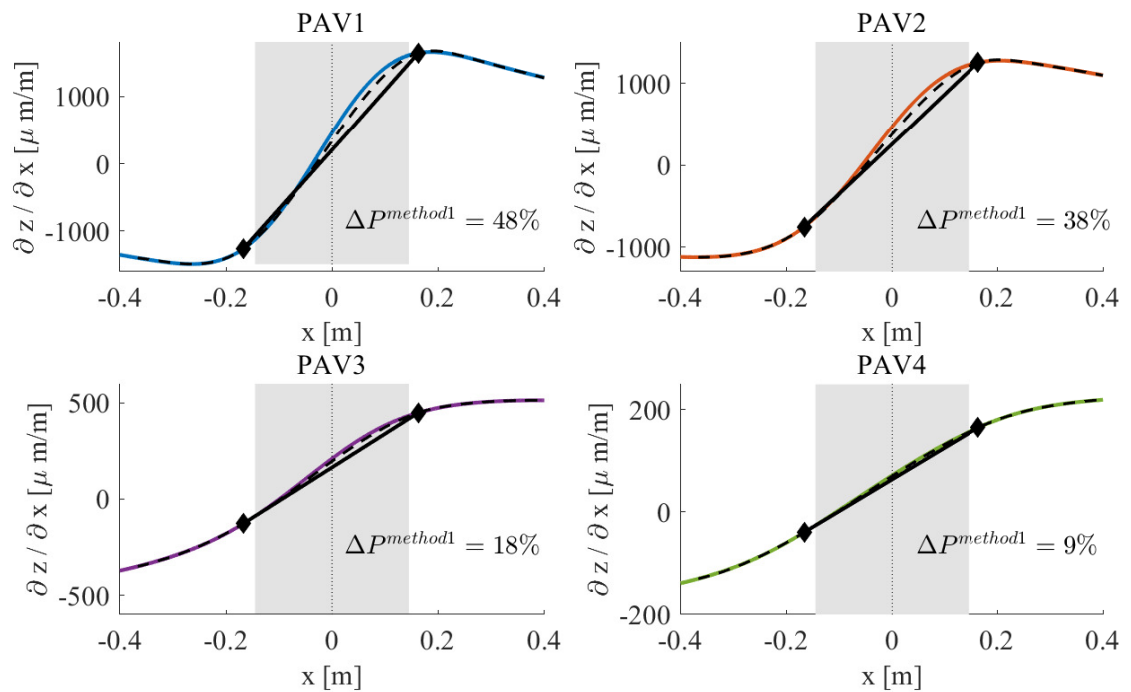


FIGURE 10.12: A linear interpolation is made between the pavement deflection slope values in  $x$ -position corresponding to sensor 3 and 4 in the TSD setup. When calculating  $P_{SRR}$  using this and comparing with  $P_{SRR}$  calculated using the simulated deflection slope we find that the linear interpolation method underestimated the value. How large the underestimation is depends on the specific pavement characteristics.

TABLE 10.4: Calculated  $P_{SRR}$  values using method 1-4 for four simulated pavements. The relative difference between a method and method 4 is given as  $\Delta P$  (eq. (10.13)).

	PAV1		PAV2		PAV3		PAV4	
	$P_{SRR}$	$\Delta P$	$P_{SRR}$	$\Delta P$	$P_{SRR}$	$\Delta P$	$P_{SRR}$	$\Delta P$
Method 1	175	48%	219	38%	140	18%	54	9%
Method 2	289	14%	325	9%	167	1%	60	0%
Method 3	391	-16%	401	-13%	179	-6%	61	-3%
Method 4	335	-	356	-	170	-	60	-

with the largest deviation found in PAV1, where  $\Delta P = 48\%$ . Assuming that method 4 provided an estimate of the real SRR value, this means that the simple approach underestimated SRR with 48% in this situation. From the analysis we can conclude that calculating SRR using a linear interpolation, provides a valid estimate when the peaks are located further away from the load than the sensors.

We also compared method 2 and 3, where a point load is assumed and the pavement deflection slope is estimated through a spline interpolation and simulation, respectively. These methods were found to improve the estimated SRR compared to method 1 and provides results closer to method 4. However, they also included more underlying assumptions than method 1.

#### 10.4.4 Conclusion about using a linear interpolation

By use of four simulated pavement deflection slope curves, we found that using a linear interpolation to estimate the deflection slope underneath the load underestimated the SRR. Thus, the simple approach provided a lower limit for the real SRR. The extent of which the simple method underestimated SRR depended on the x-position of the maximum and minimum deflection slope. If these were located further away from the load than the sensors, the underestimation was small, whereas it increased when the peaks moved closer to the load.

Using a cubic spline interpolation between nine positions corresponding to the TSD sensor positions, improved the SRR estimate considerably. Confirming that the resolution of the maximum was critical for the interpolation approach to give accurate results. However, there was still a large difference in the estimated  $P_{SRR}$  when the peak was located closer to the load than the sensors (PAV1).

The simulated pavement deflections was created such that they mimicked the behaviour seen in data with respect to the x-position of the maximum. In the TSD data, we identified changing behaviour in the maximum x-placing, which led to the coarse grained group division into group 1, 2 and 3. In group 3, the maximum was fully resolved peak and thus, based on the above analysis, we expected the simple approach to provide valid estimates of SRR. For data in group 1, however, the maximum peak was located closer to

the load than the sensor location, and thus we expected the simple approach to underestimate the SRR value.

As the peak was found to generally move closer to the load when temperature increased, we expected the calculated SRR to be underestimated to a higher degree in data for 35°C .

As a conclusion, for data sets belonging to group 1 we propose that the pavement deflection slope underneath the load is estimated using a model. Furthermore, analysis in table 10.4 indicated that a finite contact area should be included in order to obtain a good estimate of SRR.

## 10.5 Investigating dual tires vs a single load

In the derivation of the simple method, we assumed that we measure the pavement deflection slope underneath the center of the load. This does, however, not correspond with the TSD setup where we have two dual tires and measure in-between these. The underlying assumption was that since the width of the tires was much larger than the space between them, we could see it as one big tire creating a contact surface with center in the line the sensors were located. This assumption is strengthened if we consider the asphalt layer a stiff layer which bend underneath the loads, and thus helps distribute the load over a bigger area than just the contact area.

The validity of the assumption was investigated by use of simulated pavement deflections from ViscoWave II-M. In ViscoWave II-M, a double dual tire is used with a circular contact area as sketched on figure 10.8. We simulated the pavement deflection in a grid underneath the applied loads and using this, made a contour map over the pavement deflection. This is seen on figure 10.8 where the x-y plane is the pavement surface, and the pavement deflection is plotted in the z direction illustrated through contour lines. The contact areas for the dual tires is seen as white circles on each sides of the TSD sensor line.

We found that the pavement deflection due to the dual tires was manifested as one deflection basin located symmetric symmetric around  $y=0$  (seen by closed contour circles) and with two local maximum deflection points on each side of the sensor line ( $y=0$ ). Note that due to the viscous effects in the asphalt, the maximum deflections was located behind the center of the load with respect to the driving direction.

Based on the simulated pavement deflection, we calculated the  $P_{SRR}$  using the extenden approach (method 4) and taking the pavement deflection in  $y=0$  (As done in the analysis above) and in  $y = -0.13$  (underneath one of the dual tires), respectively. From this we obtain  $P_{SRR}^{y=0} = 169.7 \text{ W}$  and  $P_{SRR}^{y=\pm 0.13} = 194.8 \text{ W}$ . The relative difference between the two methods  $\Delta P$  was 3.1%.

The analysis made here was based on a numerical model study, and thus the result depended on the chosen structural characteristics of the simulated pavement. If the simulations were made with a stiffer asphalt layer (PAV4), the difference between the two

methods decrease to 0.7%, as the stiff asphalt layer helps distribute the load over a bigger area of the foundation.

Consequently, we conclude, that assuming the deflection slope measured in between two dual tires located close together to be the same as the deflection in the center of one load was valid.





## Chapter 11

# Partial conclusion on the simple approach

A novel simple method for measuring the structural rolling resistance (SRR) was presented. The method was based on the relation between SRR and the slope of the deflection basin under a moving load. For measuring the pavement deflection underneath a moving tire, we used the Traffic Speed Deflectometer (TSD) technology, which provide high resolution measurements of the pavement deflection slope. The proposed method was aimed to be simple and easy applicable, and as a result no modelling procedure of data was involved. Consequently, a linear interpolation between data points closes to the load was used to estimate the deflection slope underneath the load.

The method was used on three set of TSD data, each containing three repeated repetitions in in order to evaluate reproducibility. The method was proven to obtain highly reproducible measurements of SRR (standard deviations from three repeated measurements of 4-10%) with a high spatial resolution. From the TSD data, effect of spatial variation, temperature and velocity on SRR was studied. We found that the estimated  $C_{SRR}$  values varied considerably over the traveled distance, reflecting the spatial variation in the measured pavement deflection slope. These variations occurred since the structural properties of the road segments varied as a function of distance. The variations were completely reproducible with median standard deviation on 9% for 18°C and 5.5% for 35°C. This emphasised the robustness of the method and its ability to measure  $C_{SRR}$  with a high spacial resolution.

Furthermore,  $C_{SRR}$  increased with increased temperature. However, the percentage increase in  $C_{SRR}$  differed over the measured data sets, and we speculate that this depended on the local structural characteristic of the pavement.

The validity of using the simple approach was investigated by comparing estimated SRR values on four simulated pavement sections with an extended method. In the extended method, the pavement deflection underneath the load is simulated using a pavement response model and furthermore a finite contact area is assumed. We found that using a linear interpolation to estimate the deflection slope underneath the load in some cases underestimates the SRR. Thus, the simple approach will provide a lower limit for the real SRR. The amount of which the simple method underestimates SRR was highly dependent on the x-position of the minimum and maximum. As a result, we predicted

that the simple approach underestimated SRR for TSD data belonging to group 1. For these data sets, we recommended that a simple pavement response model was fitted to data, and a more exact estimate of the deflection slope underneath the load was obtained. Such a simple pavement response will be derived in part IV.

## **Part IV**

# **Modelling the pavement deflection underneath a moving load**



## Chapter 12

# Pavement response models

In the previous part, we concluded the need for developing a simple model that can be fitted to data in order to estimate the pavement deflection slope underneath the load. In this part, a simplified model was developed and studied. As the model is founded in physical elements, it can in addition be used to deduce information about structural characteristics of the measured pavements.

The dynamic response of a pavement subject to a moving load has been studied throughout the last decades. There exists a variety of different approaches towards simulating a pavement system, going from complex numerical methods to simple models where closed-form solutions can be obtained. Two good reviews in the area are Beskou and Theodorakopoulos (2011) and Wang et al. (2005). The different modelling approaches have advantages and disadvantages and are suited for different purposes. Thus, the end goal of the modelling process should guide the choice of model approach.

In order to model the entire pavement structure, a multi-layered model is needed, with different mechanical properties of each layer. An example is the viscoelastic solver *Viscowave* used in section 10.4.1. However, these types of models easily get complicated and often contain insensitive parameters. Another approach, which we will follow in this thesis, is to model a simplified pavement structure with limited layers. Simple models have the advantage that they contain few parameters and thus changes in the model output can, to a higher degree, be correlated with one or more specific parameters. Furthermore, the models used in this thesis are based on physical assumptions, and thus the used parameters all have a physical interpretation. As a consequence, a change in data behaviour can be related to changes in specific physical properties of the pavement structure. However, the inherent model limitations always have to be taken into account when interpreting simplified model results.

One of the simplest ways to model the dynamic response of a pavement, is to consider an elastic Euler-Bernoulli beam supported by an elastic foundation consisting of uniform distributed springs. This is known as a Winkler foundation (Saito and Terasawa, 1980). Such a model is a simple one-dimension representation of the pavement structure, with the top layer modelled by a beam and all underlying layers represented by a single foundation. The big advantage of this model is that an analytical expression can be derived, and thus the influence of the different layers on the pavement deflection can be studied

directly (Seong-Min Kim and Roesset, 2003).

Although models containing Winkler foundation have proven successful in modelling pavement response of a moving load, its simple nature puts some limitations on its use (Wang et al., 2005). E.g. the foundation in the Winkler model mimics a single elastic soil layer, however soil is known to possess damping (Michaels, 1998). As a consequence modelling the foundation as a purely elastic media might result in unrealistic behaviour in the simulated pavement response. Furthermore, as soil is a continuous medium there are interactions among the soil particles and these are not accounted for by the parallel springs in the Winkler foundation.

Damping is often included into the foundation by adding a set of uniform distributed dashpots, thus modelling the soil as a viscoelastic material (Beskou and Theodorakopoulos, 2011). This does, however, not address the problem that the foundation consists of non-interacting elements which do not model the cohesive bonds between the particles. In order to approach a more realistic behaviour of the foundation, a coupling between foundation elements is included. Several approaches to do so has been made in literature (Wang et al., 2005), one of which is to connect the top of the elements with an incompressible layer, known as a Pasternak foundation (Froio et al., 2018). The Pasternak foundation is a popular choice of foundation model when shear interactions between foundation elements have to be taken into account, and we will also be using it in this thesis (Saito and Terasawa, 1980; Yu et al., 2017; Tanahashi, 2004; Froio et al., 2018).

When modelling the pavement response through a beam model, the problem is simplified into a one-dimensional situation. A natural extension from this into a two-dimensional case, is to consider a plate resting on a foundation instead (Beskou and Theodorakopoulos, 2011). For the purpose of this thesis however, we aimed to develop as simple a model as possible which can mimic the deflection slope behaviour of the TSD data.

The response measured using the TSD was obtained between two dual tires and was of nature a two-dimensional response, where each tire affects the resulting pavement deflection basin. However, if the contributions from the tires can be assumed equal, the response is measured on a symmetric line. Furthermore, as the width between the tires are much smaller than the width of the contact area between tire and pavement, the TSD measurements will to a good approximation give us the pavement response in the center of the overall deflection basin. In this case, a simplification of the TSD measurements into a one-dimensional model was believed to be a good approximation.

It was assumed that the pavements measured on was characterised by having a stiff asphalt layer compared to the underlying foundation, and as a result the deformation occurred in the underlying layers. Consequently, the top layer acted as a stiff incompressible layer which bend underneath the tire load. Thus, it could be modelled as an Euler-Bernoulli beam.

In this part of the thesis, we derived a pavement response model consisting of a viscoelastic Euler-Bernoulli beam resting on a Pasternak foundation. The govern equation for the pavement response to a moving load of the model in a moving reference frame

is derived in section 15. Before this, the needed theory about viscoelastic materials is presented in chapter 13, and the govern equation for deflection of a viscoelastic beam is deduced in chapter 14. The author has chosen to give a thorough introduction into deflection of Euler-Bernoulli beams, as the assumptions behind is important for later discussions and no coherent introduction into the field of dynamic and viscoelastic beams was found in the literature. The part ends with an numerical study of the model presented in chapter 16, 17 and 18.

The work presented in this part is the basis of paper draft 1 (appendix A.3).





## Chapter 13

# Elasticity and Viscoelasticity

Due to viscoelastic properties of the pavement structure, energy is dissipated when it is subject to a moving load. A pavement structure consists of several different layers, each having its own mechanical characteristics. The asphalt layer consists of a mix of crushed rock aggregate, gravel and bitumen mixture, which is known to have viscoelastic behaviour affecting the dynamic response of the pavement. This is especially true under warm conditions (Lv et al., 2010). The materials in underlying layers such as soil are also known to have a damping effects, and can be treated like a visco-elastic material (Bolton and Wilson, 1990).

In this chapter, a basic introduction to linear elastic and viscoelastic theory is given. As these are two comprehensive subjects, we will mainly focus on the parts of the theories that is relevant for the work made in the thesis. For a more comprehensive review of the theory see Flügge (1975).

### 13.1 Mechanics of continuous matter

The mechanics of continuous matter is the field of studying materials which can be considered as a continuous mass instead of a set of individual particles (Lautrup, 2011). In this field, there are three important quantities; *stress*, *strain* and *displacement*.

Stress describe the forces acting on a body per unit area and is denoted by  $\sigma$ . A distinction is made between *internal stress*, acting on some cross section within the body, and *external stress* which is acting in the interface of a body and its environment. Stress can act both normal to the surface, or along a tangent in which case it is called shear stress.

Strain describes the local deformation of a body subject to an external force and is denoted by  $\epsilon$ . Like stress, deformations can occur tangent to the principal axis which results in shear strain.

Where strain describes the local deformation of a material, the displacement describes how a point or line element is moved away from its original position, with respect to some reference coordinate system, during a deformation (Flügge, 1975). The relationship between strain and displacement for a body is known as the *kinematic relation* which will be derived for a beam later on.

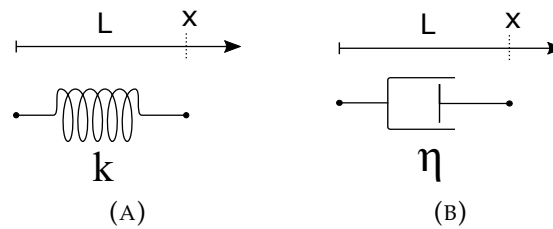


FIGURE 13.1: The mechanical response of A) an elastic material and B) a viscoelastic material can be represented by a mechanical analog in form of a linear spring and dashpot respectively.

### 13.1.1 Linear elastic solid materials

The mechanical response of an elastic material is often represented by a mechanical analog in form of a spring (fig. 13.1a). Following Hooke's law, the displacement of a spring is proportional to the applied force with a proportionality constant  $k$ , called the spring constant.

$$F = kx. \quad (13.1)$$

Likewise, an elastic solid material is characterised by having a linear relation between stress ( $\sigma$ ) and strain ( $\epsilon$ ) in all directions. If this is to be written in its most general form, it contains 81 different elastic constants describing the linear relations in all directions (Gould and Feng, 2018). The problem can be simplified by assuming the material is isotropic, hence the material properties are the same in all directions. In this situation, only two elastic constants remain and a total of six equations is needed to describe the relationship between stress and strain in the material.

In the specific situation where an uni-axial stress is applied (e.g. a vertical load on a beam), the relationship between stress and strain in the material can be described by the simple relation

$$\sigma = E\epsilon. \quad (13.2)$$

$E$  is called Young's modulus and it is a measure of the stretchability of the material (Lautrup, 2011). The higher  $E$ , the harder it is to stretch. All elastic materials considered in this thesis are assumed isotropic materials under uni-axial stress, and thus the relation between stress and strain is given by equation (13.2).

An elastic material has the property that if it is deformed and then return to its original shape, the work done is zero and thus no energy is dissipated (Wineman and Rajagopal, 2000).

### 13.1.2 linear viscous materials

The mechanical analog used to describe a linear viscous material is a viscous damper (fig. 13.1b). The response of a viscous damper is characterised by having a linear relation between stress and the rate of strain,

$$\sigma = \mu \frac{d\varepsilon}{dt}. \quad (13.3)$$

$\eta$  is the viscosity of the material.

If a viscous material is deformed and then returned to its original shape, then the work is completely converted to thermal energy (Wineman and Rajagopal, 2000).

## 13.2 Viscoelastic materials

Some materials exhibit both elastic and viscous behaviour and are called viscoelastic materials. Viscoelastic materials are characterized by having a time dependent relationship between stress and strain (Lakes, 2009).

Linear viscoelasticity describes materials in which there is a linear relation between stress and strain. Thus, if the applied stress is doubled, the resulting strain is also doubled. In this thesis, we only deal with small deformations of the materials and thus the material behaviour can be assumed linear viscoelastic.

The difference between an elastic and a viscoelastic material is sketched on figure 13.2. If a constant rate of strain is applied to an elastic material and subsequently released, a linear relationship with a slope proportional to the elastic modulus  $E$  is seen (Lakes, 2009). Furthermore, the material path is the same in both directions. For a viscoelastic material, on the other hand, the stress-strain curve is curved and will not take the exact same path back when the applied strain is removed. The difference in paths result in an energy loss, referred to as hysteresis loss (Lakes, 2009). This is a frequency-dependent loss, meaning that it depends on the specific loading frequency.

The behaviour of a viscoelastic material can be described by a combination of springs and dampers.

### 13.2.1 Relaxation function

The time dependent stress-strain relationship in viscoelastic materials is described through their relaxation function  $E(t)$ .

Imagine that a strain  $\varepsilon_0$  is applied to a viscoelastic material at time  $t = 0$ , and hold constant such that  $\varepsilon(t) = \varepsilon_0$  (fig. 13.3a). The resulting time-depending stress can then be calculated using the relaxation function  $E(t)$ ,

$$\sigma(t) = \varepsilon_0 E(t) \quad (13.4)$$

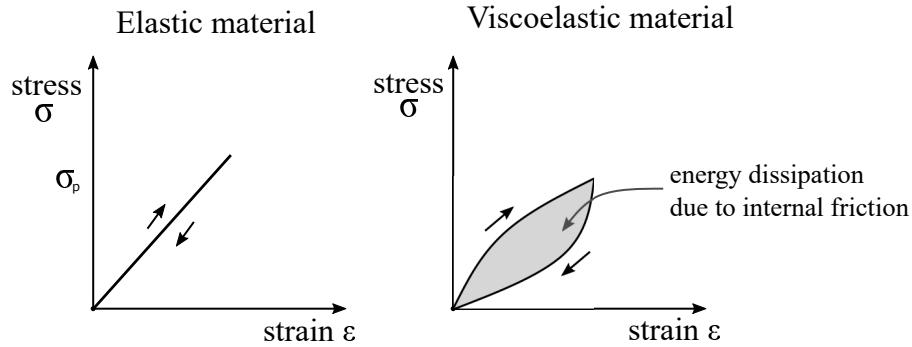


FIGURE 13.2: Stress-strain behaviour of an elastic and viscoelastic material subject to a constant rate of strain. The plot on the left shows the behaviour of an elastic material and the plot on the right for a viscoelastic material. Inspired by figure 1.2 in Lakes (2009)

Since the material is linear viscoelastic, the stress response to an arbitrary strain  $\varepsilon(t)$  can be found using the rule of linear superposition. Imagine an additional stress is applied to the material at a later time  $t = t'$ , denoted  $\Delta\varepsilon$  (fig. 13.3b). This results in an additional stress, given by

$$\Delta\sigma = \Delta\varepsilon(t')E(t - t'). \quad (13.5)$$

Now assume an applied strain which starts at  $t=0$  with an initial strain  $\varepsilon_0$ , followed by a sequence of infinitesimal step functions of width  $\delta t$  and height  $\delta\varepsilon$ . The resulting stress is then a sum of the individual stress responses caused by  $\delta\varepsilon$ . In the limit  $\delta t \rightarrow 0$ , the sequence of infinitesimal step functions converges to the function  $\varepsilon(t)$  and the resulting stress function  $\sigma(t)$  can be written as the convolution

$$\sigma(t) = \varepsilon_0 E(t) + \int_0^t E(t - t') \frac{d\varepsilon(t')}{dt'} dt' \quad (13.6)$$

Using integration by parts, equation (13.6) can be rewritten to contain  $E(t = 0) = E_0$  in the first part,

$$\sigma(t) = E_0 \varepsilon(t) - \int_0^t \frac{dE(t - t')}{dt'} \varepsilon(t') dt'. \quad (13.7)$$

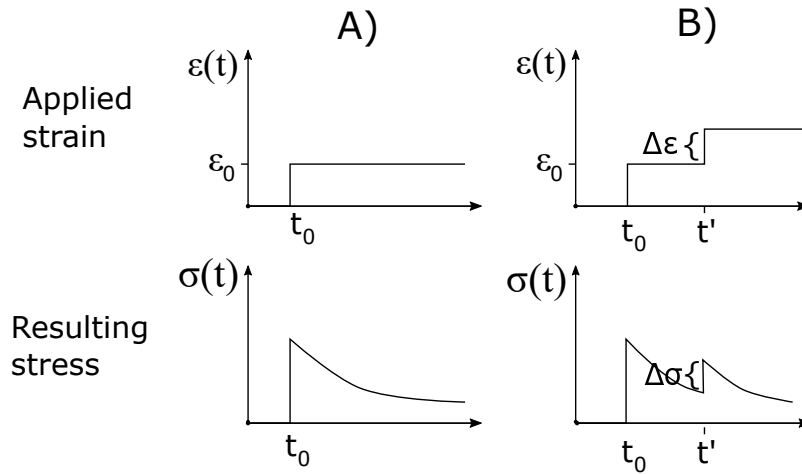


FIGURE 13.3: Sketch of an strain procedure applied to a viscoelastic material (top) and the resulting stress (bottom).

### 13.2.2 Characterising the viscoelastic behaviour through the complex modulus

Characterisation of the viscoelastic behaviour of a material can be done in the frequency domain as well, where it is described through its *complex modulus*  $E^*(\omega)$ .

Equation (13.7) can be rewritten to include all times in the past  $t < 0$ , as the responses here are zero. Thus, we get the expression

$$\sigma(t) = \int_{-\infty}^t E(t-t') \frac{d\varepsilon(t')}{dt'} dt' \quad (13.8)$$

We now introduce a new variable  $\tau = t - t'$ . Consequently,  $t' = t - \tau$  and  $dt' = -d\tau$ . If this change in variable is introduced in (13.8), we get

$$\sigma(t) = \int_{t-(-\infty)}^{t-t} E(\tau) \frac{d\varepsilon(t-\tau)}{d(t-\tau)} (-d\tau) \quad (13.9)$$

$$= \int_0^{\infty} E(\tau) \frac{d\varepsilon(t-\tau)}{d(t-\tau)} (d\tau) \quad (13.10)$$

Assume that we control the input strain and this is given by a harmonic oscillating function, written on the complex form

$$\varepsilon(t) = \tilde{\varepsilon}_0 e^{i\omega t} = \varepsilon_0 e^{i\phi_\varepsilon} e^{i\omega t}. \quad (13.11)$$

If we include equation (13.11) in (13.10), we get

$$\sigma(t) = \int_0^{\infty} E(\tau) i\omega \varepsilon_0 e^{i\phi_\varepsilon} e^{i\omega(t-\tau)} d\tau \quad (13.12)$$

$$= i\omega \varepsilon_0 e^{i\phi_\varepsilon} e^{i\omega t} \int_0^{\infty} E(\tau) e^{-i\omega\tau} d\tau \quad (13.13)$$

If we introduce a new function

$$f^*(\tau) = \begin{cases} 0, & \text{if } \tau < 0 \\ E(\tau) e^{-i\omega\tau}, & \text{if } \tau \geq 0 \end{cases} \quad (13.14)$$

equation 13.13 becomes

$$\sigma(t) = i\omega \varepsilon_0 e^{i\phi_\varepsilon} e^{i\omega t} \int_{-\infty}^{\infty} f^*(\tau) d\tau. \quad (13.15)$$

The last term corresponds to the Fourier transform of  $E(\tau)$ ,  $\mathcal{F}\{E(\tau)\}$ , as this is defined by

$$\mathcal{F}\{f(t)\} = \tilde{F}(\omega) = \int_{-\infty}^{\infty} f(t) e^{-i\omega t} dt, \quad (13.16)$$

where  $\omega$  is the transformation variable. Denoting the Fourier transform by  $\tilde{E}(\omega)$  and equation (13.15) becomes,

$$\sigma(t) = i\omega \varepsilon_0 e^{i\phi_\varepsilon} e^{i\omega t} \tilde{E}(\omega) \quad (13.17)$$

Since we have a linear response, the resulting stress can likewise be expressed through a harmonic complex function,

$$\sigma(t) = \sigma_0 e^{i\phi_\sigma} e^{i\omega t}. \quad (13.18)$$

Hence we have the relation that

$$\sigma_0 e^{i\phi_\sigma} e^{i\omega t} = i\omega \varepsilon_0 e^{i\phi_\varepsilon} e^{i\omega t} \tilde{E}(\omega) \quad (13.19)$$

$$\Downarrow \quad (13.20)$$

$$\frac{\sigma_0}{\varepsilon_0} e^{i(\phi_\sigma - \phi_\varepsilon)} = i\omega \tilde{E}(\omega) \quad (13.21)$$

$\phi_\varepsilon - \phi_\sigma$  is the phase difference between the stain and stress (fig. 13.5). Thus for an elastic material where no phase lag is present,  $\phi_\varepsilon = \phi_\sigma$ .

The term  $E^*(\omega) = i\omega \tilde{E}(\omega)$  is called the complex modulus, and this describes the relation between stress and strain in the frequency domain. A consequence of equation (13.19) is that the relationship between the Fourier transformed stress ( $\hat{\sigma}(\omega)$ ) and the Fourier

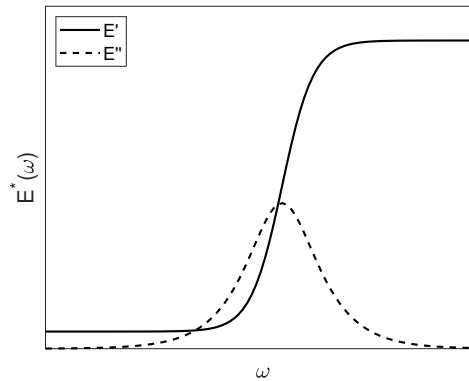


FIGURE 13.4: Sketch of a typical behaviour of  $E^*(\omega)$  for a viscoelastic material. The real part ( $E'$ ) is called the storage modulus as it accounts for the energy preserved in the material and the imaginary part ( $E''$ ) is called the loss modulus as it accounts for the dissipated energy in the material.

transformed strain ( $\hat{\epsilon}(\omega)$ ) is given by the complex modulus,

$$\hat{\sigma}(\omega) = E^*(\omega)\hat{\epsilon}(\omega) \quad (13.22)$$

On figure 13.4, a sketch of a typical behaviour of  $E^*(\omega)$  for a viscoelastic material is seen. As this is a complex function, it consists of both a real ( $E'$ ) and imaginary ( $E''$ ) part.

$$E^*(\omega) = E' + iE'' \quad (13.23)$$

The real part is called the storage modulus as it accounts for the energy preserved in the material, thus the elastic characteristics of the material. The imaginary part is called the loss modulus as it accounts for the dissipated energy in the material, thus the viscous characteristics of the material (Cheneler, 2016). The loss modulus has a characteristic bell shape, as a result the function has two elastic plateaus (with no viscous damping), at low and high  $\omega$  respectively. At low frequencies,  $E'$  is a low value which results in a *soft* material behaviour. In a similar fashion,  $E'$  is large at high frequencies, resulting in a *stiff* behaviour in the material.

### Complex modulus tests

Within pavement design, it can be valuable to have information about the viscoelastic behaviour of the asphalt layer, as this gives insight into temperature and frequency effects on the pavement response. Furthermore, comparison of  $E^*$  curves for the same asphalt taken at different times can reveal how damaged the pavement is and if maintenance is needed (Zhao and Kim, 2003; Mazurek and Iwański, 2017). The most common way to characterise the viscoelastic properties of the asphalt is to perform a *complex modulus test*.

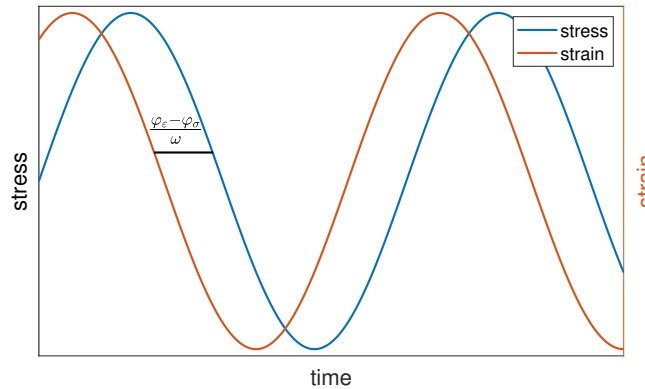


FIGURE 13.5: Sketch of a strain response (red curve) to an applied sinusoidal loading (blue curve). Due to the viscous effects in the material there is a time lag between stress and strain given by  $\frac{\phi_\epsilon - \phi_\sigma}{\omega}$ .

A complex modulus test is made in a laboratory upon a small sample of the asphalt concrete. The testing principle is to apply a sinusoidal loading upon an asphalt concrete mix and then measure the resulting strain response (Xu and Solaimanian, 2009). An example of such an applied sinusoidal stress and the resulting strain is seen on figure 13.5.

From the experiment the amplitude of the stress and strain,  $\sigma_0$  and  $\epsilon_0$ , as well as the phase shift between the signals is measured. Based on these the behaviour of the complex modulus can be studied.

In practice, the dynamic modulus  $|E^*|$ , is often used to report laboratory results as this is simply the stress amplitude over the strain amplitude.

$$|E^*| = \sqrt{(E')^2 + (E'')^2} = \frac{\sigma_0}{\epsilon_0}$$

In order to properly describe the viscous behaviour of a material, information about the complex modulus over a wide range of frequencies is needed. However, it is not possible to measure over wide enough range of frequencies. Instead the time-temperature superposition principle is used to create a master curve over a wide range of frequencies from measurements at different temperatures.

### Master curves and time-temperature superposition

The Time-Temperature superposition (TTS) principle states that a change in temperature is equivalent to a shift in timescale with a shift factor  $a_T$  with respect to some reference temperature  $T_0$ . This means, that instead of measuring  $E^*(\omega)$  over a wide range of frequencies, it can be measured at a small range, but under different temperatures. The measured  $E^*(\omega)$  values is then shifted with respect to some reference temperature and thereby covers a larger frequency range. This is illustrated on figure 13.6.



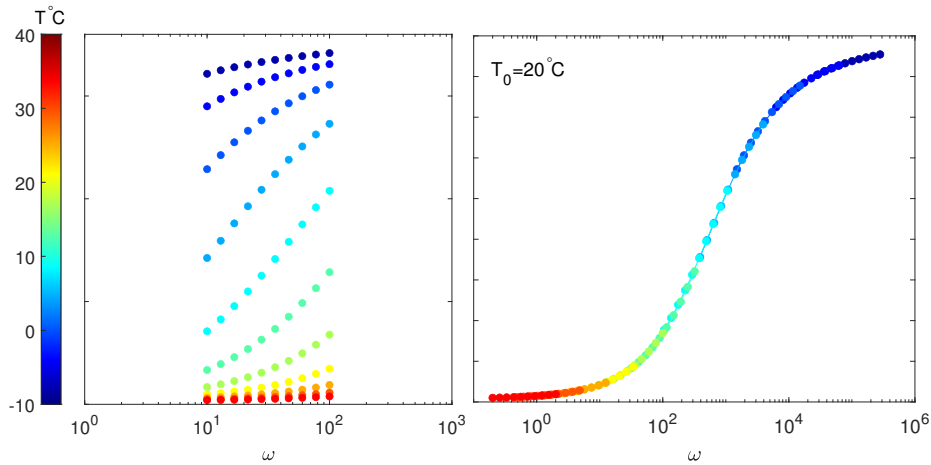


FIGURE 13.6: Illustration of the shift produced when applying the time-temperature superposition principle. A set of measurements is made within a small range of frequencies but over several temperatures (left figure). The measured values is then shifted with some shift factor  $\alpha_T$  such that they form a master curve over a wide rang of frequencies (right figure).

In the time domain this can be written using the relaxation function,

$$E(t, T) = E(a_T t, T_0). \quad (13.24)$$

A fundamental assumption behind the TTS principle is that the shape of the relaxation function do not depend on temperature. Thus, it can be written as the product of a temperature dependent amplitude  $E_0(T)$  and the functional form given by  $f(a_T t)$ ,

$$E(t, T) = E_0(T) f(a_T t). \quad (13.25)$$

Correspondingly, TTS can be performed in the the frequency domain by use of the complex modulus,

$$E'(\omega, T) = E'(\alpha_T \omega, T_0) \quad , \quad E''(\omega, T) = E''(\alpha_T \omega, T_0). \quad (13.26)$$

Each individual set of measurements at a specific temperature has a specific scale factor. When shifting with respect to the reference temperature  $T_0$ , it holds that for

$$\text{if } T < T_0, \alpha_T > 1, \quad (13.27)$$

$$\text{if } T_0 < T, \alpha_T < 1. \quad (13.28)$$

TTS is used to create master curves of asphalt materials and study their viscous behaviour. This is often done based on complex modulus tests performed in the laboratory (Mazurek and Iwański, 2017; Aidara et al., 2015; Xu and Solaimanian, 2009; Nilsson et al., 2002). However, some studies have constructed master curves based on back-calculated mechanical parameter values from Falling Weight Deflectometer tests (Solatifar et al., 2019; Gopalakrishnam et al., 2014; Solatifar et al., 2017).

In section 21.2, we perform a pilot study showing how it is possible to create master curves based on TSD data. The use of TSD measurements has the advantage that it uses a non-destructive measuring method and data collection is easy.

### 13.3 Response models

From experiments like complex modulus tests, information about the viscous behaviour of bitumen mixes is obtained. Different mathematical models of the complex modulus can be fitted to the empirical results in order to describe the viscoelastic behaviour completely.

There are two approaches when modelling the viscous behaviour; empirical mathematical models and mechanistic models (Mazurek and Iwański, 2017). In the following section, the most common models within the two kind of categories will be presented.

#### 13.3.1 Empirical response models

Empirical models are purely based on mathematical expressions which has proven suitable for describing the characteristic trends in data, and thus has no physical foundation. They are often used to describe the viscoelastic behaviour in the time-domain, and is suitable for use in backcalculating procedures of Falling Weight Deflectometer data (Zaabar et al., 2014).

An example is the viscoelastic time-domain solution *Viscowave*, developed at Michigan State University and used previously in this thesis (see appendix B) (Lee, 2014). In this, the viscoelastic behaviour of the asphalt layer is described through the relaxation function  $E(t)$ , given by a sigmoidal function in equation (13.29).

$$\log(E(t)) = c_1 + \frac{c_2}{1 + \exp(-c_3 - c_4 \log(t_R))}, \quad (13.29)$$

$$\log(t_R) = \log(t) - \log(a_T(T)), \quad (13.30)$$

$$\log(a_T(T)) = a_1(T^2 - T_{ref}^2) + a_2(T - T_{ref}), \quad (13.31)$$

where  $c_1 - c_4$  are the sigmoid coefficients,  $t_R$  is reduced time,  $a_T(T)$  is the shift factor for the master curve and  $a_1$  and  $a_2$  is shift factor coefficients.

### 13.3.2 Mechanical models

A mechanistic model uses the physical elements springs and dashpots to describe the viscous behaviour of a material (Xu and Solaimanian, 2009). Each combination of elements results in a unique model with specific physical properties and behaviour, and in theory an infinite number of constructions could be made. Based on these models, an analytical expression for  $E^*(\omega)$  can be derived. Consequently, these kinds of models have a strong physical ground, in contrast to the empirical models presented above.

In table 13.1, a schematic representation and the associated complex modulus is presented for the two simplest mechanistic models; the Maxwell and Kelvin-Voigt model and subsequently some of the most used models in the literature.

The two simple models, the Kelvin-Voigt model and the Maxwell model, both consist of a spring and a dashpot. These are placed in parallel or series respectively, and thus the expression for  $E^*(\omega)$  in both models contains two parameters. Nevertheless, the behaviour of their complex modulus is quite different. In the Kelvin-Voigt model, the storage modulus ( $E'$ ) has a constant value and the loss modulus ( $E''$ ) is linearly increasing with frequency. This does not correspond with the behaviour of bitumen mixes, and thus this is not a good model for describing the viscoelastic behaviour of asphalt. It is though often used to describe damping effects of soil in simple pavement response models (Froio et al., 2018). The Maxwell model on the other hand, has a sigmoidal shaped  $E'$  and a bell curved  $E''$ . Thus, it is considered the simplest mechanistic model with the qualitatively correct behaviour of the complex modulus. It is, however, found to be too simple to describe the complex behaviour of asphalt mixed accurately (Xu and Solaimanian, 2009). Studies by Xu and Solaimanian (2009) and Pham et al. (2015) have investigated the mechanical properties of bitumen mixes and their complex modulus. They have proposed that models consistent of several spring, dashpot and parabolic dashpot elements are needed in order to reasonably describe the viscoelastic behaviour of bituminous mixes.

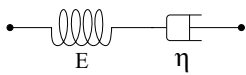
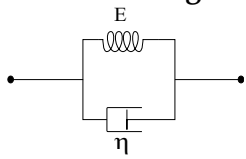
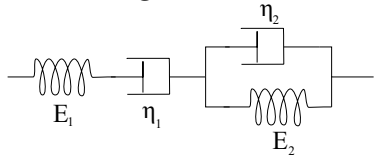
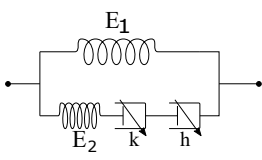
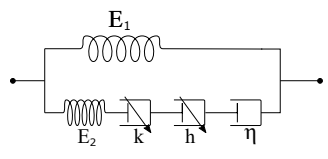
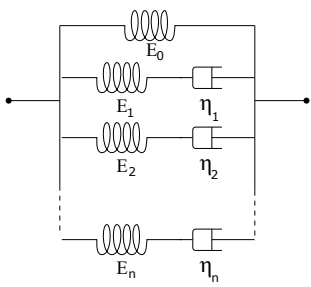
Generalized Maxwell models, which consist of  $n$  Maxwell models in parallel, can characterise the viscoelastic behaviour over a wide range of frequencies, but require a lot of free parameters to do so (Xu and Solaimanian, 2009). As a result, these are not used in this thesis as we are interested in simpler models.

Three models which are often considered good candidates to describe the viscous behaviour is the Burger model, the Huet-Sayegh model and the 2S2D1P model. The Burger model consists of a spring and dashpot in series followed by a set in parallel, and thus contains four free parameters (table 13.1).

The Huet-Sayegh model consists of two parallel branches, one with a spring and the other with a spring and two parabolic dashpots in series. In a parabolic dashpot, the relation between stress and strain is given by

$$\hat{\sigma}(\omega) = \frac{\eta}{\tau} (i\omega\tau)^\alpha \hat{\varepsilon}(\omega), \quad (13.32)$$

TABLE 13.1: Table over mechanistic models to describing the viscoelastic behaviour of bituminous mixes. The number of parameters in the Huet-Sayegh and 2S2P1D model depends whether  $\tau$ ,  $\delta$  and  $\beta$  is seen as independent parameters or not.

Schematic representation	Complex modulus	number of parameters
<p><b>Maxwell model</b></p> 	$E^*(\omega) = \frac{\eta i \omega}{1 + \frac{\eta}{E} i \omega} = E \frac{\tau i \omega}{1 + \tau i \omega'}$ <p>where <math>\tau = \frac{\eta}{E}</math></p>	2
<p><b>Kelvin-Voigt</b></p> 	$E^*(\omega) = E + \eta i \omega$	2
<p><b>Burger's model</b></p> 	$E^*(\omega) = \left( \frac{1}{E_1} \left( 1 + \frac{1}{i \omega \tau_1} \right) + \frac{1}{E_2} \frac{1}{(1 + i \omega \tau_2)} \right)^{-1}$ <p><math>\tau_i = \frac{\eta_i}{E_i}</math></p>	4
<p><b>Huet-Sayegh model</b></p> 	$E^*(\omega) = E_1 + \frac{E_2}{1 + \delta (i \omega \tau)^{-k} + (i \omega \tau)^{-h}}$ <p><math>\ln(\tau) = a + bT + cT^2, \delta = \frac{E_2 \tau}{\eta_1}</math></p>	6 (9)
<p><b>2S2P1D model</b></p> 	$E^*(\omega) = E_1 + \frac{E_2}{1 + \delta (i \omega \tau)^{-k} + (i \omega \tau)^{-h} + (i \omega \beta \tau)^{-1}}$ <p><math>\ln(\tau) = a + bT + cT^2,</math></p> <p><math>\delta = \frac{E_2 \tau}{\eta_{parabolic}}, \beta = \frac{\eta}{E_2 \tau}</math></p>	7 (10)
<p><b>Generalized Maxwell model</b></p> 	$E^*(\omega) = E_0 + \sum_{k=1}^n \frac{E_k \omega^2 \eta_k^2 + i E_k^2 \omega \eta_k}{E_k^2 + \omega^2 \eta_k^2}$	1 + 2n

where  $\omega$  is the angular frequency,  $\eta$  is the viscosity,  $0 < \alpha < 1$  is the parabolic dashpot variable and  $\tau$  is the retardation time given by  $\tau = e^{a+bT+cT^2}$  in which  $a, b, c$  are constants and  $T$  is temperature (Pronk, 2006). The original Huet-Sayegh model has two time constants  $\tau_1$  and  $\tau_2$ , one for each parabolic dashpot. However, in order to simplify the model the number of independent variable was reduced such that the model only contains one time decay constant  $\tau = \tau_1 = \tau_2$  (Pronk, 2006). The Huet-Sayegh model presented here, and the one used in the majority of the literature, is the simplified one.

The 2S2P1D model consists of two linearly elastic springs, two parabolic dashpot, and one linear dashpots, hence the name. The model is an extension of the Huet-Sayegh model with an extra linear dashpot added to the series of dashpots (Aidara et al., 2015). This improves the models ability to characterise the viscous effects at high temperatures and low frequencies (Aidara et al., 2015).

In the literature, several studies have compared the different mechanistic models ability to fit empirical data in order to establish which is best to use for characterising the viscous behaviour of asphalt (Pouget et al., 2014; Xu and Solaimanian, 2009; Pronk, 2006; Nilsson et al., 2002; Aidara et al., 2015; ?). Generally, the studies find that models like the Huet-Sayegh and the 2S2P1D model are good candidates. However, it should be mentioned that the more parameters a model contains, the better it will appear to be at fitting experimental data. In reality, it is a trade-off between the degree of freedom in the model vs. the goodness of the fit obtained. When choosing a proper viscoelastic model, the intended use of it should be taken into consideration. If the models are used to describe the behaviour of asphalt as a part of a larger pavement response model, as it is the case in this thesis, it is not not advantageous to have a lot of unknown parameters and a more simplified model is favourable.

The Burger model is often found to be the simplest model witch is capable of characterizing the viscoelastic properties of asphalt correct (Xu and Solaimanian, 2009). However, it only do so within a limited range of frequencies and temperatures (Nilsson et al., 2002). As a consequence, most studies conclude that the Huet-Sayegh model is found to be the most suitable model for characterising the mechanical behaviour as it is rather "simple" (compared to e.g. generalized Maxwell modes) and can characterize the material behaviour over a wide range of frequencies and temperatures (Xu and Solaimanian, 2009; Pronk, 2006; Nilsson et al., 2002).



## Chapter 14

# Beam theory

In this chapter, the most fundamental theory about Euler-Bernoulli beams will be presented. Furthermore, we will derive the governing equation for vertical deflection of an elastic and viscoelastic Euler-Bernoulli beam. As the use of viscoelastic beams is not widespread, a thorough description of the theory leading to the derivation of the governing equation for deflection of a viscoelastic beam is given.

### 14.1 Elastic beam theory

Beams are a widely used structure within engineering. The behaviour of elastic beams is governed by the theory of *elastostatics*. This describes the state of stress, strain and displacement of an elastic body (Gould and Feng, 2018). Geometrical speaking, a beam is a structure with one dimension being much longer than the two others (Bauchau and Craig, 2019). In the following, it will always be assumed that the beam is made of a homogeneous and isotropic material, which can have either elastic or viscoelastic properties.

The basic elements needed to describe the behaviour of a beam are; the equilibrium conditions, the kinematic relation and the constitutive equations. These relations will be described below.

Before deriving the governing equations, let's state the coordinate systems used. We operate with an inner and outer coordinate system. For the inner coordinate system, the long dimension of the beam is placed along the  $x$ -axis, as illustrated in figure 14.1a. An inner coordinate system is defined for each element on the neutral axis, and the  $x$ -axis is always aligned with the center of the beam, called the neutral axis. The  $z$ -axis is defined to be perpendicular to the neutral axis, pointing downwards. A cross-section at every  $x$  can be made in the  $y$ - $z$  direction and this is denoted  $A$ , illustrated on figure 14.1b. The cross-section can have any shape, but are assumed to be constant over  $x$ . The origin of the coordinate system is placed in the area centroid of the cross section  $A$ .

An outer coordinate system is also defined, with  $\bar{x}$  aligned with the neutral axis of the straight beam and  $w(\bar{x})$  denoting the vertical displacement of the neutral axis compared to the straight beam. Thus  $w(\bar{x}) = 0$  for a straight beam and  $w(\bar{x}) > 0$  when the beam bends downwards.

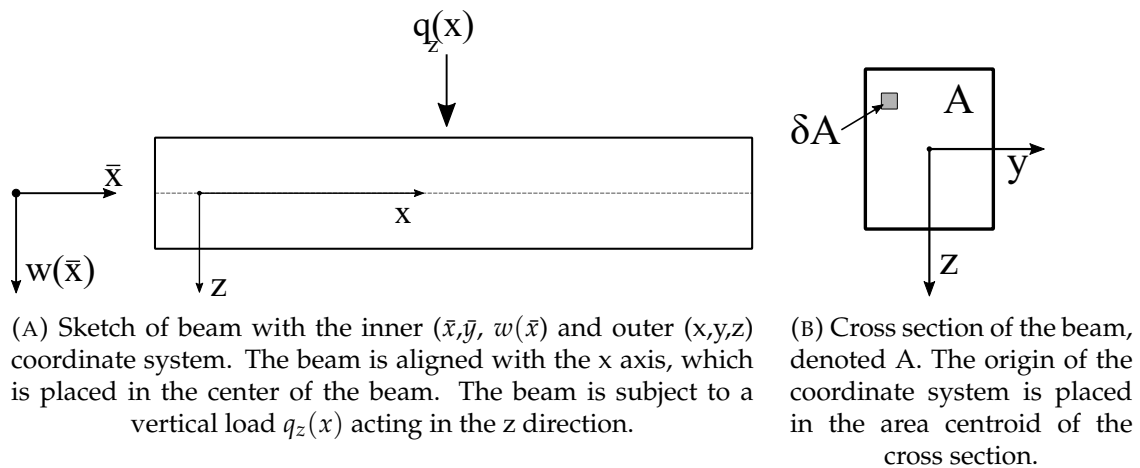


FIGURE 14.1

When describing the characteristics of the cross section, we use the *second moment of area*  $I$  around the  $x$ -axis. This is defined as the integral of  $z^2$  over the cross section area

$$I_x = \int_A z^2 dA. \quad (14.1)$$

$I_x$  depends on the shape of the cross sections and a physical interpretation of it is that the higher an  $I$  value a structure has, the harder is it to bend. In the following  $I_x = I$ , as this is the only area moment used.

### 14.1.1 The Euler-Bernoulli assumptions

The Euler-Bernoulli beam theory was formulated in the 1700s and is the most common used beam theory as it is simple and provides reasonable approximations for many engineering problems (Han et al., 1999). The main assumptions for an Euler-Bernoulli beam is listed below (Bauchau and Craig, 2019).

- 1 The cross section of the beam in the  $y$ - $z$  plane do not deform, but maintain its original shape when the beam is deformed.
- 2 After deformation of the beam, the cross section will remain planar. This means that if we look at a cross section before bending and it is flat, then it is also flat after bending. Thus, it do not curve out of its own plane.
- 3 The cross sections is always normal to the deformed axis. This is illustrated on figure 14.2, where every cross section is perpendicular to the neutral axis in that point. Recall that the  $x$ -axis is aligned with the neutral axis for every element on the  $x$ -axis.



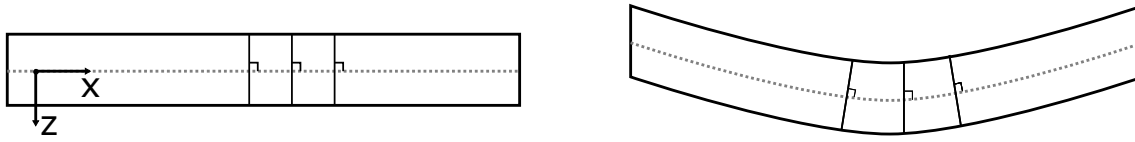


FIGURE 14.2: An underlying assumption for Euler-Bernoulli beams is that the cross sections is always normal to the deformed axis (in this case the  $x$ -axis). This is illustrated here for a straight and bent beam.

### 14.1.2 Kinematic relation

We will now write up the kinematic relation for an Euler-Bernoulli beam which relates strain and displacement of the beam. When deriving the kinematic equation, *pure bending* of the beam is assumed. This means that the bending moments and physical properties like stress and strain are constant along the beam. As a result, the beam bends into the shape of a perfect circle, shown with a extracted example in figure 14.3. This is an idealised situation and in practice this does not apply for a bent beam. However, if we look at a small subset of the beam (as illustrated with gray on fig 14.3) this idealised situation can be assumed.

Assuming pure bending, the bent beam take the shape of a circle with radius  $R$  (measured from the neutral axis (fig. 14.3)).  $R$  is called the radius of curvature, and is connected to the curvature of the beam  $\kappa$  with

$$\kappa = \frac{1}{R}. \quad (14.2)$$

If we assume shear-free bending, the beam can be considered to consist of a bunch of elastic strings that are either stretched or compressed, but which do no interact with each other. The center axis (at  $z=0$ ) is fixed such that it does not change length when the beam is bent, while strings at positive  $z$  is stretched and at negative  $z$  is compressed (Lautrup, 2011). This is illustrated on figure 14.3.

If we consider a small piece of the beam with length  $l = \Delta x$  (fig. 14.4), this will bend into a beam section where the top surface has length  $l_t$  and the bottom has length  $l_b$  but the center axis has the same length  $l$ . The length of the center axis can be expressed by the radius of curvature  $R$  by

$$l = R\theta \quad (14.3)$$

where  $\theta$  is the angle giving the beam section of the beam circle. This is illustrated on figure 14.4. The radius of curvature for the top of the beam is given by  $R - \delta r$ , where  $\delta r$  denotes half of the thickness of the beam (see fig. 14.4). As a consequence, the length of the beam section top is written  $l_t = (R - \delta r)\theta$ .

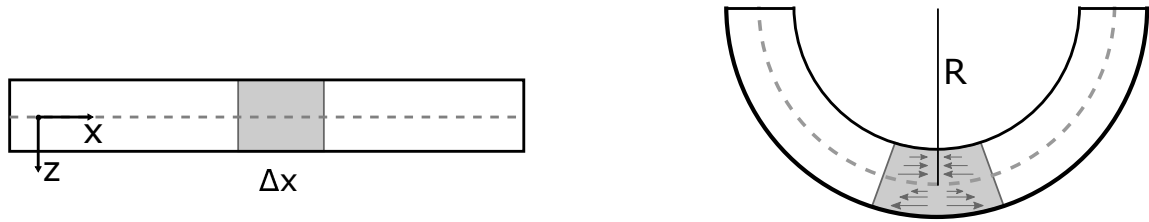


FIGURE 14.3: Sketched of an Euler-Bernoulli beam subject to pure bending. In the idealized case of pure bending, the bending moments and physical properties like stress and strain are constant along the beam. As a result, the beam bends into the shape of a perfect circle with radius of curvature  $R$ . The center axis at  $z = 0$  remains the same length during bending, while beam elements positioned at negative  $z$  is compressed and elements at positive  $z$  is stretched. In practise, this idealized situation of pure bending can no be applied to the entire beam. However if we consider a small subset of the beam, as illustrated with gray on the figure, the assumption can be applied and used to derive the kinematic relation between strain and displacement.

Thus, the strain at the top of the beam can be found by

$$\varepsilon_{top} = \frac{\Delta l}{l} = \frac{l_t - l}{l} = \frac{(R - \delta r)\theta - R\theta}{R\theta} = \frac{\delta r}{R} \quad (14.4)$$

If this is generalized by taking  $z$  instead of  $\delta r$ , the strain throughout the beam is found,

$$\varepsilon = \frac{z}{R}. \quad (14.5)$$

For small deformation, the curvature of the neutral axis of the beam can be written by the second-order derivative of the deflection,  $\kappa = -\frac{\partial^2 w(x)}{\partial x^2}$ . Using this, we can derive the important equation for relation between strain and displacement, called the kinetic relation.

$$\boxed{\text{Kinetic relation } \varepsilon(x, z) = -z \frac{\partial^2 w(x)}{\partial x^2}.} \quad (14.6)$$

The relation does not depends on which type of material the beam is made of, and thus it is true for both elastic and viscoelastic materials (Flügge, 1975).

### 14.1.3 Mechanical equilibrium

The beams used in this study are all assumed to be in a *mechanical equilibrium*, meaning that the total force acting on the body is equal to zero.

$$\sum \mathbf{F} = 0, \quad (14.7)$$

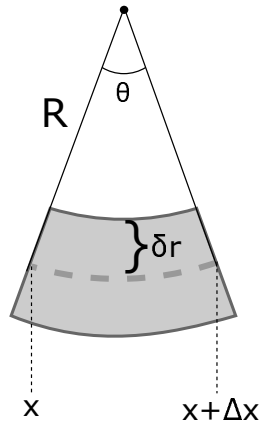


FIGURE 14.4: Zoom in on the a small beam piece of the beam with length  $\Delta x$  subject to pure bending. The length of the center axis  $l$  is expressed through the radius of curvature  $R$  by  $l = R\theta$ .

where  $\mathbf{F} = (F_x, F_y, F_z)$ . In such situation, all forces acting on the body are counterbalanced and thus the body is standing still.

For a body in mechanical equilibrium Cauchy's equilibrium equation (14.8) is true,

$$f_i + \sum_j \nabla_j \sigma_{ij} = f_i^* = 0. \quad (14.8)$$

Here  $i$  and  $j$  are the  $x, y$  and  $z$  direction,  $f$  is the long-ranged forces,  $\nabla$  is the gradient,  $\sigma$  is the stress and  $f^*$  is called the effective force density. The effective force density describes the forces acting on a local particle. Equation (14.8) states that for a local material particle the long-ranged forces (e.g. gravity) are equal all the short-range contact forces acting on its surface.

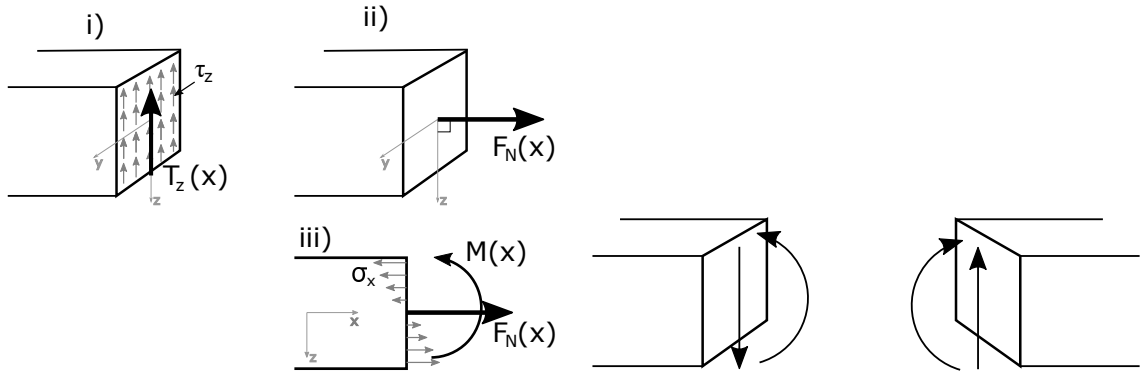
In the world of continuum physics, one can consider a body as a collection of material particles. The total moment of force  $\mathbf{M}$  around any arbitrary point  $O$  in a body with a volume  $V$  can be written as

$$\mathbf{M}_O = \int_V \mathbf{x} \times (f^* dV), \quad (14.9)$$

where  $\mathbf{x} = (x, y, z)$  is the spacial coordinates.

The moment of force around some axis, e.g. the  $x$  axis is called  $M_x$  and is a measure of how much the body is turning around this axis due to external forces. A moment occurs if a force is applied that do not go through the centroid and is not counterbalanced. In this case, the body starts to rotate. In mechanical equilibrium, we have that  $f^* = 0$  and thus  $\mathbf{M}_O = 0$ , meaning that the body do not rotate.

Imagine that we have a beam subject to a distributed load  $q_z(x)$  [N/m]. The external load gives rise to internal resultant forces; shear forces and normal forces. The shear forces act tangent to the cross section area, thus in the  $y$  or  $z$  direction (see fig. 14.5ai). These are denoted  $T_z(x)$  and  $T_y(x)$  [N]. As no external load is acting in the  $y$  direction, and we are



(A) When the beam is subject to external forces internal resultant forces occurs: shear forces ( $T_z(x)$ ) and normal forces ( $F_N(x)$ ). The stress profile through the beam section creates a bending moment  $M(x)$ .

(B) Sign convention for the direction of positive internal resultant shear force and bending moment when a small beam segment is evaluated.

FIGURE 14.5

in mechanical equilibrium,  $T_y(x) = 0$ . The resultant shear force in the  $z$  direction can be found from the shear strain  $\tau_z$  [ $\frac{N}{m^2}$ ] over the cross section ,

$$T_z(x) = \int_A \tau_z dA. \quad (14.10)$$

The normal forces  $F_N(x)$  are acting normal to the cross section area  $A$ , thus in the direction of the beam (see figure 14.5aii) (Craig Jr., 2000). As for the shear force, the resultant normal force is given as the normal stress ( $\sigma_x$ ) over the cross-section area  $A$ ,

$$F_N(x) = \int_A \sigma_x dA \quad (14.11)$$

As mentioned before, when the beam is deformed the elements above the neutral axis is compressed and the elements below the neutral axis is stretched. Thus, the normal stresses over  $A$  is not constant, but have some stress profile (fig. 14.5aiii). This creates a bending moment around the  $y$  axis  $M(x)$ ,

$$M(x) = \int_A z\sigma_x dA. \quad (14.12)$$

In order to evaluate the internal forces and moments in the beam subject to an external load, we look at a small segment of the beam with length  $\Delta x$  and draw a *free-body diagram*.

When drawing the free-body diagram, it is important to keep in mind the sign convention for the internal stress resultants, which determines which way is "positive" (Craig Jr., 2000). The sign convention states that for a cross section with the beam to the left, as in figure 14.5b left, the positive direction for the shear force is downwards and the positive

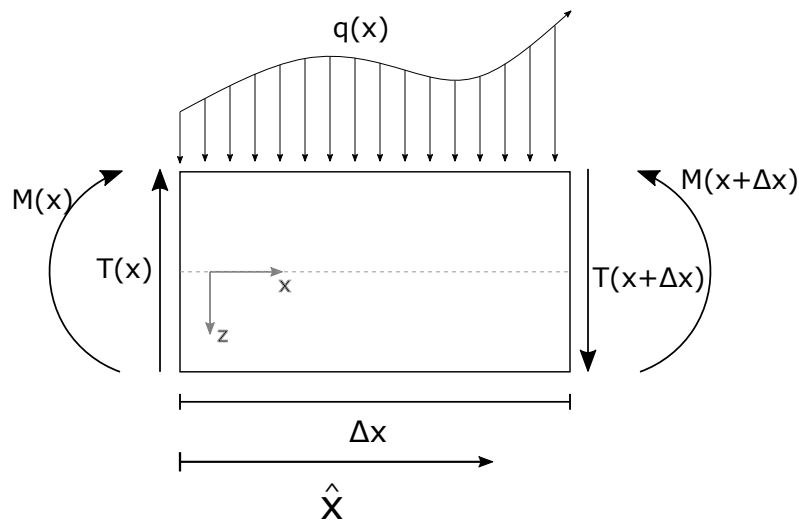


FIGURE 14.6: Free-body diagram of a small beam segment with length  $\Delta x$ . The arrows denote the direction of positive force and momentum.

direction for momentum is counterclockwise. The opposite is true for a cross section with the beam to the right, as seen on figure 14.5b right. Since we are looking at a segment in the middle of the beam, there will be internal shear forces and moments on both sides of the segment.

On figure 14.6, the positive direction for resultant forces and moments have been drawn for the points  $x$  and  $x + \Delta x$ , as well as the the distributed load  $q(x)$ .

Since we are in a static equilibrium we now that the sum of forces in the  $z$  direction should be zero.

$$\sum F_z = 0 \quad (14.13)$$

This means that the internal forces in the  $z$  and  $-z$  direction should be equal. In the  $-z$  direction, we have the shear forces, which in  $x$  is  $T(x)$  and in  $x+\Delta x$  it is  $-T(x+\Delta x)$ . In the  $z$  direction, we have the net resultant force due to the distributed load.

The force due to external distributed load can be found by integrating  $q_z(x)$  over the beam segment,

$$\int_0^{\Delta x} q_z(x) d\hat{x}. \quad (14.14)$$

Here  $\hat{x}$  gives the distance from the point  $x$ .

Thereby the force balance in the z direction is

$$T(x) - T(x + \Delta x) = \int_0^{\Delta x} q_z(\hat{x}) d\hat{x} \quad (14.15)$$

$$\Downarrow \quad (14.16)$$

$$T(x + \Delta x) - T(x) = - \int_0^{\Delta x} q_z(\hat{x}) d\hat{x} \quad (14.17)$$

Dividing with  $\Delta x$

$$\frac{T(x + \Delta x) - T(x)}{\Delta x} = - \frac{\int_0^{\Delta x} q_z(\hat{x}) d\hat{x}}{\Delta x} \quad (14.18)$$

In order to evaluate the right side of (14.18), we use the mean value theorem (Adams, 1999). From this we know that there must exist a point  $\hat{x} = c$  between 0 and  $\Delta x$  such that

$$\Delta x q_z(\hat{x} = c) = \int_0^{\Delta x} q_z(\hat{x}) d\hat{x} \Leftrightarrow q_z(\hat{x} = c) = \frac{\int_0^{\Delta x} q_z(\hat{x}) d\hat{x}}{\Delta x}. \quad (14.19)$$

Thereby equation (14.18) becomes

$$\frac{T(x + \Delta x) - T(x)}{\Delta x} = -q_z(\hat{x} = c) \quad (14.20)$$

If we take the limit when  $\Delta x \rightarrow 0$  and end up with the important result,

Conservation of momentum:  $\frac{dT(x)}{dx} = -q_z(x).$

(14.21)

The limit of the right hand side come from the fact that  $c$  is a point on  $\hat{x}$ , and when  $c = 0$  then  $\hat{x} = x$ .

Equation (14.21) is a important result within static mechanics and from this the shear forces can be calculated directly from the external load.

We now move our interest to the internal moments created inside the beam. Again we look at the body diagram on figure 14.6. We want to evaluate the moments around some point O (see fig. 14.7).

Due to the fact that we are in a static equilibrium the sum of moments around any point is zero,

$$\sum M_o = 0. \quad (14.22)$$

The total moment is a sum of the clockwise moments and counterclockwise moments. As seen on figure 14.7 we have three contributions to the clockwise moment; the bending moment in  $x$   $M(x)$ , the moment due to shear forces in  $x + \Delta x$  which gives the moment

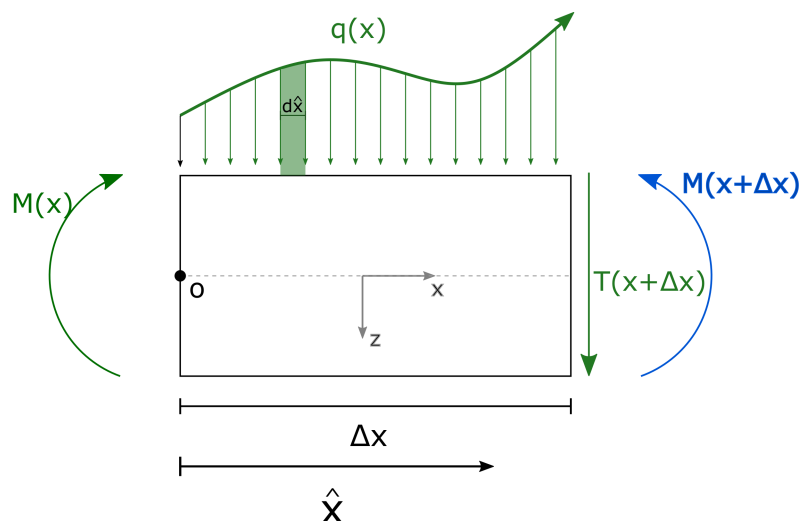


FIGURE 14.7: Beam section with length  $\Delta x$ . The total sum of moments around the point  $o$  has to be zero due to static equilibrium, and is a sum of the clockwise (green) and counterclockwise (blue) contributions.

$M_T = T(x + \Delta x)\Delta x$  and lastly the moment due to the distributed load. For the counterclockwise moment contribution we have the bending moment in  $x + \Delta x$ ,  $M(x + \Delta x)$ .

The moment due to the distributed load is found by looking at a small slice of distributed load. The force arising from this small area underneath  $q_z(x)$  corresponds to  $q_z(\hat{x})d\hat{x} = dF$ . As a result, the moment due to this small area, found by the force times the distance from  $O$  to the slice, is  $dM = dF\hat{x}$ . Integrating over all  $\hat{x}$  gives the total moment due to the distributed load,

$$M_{q_z(x)} = \int_0^{\Delta x} \hat{x}q_z(\hat{x})d\hat{x}. \quad (14.23)$$

Now we can write up the contributions to the total moment,

$$\sum M = M(x) + T(x + \Delta x)\Delta x + \int_0^{\Delta x} \hat{x}q_z(\hat{x})d\hat{x} - M(x + \Delta x) = 0 \quad (14.24)$$

$\Downarrow$

$$M(x + \Delta x) - M(x) = T(x + \Delta x)\Delta x + \int_0^{\Delta x} \hat{x}q_z(\hat{x})d\hat{x}. \quad (14.25)$$

Dividing with  $\Delta x$

$$\frac{M(x + \Delta x) - M(x)}{\Delta x} = T(x + \Delta x) + \frac{\int_0^{\Delta x} \hat{x}q_z(\hat{x})d\hat{x}}{\Delta x} \quad (14.26)$$

In order to evaluate the right hand side integral, we again apply the mean value theorem. This time we first define a function  $g(\hat{x}) = \hat{x}q_z(\hat{x})$ . The m.v.t states that there exists a point

$c$ , with  $0 \leq c \leq \Delta x$ , such that

$$g(c)\Delta x = \int_0^{\Delta x} g(\hat{x})d\hat{x} \Leftrightarrow g(c) = \frac{\int_0^{\Delta x} g(\hat{x})d\hat{x}}{\Delta x} \quad (14.27)$$

Thus equation (14.26) becomes

$$\frac{M(x + \Delta x) - M(x)}{\Delta x} = T(x + \Delta x) + g(c) \quad (14.28)$$

Taking the limit when  $\Delta x \rightarrow 0$  and we end up with the important result,

$$\boxed{\text{moment of momentum: } \frac{dM(X)}{dx} = T(x)} \quad (14.29)$$

$g(c)$  disappears as  $\hat{x} \rightarrow 0$ , when  $\Delta x \rightarrow 0$  and  $g(0) = 0$ .

Like the kinetic relation, the two important equations; conservation of momentum and moment of momentum are not dependent on the type of material the body is made of and thus are true for both elastic and viscoelastic materials.

#### 14.1.4 Static vs. dynamic beams

Above the the three important relations to relate stress, strain and displacement in a static Euler-Bernoulli beam was derived; the kinematic relation and the *equilibrium conditions* (conservation of momentum and moment of momentum).

$$\text{Static kinetic relation: } \varepsilon(x, z) = -z \frac{\partial^2 w(x)}{\partial x^2}, \quad (14.30)$$

$$\text{Conservation of momentum: } \frac{dT(x)}{dx} = -q_z(x), \quad (14.31)$$

$$\text{moment of momentum: } \frac{dM(X)}{dx} = T(x). \quad (14.32)$$

As these are derived for a static situation, they are only dependent on the position  $x$ . However, we aimed to describe the pavement response for a moving load on the form  $q(x, t)$ , which is a function of both the position  $x$  and time  $t$ . As this is a dynamic problem, the above derived equations has to be modified from a static to dynamic situation.

The kinetic equation was derived based on geometrical considerations, which is true for both the static and dynamic case. Thus, the relation will not change in a dynamic system with a time dependent strain and beam deflection and we have that the dynamic



kinetic relation is given by,

$$\text{Dynamic kinetic relation: } \varepsilon(x, z, t) = -z \frac{\partial^2 w(x, t)}{\partial x^2}. \quad (14.33)$$

The equilibrium equations are replaced with the *equations of motions* (Flügge, 1975).

When deriving the equilibrium equations for the static beam, we used that the sum of forces is zero. In the dynamic case, the sum of forces are not zero, as we have vertical acceleration of the beam. The external force on a small beam segment of length  $dx$  (as in fig. 14.6) can be found by use of newtons 2. law,

$$F = ma = \rho A(x) dx \frac{\partial^2 w(x, t)}{\partial t^2}. \quad (14.34)$$

Here  $\rho$  is the density of the beam,  $A(x)$  is the cross section and  $\frac{\partial^2 w(x, t)}{\partial t^2}$  is the acceleration of the vertical deflection. The force balance in the dynamic state (corresponding to equation (14.15) for static state) becomes

$$T(x, t) - T(x + \Delta x, t) - \int_0^{\Delta x} q_z(\hat{x}, t) d\hat{x} = \rho A(x) dx \frac{\partial^2 w(x, t)}{\partial t^2}. \quad (14.35)$$

Using the same derivations as previous, we can obtain

$$\frac{\partial T(x, t)}{\partial x} = -q_z(x, t) + \rho A(x) \frac{\partial^2 w(x, t)}{\partial t^2}. \quad (14.36)$$

Since we have assumed the beam is uniform and fulfill the Euler-Bernoulli assumption, the cross section will always be constant and  $A(x) = A$ .

An underlying assumption with the Euler-Bernoulli beam is that it do not rotate around the neutral axis. Thereby, there exists no rotational acceleration in neither the static or dynamical situation, and as result the moment of momentum can be derived using the same arguments. Doing so gives the following equation for the momentum,

$$\frac{\partial M(x, t)}{\partial x} = T(x, t). \quad (14.37)$$

Together equation (14.36) and (14.37) constitute the equations of motion of a dynamic Euler-Bernouli beam.

### 14.1.5 Governing equation for the relationship between vertical deflection and applied load

We are interested in finding a relationship between the applied vertical load  $q_z(x, t)$  and the beam deflection  $w(x, t)$ .

Consider a cross section normal to the beam axis, thus in the  $y$ - $z$  plane (figure 14.1b). As described above the external load results in internal stresses acting on the cross-section in the  $x$  direction  $\sigma_x$ . The internal stresses creates a resulting moment  $M$  around the plane  $x$ - $y$  plane (illustrated in fig. 14.5a). The resulting moment can be written as

$$M(x, t) = \int_A z\sigma(x, z, t)dA. \quad (14.38)$$

Note that the contribution for  $z=0$  is zero as this is directly on the plane (and area centroid), and thus do not create a moment.

In section 13.1.1, we found that for a body made of an elastic material subject to an uniaxial stress, the relation between stress and strain can be simplified to

$$\sigma(x, z, t) = E\varepsilon(x, z, t). \quad (14.39)$$

Inserting equation (14.39) in (14.38) gives

$$M(x, t) = \int_A zE\varepsilon(x, z, t) dA = E \int_A z\varepsilon(x, z, t) dA \quad (14.40)$$

Inserting the dynamic kinematic relation (eq. (14.33)),

$$M(x, t) = \int_A zE\varepsilon(x, z, t) dA = E \int_A z\left(-z\frac{\partial^2 w(x, t)}{\partial x^2}\right) dA = IE\frac{\partial^2 w(x, t)}{\partial x^2} \quad (14.41)$$

Equation (14.41) is called the Euler-Bernouli law and relates the bending moment and the curvature of of the beam.  $EI$  is the flexural rigidity which is a measure of how much moment that is required to bend the beam with a given curvature. It has the units  $[\text{Pa m}^4]$ .

The equations of motion (eq. (14.36) and (14.37)) combined states that

$$\frac{\partial^2 M(x, t)}{\partial x^2} = -q_z(x, t) + \rho A \frac{\partial^2 w(x, t)}{\partial t^2}. \quad (14.42)$$

Combining (14.41) and (14.42) gives

$$\frac{\partial^2}{\partial x^2} \left(-EI \frac{\partial^2 w(x, t)}{\partial x^2}\right) = -q_z(x, t) + \rho A \frac{\partial^2 w(x, t)}{\partial t^2} \quad (14.43)$$

$$\Downarrow \quad (14.44)$$

$$EI \frac{\partial^4 w(x, t)}{\partial x^4} = q_z(x, t) - \rho A \frac{\partial^2 w(x, t)}{\partial t^2} \quad (14.45)$$

Equation (14.45) describes the beam deflection  $w(x, t)$  of an elastic beam subject to a vertical load  $q_z(x, t)$  and is true under the condition that  $EI$  is constant.

## 14.2 Governing equation for deflection of a viscoelastic beam

Above we derived the relationship between beam deflection and applied load for an elastic beam. We now aimed to do the same for a linear viscoelastic beam.

In the case of an elastic beam, the Euler-Bernoulli law was used to get a relation between curvature of the beam and bending moment. However, this is derived based on the linear relationship between stress and strain that is valid for elastic beams. For linear viscoelastic beams, the relationship between stress and strain is time dependent and in general terms, it is given by equation (14.46).

$$\sigma(x, z, t) = \varepsilon(x, z, t)E_0 - \int_0^t \varepsilon(x, z, t') \frac{dE(t-t')}{dt'} dt' \quad (14.46)$$

Imagine a small piece of the beam cross section as given on figure 14.1b by  $\delta A$ . The forces acting on this are given by  $\sigma \delta A$ . This force will give a contribution to the bending moment in the x direction as given in equation (14.47) (Flügge, 1975).

$$M(x, t) = \int_A z \sigma(x, z, t) dA. \quad (14.47)$$

Inserting equation (14.46) into (14.47) gives

$$M(x, t) = \int_A \left( \varepsilon(x, z, t)E_0 - \int_0^t \varepsilon(x, z, t') \frac{dE(t-t')}{dt'} dt' \right) z dA. \quad (14.48)$$

Now applying equation (14.33) gives

$$M(x, t) = \int_A \left( \left( -z \frac{\partial^2 w(x, t)}{\partial x^2} \right) E_0 - \int_0^t \frac{dE(t-t')}{dt'} \left( -z \frac{\partial^2 w(x, t')}{\partial x^2} \right) dt' \right) z dA \quad (14.49)$$

$$= - \int_A z^2 dA \frac{\partial^2 w(x, t)}{\partial x^2} E_0 + \int_A z^2 dA \int_0^t \frac{dE(t-t')}{dt'} \left( \frac{\partial^2 w(x, t')}{\partial x^2} \right) dt' \quad (14.50)$$

$$= -I \frac{\partial^2 w(x, t)}{\partial x^2} E_0 + I \int_0^t \frac{dE(t-t')}{dt'} \left( \frac{\partial^2 w(x, t')}{\partial x^2} \right) dt'. \quad (14.51)$$

Taking the second-order derivative with respect to x on both sides gives

$$\frac{d^2}{dx^2} M(x, t) = \frac{d^2}{dx^2} \left( - \frac{\partial^2 w(x, t)}{\partial x^2} I E_0 + I \int_0^t \frac{dE(t-t')}{dt'} \frac{\partial^2 w(x, t')}{\partial x^2} dt' \right) \quad (14.52)$$

$$= - \frac{\partial^4 w(x, t)}{\partial x^4} I E_0 + I \int_0^t \frac{dE(t-t')}{dt'} \frac{\partial^4 w(x, t')}{\partial x^4} dt' \quad (14.53)$$

Combining the equations of motion and inserting gives us the governing equation for the deflection of a viscoelastic beam.

$$\rho A \frac{\partial^2 w(x, t)}{\partial t^2} - q_z(x, t) = - \frac{\partial^4 w(x, t)}{\partial x^4} I E_0 + I \int_0^t \frac{dE(t-t')}{dt'} \frac{\partial^4 w(x, t')}{\partial x^4} dt' \quad (14.54)$$

$$\Downarrow \quad (14.55)$$

$$q_z(x, t) = \tilde{\rho} \frac{\partial^2 w(x, t)}{\partial t^2} + \frac{\partial^4 w(x, t)}{\partial x^4} I E_0 - I \int_0^t \frac{dE(t-t')}{dt'} \frac{\partial^4 w(x, t')}{\partial x^4} dt' \quad (14.56)$$

## Chapter 15

# Viscoelastic beam on a damped Pasternak foundation

In this chapter, a pavement response model which can be used to fit TSD data is derived. The model consisted of a viscoelastic beam on top of a damped Pasternak foundation. The model is also presented in draft 1 in appendix A.3.

The model developed in this chapter is an extended version of the simple elastic Pasternak model for pavement response under a moving load (Uzzal et al., 2012). The model is extended by introducing viscous damping in both the beam and foundation.

The final model described the pavement deflection in a moving reference frame. In the rest of the thesis, we will define  $x'$  as spatial coordinate in a fixed frame and  $x$  as spatial coordinate in a moving frame.

### 15.1 The simple Winkler model

The simplest beam model consists of an elastic Euler-Bernoulli beam on top of an elastic foundation. In section 14.1.5, the governing equation for an elastic beam subject to a vertical load in a fixed frame  $q_z(x', t)$  was derived as

$$EI \frac{\partial^4 w(x', t)}{\partial x'^4} = q_z(x', t) + \tilde{\rho} \frac{\partial^2 w(x', t)}{\partial t^2}. \quad (15.1)$$

The beam is assumed to extend to infinity, be made from a homogeneous and isotropic material and is characterised by its elastic modulus  $E$  [ $\frac{N}{m^2}$ ] and the second moment of area pr. unit length,  $I$  [ $m^3$ ]. Note that the units of  $E$  and  $I$  are different from the classical use, since we are in a one-dimensional situation. The flexural rigidity,  $EI$ , of the beam has the classical units [ $Nm^2$ ].

The beam is resting on a foundation modelled by a set of continuously-distributed springs with spring constant per unit length  $k$  [ $\frac{N}{m^2}$ ]. Assuming a moving point load given by  $q_z(x', t) = F\delta(x' - vt)$ , the deflection of the beam ( $w(x', t)$ ) is given by the equation

$$EI \frac{d^4 w(x', t)}{dx'^4} + \tilde{\rho} \frac{\partial^2 w(x', t)}{\partial t^2} + kw(x', t) = F\delta(x' - vt), \quad (15.2)$$

where  $F$  is the amplitude of the applied load. A sketch of the simple Winkler model is seen on figure 15.2a.

Equation (15.2) is within a fixed coordinate system, and this can be changed into a moving reference frame by assuming a constant driving velocity  $v$  and applying the coordinate shift  $x = x' - vt$ . Thereby, the governing equation becomes

$$EI \frac{d^4}{dx^4} w(x) + \tilde{\rho} v^2 \frac{d^2 w(x)}{dx^2} + kw(x) = F\delta(x) \quad (15.3)$$

The solution to equation (15.3) can be found analytical in the spatial domain. If we define  $\kappa = \frac{k^{1/4}}{2(EI)^{1/4}}$ , the analytical solution to the deflection of a beam in the Winkler beam model is given by

$$w(x) = \frac{\kappa}{k} F e^{-\sqrt{2}|x|\kappa} \sin\left(\sqrt{2}|x|\kappa + \pi/4\right) \quad (15.4)$$

Equation (15.4) is solved using the Symbolic Math Toolbox in MATLAB, and as a result the derivation is not presented here. If this was to be done in hand, we would make a Fourier transform of equation (15.3), solve for the deflection and then make an inverse Fourier transform.

Equation (15.4) shows that the behaviour of the pavement deflection basin is characterised by the characteristic length  $\kappa$ .

$$\kappa = \frac{1}{2} \left( \frac{k}{EI} \right)^{1/4}$$

Hence, the relative stiffness of the beam compared to the foundation determines the behaviour of the deflection basin. On figure 15.1, the pavement deflection basin calculated using (15.4) is plotted for increasing flexural rigidity and constant foundation stiffness. This corresponds to decreasing the  $\kappa$  value. A decrease in  $\kappa$ , hence an increased stiffness in the beam compared to the foundation, makes the deflection basin more shallow and wider. The physical interpretation of this is that the beam takes part in distribution the point load over several spring elements, and thus broadening the deflection basin.

The foundation can be modelled as a viscoelastic medium instead of an elastic by adding a set of viscous dampers along the springs. In this case, the governing equation for the beam deflection in a moving reference frame is given by

$$EI \frac{d^4}{dx^4} w(x) + \tilde{\rho} v^2 \frac{d^2 w(x)}{dx^2} - cv \frac{\partial w(x)}{\partial x} + kw(x) = F\delta(x)$$

## 15.2 The Pasternak foundation

One big limitation with the Winkler foundation model is that it is a series of parallel springs (and dashpots) which do not influence each other, thus overlooking the cohesive

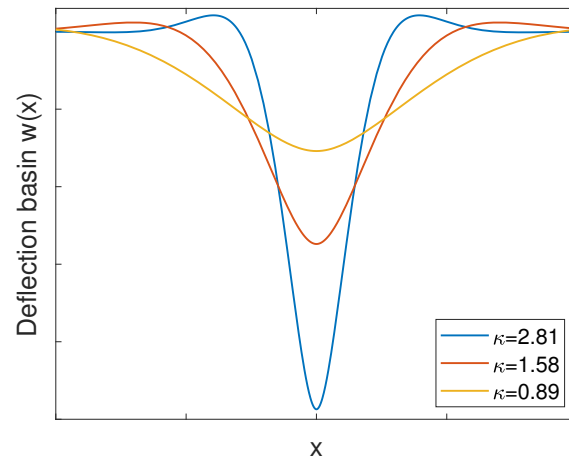


FIGURE 15.1: Pavement deflection basin calculated from equation (15.4) with varying  $\kappa$ . Parameter values used for the plot is  $F = 49000\text{N}$ ,  $k = 10^5$  and  $EI = [10^2, 10^3, 10^4]$

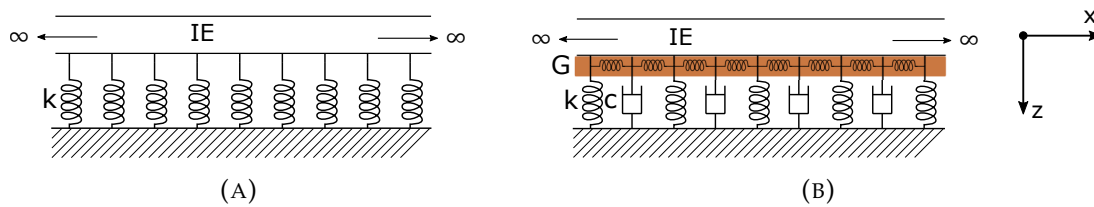


FIGURE 15.2: A) Sketch of a Euler-Bernoulli beam on top of an elastic Winkler foundation. B) Sketch of an elastic Euler-Bernoulli beam on top of a damped Pasternak foundation.

bonds between soil particles (Wang et al., 2005; Froio et al., 2018; Yu et al., 2017). As soil is a granular material, there exists shear interactions between the soil particles and thus this should be taken into account for a more realistic response.

A way to do so, is to introduce a incompressible shear layer that deforms under transverse shear (Froio et al., 2018). Such a layer is characterised by a parameter  $G$ , which is called the shear coefficient (Yu et al., 2017) or the shear parameter (Uzzal et al., 2012). The layer is connected with the top of the foundation elements (spring and dashpots) as illustrated on figure 15.2b. Physically, the shear layer can be thought of as a set of horizontal springs in between the soil elements (as illustrated on fig. 15.2b). Beside coping with the shear interactions, the layer also ensures that the applied load is distributed over multiple foundation elements, instead of just a few. Thereby, the foundation will act more like a continuous medium (Froio et al., 2018; Yu et al., 2017).

The govern equation for vertical pavement deflection,  $w(x', t)$ , of an elastic Euler-Bernoulli beam on top of a damped Pasternak foundation in a fixed reference frame is

given by equation (15.5).

$$EI \frac{\partial^4 w(x', t)}{\partial x'^4} + \tilde{\rho} \frac{\partial^2 w(x', t)}{\partial t^2} - G \frac{\partial^2 w(x', t)}{\partial x'^2} - c \frac{\partial w(x', t)}{\partial x} + kw(x', t) = q(x', t). \quad (15.5)$$

### 15.3 Viscoelastic beam on damped Pasternak foundation model

Combining the governing equation for deflection of a viscoelastic beam deduced in section 14.2 and the equation for a damped Pasternak foundation in equation (15.5) gives the following

$$E_0 I \frac{\partial^4 w(x', t)}{\partial x'^4} - I \int_0^t \frac{dE(t-t')}{d(t')} \frac{\partial^4 w(x', t)}{\partial x'^4} dt' \dots \quad (15.6)$$

$$+ \tilde{\rho} \frac{\partial^2 w(x', t)}{\partial t^2} - G \frac{\partial^2 w(x', t)}{\partial x'^2} + c \frac{\partial w(x', t)}{\partial t} + kw(x', t) = q(x', t).$$

Equation 15.6 governs the pavement response to a moving load for a viscoelastic beam on a damped Pasternak foundation in a fixed reference frame.

A solution for the pavement deflection  $w(x', t)$  can be found using an semi-analytical approach. Here an analytical solution is found in the wave number domain, and the the inverse Fast Fourier Algorithm (iFFT) is used to find the pavement deflection in spacial domain numerically.

Using the convolution theorem, the Fourier transformed of equation (15.6) with respect to time and space is derived (equation (15.7)). We use  $\omega$  and  $k_x$  as the transform variable with respect to time and space respectively.

$$(E_0 - \tilde{E}(\omega) i \omega) I k_x^4 \hat{w}(k_x, \omega) - \tilde{\rho} \omega^2 \hat{w}(k_x, \omega) + G k_x^2 \hat{w}(k_x, \omega) + c i \omega \hat{w}(k_x, \omega) + k \hat{w}(k_x, \omega) = \hat{q}(k_x, \omega) \quad (15.7)$$

We then solve for the pavement deflection,  $\hat{w}(k_x, \omega)$ .

$$\hat{w}(k_x, \omega) = \frac{\hat{q}(k_x, \omega)}{IE^*(\omega) k_x^4 - \tilde{\rho} \omega^2 + G k_x^2 + c i \omega + k} \quad (15.8)$$

$E^*(\omega) = (E_0 - \tilde{E}(\omega) i \omega)$  is the complex modulus of the beam. A specific viscoelastic model to describe the beams behaviour can be inserted as required.

#### 15.3.1 Shift to moving reference frame

Equation (15.6) accounts for the vertical deflection of the pavement in a fixed coordinate. However, we are interested in the pavement deflection in a moving coordinate system as we aimed to model the pavement response measured by the TSD. Consequently, equation (15.6) has to be changed into a moving reference frame. This is done by assuming a steady state situation, where the driving velocity ( $v$ ) is constant. In this case, we can make the



coordinate shift  $x = x' - vt$ , where  $x$  is our new time dependent  $x$  coordinate. Applying a coordinate shift in equation (15.6) is not as trivial as in the case of the Winkler model, since it contains a convolution integral. As a result, the coordinate shift is made in the frequency domain. This means that we have to find the appropriate coordinate shift in the frequency domain and apply it to equation (15.8).

We start of by showing how this is done for a general system on the form  $Lw(x', t) = q(x', t)$ , where  $L$  is a linear differential operator, and afterwards it is applied to our particular system (equation (15.6)).

The solution to a system on the form  $Lw(x', t) = q(x', t)$  can be found using the Green's function. The Greens function is the fundamental solution to a partial differential equation and is given by the solution to a system subject to an impulse load (Sun, 2001). Thus, for a system on the form  $Lw(x', t) = q(x', t)$ , the Greens function is the solution to

$$Lw_\delta(x', t) = \delta(x')\delta(t). \quad (15.9)$$

The solution to the original system is then given by the convolution  $w(x', t) = w_\delta(x', t) * q(x', t)$ . Due to the convolution theorem, transforming the system into the frequency domain gives the simple solution  $\hat{w}(k_x, \omega) = \hat{w}_\delta(k_x, \omega) \cdot \hat{q}(k_x, \omega)$ .

Using this relation, we can write up the general expression for the inverse Fourier transformed pavement deflection in a fixed frame.

$$w(x', t) = \frac{1}{(2\pi)^2} \int_{-\infty}^{\infty} \int_{-\infty}^{\infty} \hat{w}(k_x, \omega) e^{ik_x x'} e^{i\omega t} dk_x d\omega \quad (15.10)$$

$$= \frac{1}{(2\pi)^2} \int_{-\infty}^{\infty} \int_{-\infty}^{\infty} \hat{w}_\delta(k_x, \omega) \hat{q}(k_x, \omega) e^{ik_x x'} e^{i\omega t} dk_x d\omega \quad (15.11)$$

Now, lets start by evaluate the loading function term  $\hat{q}(k_x, \omega)$  in equation (15.11). From the definition of the Fourier transform we have that

$$\hat{q}(k_x, \omega) = \int_{-\infty}^{\infty} \int_{-\infty}^{\infty} q(x', t) e^{-ik_x x'} e^{-it\omega} dx' dt \quad (15.12)$$

For a moving load at constant velocity the loading function can be written on the form

$$q(x', t) = Q(x' - vt). \quad (15.13)$$

Including this into equation (15.12) gives

$$\hat{q}(k_x, \omega) = \int_{-\infty}^{\infty} \int_{-\infty}^{\infty} Q(x' - vt) e^{-ik_x x'} e^{-it\omega} dx' dt \quad (15.14)$$

Introducing the coordinate shift  $x = x' - vt$  and exploiting that  $\frac{dx}{dx'} = \frac{d(x' - vt)}{dx'} = 1$  gives,

$$\hat{q}(k_x, \omega) = \int_{-\infty}^{\infty} \int_{-\infty}^{\infty} Q(x) e^{-ik_x(x+vt)} e^{-it\omega} dx dt \quad (15.15)$$

$$= \int_{-\infty}^{\infty} Q(x) e^{-ik_x x} dx \int_{-\infty}^{\infty} e^{-it(vk_x + \omega)} dt. \quad (15.16)$$

Since the limits is from minus infinity to infinity, changing the coordinate does not affect these. Using that  $\int_{-\infty}^{\infty} e^{it(x-a)} dt = 2\pi\delta(x-a)$ , we get the expression for the loading function in a moving reference frame:

$$\hat{q}(k_x, \omega) = 2\pi \int_{-\infty}^{\infty} Q(x) e^{-ik_x x} dx \delta(vk_x + \omega) = 2\pi \hat{Q}(k_x) \delta(vk_x + \omega). \quad (15.17)$$

We now return to the Fourier transform of the pavement deflection in equation (15.11).

$$w(x', t) = \frac{1}{(2\pi)^2} \int_{-\infty}^{\infty} \int_{-\infty}^{\infty} \hat{w}_\delta(k_x, \omega) \hat{q}(k_x, \omega) e^{ik_x x'} e^{i\omega t} dk_x d\omega \quad (15.18)$$

$$= \frac{1}{2\pi} \int_{-\infty}^{\infty} \int_{-\infty}^{\infty} \hat{w}_\delta(k_x, \omega) \hat{Q}(k_x) \delta(vk_x + \omega) e^{ik_x x'} e^{i\omega t} dk_x d\omega \quad (15.19)$$

$$= \frac{1}{2\pi} \int_{-\infty}^{\infty} \hat{Q}(k_x) e^{ik_x x'} \int_{-\infty}^{\infty} \hat{w}_\delta(k_x, \omega) \delta(vk_x + \omega) e^{i\omega t} d\omega dk_x \quad (15.20)$$

In order to solve the integral over  $\omega$ , we use the fact that a delta function  $\delta(x-a)$  is zero all other places than in  $a$ . Hence, if we have a function  $\int_{-\infty}^{\infty} f(t) \delta(t-t_0) dt = f(t_0)$ . Thus we get

$$w(x', t) = \frac{1}{2\pi} \int_{-\infty}^{\infty} \hat{Q}(k_x) e^{ik_x x'} \hat{w}_\delta(k_x, -vk_x) e^{-ivk_x t} dk_x \quad (15.21)$$

$$= \frac{1}{2\pi} \int_{-\infty}^{\infty} \hat{Q}(k_x) \hat{w}_\delta(k_x, -vk_x) e^{ik_x(x'-vt)} dk_x \quad (15.22)$$

$$= \frac{1}{2\pi} \int_{-\infty}^{\infty} \hat{Q}(k_x) \hat{w}_\delta(k_x, -vk_x) e^{ik_x x} dk_x \quad (15.23)$$

This shows that making a coordinate shift in the wave number domain corresponds to the substitution  $\omega = -vk_x$ . Thus, a general expression for the the Fourier transformed pavement deflection in a moving frame is

$$\hat{w}(k_x, \omega) = \hat{w}_\delta(k_x, -vk_x) \hat{Q}(k_x). \quad (15.24)$$

As for the loading function, the pavement deflection can be rewritten in terms of the new moving reference coordinate

$$w(x', t) = W(x - vt) = w(x). \quad (15.25)$$

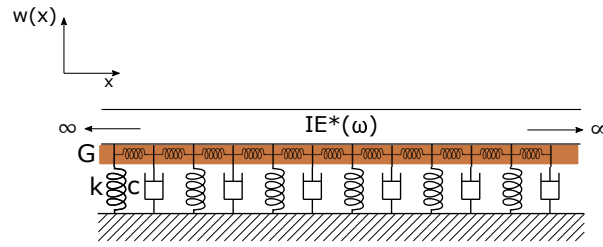


FIGURE 15.3: Sketch of a viscoelastic beam resting on a damped Pasternak-Winkler foundation. Here  $E^*(\omega)$  is the complex modulus of the beam,  $I$  is the beams second moment of area,  $k$  is the foundation spring constant,  $c$  is the viscous damping constant and  $G$  is the shear interaction parameter. The elastic Winkler-Pasternak model is obtained by setting  $c = 0$  and  $E^*(\omega) = E$ .

For the system in equation (15.6), the Fourier transformed Green's function in a moving reference frame is

$$\hat{w}_\delta(k_x, -vk_x) = \frac{1}{IE^*(-vk_x)k_x^4 - \tilde{\rho}v^2k_x^2 + Gk_x^2 - cik_xv + k}$$

Using this, we obtain the expression for the Fourier transformed pavement deflection,

$$\hat{w}(k_x, -vk_x) = \frac{\hat{Q}(k_x)}{IE^*(-vk_x)k_x^4 - \tilde{\rho}v^2k_x^2 + Gk_x^2 - vcik_x + k}. \quad (15.26)$$

The pavement deflection of the beam,  $w(x)$  can then be found using the inverse Fast Fourier Algorithm (iFFT) for numerical inversion of equation (15.26).

The term  $\tilde{\rho}v^2k_x^2$  account for any contributions to the pavement response from the vertical acceleration of the pavement. If we assume that inertial effects in the pavement is much faster than the movement of the load, this can be neglected (Di Paola et al., 2013). This simplification is possible as we have a moving load, whereas for a stationary load the effects of vertical acceleration can no be neglected.

For simplicity, the load is often modelled as a point load (described by the Dirac delta function) with constant amplitude  $F$  [N]. In this case, we have  $Q(x' - vt) = F\delta(x' - vt)$  and  $\hat{Q}(k_x) = F$ . Since we are working with an beam model, where the assumption is that the beam only deflect and not deform, the beam will contribute to distributing the load over foundation elements and thus assuming a point load and not a distributed load will not change the model output much.

## 15.4 Layer dimensions in a 1D model

The presented model is a one-dimensional simplification of the pavement structure, which in its nature is 3 dimensional. As a consequence, the model contains no direct notion of

length, width or layer thicknesses. Through the model parameters, an approximate notion of width and layer thickness can be given.

The width of the pavement is introduced as an underlying assumption when connecting the spring stiffness  $k$  and shear parameter  $G$  to the material parameters elastic modulus  $E$  and shear modulus  $\tilde{G}$  of the soil layer. The shear parameter  $G$  is connected with the shear elastic modulus  $\tilde{G}$  of the foundation material through equation (15.27) (Tanahashi, 2004). Here we assume that the vertical displacement  $W(x', z)$  throughout the layers can be expressed in form of the surface displacement  $w(x')$  and a shape function  $\phi(z)$ , where  $z$  is the coordinate going down the pavement (see fig. 15.2b).

$$G = B\tilde{G} \int_0^H \phi(z)^2 dz, \quad (15.27)$$

where  $H$  is the depth of the soil layer and  $B$  is the effective width of beam and soil (assumed to be 1 meter (Tanahashi, 2004)). For shallow layers the shape function can be approximated as  $\phi(z) = 1 - \frac{z}{H}$ , and thus equation (15.27) becomes

$$G = \frac{H}{3} \tilde{G}. \quad (15.28)$$

Likewise the spring stiffness  $k$  is connected to the elastic modulus of the foundation through

$$k = E \frac{A}{H}, \quad (15.29)$$

where  $A$  is the area over which the force is applied (as  $k$  is spring constant per unit length  $A = 1$  m) (Lautrup, 2011).

The layer thickness of the soil layer is given by  $H$  and is introduced when converting from one-dimensional parameters to the more familiar material parameters  $E$  and  $\tilde{G}$ .

The layer thickness of the top layer is introduced through the second moment of area per unit length  $I$ . If the beam is assumed a rectangle,  $I$  is given by

$$I = \frac{1}{12} h^2 \quad (15.30)$$

where  $h$  is the beam thickness.

The spring and dashpot elements in the foundation layer are attached to a hard bottom. Thus, we implicitly assume the presence of a third underlying layer in the form of a hard rock foundation which is not compressed. One of the reasons behind developing a simple pavement response model was to fit it to TSD measurements in order to estimate the pavement deflection slope underneath the load. However, in Denmark (where some of the TSD measurements are made) there are no underlying hard rock foundation and thus

---

a more realistic model would be a viscoelastic half-space medium which continues indefinitely in the downwards direction. In an infinite half-space, the wave-propagation created by the deflection of the surface will continue downwards, whereas it for a hard bottom will be bounced back and influence the total deflection basin. However, we expected this inconsistency in the model to affect the output at high wavelengths and thus far away from the area where our model fitting was happening. Therefore, this was believed not to influence the accuracy of the model fit performed in part V.



## Chapter 16

# Numerical study of the pavement response model

By use of inverse FFT algorithm, equation (15.26) can be solved in the spatial domain and the pavement response to a moving load found. In the rest of this part of the thesis, a numerically study of the model will be presented. To begin with a viscoelastic model for the beam and a set of parameter values had to be chosen. This is done in section 16.1 and 16.2, followed by an initial analysis of the resulting pavement deflection basin and slope in section 16.3.

### 16.1 Choice of viscoelastic model for the beam

The viscoelastic behaviour of the beam can be described through mathematical or mechanistic model. In this study, we considered mechanistically models where physically elements was used to describe the viscoelastic behaviour. We aimed to develop the simplest possible model, as it was intended to use this to fit to TSD measurements which contained merely 9-10 datapoints. Thus, we chose to use the simplest model that had the correct  $E^*(\omega)$  behaviour, namely the Maxwell model. The complex modulus for the Maxwell model can be written in terms of elastic modulus  $E$  and characteristic time  $\tau$ ,

$$E^*(\omega) = E \frac{i\omega\tau}{1 + i\omega\tau}. \quad (16.1)$$

### 16.2 Choice of parameters

In order to perform a numerical study, a set of parameter values is needed. In this section, a set of default parameter values will be presented and these will be used throughout the rest of the numerical study, in order for results to be comparable. The default parameter values are listed in table 16.1 and bellow a short discussion of them is made.

### External parameters

A point load was used unless otherwise is specified. This was given by  $Q(x' - vt) = F\delta(x' - vt)$ , where  $F$  is the magnitude of the load. As default we simulated a truck with a 10 tonnes axle-load, thus 5 tonnes on each tire pair. The driving velocity are set to be 60 km/h.

### Foundation parameters

Parameter values for the stiffness ( $k$ ) and shear parameter ( $G$ ) for the foundation were adopted from Mallik et al. (2006). This particular foundation stiffness value is also used in Elnashar et al. (2019) and Uzzal et al. (2012) and is referred to as a medium stiff soil. Assuming the foundation is isotropic, the parameters  $k$  and  $G$  can be converted to a measure of elastic modulus  $E$  and shear modulus  $\tilde{G}$  of the soil layer, respectively.

$$k = E \frac{A}{H}, \quad G = B\tilde{G} \frac{H}{3}, \quad (16.2)$$

where  $A$  is the area over which the force is applied (as  $k$  is spring constant per unit length  $A = 1$  m),  $H$  is the height of the soil layer and  $B$  is the width of the beam and foundation layer (Tanahashi, 2004; Lautrup, 2011). Assuming  $H = 3$  m gives  $E_{soil} = 12$  MPa, which is relative low for soil. Thus, we expected the foundation to behave rather soft. Assuming  $B=1$  m (as done in Tanahashi (2004)), the shear modulus corresponding to  $G$  was found to be  $\tilde{G} = 0.6$  MPa. This exact value for  $G$  was used in several numerical studies about the Pasternak foundation and for this reason was adapted here (Elnashar et al., 2019; Snehasagar et al., 2019; Uzzal et al., 2012; Mallik et al., 2006).

The damping in the foundation is characterised by the foundation damping pr. unit length  $c$ . A more conventional way to characterise it, is through the damping ratio,  $\zeta$ .  $\zeta$  is defined from the viscous damping coefficient  $c$  and the critical damping  $c_c$  of the system,

$$\zeta = \frac{\text{actual damping}}{\text{critical damping}} = \frac{c}{c_c} \quad (16.3)$$

For a system of springs and dashpots in parallel, the critical damping is given by

$$c_c = 2m\sqrt{k/m}, \quad (16.4)$$

where  $m$  is the mass of the system and  $k$  the spring constant.

In a 3-dimensional model,  $k$  has units  $[\frac{N}{m}]$ , the mass  $m$  is found in [kg], and thus  $c_c$  has the units  $[\frac{Ns}{m}]$ . However, in our 1D model  $k$  is the spring constant per unit length  $[\frac{N}{m^2}]$  and we had to use the mass per unit length  $[\frac{kg}{m}]$ . Thus the units for  $c_c$  is  $[\frac{Ns}{m^2}]$  and this is called the critical damping coefficient per unit length. It has similar units as the viscous damping coefficient pr unit length, and thus  $\zeta$  is dimensionless. We assumed a damping ratio  $\zeta = 0.3$ , as we aimed to study a system with significant damping in the foundation.



### Beam parameters

Parameters for the viscoelastic model for the beam (equation (16.1)) was based on rheological experiments made in Pronk (2006). In this, the Huet-Sayegh model was fitted to data and the associated parameter values listed. Using this as a reference, we have fitted equation (16.1) and obtained parameters in table 16.1 (fig. 16.1). As seen on figure 16.1, the Maxwell model provided a rather bad fit to the Huet-Sayegh model, as a result of its simplicity. However, this procedure was followed as no studies with Maxwell model fit to data were found, and we aimed to ensure realistic values for  $E_{visco}$  and  $\tau$ .

Beside the parameters for the complex modulus, the beam is also described by its second moment of area per unit length,  $I$ . The beam was assumed a rectangle and  $I$  was given by  $I = \frac{1}{12}h^3$ . We assumed that the beam was 10 cm thick.

To enable a comparison between elastic and viscoelastic beams, we chose a value for the elastic module,  $E_{elastic}$ , which gives a similar maximum deflection amplitude for the elastic and viscoelastic response. Thus, the two solution has the same effective stiffness and only the amount of damping is different (as seen on figure 16.2a).

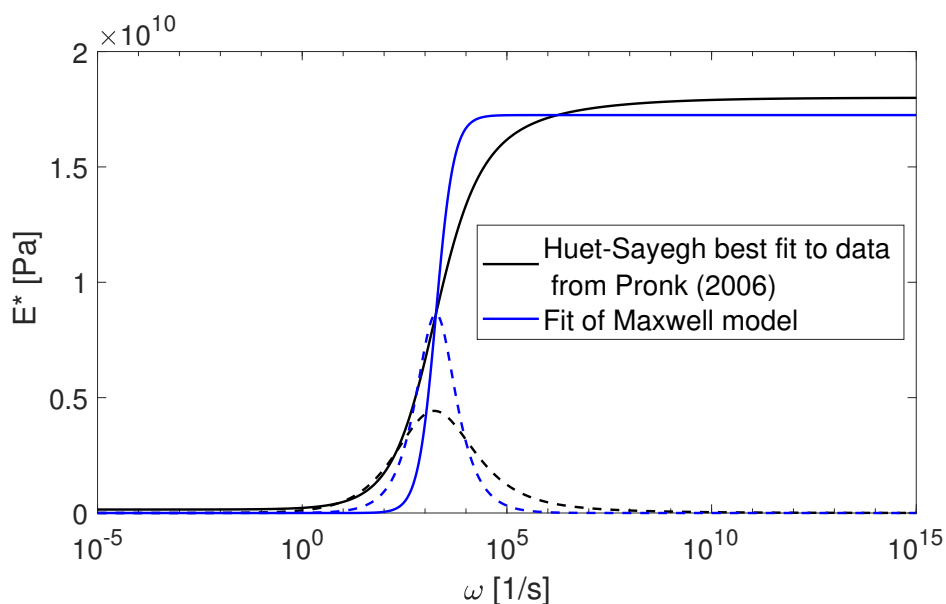


FIGURE 16.1: In Pronk (2006) the Huet-Sayegh model is fitted to rheological data and the best fit found (black line). Using this as a reference, we have fitted equation (16.1) and obtained the best fit (parameters in table 16.1). As seen, the Maxwell model provides a rather bad fit due to its simple form.

TABLE 16.1: Parameter values used for numerical study.

Default simulation parameters				
Description	symbol	value	unit	based on
Moving load	F	49000	N	
Vehicle velocity	v	16.67	m/s	
<b>Foundation</b>				
foundation stiffness per unit length	k	$40.8 \cdot 10^5$	N/m <sup>2</sup>	Mallik et al. (2006)
shear interaction parameter	G	$66.7 \cdot 10^4$	N	Mallik et al. (2006)
damping ratio	$\zeta$	0.3		
foundation damping per unit length	c	$8.5 \cdot 10^4$	$\frac{Ns}{m^2}$	
<b>Beam</b>				
Elastic modulus per unit length	$E_{visco}$	$1.7 \cdot 10^{10}$	$\frac{N}{m}$	Pronk (2006)
Second moment of area per unit length	I	$8.3 \cdot 10^{-5}$	m <sup>3</sup>	
Characteristic time	$\tau$	$5.4 \cdot 10^{-4}$	s	Pronk (2006)
Elastic modulus per unit length	$E_{elastic}$	$4.2 \cdot 10^8$	$\frac{N}{m}$	
Temperature	T	25	°C	Pronk (2006)

### 16.3 Simulated pavement deflection basin and slope

In figure 16.2, a plot of simulated pavement deflection basin and slope is seen for the model using an elastic beam and a viscoelastic beam. In the pavement deflection basin (fig. 16.2a), the viscoelastic effects manifested itself by the maximum deflection occurring behind the load ( $x=0$ ). Furthermore, we found that the time delay in the pavement made the deflection basin broader behind the load than in front of it. This effect was bigger when damping is included in both foundation and beam, as we would expect. Recall that the parameter values was chosen such that the maximum deflection in the two scenarios were the same, and thus no change was seen here.

The associated pavement deflection slope curves were characterised by having a minimum behind behind the load and a maximum in front of the load. Introducing a viscoelastic top layer affected the amplitude of the maximum and minimum as well as the slope underneath the load ( $x=0$ ), which became larger. In section 10, the slope underneath the load was associated with the structural rolling resistance loss and thus, as expected, we find a bigger loss when damping was present in both layers.

### 16.4 Influence of asphalt thickness

Through numerical study of the model, we investigated how different components of the model influenced the pavement response. In this section, we will investigate how changing the beam thickness influence the resulting pavement deflection. The beam thickness is a desired physical property to investigate as the asphalt thickness often changes in real life situations.

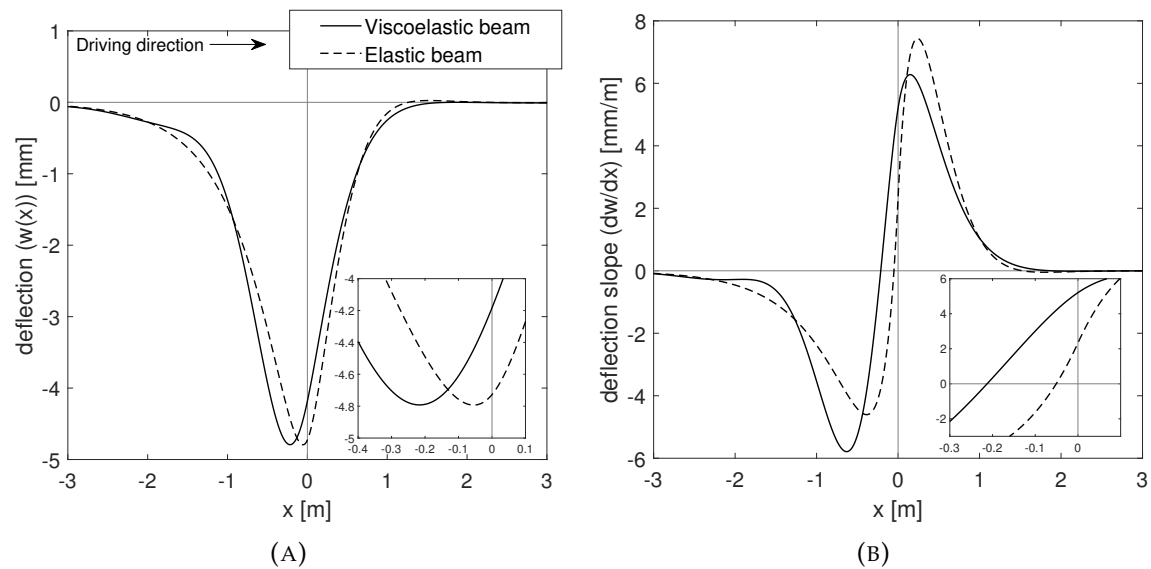


FIGURE 16.2: A) Pavement deflection underneath a moving load for the model with an elastic and viscoelastic beam. The viscoelastic effects manifest itself in the maximum deflection occurring behind the load ( $x=0$ ). B) Associated pavement deflection slope. Introducing a viscoelastic top layer affects the amplitude of the maximum and minimum as well as the slope underneath the load ( $x=0$ ). The simulation is made using default parameter values listed in table 16.1.

The beam thickness  $h$  was introduced into the model through the second moment of area per unit length  $I$ . Thus, the beam thickness influence the flexural rigidity ( $EI$ ) of the beam by,

$$EI = \frac{1}{12}h^3E. \quad (16.5)$$

There are some limitations to the value which  $h$  can take as it has to stay within the models validity domain.

A fundamental assumption for a beam structure is that one dimension has to be much larger than the other, meaning that the length of the beam has to be much larger than the height,  $L \gg h$ . Furthermore, its thickness has to be much smaller than the radius of curvature. When investigating how  $h$  influence the pavement response, this assumption should always be fulfilled in order to obtain trustworthy results.

Likewise, there are restrictions for the flexural rigidity ( $EI$ ) of the beam when it is on top of an Pasternak foundation.  $EI$  is a measure of how much moment that is required to bend the beam with a given curvature. As a result, decreasing  $h$  (and thereby  $EI$ ) will at some point result in a nonphysical behaviour of the deflection basin. In the limit  $I \rightarrow 0$ , equation (15.6) will be reduced to a second order linear partial differential equation. The solution to this is on the form of an exponential function, and thus if we predict the pavement response from this model, we will obtain a deflection basin that is constructed by two exponential functions approaching each other in the maximum deflection. This is clearly an nonphysical behaviour and should be avoided.

Provided that we are within the limits of the models validity domain, the influence of  $h$  can be investigated. On figure 16.3, a plot of the pavement response simulated for different beam thicknesses are seen. The thickness was changed within 5-15 cm, as these are realistic thicknesses for an asphalt layer. The flexural rigidity is also listed for each height. We found that when  $h$  (and  $IE$ ) was increased, the maximum deflection was decreased and the deflection basin became increasingly broad. Furthermore, the maximum deflection moved away from the center of the load as increased  $IE$  acts as a scaling of the beam damping.

Evaluating the deflection slope at increased  $h$  revealed that it had a different effect on the minimum and the maximum. Both experience decreasing amplitudes when  $h$  is increased, but only the x-placing of the minimum is affected by moving further away from the load.

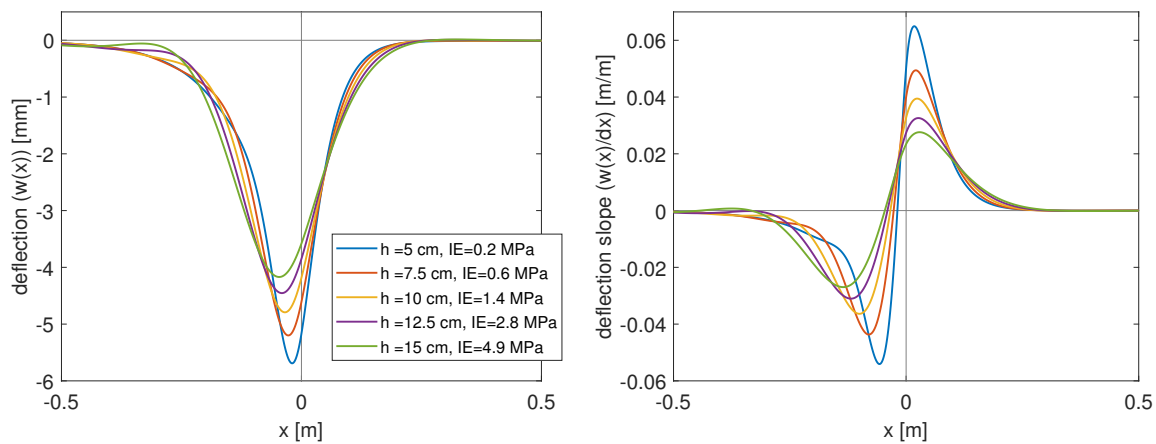


FIGURE 16.3: Simulated pavement response at different height of the top layer. We found that when  $h$  (and  $IE$ ) was increased, the maximum deflection decreased and the deflection basin became increasingly broad. Furthermore, the maximum deflection moved away from the center of the load as  $IE$  acts as a scaling of the beam damping.



## Chapter 17

# How the complex modulus of the beam influence the pavement response

The simple pavement response model derived in chapter 15, is given by

$$\hat{w}(k_x, -vk_x) = \frac{\hat{Q}(k_x)}{IE^*(-vk_x)k_x^4 + Gk_x^2 - vcik_x + k}. \quad (17.1)$$

For the model presented in equation (17.1) it holds that

$$\lim_{k_x \rightarrow 0} \hat{w}(k_x, -vk_x) = \frac{\hat{Q}(k_x)}{k}, \quad (17.2)$$

$$\lim_{k_x \rightarrow \infty} \hat{W}(k_x, -vk_x) = \frac{\hat{Q}(k_x)}{IE^*(-vk_x)k_x^4}. \quad (17.3)$$

Equation (17.2) states that the behaviour of the pavement response at small wave numbers (big wavelengths) is dominated by the elastic behaviour of the foundation. On the other hand, the behaviour of the pavement response at high wave numbers (low wavelengths) is dominated by the viscoelastic beam term (eq. (17.3)). Note that strictly speaking, equation 17.1 will go to zero as  $k_x$  goes to infinity.

Equation (17.2) and (17.3) implies that the pavement behaviour close to the load is dictated by the beam properties, whereas the behaviour far away from the load is determined by the foundation parameters. The viscoelastic behaviour of the beam is determined by the chosen model for the complex modulus. In this study, we have chosen to primarily use the Maxwell model whose complex modulus in a moving reference frame is

$$E^*(-vk_x) = E \frac{-ivk_x\tau}{1 - ivk_x\tau}. \quad (17.4)$$

We aimed to study how the the model output, thus the pavement response, was affected by the complex modulus of the beam. A systematic way to do so is by looking at the *sensitivity function*. The sensitivity function of a given parameter can be found by looking

at the partial derivative of the model with respect to that parameter. Thus, the sensitivity of the pavement response in the wave number domain with respect to  $E^*(-vk_x)$  can be found by

$$\frac{\partial \hat{w}(k_x, -vk_x)}{\partial E^*(-vk_x)} = -\frac{FIk_x^4}{(E^*(-vk_x)Ik_x^4 + Gk_x^2 - icvk_x + k)^2}. \quad (17.5)$$

The sensitivity function  $\frac{\partial \hat{w}(k_x, -vk_x)}{\partial E^*(-vk_x)}$  is a function of wave number, and provides information about for which wave numbers  $E^*(-vk_x)$  influence the model output. On figure 17.1a, a plot of the sensitivity function using default values in table 16.1 is shown (blue area curve). As equation (17.5) is a complex function we chose to plot the absolute value. As seen, the sensitivity function for  $E^*(-vk_x)$  is bell shaped around some maximum. The magnitude of the sensitivity function indicated how sensitive the model output was to  $E^*(-vk_x)$  at a given wave number. Consequently, we observed that there existed an interval in the wave number domain where  $\frac{\partial \hat{w}(k_x, -vk_x)}{\partial E^*(-vk_x)} > \epsilon$ , with  $\epsilon$  being a small number. For the rest of the wave number domain, the sensitivity function was approximately zero. This interval of wave numbers where the sensitivity function was nonzero is called the *sensitivity interval*.

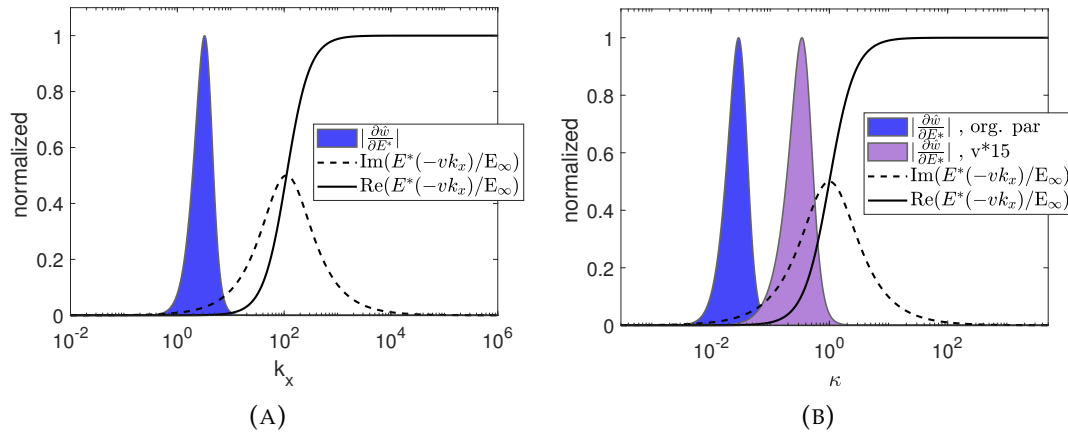


FIGURE 17.1: A) plot of the sensitivity function  $\frac{\partial \hat{w}(k_x, -vk_x)}{\partial E^*(-vk_x)}$  and the Maxwell model (eq. (17.4)) using default parameters from table 16.1. B) Maxwell model and the sensitivity function  $\frac{\partial \hat{w}(k_x, -vk_x)}{\partial E^*(-vk_x)}$  plotted on normalized axis. The use of normalized wave numbers  $\kappa = -v\tau k_x$  makes it possible to compare complex modulus curves and the sensitivity function when parameter values are changed.

On figure 17.1a, the complex modulus using default parameters is also plotted. The sensitivity interval was found to not cover all of the complex modulus curve but only some small part of it. As a result, only the behaviour of the storage and loss modulus within this interval of wave numbers influenced the modelled pavement response.

Changing the value of parameters in the model will shift the the sensitivity interval



and/or the  $E^*(-vk_x)$  curve and as a result a different part of storage and loss modulus was covered by the sensitivity interval. Thus, different amount of damping and stiffness expressed in the simulated pavement response.

A consequence of being in a moving reference frame is that the complex modulus is a function of  $k_x$ , and furthermore has the driving velocity as a parameter. Thus changing the driving velocity will affect what part of the complex modulus is within the sensitivity interval, and as a result, affects the pavement response. On figure 17.1b, the complex modulus is plotted on normalized x and y axis. In addition, a plot of the sensitivity interval using default parameter values (blue) and with increased driving velocity (purple) are plotted. The use of normalized wave numbers ( $\kappa$ ) entails that that the complex modulus curve is fixed and the sensitivity function will shift up or down when parameter values are changed. This makes a comparison of different parameter sets possible.

Through this, we found that increasing the driving velocity shifted the sensitivity function to a higher normalized wave number. This resulted in a pavement response with a higher degree of viscous damping and a slightly higher stiffness. If  $v$  was increased further, the sensitivity interval would pass the loss modulus peak and the behaviour would be like an elastic beam with  $E^*(\infty)$  as an elastic modulus, thus experience no damping from the beam.

In conclusion, the pavement response of a viscoelastic pavement subject to a moving load depended on the given driving velocity. This was opposite to the purely elastic case, where the deformation is independent on the loading frequency as  $E^*(-vk_x)$  is constant over all  $k_x$ .

The pavement response will also depend on the temperature. Changing the temperature of the viscoelastic beam correspond to changing the parameter values of  $\tau$  and  $E$  and thus is effectively a shift of the complex modulus curve. In order to investigate the effect of temperature on the pavement response, we use the relation between asphalt temperature and Huet-Sayegh model parameter values found from rheological measurements in Pronk (2006). From these, associated Maxwell model parameter values can be found and the sensitivity function calculated.

On figure 17.2 the sensitivity function and  $E^*(-vk_x)$  on normalized axis for different temperatures is plotted. Here we see that increasing the temperature of the beam result in the sensitivity interval being shifted from high to low normalized wave numbers. As a result, having a low road temperature result in a stiff pavement behaviour and having a warm road result in a softer behaviour. The amount of damping expressed by the pavement depends on the specific location of the sensitivity interval with respect to the  $E''$  peak.

### 17.0.1 How choice of $E^*(\omega)$ influence the pavement response

A consequence of the existence of the sensitivity interval is that the effect of different complex modulus models on the pavement response differs depending on where the sensitivity interval is located.

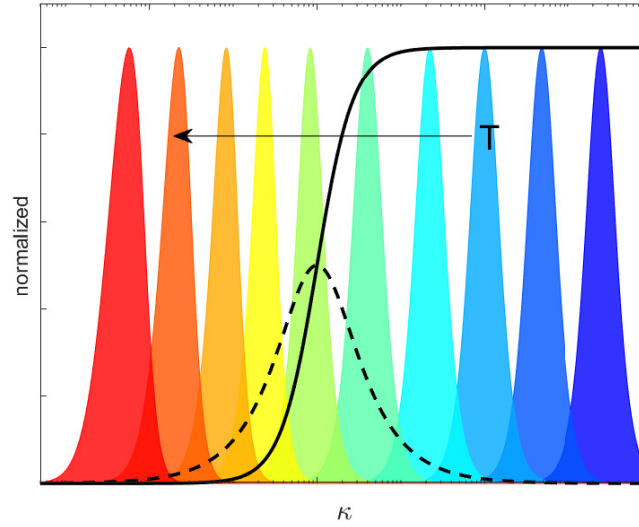


FIGURE 17.2: Plot of the sensitivity interval and the  $E^*(-vk_x)$  curve on normalized axis. Changing the temperature of the asphalt layer changes the parameter values for  $E$  and  $\tau$ , which correspond to shifting the  $E^*(-vk_x)$  curve. On normalized axis, this is like moving the sensitivity function downwards with respect to the  $E^*(-vk_x)$  curve.

An example with three mechanistic models; Maxwell, Burger's and Huet-Sayegh (see section 13.3), is shown on figure 17.3. Overall, the complex modulus curve for the different models has the same trends, with a peak in the loss modulus and a elastic regime at low and high frequencies. If we considered the complex modulus for the models at high frequencies, we found that they all went towards some plateau value, determined by the spring constants (eq. (17.6) ). However, if we considered their behaviour at low frequencies (eq. 17.7), the Maxwell and Burger model went to zero whereas the Huet-Sayegh model went to a nonzero plateau value.

$$\lim_{k_x \rightarrow \infty} E_{Maxwell}^* = E, \quad \lim_{k_x \rightarrow \infty} E_{Burger}^* = E_1, \quad \lim_{k_x \rightarrow \infty} E_{Huet-Sayegh}^* = E_2 + E_1 \quad (17.6)$$

$$\lim_{k_x \rightarrow 0} E_{Maxwell}^* = 0, \quad \lim_{k_x \rightarrow 0} E_{Burger}^* = 0, \quad \lim_{k_x \rightarrow 0} E_{Huet-Sayegh}^* = E_1 \quad (17.7)$$

Consequently, if the sensitivity interval was located at high frequency (scenario 1 fig. 17.3), no difference in the pavement response would occur when changing  $E^*(-vk_x)$  model. On the other hand, if the sensitivity interval was located around the loss peaks (scenario 2 fig. 17.3) a big difference between the different models was seen. Thus, the validity of using the simple Maxwell model to represent the viscoelastic behaviour of the

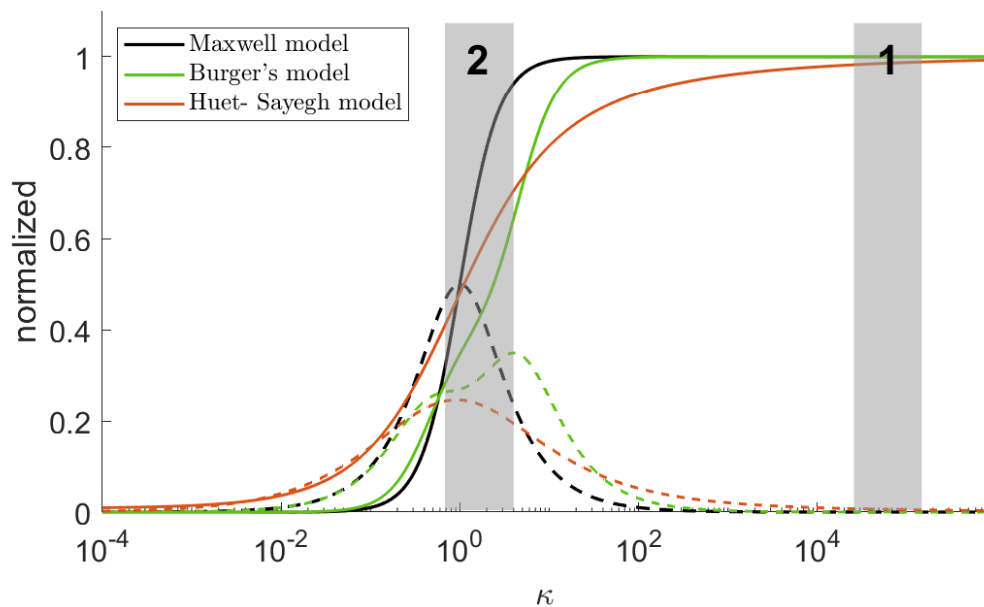


FIGURE 17.3: Complex modulus for the three mechanistic models; Maxwell, Burger's and Huet-Sayegh. For details see table ???. The curves is made using parameters from table 17.1.

beam was higher if the sensitivity interval is located at either high or low wave numbers. For the chosen default parameter values, we found that the sensitivity interval was located at relative low wave numbers (fig. 17.1b) and consequently using the Maxwell model might be a good enough approximation.

TABLE 17.1: Parameters used for simulation in figure 17.3. The parameter values is chosen such that the complex modulus curves is comparable at normalized frequency.

Simulation parameters for $E^*(-vk_x)$ models								
Maxwell model			Burger's model			Huet-Sayegh model		
$E$	$1.7 \cdot 10^{10}$	$\frac{\text{N}}{\text{m}}$	$E_1$	$1.7 \cdot 10^{10}$	$\frac{\text{N}}{\text{m}}$	$E_1$	$150 \cdot 10^6$	$\frac{\text{N}}{\text{m}}$
$\tau$	$5.4 \cdot 10^{-4}$	s	$\tau_1$	$5.4 \cdot 10^{-4}$	s	$\tau$	$1.3 \cdot 10^{-5}$	s
			$E_2$	$1.7 \cdot 10^{10}$	$\frac{\text{N}}{\text{m}}$	$E_2$	$1.8 \cdot 10^{10}$	$\frac{\text{N}}{\text{m}}$
			$\tau_2$	$2.7 \cdot 10^{-4}$	s	$k$	0.7	-
						$h$	0.2	-
						$\delta$	0.08	-

## Chapter 18

# Sensitivity analysis of the model

A mathematical model is a tool used in the attempt to explain the world around us. Often the real world are incredible complex and in order to understand it we seek to simplify it by a mathematical model. Roughly speaking, a model has an input and an output (these can be an multi-dimensional). The input can be subject to many sources of uncertainties, this includes measurement errors, absence of information or poor understanding of the driving forces of the modeled mechanism (Saltelli et al., 2000). This limits our confidence in the model output.

Sensitivity analysis is the study of how the output of a model depends on the inputs. It can be use to evaluate how confident we are in the model and assessing the uncertainties associated with the model (Saltelli et al., 2000).

A sensitivity analysis can be used for different purposes:

- 1) to investigate which inputs have the biggest influence on the output. This can help in designing the experiments and deciding which data are important to obtain in order to be able to estimate all parameters uniquely.
- 2) to investigate whether any parts or parameters in the model can be eliminated due to it being insensitive or correlated with other parameters. This can lead to an reduction in the parameter space and might simplify the model. This is also called model lumping.

There exists many different methods and approaches to analyse the sensitivity of a model, each with individual strengths and weaknesses. What methods to chose should be guided by the intended information one wish to obtain.

The model investigated is the pavement response model developed in chapter 15 with a point load and the Maxwell model as  $E^*(-vk_x)$ .

$$\hat{w}(k_x, -vk_x) = \frac{F}{(IE \frac{-vk_x i \tau}{1 - vk_x i \tau})k_x^4 + Gk_x^2 - vcik_x + k}. \quad (18.1)$$

The model has five parameters,  $\Theta = \{IE, \tau, k, c, G\}$ , each corresponding to a physical characteristics of the system. The direct output of the model in equation (18.1), is the

pavement deflection in the frequency domain  $\hat{w}(k_x, -vk_x)$ . Using numerical inverse Fast Fourier Algorithm (iFFT) we can obtain the pavement deflection  $w(x)$  as a model output.

The aim of this chapter is to investigate how the different physical parameters influence the models output in the spatial domain, namely the pavement deflection. This can be either in the form of the deflection basin  $w(x)$  or the deflection slope  $\frac{dw(x)}{dx}$ .

This was done through a local sensitivity analysis evaluating the individual parameters impact and subsequently a global analysis which evaluates any correlations between parameters as well as a much larger parameter space. Both types of sensitivity analysis performed here was numerical, and thus requires some set of starting parameter values denoted  $\theta_0$ , which was the default values presented in table 16.1.

## 18.1 Local sensitivity analysis

We started by performing a local sensitivity analysis, where we pertubated one parameter while all others were hold constant. The resulting change in model output was then monitored in the form of the magnitude and x-position of the maximum deflection and the maximum and x-position of the maximum and minimum deflection slope. We chose to look at not only the deflection basin, but also characteristic features of the deflection slope as this was the output of the TSD and thereby the influence of various physical parameters on this quantity is interesting.

In the deflection basin, the time delay in the pavement response due to viscous effects in the pavement was manifested by the maximum deflection occurring behind the load. The larger a time delay experienced, the further away from the center of the load ( $x=0$ ) the maximum deflection occurred. Thus, we expected this quantity to describe the amount of damping in the pavement. Similarly, the magnitude of the maximum deflection, reflected how stiff or soft the pavement behaves. The behaviour of the pavement deflection slope is more complicated to interpret.

Figure 18.1 showed a combined plot of the influence on the characteristic values when changing the parameter values of  $k, G, \zeta, \tau$  and  $E$ , respectively. This yielded information about how the pavement response is influenced by a particular parameter. Note that all parameter values were decreased with a factor 0.01 and increased with 1000 times. This gave some unrealistic parameter values for some parameters, and also resulted in some unnatural deflection basins. However, these plots can be used to get a general idea about how each parameter influences the model output and to which parameter the model output is most sensitive. The most important results from figure 18.1 is reviewed below.

On figure 18.1a-b, the behaviour of the amplitude and x-position of the maximum deflection is shown. Three interesting features were worth noticing based on the plot. First of all, we found that the foundation stiffness  $k$  had the biggest influence on the amplitude of the maximum deflection among all the parameters. This was particularly evident when  $k$  became small and the foundation became soft, and the result was a deep and narrow deflection basin.

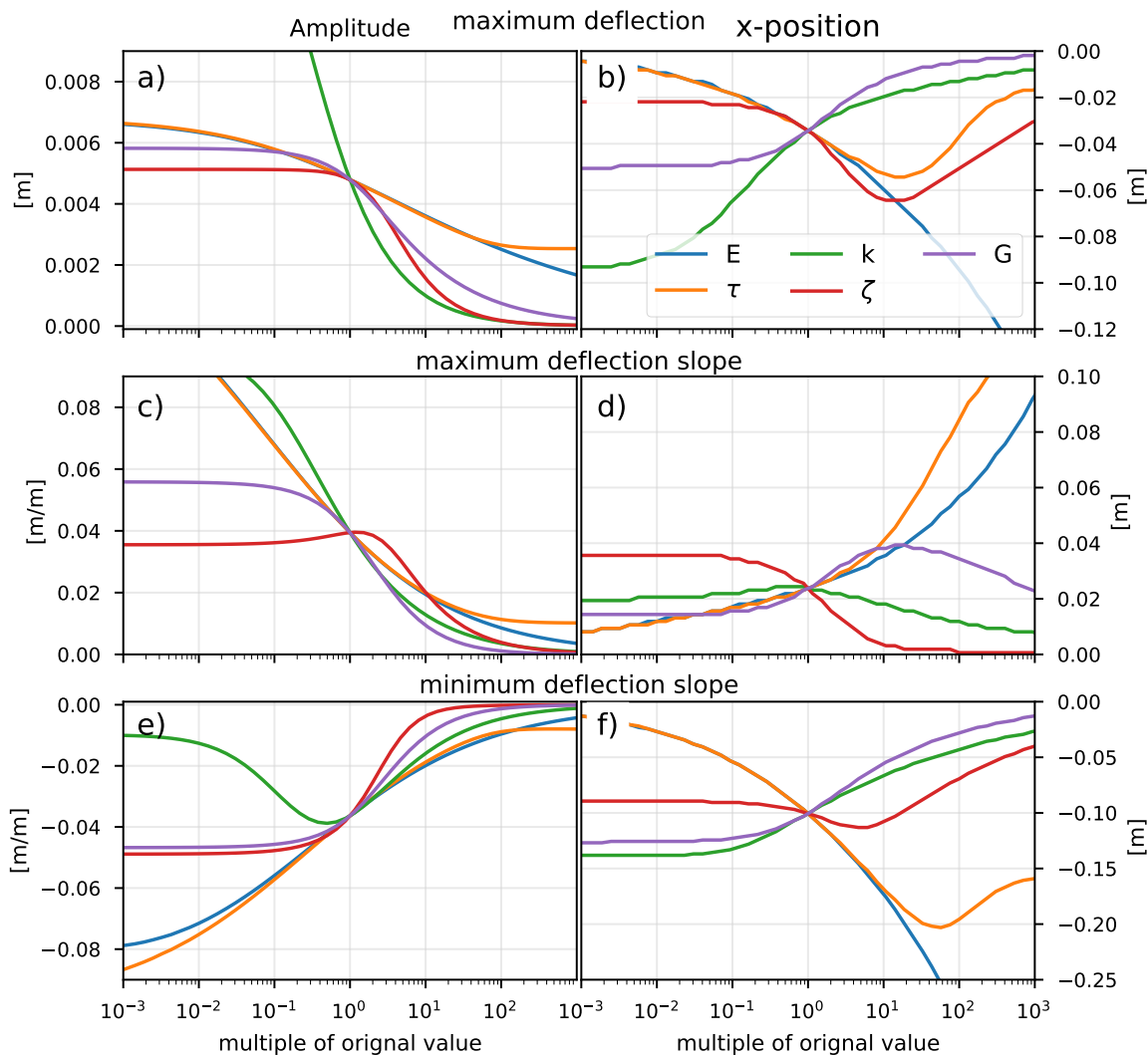


FIGURE 18.1: The influence of the physical parameters in the model on the pavement response. The parameters influence will be evaluated with respect to their impact on the maximum deflection, and the maximum and minimum deflection slope. We are looking at both the magnitude and x-location, as these gives separate information.

Secondly, a peak in the  $x$ -position curves for both the foundation and beam damping was found. This quantity is often correlated with the amount of damping in the pavement and thus this indicated that there existed a value for both  $\tau$  and  $\zeta$  which yielded a maximum amount of damping. This behaviour was not surprising for  $\tau$ , as the loss modulus of the beam has a peak value. A similar behaviour is not seen for the  $E$  curve, as this acts as a scaling in the Maxwell model (eq. (17.4)), and thus just amplified the value of  $E''$ . More surprising was it to see this behaviour for the foundation damping  $\zeta$  as this was expected to influence the damping in the model in a linear way. The explanation is that the values at which the maximum damping behaviour is seen, were so large that the dash-pot became increasingly difficult to compress and thus begun to act stiff.

The third thing worth noticing about the deflection basin was that increasing foundation stiffness in form of  $k$  or  $G$  could counteract an increase in foundation damping. Thus, the "actual damping" experienced by the pavement from the foundation was not just determined by the damping parameter  $\zeta$ , but a function of all foundation parameters.

On figure 18.1c-f, the parameters influence on the deflection slope was plotted. A common trend is observed, that for increased parameter values the magnitude of both the minimum (18.1e) and maximum (18.1c) went towards zero. On the other hand, the behaviour of the  $x$ -position of the two peaks is behaving different with respect to the different parameters. This made us capable of distinguishing between changes in the different parameter values based on the pavement deflection slope signals. E.i. it is possible to distinguish between increased (or decreased) stiffness in the top layer and the foundation. Where an increase in  $k$ , and in some extend  $G$ , made the peaks move closer to  $x=0$ , an increase in  $\eta$  and  $E$  moved the peaks away from  $x=0$ .

The influence of driving velocity  $v$  was also investigated and it was found that for a big range, it had the same influence on the pavement response at  $\tau$ . This was due to  $v$  being multiplied on  $\tau$  in equation (18.1), and thus these were correlated. However,  $v$  was also correlated with the foundation damping  $\zeta$ , and thus deviated from the behaviour of the beam parameters when  $v$  was large.

The analysis performed above is a local sensitivity analysis, meaning that it takes its starting point in  $\theta_0$  and explores the parameter space in the neighbourhood of this. This method assumes a linear input-output relationship, which in some cases is not enough to obtain reliable estimates of the output uncertainty in the model (Saltelli et al., 2000). Furthermore, this approach is highly dependent on the chosen starting point and it gives only a local interpretation of the parameters influence on the model output.

In order to get a more comprehensive analysis, a global sensitivity analysis should be made where all parameters are varied simultaneously and the sensitivity is measured over all input parameters.



## 18.2 Global sensitivity analysis

In this section, a global sensitivity analysis was made using the Metropolis Monte-Carlo (MMC) method. Using this, we can obtain information about the sloppiness and degree of correlation within the parameters. The Metropolis Monte-Carlo (MMC) method is used to explore a bigger part of the parameter space. It has the advantage that it is less likely to get stuck in a local minimum compared to other methods and that it can explore more than 2 dimensional parameter spaces. In the MMC method, the parameter values  $\theta$  is varied in an iterative way and then the given cost function,  $C(\theta)$ , is evaluated. The new parameter set is then either accepted and saved or rejected based on some criteria. This procedure is repeated until a certain amount of parameter sets has been accepted. The method is described in detail in appendix C.

Using the MMC method, we have analysed the model. For this analysis we used the following cost function

$$C(\theta_{new}) = \sum_{i=1}^m \left( (w(x_i, \theta_0) - w(x_i, \theta_{new}))^2 \right), \quad (18.2)$$

where  $m$  is the number of data points and  $\theta_0$  is original parameter values. The sampling temperature used is defined as

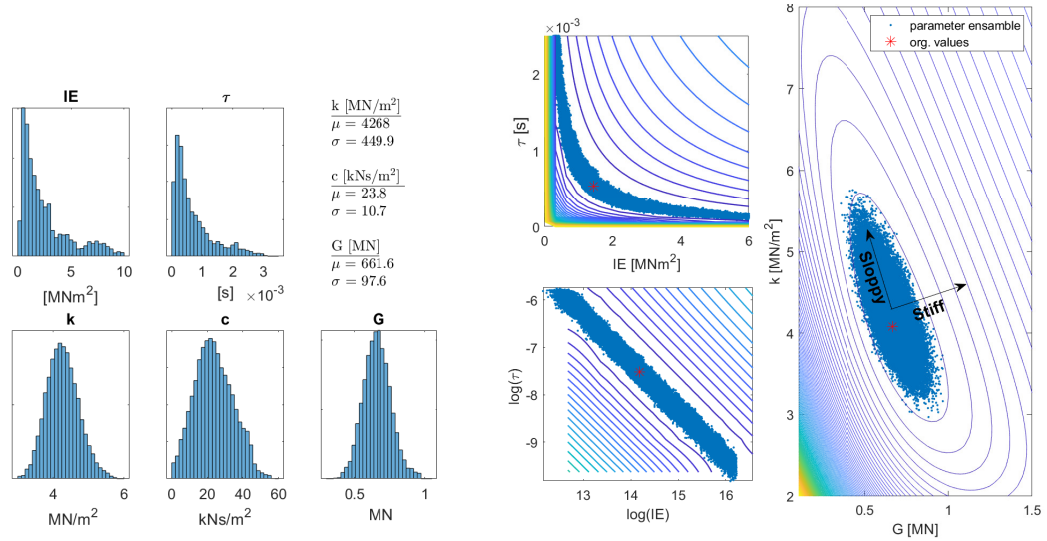
$$T_s = \frac{2C(\theta_0)}{N}, \quad (18.3)$$

where  $N$  is the number of parameters in  $\theta$  (Frederiksen et al., 2004; Tofteskov et al., 2019). The step size in the algorithm was determined by  $\delta\theta_0$ , which was chosen such that the acceptance ratio (number of accepted attempts / number of attempts) was around 0.5 according to recommendation in Tofteskov et al. (2019).

For the analysis, a synthetic set of  $m$  data points ( $w(x, \theta_0)$ ) was generated using the model with initial parameter values listed in table 16.1 plus some white noise. This was done to avoid the algorithm to get stuck in a minimum corresponding to  $\theta_0$ .

The result of the MMC algorithm was an ensemble of parameter value sets, which are seen represented as histograms on figure 18.2a. The foundation parameters ( $k$ ,  $c$  and  $G$ ) was found to be well defined, illustrated by the normal distribution of the parameter ensemble. On the other hand, the beam parameters  $IE$  and  $\tau$  were found to be sloppy, indicated by a skewed distribution of their parameter ensemble (fig. 18.2a). The fact that  $IE$  and  $\tau$  were sloppy, and thus could not well defined as individual parameters, was not surprising when looking at the analytical expression in equation (18.1) and it meant that it was not possible to obtain good estimates of these parameters individually based on a model fit.

The complex modulus of the Maxwell model is given by equation (18.4) where it is



(A) histogram over parameter ensemble accepted in the Metropolis Monte-Carlo algorithm. (B) contour plot over the cost function for the parameter sets  $IE$ - $\tau$  and  $G$ - $k$ . The original parameter values are indicated with a red star.

FIGURE 18.2

clear that  $E$  and  $\tau$  are correlated. When  $k_x$  goes towards small wave numbers the behaviour of the complex modulus is dominated by the term  $-Eiv\tau k_x$ , whereas for large  $k_x$  the behaviour is dominated by  $E$ . In chapter 17, we found that the sensitivity interval was located at low wavelengths and thus only some part of the complex modulus curve was described.

$$E^*(-vk_x) = E \frac{-iv\tau k_x}{1 - ivk_x\tau} \rightarrow \begin{cases} -iv\tau k_x, & \text{if } k_x \text{ small} \\ E, & \text{if } k_x \text{ large} \end{cases} \quad (18.4)$$

The consequence of having a sensitivity interval that only covers some part of the complex modulus curve is that we cannot characterise the entire viscoelastic behaviour of the beam based on one single deflection measurements. As only the part of  $E'$  and  $E''$  within the sensitivity interval affects the pavement response, this is what we can hope to characterise based on a model fit. As equation (18.4) illustrated, if the sensitivity interval e.g. is located at high wave numbers, only information about  $E$  can be obtained.

In order to characterise the entire complex modulus curve, we need several measurements where all but the beam parameters, are hold constant. This could be done by making measurements at different known temperatures and assuming that temperature effects do not affect underlying layers.

Beside  $IE$  and  $\tau$ , the parameters  $k$  and  $G$  were also found to correlate, with stiff and sloppy direction indicated on figure 18.2b. Here it was found that increasing  $G$  while simultaneously decreasing  $k$  had a little effect on the model output (sloppy direction)

---

whereas decreasing (or increasing)  $G$  and  $k$  simultaneously had a big effect on the model output. Thus, a reduced stiffness in the foundation can be compensated for by an increased shear interaction and vice versa. But a decrease/increase in both parameters will affect the pavement response significantly. Furthermore, this was found to be a well defined minimum (closed contour lines).



## **Part V**

# **Comparing pavement response model with TSD data**



## Chapter 19

# Structural rolling resistance from model fit

In the previous part, a simple pavement response model was developed for modelling the pavement response underneath a moving load. In this chapter, results from fitting the model to TSD data was used to calculate the structural rolling resistance. This was done using equation (10.12) derived in chapter 10.

On figure 19.1, a plot of  $C_{SRR}^{model}$  is shown for Måløv data measured at 18°C and 35°C . A similar plot was shown in section 10.2 using the linear interpolation method. Overall the same trends was observed, namely that the structural rolling resistance increased with temperature. A comparison between  $C_{SRR}^{model}$  and  $C_{SRR}^{linear}$  across data groups is shown in table 19.1. In general, calculating SRR using the model fit gives a higher  $C_{SRR}$  for all data groups, with the highest increase in group 1. This supported the main conclusions made in chapter 10, where it was found that the linear interpolation method to a large extent underestimated the SRR for data sets with the maximum closer to the load than the sensor position. However, the relative increase seen in  $C_{SRR}^{model}$  for 35°C was smaller than for 18°C, meaning that linear interpolation method underestimated SRR in data for 18°C to a higher degree than for 35°C .

The difference seen in the accuracy of the SRR values calculated using the linear interpolation method can be explained by the fundamental changed behaviour of the minimum peak with increased road temperature. A set of general guidelines for the connection between the maximum and minimum peak x-position and the accuracy of the linear interpolation method is given by the following:

- If the left side of the maximum is partly resolved and the right hand side of the minimum is fully resolved, the linear interpolation method tends to underestimate the SRR. An example of such a situation is shown in figure 19.2b and was the case for a majority of the data sets measured at 18°C .
- If the right hand side of the minimum is not fully resolved, the linear interpolation overestimates the SRR. An example of such a situation is seen in figure 19.2a.
- In the case where the left side of the maximum and the right hand side of the minimum is resolved by the sensors, the linear interpolation method calculates SRR values similar to the model. An example of such a situation is seen in figure 19.2c.

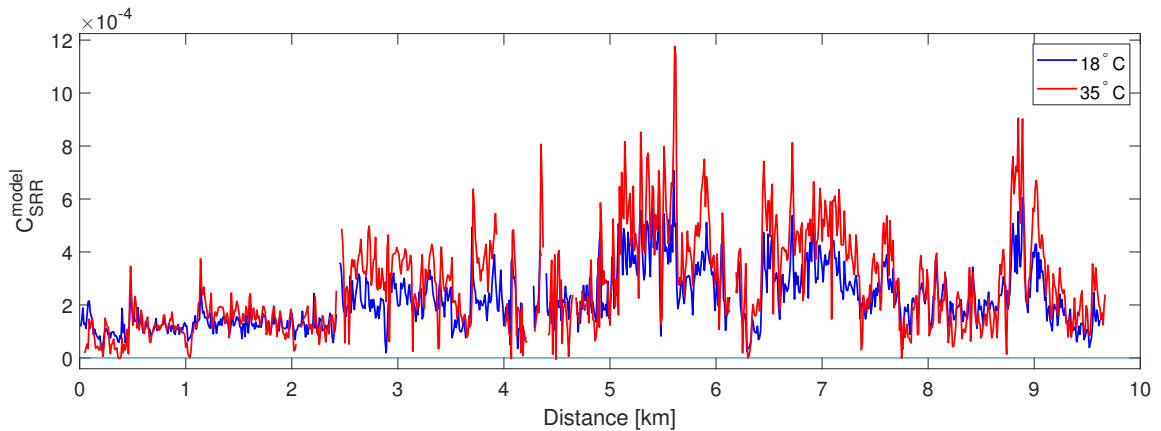


FIGURE 19.1: Structural rolling resistance coefficient calculated using the estimated pavement deflection based on a model fit to data for data series measured at 18°C and 35°C .

In conclusion, in which situations the simple approach provided valid estimates of SRR could be determined based on the qualitatively behaviour of the maximum and minimum deflection slope peaks. It should be stressed, that the two methods provided SRR values within the same order of magnitude. Consequently, the simple approach could be used as a fast method for easily calculating the SRR over large amount of TSD data. If a more accurate estimate is desired, the more sophisticated method using a pavement response model can be applied.

TABLE 19.1: Average values for  $C_{SRR}$  calculated using linear interpolation ( $C_{SRR}^{linear}$ ) and simulated pavement deflection ( $C_{SRR}^{model}$ ) divided into groups.

	$C_{SRR}$ using linear interpolation	$C_{SRR}$ using model fit	$\frac{C_{SRR}^{model} - C_{SRR}^{linear}}{C_{SRR}^{model}}$
Road surface temperature 18 °C			
Group 1	$1.8 \cdot 10^{-4}$	$2.8 \cdot 10^{-4}$	36%
Group 2	$1.2 \cdot 10^{-4}$	$1.6 \cdot 10^{-4}$	25%
Group 3	$0.9 \cdot 10^{-4}$	$1.0 \cdot 10^{-4}$	10%
Road surface temperature 35 °C			
Group 1	$2.9 \cdot 10^{-4}$	$3.5 \cdot 10^{-4}$	17%
Group 2	$1.2 \cdot 10^{-4}$	$1.4 \cdot 10^{-4}$	14%
Group 3	$0.6 \cdot 10^{-4}$	$0.6 \cdot 10^{-4}$	0%



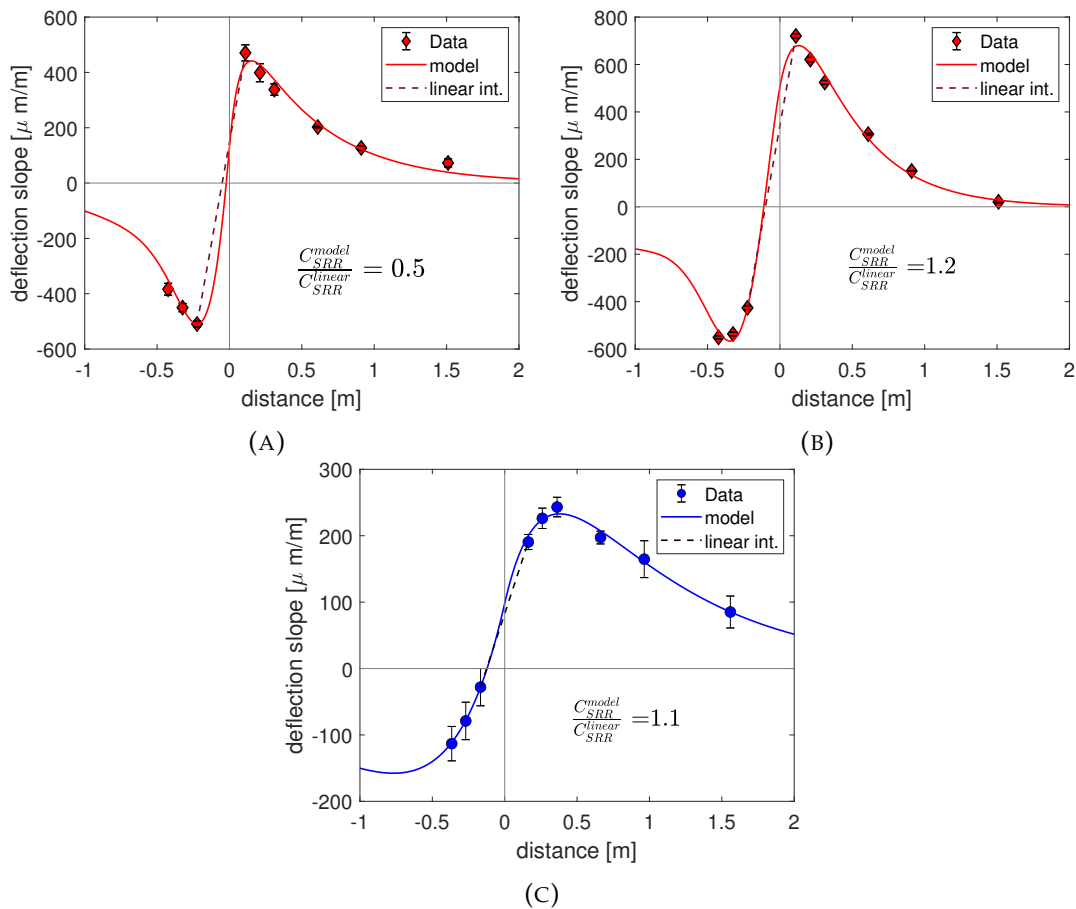


FIGURE 19.2: Exemplary data sets illustrating a deflection slope behaviour where using the linear interpolation method A) overestimates  $C_{SRR}$ , B) underestimates  $C_{SRR}$  and C) gives a similar value compared to using the modelled pavement deflection.



## Chapter 20

# Analysis of pavement characteristics based on model fit to TSD data

In this chapter, we studied what may be inferred about the pavement structure and characteristics from the TSD deflection data. This was done by analysing the results from fitting the simple pavement response model to data measured in Måløv. As the applied pavement response model is a simplified one-dimensional model, this has some limitations which has to be kept in mind when interpreting the estimated parameter values. Nonetheless, the results from fitting the model to data provides useful information about structural changes in the pavement measured on, and how these were expressed through the deflection slope curves.

Overall, the chapter consists of three different analysis, each providing information about pavement characteristics. First, the characteristic behaviour in data resulting in data group division is related to structural properties of the pavement. Secondly, the influence of different sources of damping is studied through a comparison study of different simplified models. The two initial analysis are made based on measurements made at road temperature 18°C . Lastly, the influence of increased road temperature is studied.

### 20.1 Goodness of fit

The pavement response model used to fit data is the one developed in chapter 15, assuming a point load with an fixed magnitude  $F$  of 5 tonnes and a viscoelastic beam modelled by the simple Maxwell model,

$$\hat{w}(k_x, -vk_x) = \frac{F}{IE \frac{-ivk_x\tau}{1-ivk_x\tau} k_x^4 + Gk_x^2 - vcik_x + k}. \quad (20.1)$$

Here  $\hat{w}(k_x, -vk_x)$  is the pavement deflection in the wave number domain,  $E$  and  $\tau$  was the elastic modulus and characteristic time of the Maxwell complex modulus,  $I$  is the second moment of area pr. unit length of the beam,  $G$  is the shear interaction parameter of the foundation and  $k$  and  $c$  are the spring constant per unit length, and viscous damping coefficient per unit length respectively. The free parameters to fit are  $IE$ ,  $\tau$ ,  $k$ ,  $c$ ,  $G$ . The driving velocity  $v$  is measured during the measurements and thus we used the specific driving velocity measured for each data set.

The model was fitted to each data set in the data series, using the fitting algorithm `lsqnonlin` in MATLAB. The fitting procedure found the set of parameter values  $\theta$ , for which the sum of squared residuals  $f(x, \theta)$  is minimised,

$$f(x, \theta) = \sum_{i=1}^N (Y(x_i) - y(x_i, \theta))^2. \quad (20.2)$$

$Y(x_i)$  is the measured deflection slope value in  $x_i$ ,  $y(x_i, \theta)$  is the simulated deflection slope in  $x_i$  using the parameter values  $\theta$  and  $N$  is the number of data points in each data set. In order to evaluate the model fit, we evaluated the *goodness of the fit*. This was done by calculating the  $R^2$  value, which yielded a quantitative way to evaluate how good the model fit is. The  $R^2$  value is given by

$$R^2 = 1 - \frac{f(x, \theta)}{SS_{total}} \quad (20.3)$$

where,

$$SS_{total} = \sum_{i=1}^N (Y(x_i) - \mu(Y(x)))^2. \quad (20.4)$$

Here  $\mu(Y(x_i))$  is the average of all data points in the data set. The  $R^2$  value has the advantage that it takes into account the variance in data, and thus model fit to data sets with large differences in their absolute values can be compared. In the case where the predicted values  $y(x_i, \theta)$  was the same as the data,  $F(x, \theta) = 0$  and thus  $R^2 = 1$ . For big deviations from data,  $R^2$  becomes small. Note that for bad fits, the value can become negative.

On figure 20.1a, a plot of  $R^2$  values calculated for each data set measured at  $18^\circ\text{C}$  is shown. Overall, the simple pavement response model performed well with  $R^2$  values close to 1. For data sets between 0.5-1 km, we found a decrease in  $R^2$ , meaning that the model did not fit data in this area as well as the rest. On figure 20.1b, a plot of measured TSD data and best fit with the model is shown for the data set at 1.04 km. We found that the model in this case, in contrast to the majority of data, was not able to capture the correct shape of the maximum deflection slope.

## 20.2 Estimated parameter values

The result of the model fitting procedure was a set of estimated parameter values obtained for each data set. As the measurements were made on a heterogeneous road segment where the pavement structure and material specific parameters changes, we did not expect the estimated values to be constant over the measured distance. On figure 20.2, a plot of the estimated parameter values as a function of the measured distance is shown. The fitting procedure was made with the constraint that none of the parameters can be negative. For each parameter value, the 95 % confidence interval is shown in a light shaded

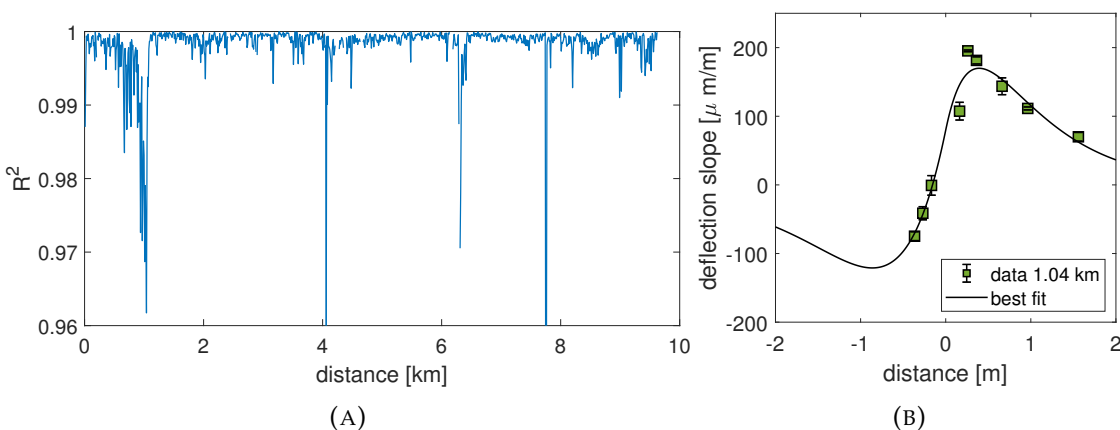


FIGURE 20.1: A) The goodness of fit is evaluated by calculating  $R^2$  for each data set in the data series. Overall the model perform very well in fitting data, however around 0.5-1 km. the fit is worse compared to the rest. B) Example of a data set with lower than average  $R^2$  value,  $R^2 = 0.96$ . The data set is measured at 1.04 km.

color behind the plot.

The estimated values of  $k$  and  $c$  were found to be relative constant over the measured road segment, demonstrated by a narrow normal distribution in the histogram on figure 20.2. With respect to the third foundation parameter  $G$ , a drop in the estimated parameter values was observed around 2.5 km, indicating a shift in the underlying structure of the road. All three parameter values were found to have narrow 95% confidence intervals and thus were well defined.

For the parameter values associated with the beam on the other hand, we found a high spatial variation. Furthermore, they were found to be ill-defined with large confidence intervals, particularly with regard to  $\tau$ . This indicated that they were sloppy, which was expected based on results from the sensitivity analysis. Note that  $\tau$  on figure 20.2 is plotted as  $\log(\tau)$ , as its estimated value spans over several decades.

In figure 20.2, it was observed that the confidence interval of all parameter values increased for data between 0.5-1 km, meaning that the parameter values were less well-defined for data sets in this interval. This was consistent with the  $R^2$  values being lower for this particular road section, indicating an overall bad model fit in this area.

## 20.3 Interpreting data groups based on model results

We will now use the estimated parameter values to characteristic behaviour in data used for data division into groups. This will enable us to connect these qualitatively observations about the deflection slope curve with changing structural characteristics in the pavement.

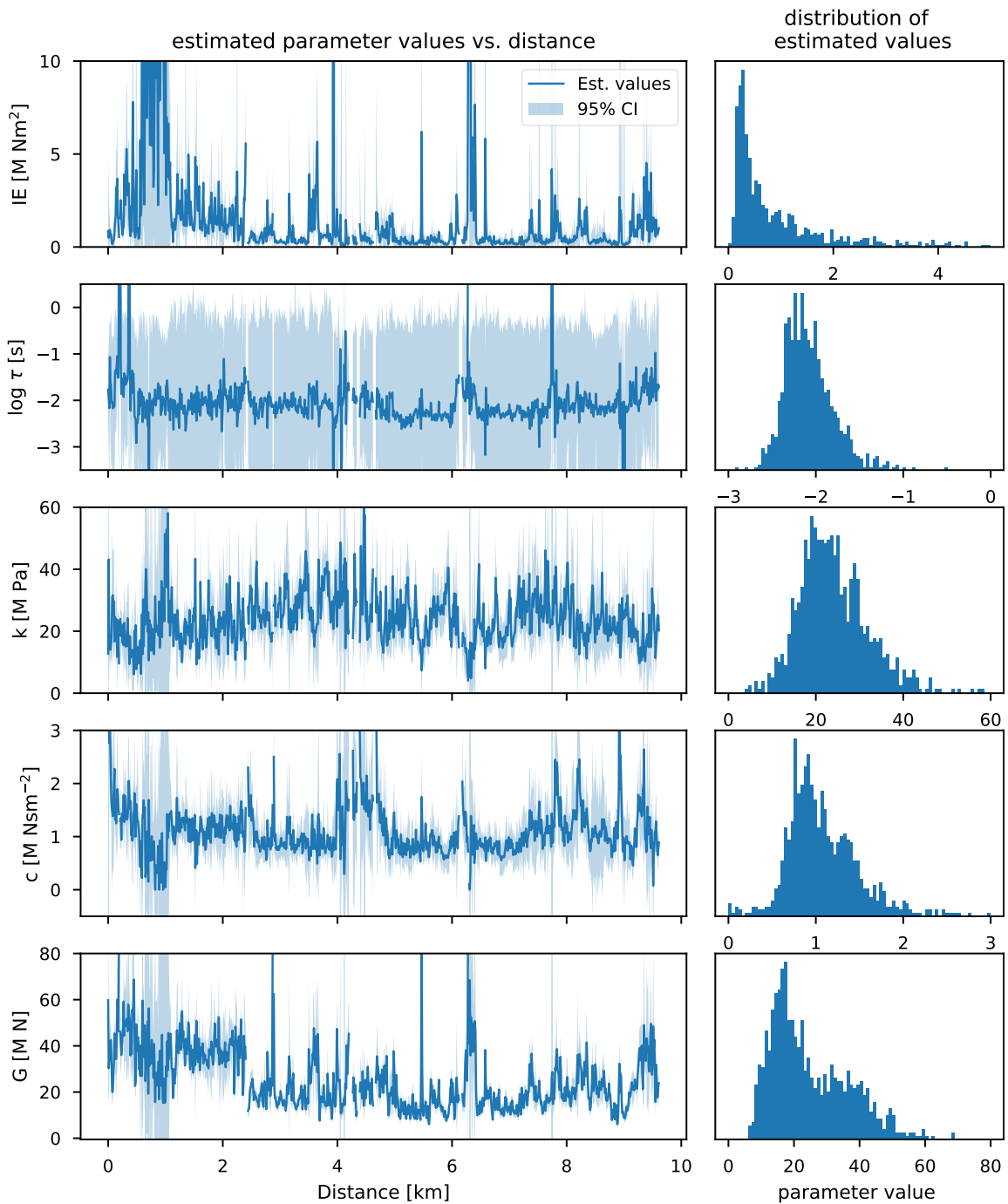


FIGURE 20.2: For each data set a set of best estimated parameter values is obtained. These is illustrated as a function of distance and in the form of a histogram. For each parameter value the 95 % confidence interval is shown in a light shaded color. As the measurements was made on a heterogeneous road segment where the pavement structure and material specific parameters changes, we do not expect the estimated values to be constant over the measured distance. However, a somewhat constant value of  $k$  and  $c$  is found indicating that these do not change much over the measured distance.

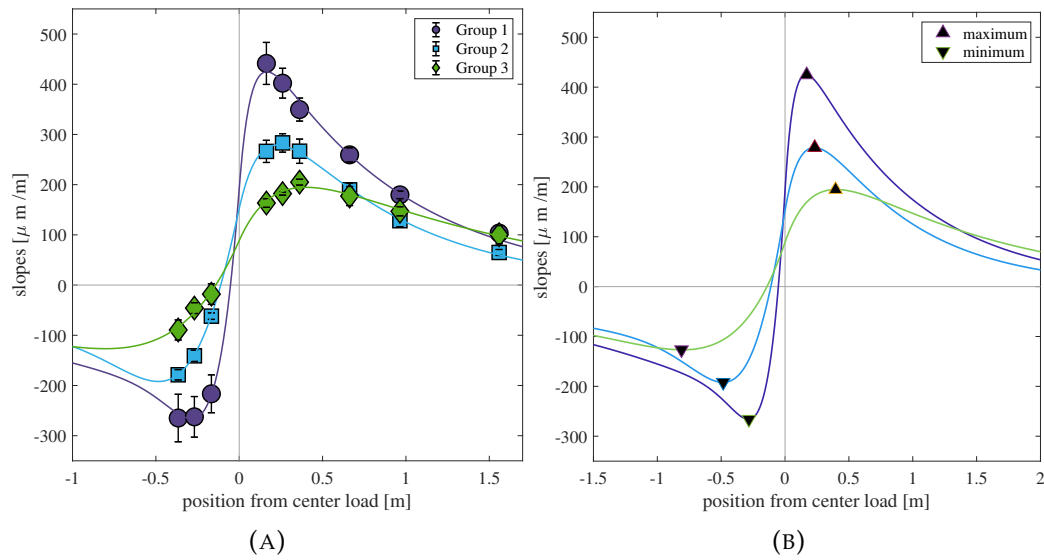


FIGURE 20.3: A) Data was divided into groups based on the x-position of the maximum deflection slope. This is here illustrated for three data sets belonging to each of the groups. B) By fitting the model to data and using the estimated parameter values we obtain a more precise estimate of the location of both the maximum and minimum.

In chapter 9, the TSD measurements was divided into data groups based on two characteristics; the x-position and amplitude of the maximum deflection slope. As this was done based on the three closest sensors in front of the load, the result was a coarse-grained division of the data sets (fig. 20.3a). Through the model fitting procedure, a set of best estimated parameter values were found for each data set and using these, the corresponding deflection slope modelled. Through this, a higher resolution of the maximum and minimum and its characteristic behaviour across groups was found and analysed (fig. 20.3b).

### 20.3.1 Division based on x-position of the maximum deflection slope

The way a pavement behaves underneath a moving load is highly influenced by the relative stiffness between the layers. In a simple two layer model like ours, this is given by the relation between foundation stiffness  $k$  and beam flexural rigidity  $IE$ . In section 15.1, this relationship was found for the simple case of an elastic beam on an elastic foundation and the characteristic length scale found to be given by

$$\kappa = \frac{1}{2} \left( \frac{k}{EI} \right)^{1/4}. \quad (20.5)$$

Even though this result was derived for an idealized model, the idea that the deflection basin is characterised through the relative stiffness is still applicable to a more complex pavement structure. On figure 20.4, the estimated  $\frac{k}{EI}$  values and the maximum x-position

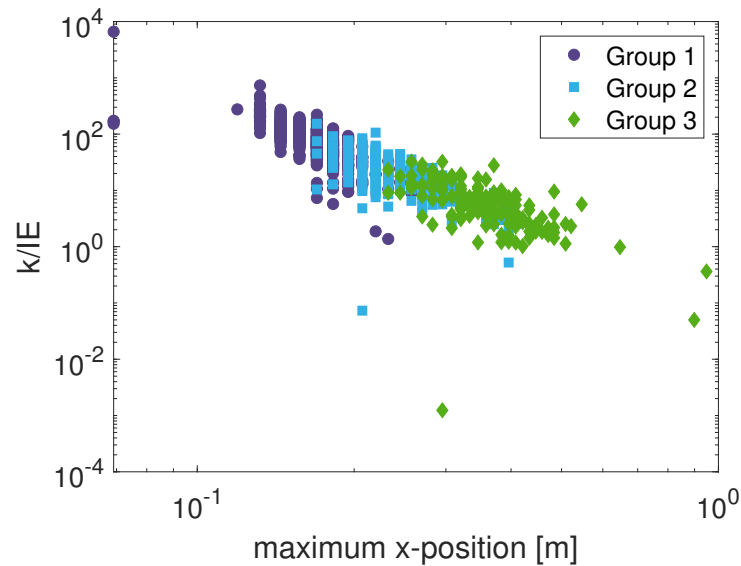


FIGURE 20.4: Logarithmic plot of the relative stiffness  $k/IE$  estimated for each data set as a function of the x-position of the maximum deflection slope. The different data groups 1, 2 and 3 is indicated with different markers and color. Best linear fit is given by  $\log(y) = -3.5\log(x) - 0.9$ . As the simulated deflection slope consist of discrete elements, the maximum x-position is not distributed continuously but in discrete interval as shown. This behaviour becomes clear when using a logarithmic axis and is not notable on a linear axis.

for each data set is shown to correlate on a log-log scale. Consequently, movement of the x-position of the maximum was highly correlated with a change in the relative stiffness  $\frac{k}{IE}$  between the layers. If we assume that the foundation stiffness is constant, which was supported by the estimated values of  $k$  in figure 20.2, the change in relative stiffness seen for this road section is due to changing properties of the top layer.

In conclusion, the movement of the x-position observed in data is correlated with changing properties of the top layer. Two physical explanations of the changing properties are either a change in the type of asphalt mix used on the measured road segment, or that the thickness of the asphalt layer varies. In the model, the asphalt thickens ( $h$ ) is correlated with the flexural rigidity of the beam as  $EI = E(\frac{1}{12}h^3)$ . Consequently, an increase in  $EI$  can be due to either an increase in elastic modulus  $E$  of the asphalt mix or the thickness  $h$ . Based on the data presented here, we were not able to distinguish further between the two effects, but only conclude that the changes observed in the x-position of the maximum slope were caused by changes in the asphalt layers flexural rigidity.

### 20.3.2 Division based on amplitude of maximum deflection slope

The second way the measurements were divided, was based on the amplitude of the maximum deflection. Correlations between the amplitude of the maximum deflection



slope and the estimated parameter values were investigated by both visual inspection (fig. 20.5a and 20.5b) and computing the correlation matrix (tab. 20.1).

The method used to find the correlation matrix here was the *Pearson correlation coefficient*, PCC (Kellermann, 2009), which provided a matrix where each element described the strength of the linear relationship between two variables  $x$  and  $y$ . It is defined as

$$PCC = \frac{cov(x, y)}{(\sigma(X)\sigma(Y))}, \quad (20.6)$$

$$cov(x, y) = \frac{1}{n} \sum_{i=1}^n (x_i - \mu(X)) \cdot (y_i - \mu(Y)), \quad (20.7)$$

where  $n$  is the number of estimated parameter values,  $cov(x, y)$  is the covariance between  $x$  and  $y$ ,  $\sigma(x)$  is the standard deviation of  $x$  and  $\mu(x)$  is the mean value of  $x$ .

A strong negative correlation between the estimated values of shear parameter  $G$  and the amplitude of the maximum deflection slope was found (fig. 20.5a). This meant that decreasing the value of  $G$  resulted in an increase in the amplitude of the maximum (corresponding to going from group A to C). Furthermore, a correlation between  $IE$  and the amplitude was found (PCC=-0.86) and a weak correlation between  $G$  and  $EI$  was observed (PCC=0.72). In our model, the flexural rigidity of the beam and the shear interaction layer had some of the same functions, as they both facilitated a distribution of the load over several foundation elements, resulting in a broadening of the deflection basin. Consequently, their influence on the pavement deflection is to some degree the same.

When analysing deflection slope data, we found that a significant shift in the amplitude was observed around 2.5 km. This correlated with a drop in the estimated  $G$  value, as shown on figure 20.6. Consequently, we can conclude that a shift in the underlying foundation structure took place around 2.5 km., resulting in a significantly higher maximum amplitude in data sets located after the shift.

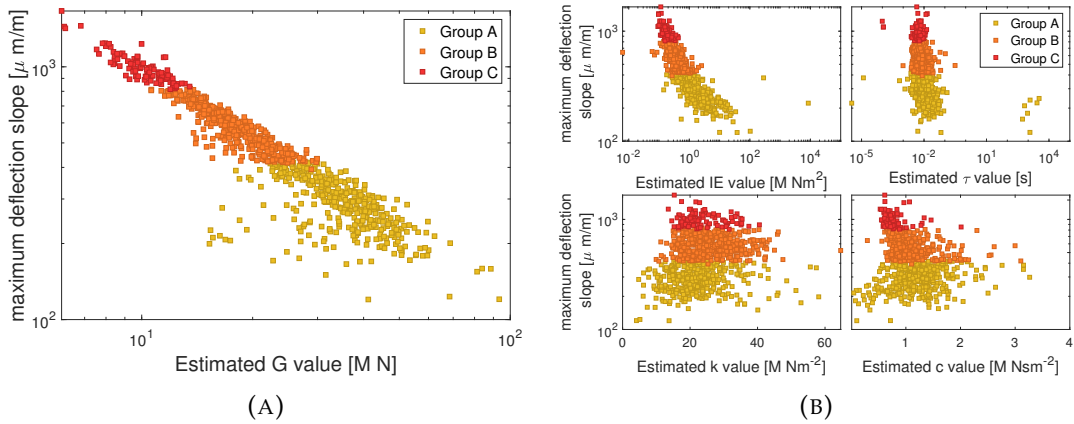


FIGURE 20.5: Correlation between the amplitude of the maximum deflection slope and A) shear interaction parameter G and B) all other parameters. A clear log-log correlation is found between the amplitude and G, while a correlation to a smaller degree is also seen for IE. k, c and  $\tau$  is found not to correlate with the amplitude. The different data groups is indicated by color.

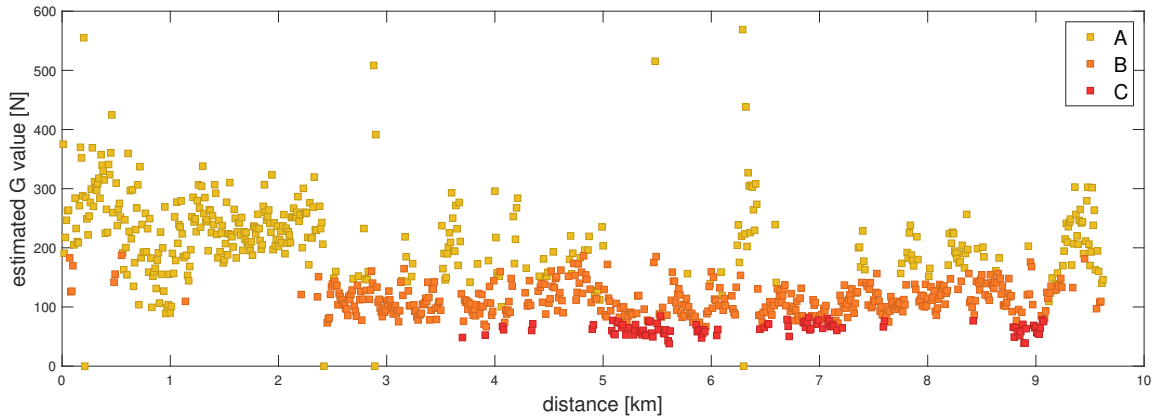


FIGURE 20.6: Estimated values of G is plotted as a function of distance and the different groups A, B and C is indicated with color. A shift in estimated G value is seen around 2.5 km, where previous to this point the most dominating data group is A (lowest amplitude).

TABLE 20.1: Correlation matrix for the estimated parameter values and the amplitude of the maximum deflection slope. Each element in the matrix describes the strength of the linear relationship between two variables  $x$  and  $y$ , and denotes the Pearson correlation coefficient PCC for the two variables. PCC= 1 or PCC= -1 means that there are a strong positive or negative linear correlation between the two parameters, whereas PCC=0 means that no linear correlation exist. The closer to -1 or 1 the estimated PCC value is, the stronger a correlation exist. Note that the correlation matrix is symmetric.

	amplitude	IE	tau	k	c	G
amplitude	1.00	-0.86	-0.34	0.21	0.14	-0.92
IE	-0.86	1.00	0.11	-0.30	-0.27	0.72
$\tau$	-0.34	0.11	1.00	-0.10	0.01	0.27
k	0.21	-0.30	-0.10	1.00	-0.05	-0.40
c	0.14	-0.27	0.01	-0.05	1.00	0.08
G	-0.92	0.72	0.27	-0.39	0.08	1.00

## 20.4 Comparison of different simplified models

The model used to fit data (eq. 20.1) contains two sources of damping; in the foundation and in the top layer. An analysis of the impact different sources of damping have on the models ability to fit data was performed by comparing four different variations of the model, sketched on figure 20.7. This included a full viscoelastic pavement (damping in top layer and foundation), an elastic beam on a damped foundation, a viscoelastic beam on an elastic foundation and a purely elastic pavement. As the model variants contains different amounts of free parameters, the goodness of fit (eq. (20.3)) was calculated using the weighted sum of squares  $f_w(x, \theta)$ . This is given by

$$f_w(x, \theta) = \frac{\sum_{i=1}^N (Y(x_i) - y(x_i, \theta))^2}{N - n}, \quad (20.8)$$

where  $N$  is the number of data points, and  $n$  is the number of free parameters in the model.

Comparison of the goodness of fit for these four models reveal if any damping parameters are insignificant with respect to fitting the data, given by no change between fitting the full model and a reduced one. If this is the case, it implies that this particular source of damping dis not influence the pavement response and can be neglected.

On figure 20.8, a plot of the weighted  $R^2$  values obtained for each variation of the model are shown. The values of  $R^2$  is ordered from highest (best fit) to lowest (worst fit), such that it is easier to see the difference between the models. This means that we are not comparing the models with respect to each data set, but for the entire data series as a whole. A general behaviour for all four models was that a steep decrease in  $R^2$  was seen

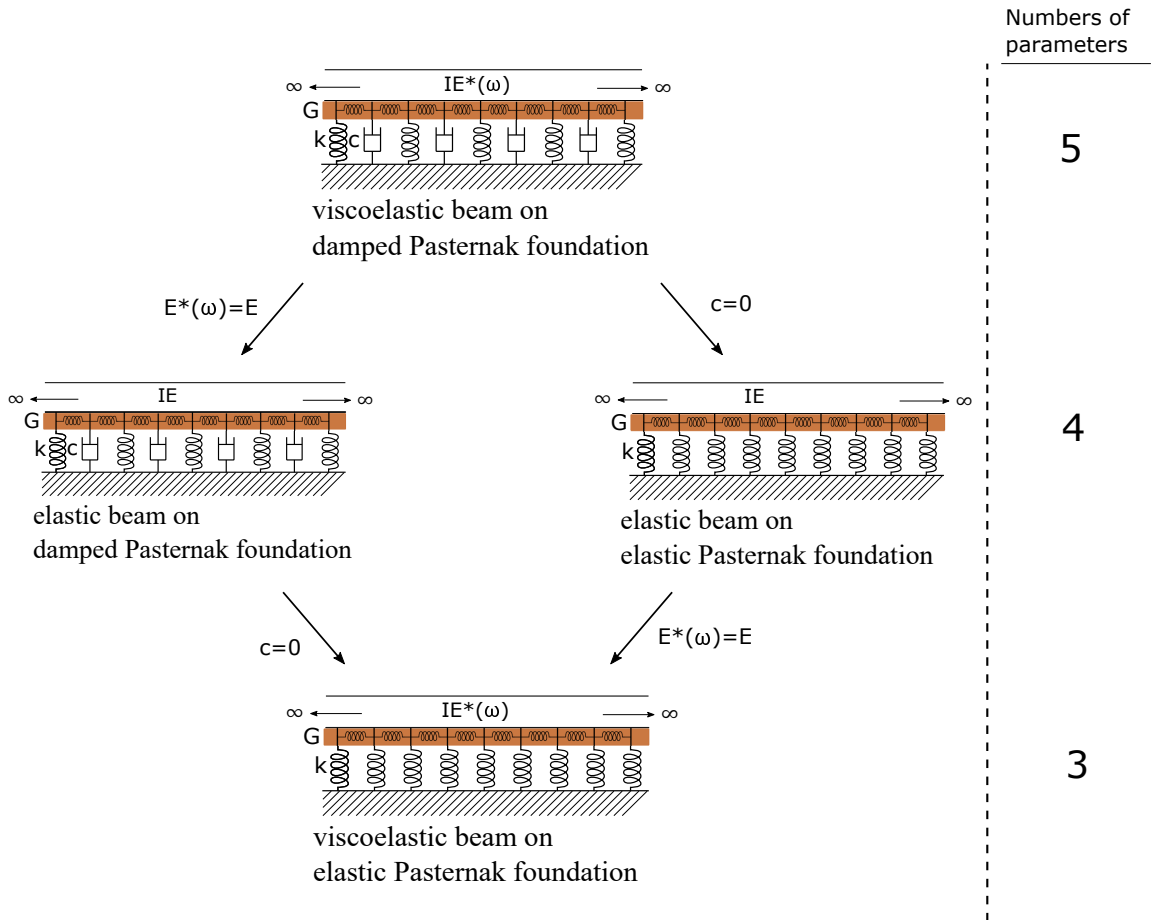


FIGURE 20.7: Sketch of the four different variations of the model used in this comparison study. From the top we have a full viscoelastic pavement (damping in top layer and foundation), a viscoelastic beam on an elastic foundation, an elastic beam on a damped foundation, and a purely elastic pavement.

in the end. This was due to the area of the road where the model yielded an overall bad fit and thus a lower  $R^2$  value. This indicated that the underlying reasons for the bad model fit in this area was not connected to the damping parameters, but probably originated from a more fundamental issue with the model.

As expected, we found that the full model provided the highest weighted  $R^2$  values, even when corrected for degrees of freedom. Comparing the model with no damping in the foundation (green) and the model with no damping in the beam (red) showed a clear trend that removing damping in the foundation resulted in a lower  $R^2$  value compared to if we removed damping in the beam. This indicated that for this specific data set, foundation damping was the most important source of damping. Damping in the top layer was, however, not insignificant as there were a difference between the elastic beam model and the fully viscoelastic model.

We now consider how beam and foundation damping affect the goodness of fit within different data groups. On figure 20.9, a plot of the ordered  $R^2$  values for the full model and the two variants with one damping component are shown for data sets belonging to the different groups. From this plot, a big difference in how removing damping elements influenced the weighted  $R^2$  value across groups was found. Comparing group 1, 2 and 3 revealed that beam damping had an increasing influence when the maximum moved further away from the load. This movement corresponded to a decrease in relative stiffness of the pavement and, as the foundation stiffness is found to be constant, correspondingly, an increase in flexural rigidity of the beam. Due to the fact that increased stiffness was accompanied with an increased beam damping, we predicted that the sensitivity interval with respect to  $E^*(-vk_x)$  was located at the left side of the loss peak. Consequently, when the stiffness decreased, so did the damping and an almost elastic beam behaviour was seen (group 1). A similar behaviour was seen comparing group A, B and C. Group A was characterised by having a low maximum amplitude and correlated with having a high shear interaction parameter  $G$ .

Lastly, figure 20.9 provided information about under which pavement conditions the model performed the best. By comparing the weighted  $R^2$  values for the full model across groups, we found that group 3 and A had the lowest values. This indicated that an increased influence of beam damping and a high  $G$  value resulted in a deterioration of the goodness of fit. We speculated, that the choice of the simple Maxwell model for the top layer complex modulus in these cases was insufficient to properly describe the viscoelastic behaviour and as a result, the models ability to mimic data declined.

## 20.5 Effect of increased road temperature

We will now discuss what influence increased road temperatures have on the pavement deflection behaviour and estimated parameters. This was done by comparing results from fitting the model to data measured in Måløv at  $18^\circ\text{C}$  and  $35^\circ\text{C}$ . In figure 20.10, an comparison of the goodness of fit was made for the two road temperatures. Overall, the model

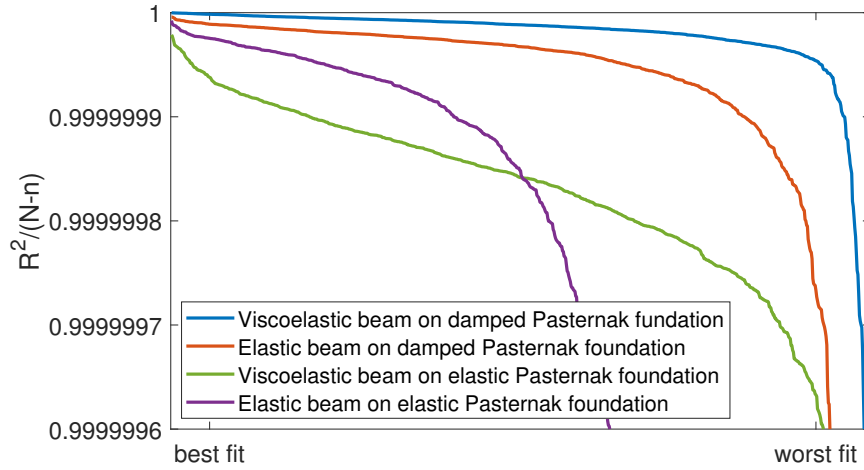


FIGURE 20.8: Comparison of models with different degrees of damping. The weighted  $R^2$  value is calculated for each data fit and plotted on a ordered x-axis. The very small difference in absolute numbers on the y-axis is due to the residuals being normalized with the degree of freedom for each model.

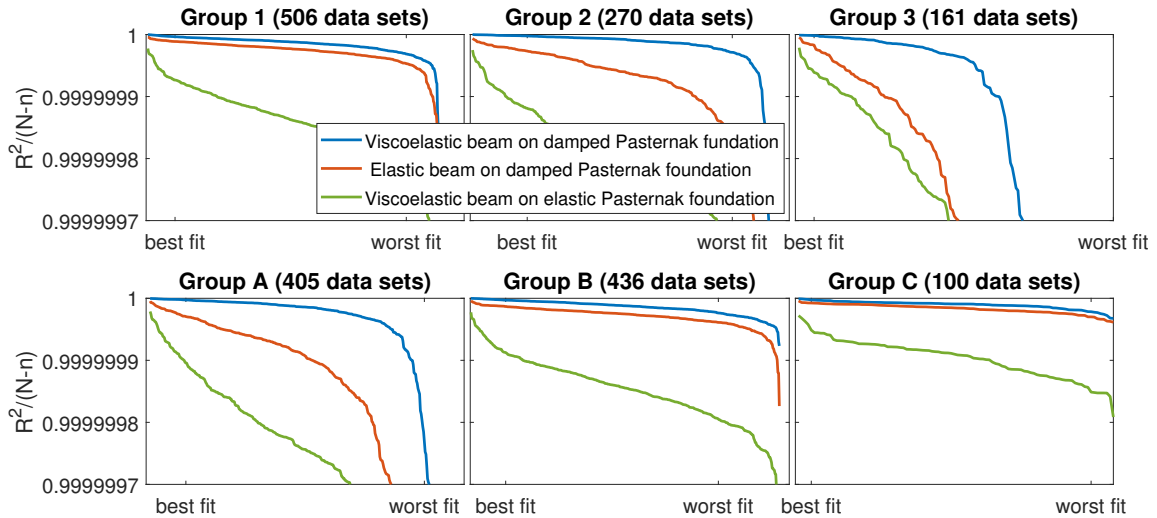


FIGURE 20.9: Weighted  $R^2$  value divided into groups for the full model and the two simplified versions with damping in the beam and foundation respectively. The number of data sets in each group is listed in parentheses above each figure. Note that the total amount of data sets within the two types of group divisions is not the same, as a few data sets had to large standard deviations in sensors in front of the load to categorise them based on the maximum peak. The very small difference in absolute numbers on the y-axis is due to the residuals being normalized with the degree of freedom for each model.

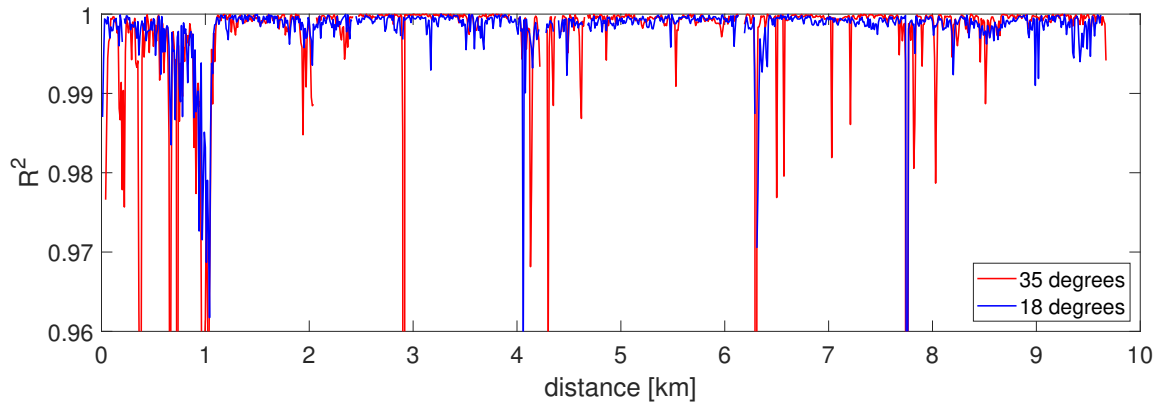


FIGURE 20.10: Goodness of fit given by the  $R^2$  value for each data set under  $18^\circ\text{C}$  and  $35^\circ\text{C}$ . Overall, the model performs well also under high road temperatures with  $R^2$  values well above 0.99. An exception is the area between 0.5-1 km., as well as spatial low values distributed over the road segment.

performs well also under high road temperatures with  $R^2$  values well above 0.99. Similar to the situation at colder road temperature, the area between 0.5-1 km has relatively low  $R^2$  values. Furthermore, for the warm data series an increased amount of data sets with low  $R^2$  was observed, spread out over the measured distance. This suggests that the overall model fit was slightly poorer for  $35^\circ\text{C}$  compared to  $18^\circ\text{C}$ .

Through visual inspection, a fundamental difference in the deflection slope behaviour resulting in low  $R^2$  values was observed before and after 1 km. For data sets located before 1 km., the low  $R^2$  values arose from the model not being able to mimic the behaviour in the maximum as illustrated on figure 20.11a. For data sets above 1 km on the other hand, the low  $R^2$  value was due to a change in the minimum deflection slope behaviour is seen when temperature is increased, resulting in both the maximum and minimum peak not being captured by the data points (fig. 20.11b). However, it should be stressed that with  $R^2$  values well above 0.9, the model performs well for both  $35^\circ\text{C}$  and  $18^\circ\text{C}$ .

The behaviour observed in 20.11b indicated that the fundamental assumption of a stiff and incompressible top layer was not valid. In this situation, the top layer will also deform in addition to the foundation (sketched in fig. 20.12). As a consequence, the top layer does not behave as an undeformable Euler-Bernoulli beam, but rather like a deformable elastic medium.

The idealized case where the pavement is described as a purely elastic half-space subject to a point load is given by the Boussinesq problem (Verruijt, 2010). In this case, the pavement deformation  $w_B(x)$  is given by

$$w_B(x) \sim A \frac{1}{|x|}, \quad (20.9)$$

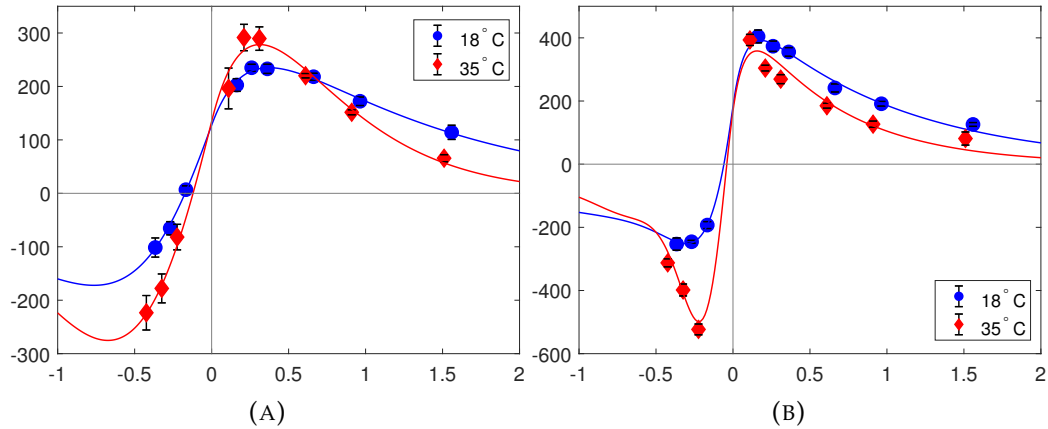


FIGURE 20.11: A) data set representing the deflection slope behaviour for data sets before 1 km. This particular data set is measured at 0.77 km and has  $R_{35^{\circ}\text{C}}^2 = 0.992$  and  $R_{18^{\circ}\text{C}}^2 = 0.999$ . B) Data set representing the general behaviour in data sets located after 1 km. and having a low  $R^2$  value. Here the minimum deflection slope at  $35^{\circ}\text{C}$  changes shape such that both the maximum and minimum peak is unresolved. This particular data set is measured at 8.51 km and has  $R_{35^{\circ}\text{C}}^2 = 0.989$  and  $R_{18^{\circ}\text{C}}^2 = 0.998$ .

where  $A$  is a constant consistent of material constants and the applied load. The Boussinesq solution is an idealized situation and not applicable to realistic modelling of the overall pavement. However, it provides an explanation for the behaviour seen in the pavement close to the load. Imagine that the top layer of a pavement is acting as an elastic half-space and as a result, the pavement deflection at small wavelengths, thus close to the load, is governed by this behaviour. Consequently, an reciprocal behaviour will occur close to the load.

On figure 20.13, a plot of the function  $\frac{dw_B(x)}{dx}$  is seen together with a data set at  $18^{\circ}\text{C}$  and  $35^{\circ}\text{C}$ , the best fitted deflection slope curve and the associated deflection basin. This illustrated how the shift in behaviour seen in data under warm conditions in fact agrees with a reciprocal behaviour close to the load, and thus implied that in order for the model to be able to mimic this behaviour in data, a deformable top layer should be considered.

### 20.5.1 Influence of temperature on estimated parameters

A comparison between estimated parameters from fitting the model to data for  $18^{\circ}\text{C}$  and  $35^{\circ}\text{C}$  is seen on figure 20.14. In section 9.1.3, the qualitatively effect of temperature on the measured deflection slope behaviour was evaluated. It was observed that the maximum and minimum deflection slopes, in general, were shifted towards the load when temperature increased, as well as getting an increased amplitude. Based on the analysis made in section 20.3, this corresponded to an increased relative stiffness of the pavement. Furthermore, analysis of data at  $18^{\circ}\text{C}$  indicated that the sensitivity interval for  $E^*(-vk_x)$  was located at the left side of the loss peak and as a result, we predicted that increased



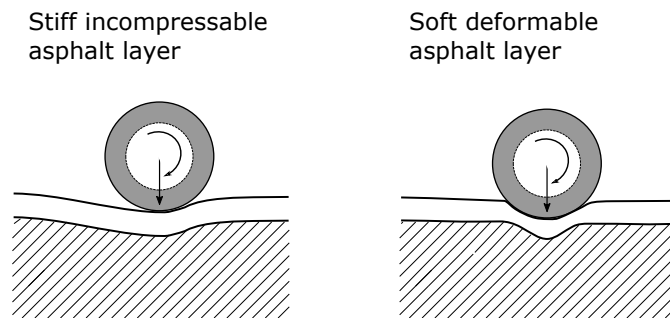


FIGURE 20.12: A fundamental assumption behind modeling the asphalt layer as an Euler-Bernoulli beam is that its cross section do not deform, thus it acts as a stiff incompressible layer which distributes the load (left). This assumption breaks down then the top layer gets to soft and as a result, the layer deforms locally around the load (right).

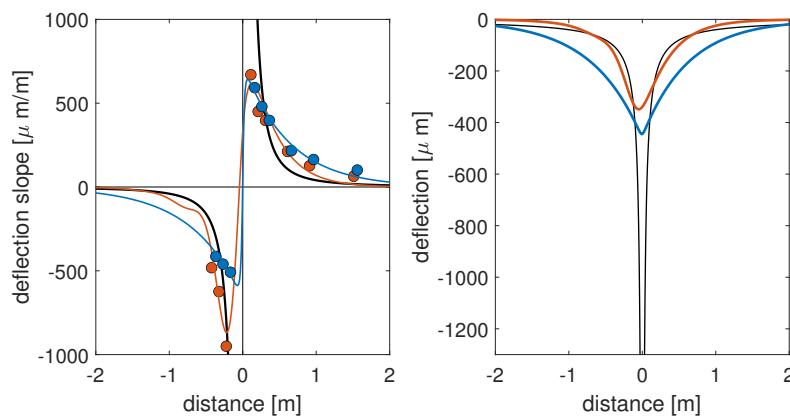


FIGURE 20.13: Illustration of how the pavement response close to the load goes towards a  $1/|x|$  behaviour when temperature increases. On the plot is on the right the function  $w(x) = 15\frac{1}{x}$  together with simulated deflection basin associated to the data sets. On the left is  $\frac{dw(x)}{dx}$ , data set at  $18^\circ\text{C}$  (blue) and  $35^\circ\text{C}$  (red) and the best fitted deflection slope curve.

temperature will result in less beam damping.

Based on the model fit, we found that  $EI$  varied a lot over the measured distance and was found to be more ill-defined than in the case of  $18^\circ\text{C}$ , indicated by high confident intervals. On the other hand,  $\tau$  was more well-defined with a more narrow confident interval and was found to decrease compared to  $18^\circ\text{C}$ . This behaviour in  $\tau$  meant that the characteristic time of the asphalt mix (given by  $1/\tau$ ) increased with temperature and, as a result, the sensitivity interval with respect to  $E^*(-vk_x)$  moved towards the lower elastic plateau. This behaviour with increased temperature was consistent with the behaviour predicted in chapter 17.

Road temperature changes is expected primarily to affect the top layer, and consequently we did not expect the foundation parameters to change between the two measurements. However, a small increase in the estimated value for  $k$  was found and furthermore,  $G$  was found to be much more ill-defined with large confident intervals compared to estimates for  $18^\circ\text{C}$ . The sensitivity analysis in chapter 18 showed that the parameters  $k$  and  $G$  are correlated such that increasing  $k$  and decreasing  $G$  simultaneously does not affect the model output. This might explain the small change observed. With respect to the foundation damping  $c$ , no significant change was seen overall. In some places however, the estimated value was very low, indicating that the foundation was almost purely elastic there. These data sets were not found to have a spatial trend and thus it was not one particular place on the road that behaved like this.

## 20.6 The models limitations to fit data

From figure 20.1a and 20.10, we found that the model was bad at fitting data sets located between 0.5-1 km., resulting in lower  $R^2$  values compared to rest of the road segment. By visual inspection of these deflection slope data, we found that they all had a well defined maximum, meaning that both the right and left hand sides of the maximum was captured by the sensors (fig. 20.1b). Furthermore, the maximum peak had a pointy shape whose behaviour could not be mimicked by the model.

By visual inspection of the road, we did not find any obvious visual signs on damaged asphalt or other external features which explained the changes in  $R^2$ . Furthermore, data sets in this area did not stand out compared to surrounding data sets when looking at the measured slope signals (fig. 9.2). Thus, we expected the bad fit to be due to some underlying model assumptions which were invalid for the given road section. Two potential explanations for the bad model fit was proposed below.

The first potential reason is the choice of viscoelastic model in the beam. All data sets with low  $R^2$  values belonged to group 2 and 3, for which beam damping had an increased effect compared to the rest of the data. Consequently, the choice of complex modulus model for the beam had a higher impact on the model fit in this groups. For the given model used to fit data, a simple Maxwell model was used to describe the viscoelastic

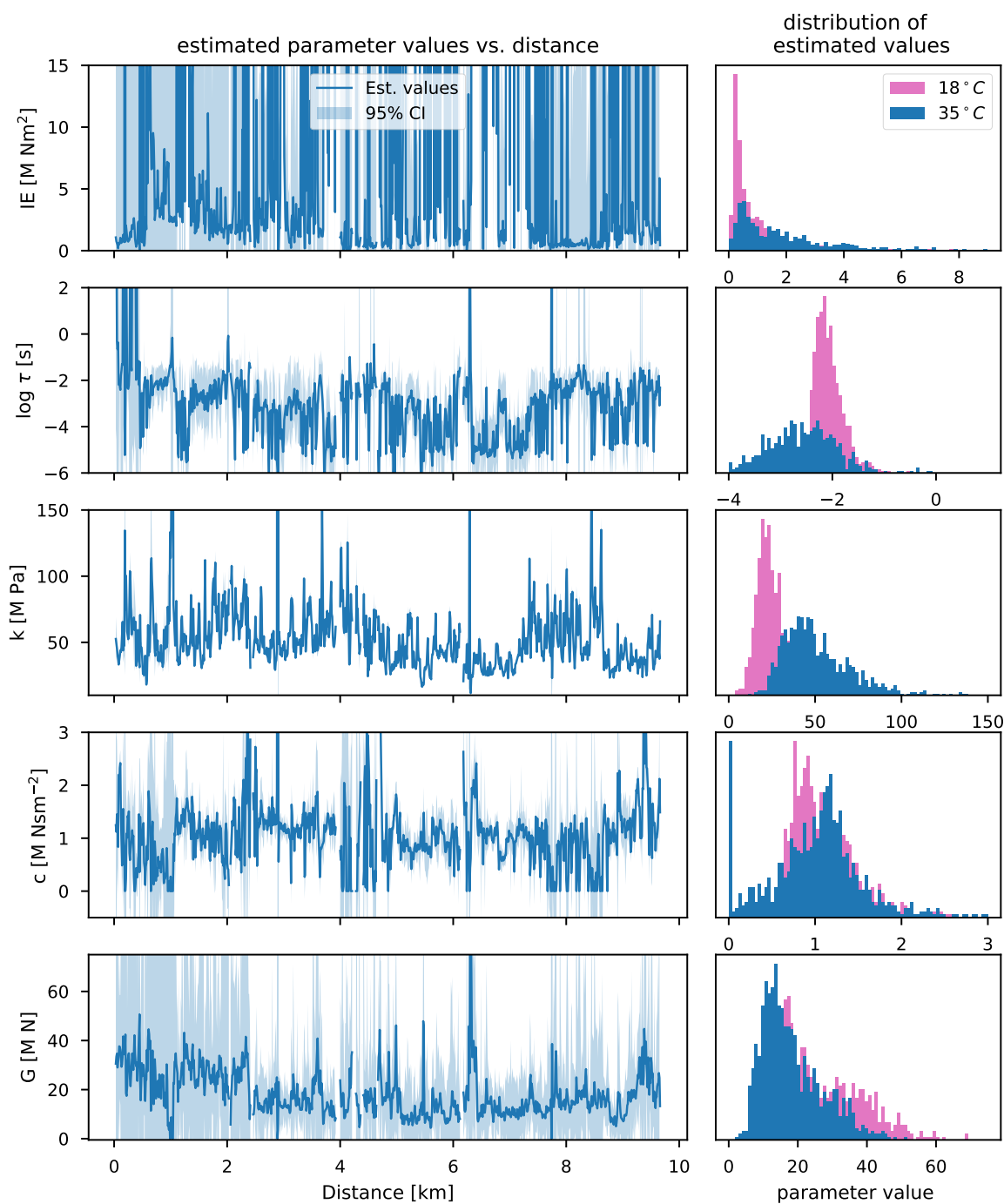


FIGURE 20.14: Estimated parameter values from model fit to data sets measured in Måløv with road temperature at 35°C . Note that the value of  $\tau$  is given as a logarithmic value as the spread is over multiple decades. The 95% confident interval is plotted with light gray color behind the estimated parameter value. In order to compare estimated values with those from 18°C , these are plotted on the histograms with pink color.

behaviour of the beam. However, this might be too simple and thus result in a bad model fit.

Another potential reason for the bad model fit has to do with the underlying assumption behind the use of a beam model. As the asphalt layer was modelled as an Euler-Bernoulli beam, it was assumed to not deform in the vertical direction. This corresponded to the assumption that the asphalt layer was so stiff that all deformation of the pavement was happening in the underlying layers. However, if this assumption does not hold and the top layer experiences some deformation as well, the model assumption breaks down and cannot describe the pavement response accurately.

## 20.7 Summarising discussion

Through analysis of the estimated parameter values obtained from fitting the pavement response model to data at 18°C and 35°C, we have derived information about structural changes in the pavement measured on. In data, a change in x-position and amplitude of the maximum deflection slope was used to divide measurements into data groups. The movement of the x-position was correlated with a change in relative stiffness between the top layer and the foundation. As the foundation stiffness was found to be constant in the measured road segment, this indicated that the top layer properties changed. An increase in top layer stiffness was manifested in the pavement deflection by a broad and shallow deflection basin. In addition, by analysing the amplitudes of the maximum deflection we concluded that a shift in the underlying foundation structure took place around 2.5 km, resulting in a significantly higher maximum amplitude in data sets located after the shift.

By comparing different simplified versions of the model, we found that, overall, foundation damping was the most dominating source of damping in the road section measured on. In some data groups, we found that the beam damping had an increasing effect on the model fit. This was found in data sets characterised by a relatively high flexural rigidity of the beam as well as a high G value. For data sets belonging to these data groups, the choice of complex modulus has to be reconsidered as the Maxwell model might be too simple to properly describe the viscoelastic behaviour.

Finally, the effect of increased road temperature on the pavement response was studied. It was found to affect the top layer, making it behave more soft and elastic which was shown in the deflection slope curve with the maximum and minimum moving close to the load. In the most extreme cases, the model failed to mimic the behaviour and a bad fit is obtained. We hypothesise that the validity of assuming a stiff in-compressible top layer breaks down in these cases, and propose that a deformable top layer should be considered in order to fit these data sets better. However, it should be stressed that for both the cold and warm data series, the model overall performed well with  $R^2$  values close to 1.

## Chapter 21

# Characterising pavement damping based on TSD data at different temperatures and driving velocities

In this chapter, we exploited that we have TSD measurements at different velocity and temperature configurations (Finland data), which allow us to characterise both the foundation and top layer damping behaviour. As in chapter 20, the developed pavement response model (eq. (20.1)) was fitted to data and the resulting best estimated parameters were analysed. Three separate analyses were performed based on the model fit results. First, the influence of velocity and temperature on the pavement deflection basin was studied as well as the estimated parameters.

Secondly, the viscoelastic behaviour of the top layer was characterised by creating an asphalt complex modulus master curve. The creation of these master curves is used in pavement design and management as a tool to characterise the viscoelastic properties of the asphalt material (Gopalakrishnam et al., 2014). These master curves are traditionally made based on laboratory test. However, the process involves a lot of work and thus is a time consuming task. Furthermore, it requires a sample of the asphalt mix. As a result, there is an interest in developing procedures for testing the viscous behaviour of asphalt using nondestructive in-situ measurement techniques. A pilot study presenting a procedure for developing such curves based on TSD data is presented in section 21.2.

Lastly, the foundation damping was characterised by using the velocity dependence in data and the used damping model is evaluated in section 21.3.

### 21.1 How velocity and temperature influence the pavement deflection

The data set analysed in this chapter consisted of pavement deflection slope measurements at five different driving velocities and two different temperatures. In section 9.2, decreased velocity was found to increase the amplitude of both maximum and minimum deflection slope, as well as move the minimum closer to the load. Using the best estimated parameter values, the associated deflection basins for measurements at different velocities were modelled on figure 21.1a. We found that the maximum deflection decreased when

driving velocity increased. The same behaviour was seen for a decrease in temperature (fig. 21.1b), where the changes in the deflection basin with temperature was largest for low driving velocities.

Comparing figure 21.1a and 21.1b showed that while a change in driving velocity only influenced the deflection behaviour close to the load, a change in temperature influenced the overall shape of the deflection. A physical interpretation of this was that velocity mainly influence the top layer, thus affecting the behaviour close to the load, whereas temperature affected both the top and foundation and thus affected the overall deflection. In chapter 17, the influence of decreased driving velocity and increased temperature on the viscoelastic behaviour of the top layer, were predicted to shift the sensitivity interval to lower frequency, resulting in a softer top layer behaviour. The fact that the maximum deflection moved closer to the load, indicating a decrease in damping, demonstrated that the sensitivity interval was located on the left side of the loss peak.

### 21.1.1 Estimated parameters

Through the model fit, a set of best estimated parameter values were obtained. An overview of these as a function of velocity is seen on figure 21.2 for location 1 and 2. Here the measurements at daytime ( $22/24^{\circ}\text{C}$ ) is illustrated with red markers and nighttime ( $14^{\circ}\text{C}$ ) with blue markers. As we were measuring on the same location, we expected the foundation parameters to be constant, as these are not expected to be affected by velocity or temperature. We found that this was true for the parameter  $k$  and  $G$ , but not for  $c$ . This is discussed in detail in section 21.3. The estimated beam parameters is used in section 21.2 to develop a master curve describing the viscoelastic behaviour of the asphalt layer.

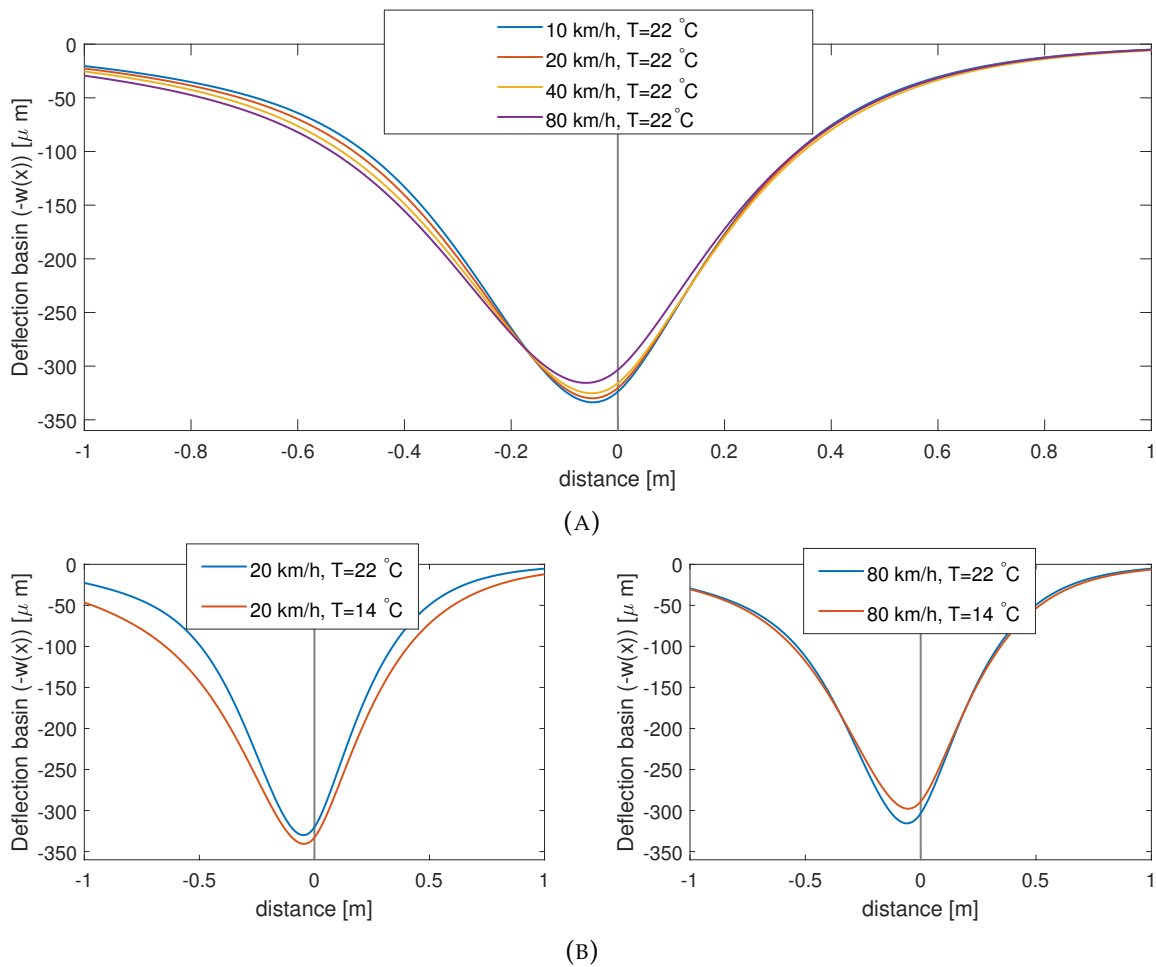


FIGURE 21.1: Simulated pavement deflection basin based on best estimated parameter values from the model fit procedure. A) Changing the driving velocity at fixed road temperature. B) different road temperatures shown for two different velocities as a bigger change with temperature is seen for 20 km/h than for 80 km/h.

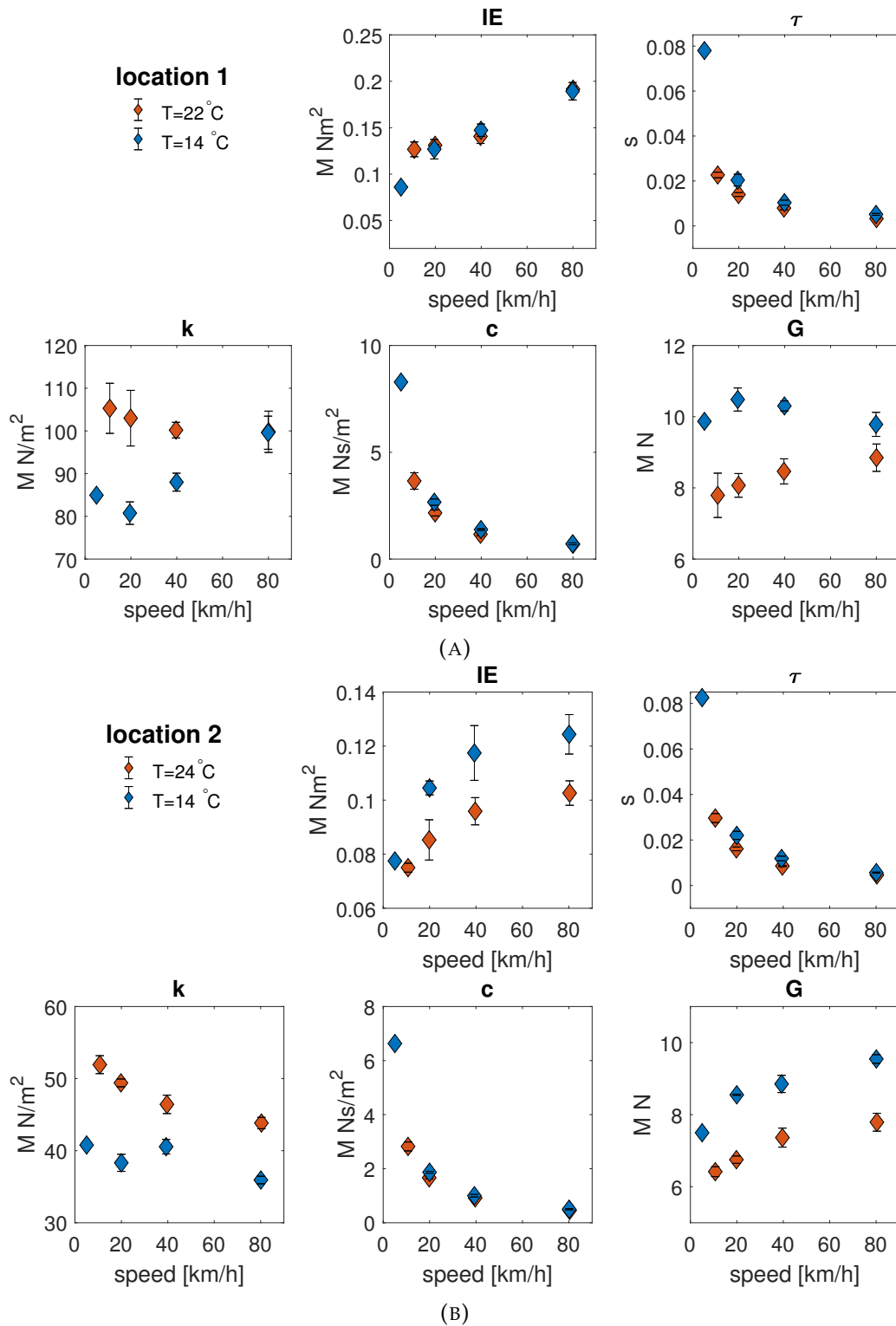


FIGURE 21.2: Estimated parameter values for Finland data at A) location 1 and B) location 2. The foundation parameters  $G$  and  $k$  is found to be varying only little and not systematic as a function of velocity, whereas  $c$  changes a factor of 10 between lowest and highest velocity. The unexpected behaviour of  $c$  is discussed in section 21.3.



## 21.2 Development of asphalt complex modulus master curves using TSD measurements

In this section, we present a pilot study which showed how to create an asphalt complex modulus master curve based on TSD measurements.

The idea behind the creation of a master curve was to measure the storage and loss modulus of the asphalt at several frequencies and at several temperatures. The time-temperature superposition principle could then be applied to shift the measured values, thus covering a larger frequency range (see section 13.2.2 for more details). The study presented here included five different driving velocities at two different temperatures. As a result, we did not expect to create a full master curve of the viscoelastic behaviour. We aimed to explore if it was possible to create such curves based on TSD data and our simple modeling framework.

When fitting the model to data, we had to choose which model was used for the complex modulus of the beam. The choice might influence the resulting master curve, as the different models can behave differently within the sensitivity interval. In the following, we will use two different models; the Maxwell model and the hysteretic damping model and subsequently compare the resulting master curves.

### 21.2.1 TTS based on Maxwell fit

Initially, we use the Maxwell model to describe the viscoelastic properties of the beam. For simplicity, the procedure is shown for location 2 data and later on the resulting master curve for location 1 is presented as well.

The model was fitted to data (as described above) and a set of parameter values was obtained. Using the estimated parameter values, we could describe the complex modulus for every velocity-temperature combination. On figure 21.3a, an example is shown for the data set at 11 km/h and 23°C. Since we are in a moving reference frame, the pavement response was only sensitive to the complex modulus behaviour within some range of frequencies, the sensitivity interval. The sensitivity interval was found as the range of wave numbers where the sensitivity function is nonzero. In figure 21.3a, this is illustrated by the red area curve. Based on the sensitivity function, a characteristic value for the loss and storage modulus was found. These values were chosen to be at the wave number where the sensitivity function peaks ( $k_x^c$ ) and was marked with triangles in figure 21.3a. Furthermore, the wave number at which  $E'$  and  $E''$  was selected is saved as the characteristic wave number for this velocity-temperature combination. This procedure was carried out for each velocity-temperature combination and on figure 21.3b, the characteristic storage and loss modulus is plotted as a function of driving velocity for all velocities and temperatures in location 2.

Note that due to the way the model is parameterised, we estimated  $IE$  and not  $E$  for the beam and thus the complex modulus was scaled by  $I$ . As a result, the found storage and loss modulus was scaled by a factor  $I$ . This has no impact on the behaviour of  $E'$  and

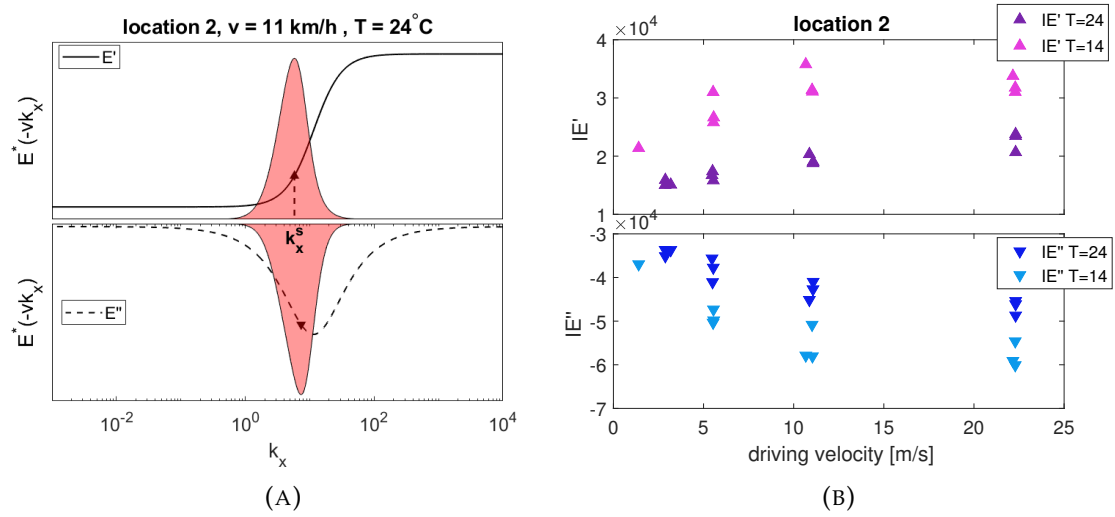


FIGURE 21.3: A) For each velocity-temperature configuration the complex modulus values within the sensitivity interval is found. This correspond to the characteristic storage modulus ( $E'$ ) and loss modulus ( $E''$ ). B)  $E'$  and  $E''$  for different driving velocities and temperatures. Note that the found loss and storage modulus is multiplied with the second moment of area  $I$ , due to the parametrization of the model.

$E''$ , but should be kept in mind if the obtained master curves were compared with results in the literature.

We aimed to construct a master curve which required a plot as a function of frequency. The corresponding frequency  $\omega$  was found from the driving velocity  $v$  and the characteristic wave number at the maximum sensitivity,  $k_x^s$ .

$$\omega = -vk_x^s. \quad (21.1)$$

Using this provided the values at negative  $\omega$  values. Taking the complex conjugate of the complex modulus converts to positive  $\omega$ .

Using the principle of time-temperature superposition (TTS) introduced in section 13.2.2, we could shift measurements made at some frequency range to a higher or lower frequency range based on their temperatures. Thus, the measurements  $E^*(\omega, T)$  was shifted with respect to some reference temperature  $T_0$  by the shift factor  $a_T$ ,

$$E'(\omega, T) = E'(\omega a_T, T_0) \text{ and } E''(\omega, T) = E''(\omega a_T, T_0). \quad (21.2)$$

The appropriate shifting factor was found by eye, such that both the loss and storage modulus curves is appropriately shifted. On figure 21.4, the best shift for location 2 data was made using  $T = 24^\circ\text{C}$  as a reference temperature.

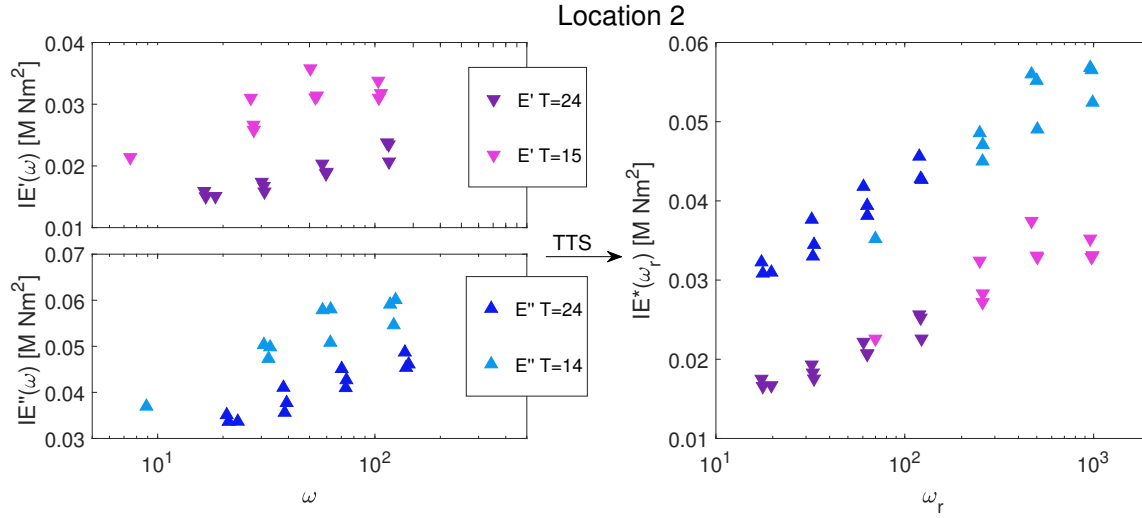


FIGURE 21.4: We apply the time temperature superposition principle, in which the loss and storage modulus values are shifted to form a master curve. To the right is the resulting master curve for reference temperature 23 °C.

### 21.2.2 Using the hysteretic damping model to estimate $E'$ and $E''$

In the analysis above, we used a Maxwell model to describe the viscoelastic properties of the beam. In order to extract one characteristic value for  $E'$  and  $E''$ , we used the value of  $E^*(-vk_x)$  at  $k_x^S$ , thus the wave number corresponding to the maximum of the sensitivity function. This had to be done for each temperature-velocity combination. If we assume that the behaviour of  $E'$  and  $E''$  do not change significantly within the sensitivity interval, we can use the *hysteretic damping model* (Nielsen, 2019) to extract the characteristic  $E'$  and  $E''$  values directly from a model fit. The complex modulus of the hysteretic damping model is given by

$$E^*(-vk_x) = E_f + i \text{sign}(-vk_x)\eta, \quad (21.3)$$

where  $E_f$  is the Young's modulus of the foundation and  $\eta$  is the viscosity. This model is not founded in physical elements like the other mechanistic response models otherwise used in this thesis as it simply has a constant real part determine by  $E_f$  and a constant imaginary part at  $\eta$ . As a result, it does not describe the viscoelastic behaviour of asphalt properly. However, if we assume that the behaviour of  $E^*(-vk_x)$  within the sensitivity interval is constant, using the hysteretic model give us the values of the characteristic value for storage ( $E'$ ) and loss ( $E''$ ) modulus directly as

$$E' = E \quad (21.4)$$

$$E'' = \text{sign}(-vk_x)\eta \quad (21.5)$$

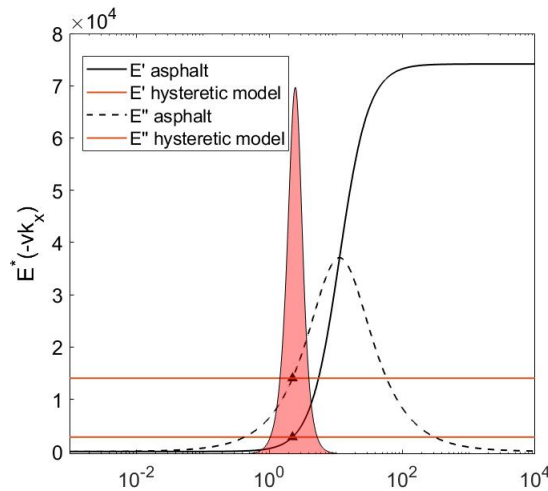


FIGURE 21.5: With black is the complex modulus using a Maxwell model sketched. If we assume that the complex modulus behaves constant within the sensitivity interval, using a hysteretic damping model will provide the characteristic storage and loss modulus. The validity of this method rely on the assumption that  $E^*(-vk_x)$  is constant within the sensitivity interval which might not be valid always.

This is illustrated on figure 21.5.

On figure 21.6 left,  $E'$  and  $E''$  are plotted for all data as a function of frequency. Note that for this model, the found loss and storage modulus values will also be multiplied with the second moment of area  $I$ . The values can be plotted as a function of frequency by using the characteristic wave number, found from the sensitivity function in a similar fashion as before.

Using TTS, the values were shifted as described before and the resulting master curve seen on the right-hand side of figure 21.6 right.

### 21.2.3 Results

A complex modulus master curve was made using two different viscoelastic models, the Maxwell model and a hysteretic model. The procedure was made on data from two different road locations. The resulting mater curves for the two location are seen on figure 21.7. Common for both model approaches was that data from location 2 were more suited for development of a master curve than location 1. This was seen as the shifting yielded a more consistent curve in location 2. For the two methods, the shift was most successful for the method using the Maxwell model. However, the two methods yielded resulting master curves within the same range, and at low frequencies they were quite similar.

During the measurements, we observed a change in the asphalt close to the location where location 1 data is measured. This had no influence on the measured deflection

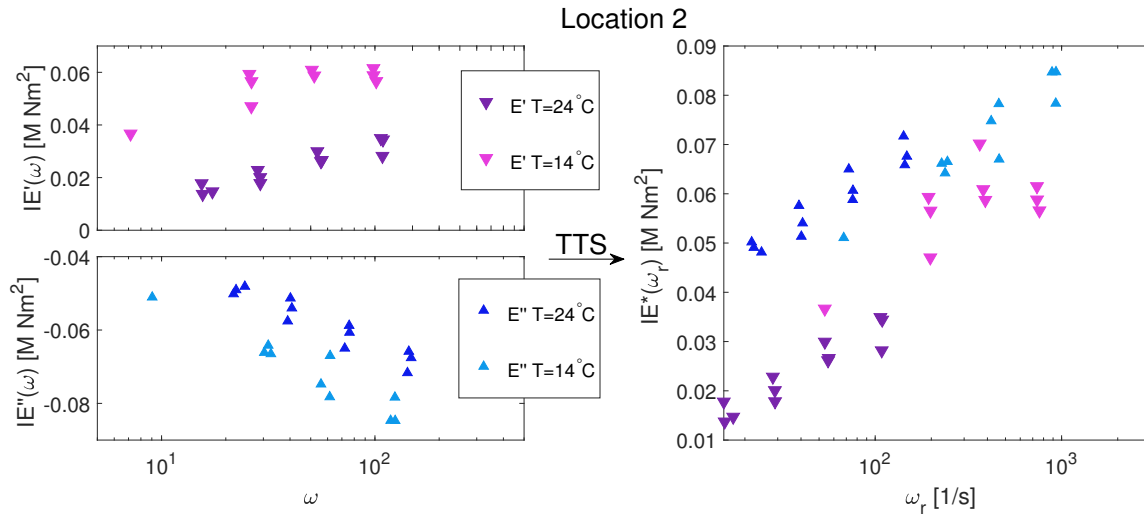


FIGURE 21.6: Characteristic storage ( $E'$ ) and loss ( $E''$ ) modulus values found by using the hysteretic damping model in the beam. Using TTS the values are shifted using  $T=24^\circ\text{C}$  as a reference temperature.

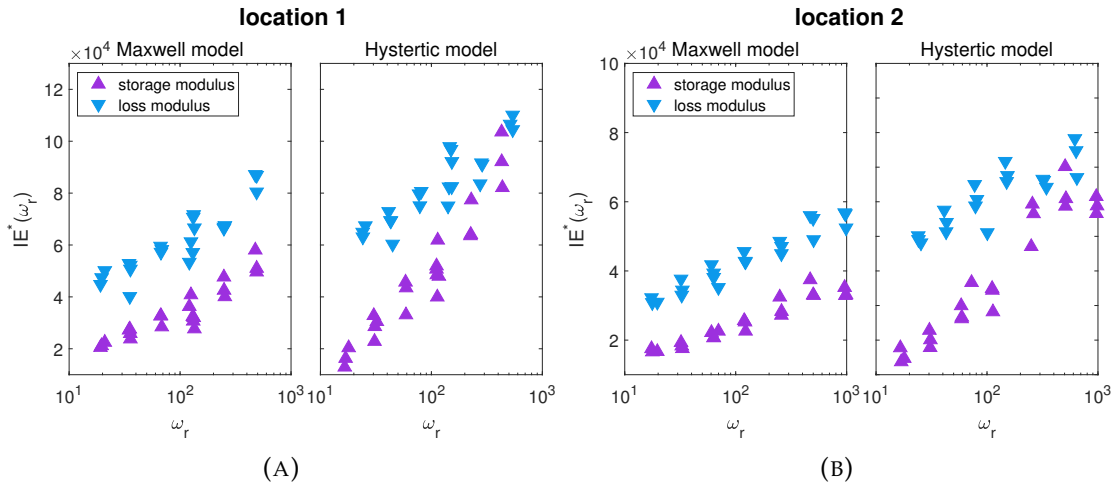


FIGURE 21.7: Master curve calculated based on Maxwell and hysteretic model in the beam. A) is for location 1 and B) for location 2. Note the difference in magnitude on the two locations.

slopes, but since this particular analysis was highly dependent on the specific properties of the asphalt layer, it might influence the results here. Consequently, we will not use results from location 1 to compare with literature.

In table 21.1, the shift factors used for both methods on location 2 data are presented. The two methods required the same amount of shifting, indicating that they provided quite similar results. The shift factor can be interpreted as a measure of how much the viscosity was increased when temperature was increased  $10^{\circ}\text{C}$  (difference between day and nighttime measurements). Compared with literature values, a shift factor of 9 is found to be reasonable when having a reference temperature of  $24^{\circ}\text{C}$  (Xu and Solaimanian, 2009; Zhao and Kim, 2003). If more temperatures were measured, the individual shift factors can be used to study how the characteristic time for each temperature is correlated with the viscosity. However, as we only had two different temperatures, no meaningful information can be derived about this correlation.

We aimed to compare the found values with studies from literature in order to evaluate if the proposed procedure provided reasonable results. This was done by fitting the Huet-Sayegh model and compare the obtained parameter values. However, it was not possible to obtain a decent fit to the complex modulus curve and instead a fit to the dynamic modulus  $|E^*|$  was made. A plot of the dynamic modulus  $|E^*|$ , calculated from the master curves, and the associated best fit of a Huet-Sayegh model is shown on figure 21.8, with the best estimated parameter values listed in table 21.1.  $|E^*|$  is often used to report results about complex modulus test on asphalt mixes (Xu and Solaimanian, 2009) and a comparison with literature revealed that the estimated values for  $E_0$  was a bit high whereas the value for  $E_{\infty}$  was a bit low (Aidara et al., 2015; Nilsson et al., 2002; Xu and Solaimanian, 2009). If we evaluate the quantitative placing of  $|E^*|$  with respect to the model fit, this corresponds to the one seen in Xu and Solaimanian (2009). A detailed comparison of the model fit with literature is not appropriate, as we only had a small range of frequencies to fit the model to and thus the behaviour outside these frequencies had a great deal of uncertainties.

A main assumption behind the proposed method was that the behaviour of the complex modulus was almost constant within the sensitivity interval and thus can be described by a single value of  $E'$  and  $E''$ . As seen on figure 21.7, this might be a invalid assumption, which can create errors in the resulting master curve. However, the fact that the approaches using the hysteric model and the Maxwell model provided similar master curves indicated that it was a reasonable procedure.

In conclusion, we have successively created a complex modulus master curve describing the viscoelastic behaviour of the asphalt layer based on TSD data. The created master curve had a quantitative behaviour which was comparable to others found in the literature. However, the limited range of frequencies made a direct comparison unappropriated. Further work should include a study with numerous temperatures in order to cover a broader range of frequencies.

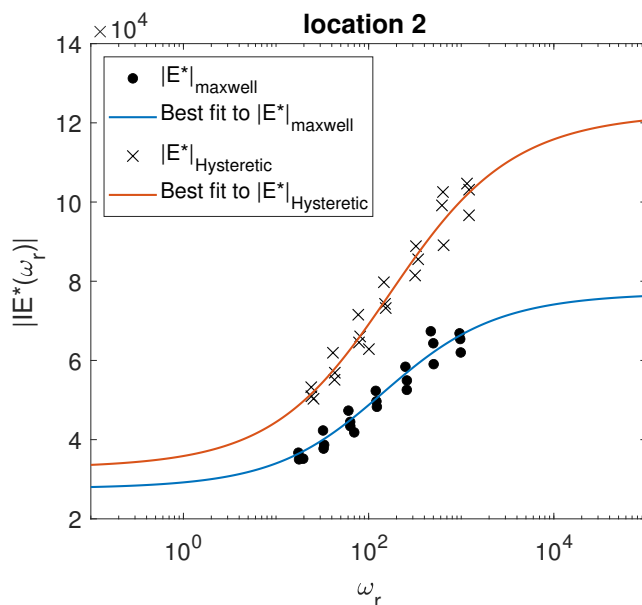


FIGURE 21.8: Dynamic modulus calculated from master curves derived using a Maxwell model and a hysteretic model on data from location 2. A Huet-Sayegh model is fitted to data, with best fit shown by the lines.

TABLE 21.1: Shift factor for the two methods for location 1 and 2 data. A Huet-Sayegh model was fitted to the dynamic modulus curves for both methods and locations and the associated best fitted parameters listed here. As the master curves are scaled by I, so is the dynamic modulus. We have assumed a asphalt thickness of 10 cm in order to obtain an estimate of  $E_0$  and  $E_\infty$ .

		Shift factor $\alpha_T$	Estimates prameter values to Huet-Sayegh model					
			$E_0$	$E_\infty$	$\delta$	$\tau$	k	h
location 2	Maxwell model	9	$3,3 \cdot 10^8$	$9.3 \cdot 10^8$	0.4	$1.1 \cdot 10^{-2}$	0.67	0.67
	hysteretic model	9	$4.0 \cdot 10^8$	$1.5 \cdot 10^9$	0.96	$1.6 \cdot 10^{-2}$	0.56	0.56

### 21.3 Characterising foundation damping

In the estimated parameter values presented on figure 21.2, a clear correlation between the foundation damping coefficient  $c$  and driving velocity  $v$  is observed. This contradicted the assumptions in the Kelvin-Voigt model used to describe the foundation damping, where the viscous behaviour is described by

$$\hat{\sigma}(-vk_x) = -cvik_x\hat{\epsilon}(-vk_x). \quad (21.6)$$

Hence  $c$ , the viscous damping coefficient, does not depend on velocity and should be constant. Consequently, figure 21.2 indicated that using this simple Kelvin-Voigt model to describe foundation damping was not appropriate.

If the foundation damping is not described by the simple Kelvin-Voigt model but a more complicated expression depending on velocity, we were not able to estimate it based on a typical TSD measurements which was obtained at one particular driving velocity. This was a situation similar to the one with the viscoelastic beam behaviour, where only the behaviour within the sensitivity interval can be estimated. As a result, we introduced the hysteretic damping model to describe damping behaviour in the foundation. This model was previously shown to be able to estimate the characteristic values of the storage and loss modulus within the sensitivity interval.

Inserting hysteretic damping in the foundation gave us the following expression for the deflection due to a point load of a viscoelastic Euler-Bernoulli beam on a hysteretic damped foundation,

$$\hat{w}(k_x, -vk_x) = \frac{F}{IE^*(-vk_x)k_x^4 + Gk_x^2 + E_f + i\text{sign}(-vk_x)\eta'}, \quad (21.7)$$

where  $E_f$  is the elastic modulus of the foundation [ $N/m^2$ ] and  $\eta$  is the damping coefficient [ $Ns/m^2$ ].

A model fit of the new model in equation (21.7) was performed and the resulting best estimated parameter values for the foundation parameters are shown on figure 21.9. A higher degree of non systematic behaviour with velocity was found compared to figure 21.2. Consequently, using the hysteretic damping model in the foundation provided a better estimate of the damping coefficient. As a result, we propose that the hysteretic damping model should be used to model foundation damping.

#### 21.3.1 Characterising the velocity dependent behaviour

We introduced hysteretic damping into the pavement response model as it, under normal conditions, was not possible to properly characterise the foundation damping based on one single TSD measurement. However, through Finland data we had information about the velocity dependence of the damping coefficient and as a result, the foundation damping for this particular road section could be characterised.

Instead of a linear dashpot, the viscoelastic foundation damping was modelled by a parabolic dashpot. The parabolic dashpot was previous used in the Huet-Sayegh model



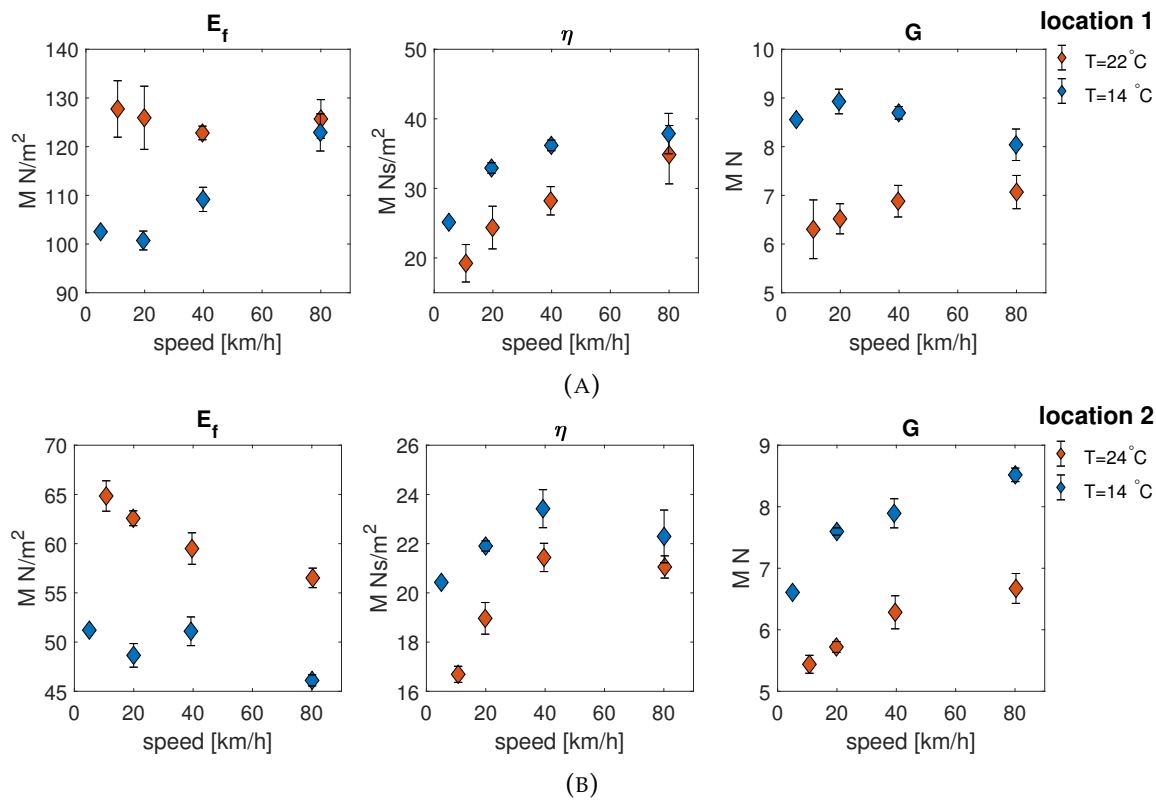


FIGURE 21.9: A new model was proposed in equation (21.7) where the foundation damping was modelled through a hysteretic damping model. Using this, a model fit to data was performed and a set of best estimated parameter obtained. Here the values for foundation parameter  $E_f$ ,  $\eta$  and  $G$  was shown as a function of velocity for A) location 1 and B) location 2. Overall a higher degree of velocity independence is found.

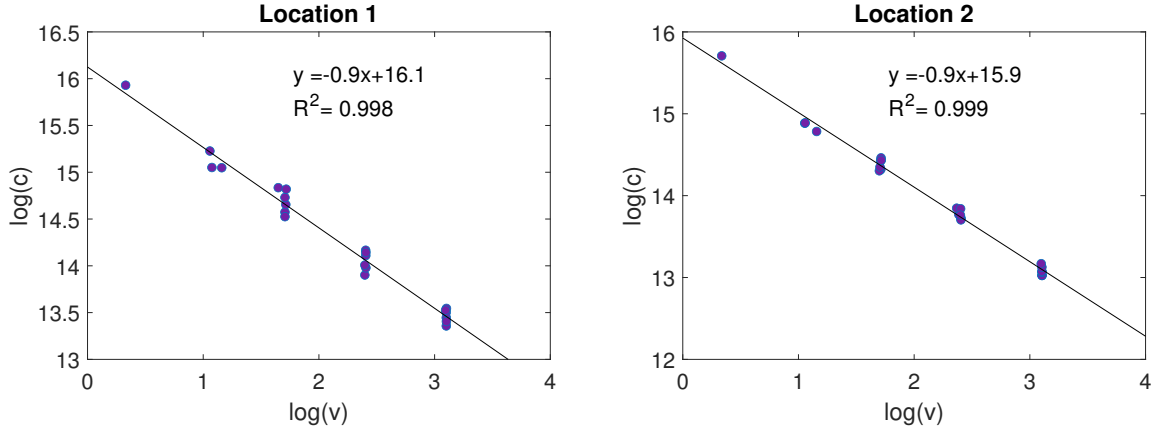


FIGURE 21.10: Logarithmic plot of the estimated parameter value  $c$  and velocity. A good linear relation was found for both locations. The plotted values for  $c$  included both estimated values for night and daytime measurements.

(Xu and Solaimanian, 2009; Pronk, 2006) and had the following relation between stress and strain,

$$\hat{\sigma}(\omega) = \frac{\eta}{\tau} (i\omega\tau)^\alpha \hat{\varepsilon}(\omega), \quad (21.8)$$

where  $\omega$  angular frequency,  $\eta$  is the viscosity,  $0 < \alpha < 1$  is the parabolic dashpot variable. In a moving reference frame this becomes

$$\hat{\sigma}(-vk_x) = \frac{\eta}{\tau} (-ivk_x\tau)^\alpha \hat{\varepsilon}(-vk_x). \quad (21.9)$$

In the special case of  $\alpha = 1$ , it behaved as the simple linear dashpot.

Taking the logarithm of the complex modulus of equation 21.9 yielded a linear relation between velocity and the complex modulus on a double logarithmic scale.

$$\log(E^*(-vk_x)) = \log\left(\frac{\eta}{\tau}\right) + \alpha \log(-ik_x\tau) + \alpha \log(v) \quad (21.10)$$

On figure 21.10, a plot of estimated parameter value  $c$  and velocity on logarithmic scales is shown, and we found a good linear relation between the two. This indicated that it was possible to use a parabolic dashpot to characterise the foundation damping. However, if the linear dashpot is replaced with an parabolic dashpot in the model, we introduce two additional parameters. Furthermore, some of the parameters depended on velocity and thus the foundation damping cannot be fully characterised based on a single measurement, but requires measurements at several driving velocities. As a consequence, using a parabolic dashpot was not recommended for the foundation.

## Chapter 22

# Manifestation of viscoelastic effects through the pavement deflection slope

A correlation between the amplitudes of the maximum and minimum deflection slope and the location of damping within the pavement layers, was observed while working with different kinds of pavement response models and data. It appeared that damping originating from the top layer and damping originating from underlying layers affected the deflection slope curve in different ways. As a result, the origin of damping was reflected in the relative difference between the amplitudes of the maximum and minimum deflection slope. The phenomenon is examined in this chapter, first by a theoretical model study and afterwards through data.

### 22.1 Formulation of hypothesis

Using the pavement response model developed in chapter 15, three scenarios were considered:

- 1) the response of a purely elastic pavement,
- 2) the response of a viscoelastic beam on an elastic foundation,
- 3) the response of an elastic beam on a viscoelastic foundation.

A plot of the pavement deflection basin and slope using the theoretical default parameters from section 16.2 is seen in figure 22.1.

For the purely elastic pavement (scenario 1), the deflection basin was symmetric around the load ( $x=0$ ). As a result, the deflection slope was anti-symmetric around the  $y$ -axis and hence the amplitude of the maximum and minimum was equal. On the other hand, for the deflection slope curves with damping included in either the beam or foundation, an asymmetric behaviour was observed. When damping was included in the beam, the maximum and minimum peaks were shifted downwards compared to the elastic case. Conversely, when damping was included in the foundation they were shifted upwards.

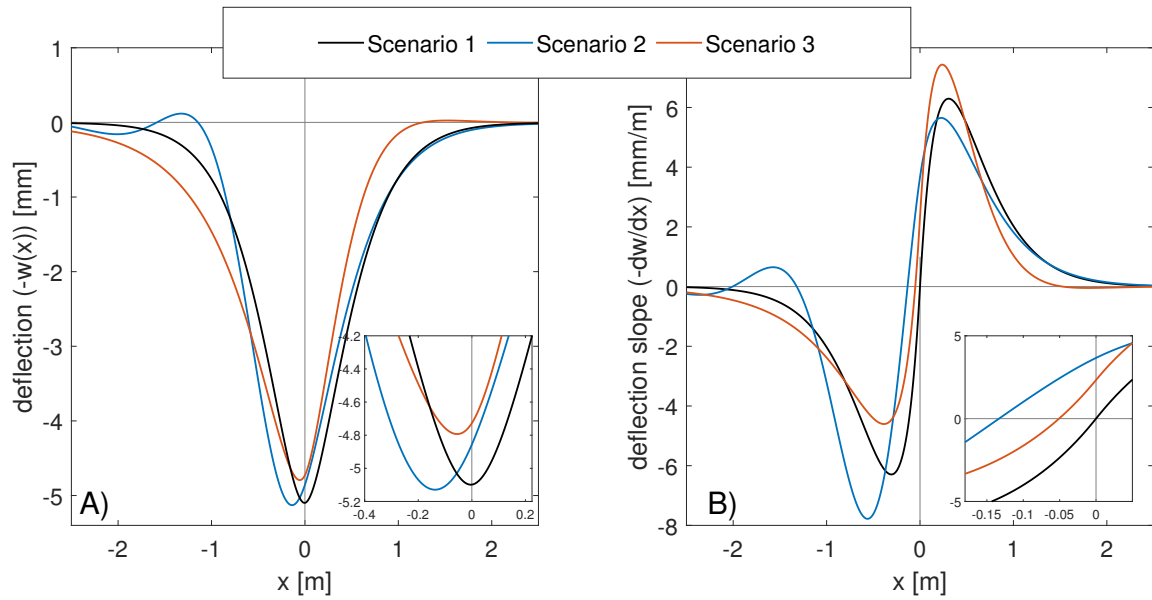


FIGURE 22.1: Simulated pavement response in three different scenarios; 1) purely elastic pavement, 2) a viscoelastic beam on an elastic foundation and 3) an elastic beam on a viscoelastic foundation. A) shows the pavement deflection basin and B) the associated pavement deflection slope. The simulations are made using default parameter values listed in section 16.2.

The asymmetry in the deflection slope curve can be quantified by looking at the ratio between the minimum and maximum peak amplitude. This ratio will be denoted  $\Omega$  in the following section.

$$\Omega = \left| \frac{\max\left(\frac{dw(x)}{dx}\right)}{\min\left(\frac{dw(x)}{dx}\right)} \right|. \quad (22.1)$$

In table 22.1, the values of  $\Omega$  for the three scenarios in figure 22.1 are listed. We found that in the case of a viscoelastic beam  $\Omega < 1$ , and in the case of a viscoelastic foundation  $\Omega > 1$ . Based on this observation, we formed the following hypothesis about the relation

TABLE 22.1: Maximum and minimum deflection slope value for the three scenarios. The ratio between the maximum and minimum peak amplitude is denoted  $\Omega$  and we hypothesize that this reveals information about the location of damping in the pavement.

	$\max\left(\frac{dw(x)}{dx}\right)$ [mm/m]	$\min\left(\frac{dw(x)}{dx}\right)$ [mm/m]	$\Omega$
Scenario 1	6.3	-6.3	1.0000
Scenario 2	5.7	-7.8	0.7262
Scenario 3	7.4	-4.6	1.6148

between viscoelastic effects in different pavement layers and the value of  $\Omega$ .

Viscoelastic effects in the pavement affect the pavement deflection slope differently depending on where they originate. By evaluating  $\Omega$ , the location of the most dominating form of damping can be found. For  $\Omega > 1$ , the most dominating viscoelastic effects are affiliated with the foundation. Conversely, for  $\Omega < 1$  the most dominating viscoelastic effects are affiliated with the top layer. The special case of  $\Omega = 1$  occurs for either a perfectly elastic pavement, or when the viscoelastic contributions from the different layers are equal.

In section 22.2, the difference in behaviour between scenario 2 and 3 and how the location of damping affect the deflection slope curve was investigated using our simple one-dimensional pavement response model. The advantage of this was that we could study the analytical expression in the frequency domain. In section 22.3, the phenomenon was studied by a more complex two-dimensional model as this mimics the real pavement dynamics better. However, due to the complexity of the model, only a numerical study was made in this case.

## 22.2 Investigation through pavement model study

The hypothesis stated above was, initially, investigated through a model study. For this purpose, we used the two layered pavement response model developed in section 15. The simple nature of the model with only two layers simplified the analysis.

The analysis of the phenomenon begins by using Fourier analysis to separate the different contributions to the deflection slope curve. Using this, we found that the asymmetry in the deflection slope curve was caused by the real part of the Fourier transformed deflection slope. As a result, the analytical expression for this and how it affects  $\Omega$  were investigated. This was initially done using the simple Kelvin-Voigt model and subsequently using the more complex Huet-Sayegh model for the complex modulus of the beam.

Using the definition of Fourier transformation, the pavement deflection  $w(x)$  can be written as followed:

$$w(x) = \frac{1}{2\pi} \int_{-\infty}^{\infty} \hat{w}(k_x, -vk_x) e^{ixk_x} dk_x. \quad (22.2)$$

$w(x)$  is a measure of how much the beam deflect compared to a straight beam. As result,  $w(x)$  is a positive value when the beam is deflected. In order to get a depiction of the deflection basin (as on figure 22.1), we had to plot  $-w(x)$ . This meant that the pavement deflection slope we were interested in investigating was in fact  $\frac{d(-w(x))}{dx}$ , as this was comparable with the signal measured by the TSD.

Using the Fourier transform definition, we introduced the function  $\hat{S}(k_x, -vk_x)$ ,

$$\frac{d(-w(x))}{dx} = \frac{1}{2\pi} \int_{-\infty}^{\infty} -ik_x \hat{w}(k_x, -vk_x) e^{ixk_x} dk_x = \frac{1}{2\pi} \int_{-\infty}^{\infty} \hat{S}(k_x, -vk_x) e^{ixk_x} dk_x. \quad (22.3)$$

$\hat{S}(k_x, -vk_x)$  was a complex valued function, and as a result it could be divided into a real ( $S'$ ) and imaginary ( $S''$ ) part,

$$\hat{S}(k_x, -vk_x) = S'(k_x, -vk_x) + iS''(k_x, -vk_x). \quad (22.4)$$

For simplicity, we refer to these just as  $S'$  and  $S''$ . Including this in equation (22.3) yields

$$\frac{d(-w(x))}{dx} = \frac{1}{2\pi} \int_{-\infty}^{\infty} (S' + iS'') e^{ixk_x} dk_x \quad (22.5)$$

Equation (22.5) can be rewritten.

$$\frac{d(-w(x))}{dx} = \frac{1}{2\pi} \int_{-\infty}^{\infty} (S' + iS'') e^{ixk_x} dk_x \quad (22.6)$$

$$= \frac{1}{2\pi} \int_{-\infty}^{\infty} S' \cos(xk_x) - S'' \sin(xk_x) dk_x + i \frac{1}{2\pi} \int_{-\infty}^{\infty} S' \sin(xk_x) + S'' \cos(xk_x) dk_x \quad (22.7)$$

$$= \frac{1}{2\pi} \int_{-\infty}^{\infty} S' \cos(xk_x) - S'' \sin(xk_x) dk_x \quad (22.8)$$

The last equality is due to the fact that the imaginary part of a Fourier transform of a real function,  $\mathcal{F}\{f(x)\} = \hat{f}(k_x)$ , must be zero when inverse transformed, as the resulting function  $\mathcal{F}^{-1}\{\hat{f}(k_x)\} = f(x)$  is real. In equation (22.7) this means that

$$F(x, k_x) = i \frac{1}{2\pi} \int_{-\infty}^{\infty} S' \sin(xk_x) + S'' \cos(xk_x) dk_x = 0. \quad (22.9)$$

The step is proven in more detail below.

The function  $\hat{S}(k_x, -vk_x)$  can be rewritten by use of the definition of Fourier transform

$$\hat{S}(k_x, -vk_x) = \int_{-\infty}^{\infty} \frac{d(-w(x))}{dx} e^{-ik_x x} dx \quad (22.10)$$

$$= \int_{-\infty}^{\infty} \frac{d(-w(x))}{dx} \cos(xk_x) dx + i \int_{-\infty}^{\infty} -\frac{d(-w(x))}{dx} \sin(xk_x) dx \quad (22.11)$$

$$= S' + iS'' \quad (22.12)$$

If we include the expression for  $S'$  and  $S''$  found in (22.12) into (22.9), we get that

$$F(x, k_x) = i \frac{1}{2\pi} \int_{-\infty}^{\infty} \left[ \left( \int_{-\infty}^{\infty} \frac{d(-w(x'))}{dx'} \cos(x'k_x) dx' \right) \sin(xk_x) + \dots \right. \\ \left. \left( \int_{-\infty}^{\infty} -\frac{d(-w(x'))}{dx'} \sin(x'k_x) dx' \right) \cos(xk_x) \right] dk_x \quad (22.13)$$

$$= i \frac{1}{2\pi} \int_{-\infty}^{\infty} \left[ \int_{-\infty}^{\infty} \frac{d(-w(x'))}{dx'} \cos(x'k_x) \sin(xk_x) dx' + \dots \right. \\ \left. \int_{-\infty}^{\infty} -\frac{d(-w(x'))}{dx'} \sin(x'k_x) \cos(xk_x) dx' \right] dk_x \quad (22.14)$$

$$= i \frac{1}{2\pi} \int_{-\infty}^{\infty} \left[ \int_{-\infty}^{\infty} \frac{d(-w(x'))}{dx'} (\cos(x'k_x) \sin(xk_x) - \sin(x'k_x) \cos(xk_x)) dx' \right] dk_x. \quad (22.15)$$

Since both integrals are from  $-\infty$  to  $\infty$ , we can change the order of integrations such that

$$F(x, k_x) = i \frac{1}{2\pi} \int_{-\infty}^{\infty} \left[ \int_{-\infty}^{\infty} \frac{d(-w(x'))}{dx'} (\cos(x'k_x) \sin(xk_x) - \sin(x'k_x) \cos(xk_x)) dk_x \right] dx'. \quad (22.16)$$

Using that  $\sin(x - y) = \sin(x) \cos(y) - \sin(y) \cos(x)$ ,

$$F(x, k_x) = i \frac{1}{2\pi} \int_{-\infty}^{\infty} \left[ \int_{-\infty}^{\infty} \frac{d(-w(x'))}{dx'} \sin(xk_x - x'k_x) dk_x \right] dx' \quad (22.17)$$

$$= i \frac{1}{2\pi} \int_{-\infty}^{\infty} \frac{d(-w(x'))}{dx'} \left[ \int_{-\infty}^{\infty} \sin(k_x(x - x')) dk_x \right] dx'. \quad (22.18)$$

The inner integral in equation (22.18) is over the function  $\sin(k_x(x - x'))$  which is an odd function. The integral of an odd function  $f(x)$  over an interval symmetric about zero is zero (Adams, 1999, p. 318),

$$\int_{-M}^{+M} f(x) dx = 0. \quad (22.19)$$

Strictly speaking the integral of  $\int_{-\infty}^{\infty} \sin(k_x(x - x')) dk_x$  do not converge. However, since in practice, the  $k_x$  integration is between large but finite limits, we can use the result (22.19). Consequently,

$$F(x, k_x) = i \frac{1}{2\pi} \int_{-\infty}^{\infty} \frac{d(-w(x'))}{dx'} [0] dx' = 0. \quad (22.20)$$

Thereby, we have proven the steps from (22.7) to (22.8) to be true.

We return to the expression for the pavement deflection slope, which as a consequence can be written as followed

$$\frac{d(-w(x))}{dx} = \frac{1}{2\pi} \int_{-\infty}^{\infty} S' \cos(xk_x) dk_x + \frac{1}{2\pi} \int_{-\infty}^{\infty} -S'' \sin(xk_x) dk_x. \quad (22.21)$$

Define the functions  $G(x)$  and  $H(x)$  as

$$G(x) = \frac{1}{2\pi} \int_{-\infty}^{\infty} S' \cos(xk_x) dk_x, = F^{-1}\{S'\} \quad (22.22)$$

$$H(x) = \frac{1}{2\pi} \int_{-\infty}^{\infty} -S'' \sin(xk_x) dk_x = F^{-1}\{iS''\} \quad (22.23)$$

$G(x)$  corresponds to taking the inverse Fourier transform of  $S'$ , and  $H(x)$  corresponds to taking the inverse Fourier transform of  $iS''$ . On figure 22.2, a plot of  $G(x)$ ,  $H(x)$  and the inverse Fourier transform of  $\hat{S}$  is shown.  $H(x)$  represents the elastic contribution to the total deflection slope curve and is an even function, thus anti-symmetric around the  $y$ -axis.  $G(x)$ , on the other hand, is an odd function, and contributes to the asymmetric behaviour in the total deflection slope. The maximum of  $H(x)$  is indicated to be at  $x = x_1$ . As  $H(x)$  is anti-symmetric, the minimum is located at  $x = -x_1$ .

In the case of a perfectly elastic pavement,  $\frac{d(-w(x))}{dx} = H(x)$ . For small perturbations to the elastic solutions ( $|G(x)| \ll 1$ ), the maximum and minimum of  $\frac{d(-w(x))}{dx}$  is assumed to be located in the same place as maximum and minimum of  $H(x)$ . This assumption does not hold in case of substantial amount of damping where the viscoelastic effects will shift the  $\frac{d(-w(x))}{dx}$  signal to the left, thus affecting the  $x$ -position of the maximum and minimum. As we were interested in understanding the fundamental characteristics of the problem, we conducted the analysis in the simple framework of a small perturbation and studied the behaviour of  $H(x)$  and  $G(x)$  both in  $x = x_1$ .

For the two layered pavement response model derived in chapter 15, the Fourier transformed pavement deflection slope (using a point load) is given by

$$\hat{S}(k_x, -vk_x) = \frac{-Fik_x}{IE^*(-vk_x)k_x^4 + Gk_x^2 + k - civk_x}. \quad (22.24)$$

Here  $F$  is the magnitude of the load,  $I$  is the second moment of area pr. unit length,  $E^*(-vk_x)$  is a general expression for the complex modulus of the asphalt layer and  $k$ ,  $c$  and  $G$  is the foundation spring constant per unit length, viscous damping coefficient per unit length and shear interaction parameter of the foundation, respectively.



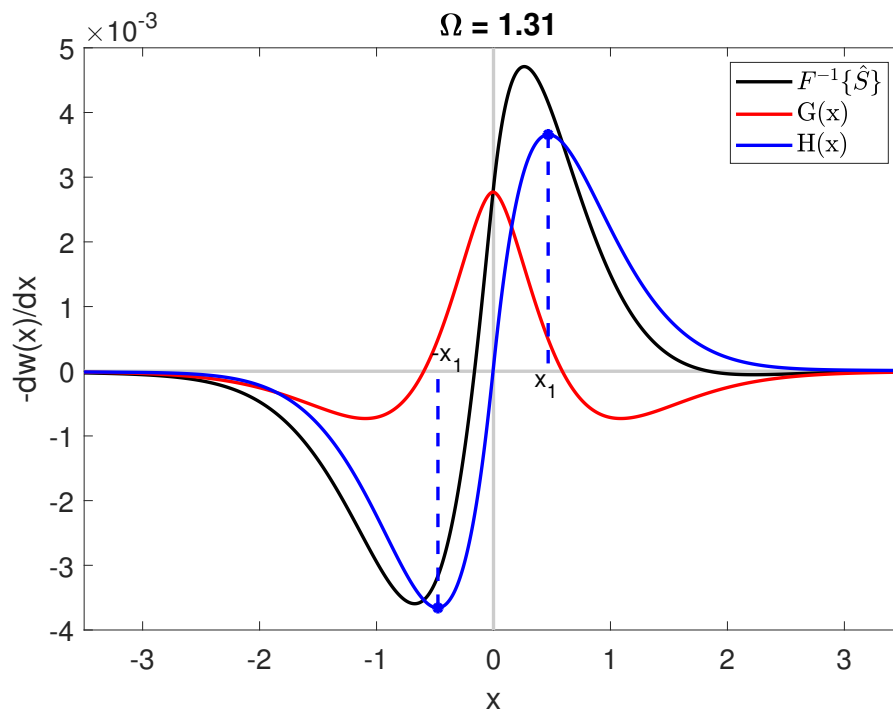


FIGURE 22.2: Pavement deflection slope found by inverse Fourier transform  $F^{-1}\{\hat{S}\}$  together with the anti-symmetric contribution to the slope ( $H(x)$ ) and the asymmetric contribution to the slope ( $G(x)$ ).

$E^*(-vk_x)$  can be divided into real and imaginary parts:  $E^*(-vk_x) = E' + iE''$ . Introducing this into equation (22.24) gives

$$\hat{S}(k_x, -vk_x) = \frac{-Fik_x}{I(E'(-vk_x) + iE''(-vk_x))k_x^4 + Gk_x^2 + k - civk_x} \quad (22.25)$$

$$= \frac{-Fik_x}{IE'k_x^4 + Gk_x^2 + k + i(IE''k_x^4 - cvk_x)} \quad (22.26)$$

$\hat{S}(k_x, -vk_x)$  is then rewritten in terms of imaginary and real parts by multiplying the denominator and numerator with the complex conjugated value of  $\hat{S}(k_x, -vk_x)$ .

$$\hat{S}(k_x, -vk_x) = \frac{-Fik_x}{IE'k_x^4 + Gk_x^2 + k + i(IE''k_x^4 - cvk_x)} \frac{(IE'k_x^4 + Gk_x^2 + k) - i(IE''k_x^4 - cvk_x)}{(IE'k_x^4 + Gk_x^2 + k) - i(IE''k_x^4 - cvk_x)} \quad (22.27)$$

$$= \frac{-Fk_x(IE''k_x^4 - cvk_x)}{(IE'k_x^4 + Gk_x^2 + k)^2 + (IE''k_x^4 - cvk_x)^2} + i \frac{-Fk_x(IE'k_x^4 + Gk_x^2 + k)}{(IE'k_x^4 + Gk_x^2 + k)^2 + (IE''k_x^4 - cvk_x)^2} \quad (22.28)$$

Consequently, we found that for the two layered pavement response model  $S'$  and  $S''$  is given by the following

$$S' = \frac{-Fk_x(IE''k_x^4 - cvk_x)}{(IE'k_x^4 + Gk_x^2 + k)^2 + (IE''k_x^4 - cvk_x)^2} \quad (22.29)$$

$$S'' = \frac{-Fk_x(IE'k_x^4 + Gk_x^2 + k)}{(IE'k_x^4 + Gk_x^2 + k)^2 + (IE''k_x^4 - cvk_x)^2} \quad (22.30)$$

From relations (22.29) and (22.30), it is clear that in the case of a perfectly elastic pavement ( $E'' = 0$  and  $c = 0$ ),  $S' = 0$ . This means that the pavement response, in this case, is determined by the imaginary part  $iS''$  of  $\hat{S}(k_x, -vk_x)$  and consequently, the black and blue curve on figure 22.2 will collapse. Therefore, in order to understand the asymmetry seen in the deflection slope, we had to investigate the real part of  $\hat{S}(k_x, -vk_x)$  given by  $G(x)$ .

### Kelvin-Voigt model for $E^*(-vk_x)$

In order to understand the fundamental characteristics of the problem, we started by using the highly simple Kelvin-Voigt model for beam behaviour. This model may not describe the complete asphalt behaviour completely correctly, but was used due to its simplicity and linear relationship between stiffness ( $E_0$ ) and damping ( $\eta$ ).

$$E^*(-vk_x) = E_0 - ivk_x\eta \quad (22.31)$$

As mentioned, we were interested in the behaviour of  $G(x)$  and how this influenced the behaviour of  $\Omega$ . Thus, we started by looking at the value of  $G(x_1)$  and subsequently

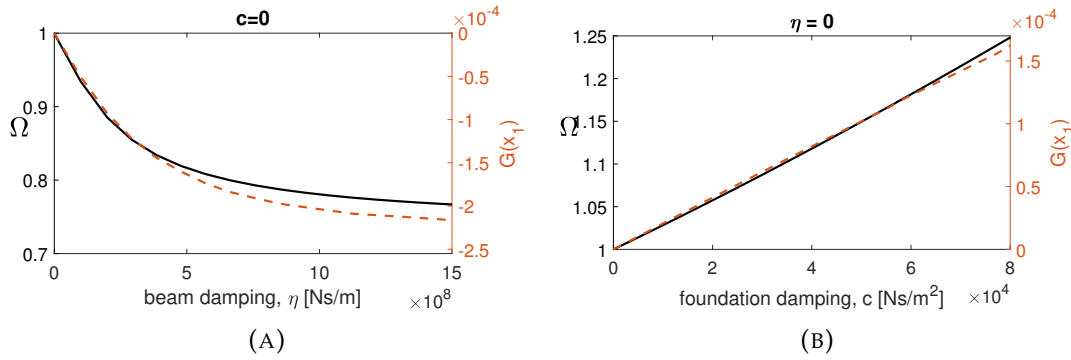


FIGURE 22.3: Value of  $G(x_1)$  (right y-axis) and  $\Omega$  (left y-axis) for increased beam and foundation damping respectively. A) viscoelastic beam on a elastic foundation and B) elastic beam on viscoelastic foundation. Both plot use the Kelvin-Voigt model to describe the beam behaviour. A high correlation between  $G(x_1)$  and  $\Omega$  was found.

its analytical expression.

The value of  $G(x_1)$  provided an insight into how the curve deviated from the elastic solution. If  $G(x_1) > 0$ , the  $\frac{d(-w(x))}{dx}$  curve will be shifted upwards compared to  $H(x)$  in both  $x_1$  and  $-x_1$ . On the other hand if  $G(x_2)$  is negative, the curve is shifted downwards. The relationship between  $G(x_1)$  and  $\Omega$  was investigated on figure 22.3 in the two simple cases where either beam or foundation damping was present. A clear correlation between the behaviour of  $G(x_1)$  and  $\Omega$  was found. In order to understand the behaviour of  $G(x_1)$ , we had to understand the behaviour of its components.

$G(x_1)$  is given by the integral over the function  $S' \cos(x_1 k_x)$ . In figure 22.4, a plot of  $S'$ ,  $\cos(x_1 k_x)$  and  $S' \cos(x_1 k_x)$  is seen for different values of  $\eta$  with constant  $c=0$ . The value of  $\eta$  affected both the behaviour of  $S'$  and  $\cos(x_1 k_x)$ , and thus these were shown on normalized axis in figure 22.4a. From this, it is found that increasing  $\eta$  shifted the  $S'$  curve to higher wave number, resulting in the product curve in 22.4b being increasingly more negative. As a consequence,  $G(x_1)$  decreases. This explains the trend seen in figure 22.3a.

We will now examine which parameters influenced the behaviour of  $S'$  by looking at the analytical expression. Recall that  $S'$  is given by

$$S' = \frac{-Fk_x(IE''k_x^4 - cvk_x)}{(IE'k_x^4 + Gk_x^2 + k)^2 + (IE''k_x^4 - cvk_x)^2}. \quad (22.32)$$

In the case, where all elastic parameters were fixed and thus only pavement damping is changed, the shape of  $S'$  was determined by the term  $(IE''k_x^4 - cvk_x)$ , which was present in both numerator and denominator. If we use a Kelvin-Voigt model to describe beam damping and has the simple case of an elastic foundation ( $c=0$ ) the term becomes,

$$(IE''k_x^4 - cvk_x) = -Iv\eta k_x^5. \quad (22.33)$$

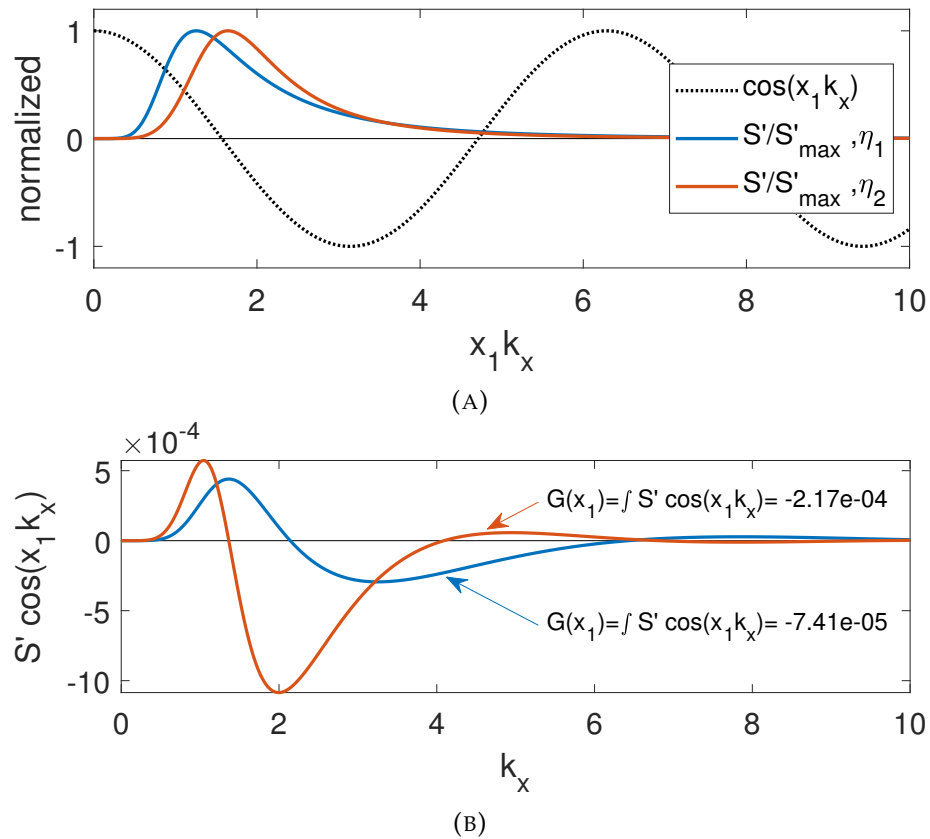


FIGURE 22.4: A)  $S'$  and  $\cos(x_1 k_x)$  for two values of  $\eta$  ( $\eta_1 = 2 \cdot 10^8$  Ns/m and  $\eta_2 = 8 \cdot 10^8$  Ns/m) with  $c=0$ . The x-axis was normalized with  $x_1$  such that the period of cosine was the same for both situations. Looking at the  $S'$  curve, we found how it was shifted to higher wavenumbers than  $\eta$  increased. B) Show the product  $S' \cos(x_1 k_x)$ , which was increasingly negative for higher  $\eta$ . Thus the integral, corresponding to  $G(x)$ , became a higher negative value again resulting in an decreasing  $\Omega$  value.

On the other hand, in the case of an elastic beam ( $\eta = 0$ ) and viscoelastic foundation the term becomes,

$$(IE''k_x^4 - cvk_x) = -cvk_x. \quad (22.34)$$

Thus the main difference on the two types of damping was the power in which  $k_x$  was raised in  $S'$ . This affected at which  $k_x$  the peak in  $S'$  was placed with respect to  $\cos(x_1k_x)$ , and as a result, whether  $G(x_1)$  ended up being positive or negative.

In the case where damping was present in both the beam and foundation, the situation became more complicated as both terms in  $(IE''k_x^4 - cvk_x)$  was present.

In figure 22.5, the value of  $\Omega$  was shown in the form of a contour plot, with beam and foundation damping on the axis. We found that increasing beam damping always resulted in a decrease in  $\Omega$  and vice versa for foundation damping, which always resulted in an increase of  $\Omega$ . The plot of  $\Omega$  on figure 22.3 corresponded to the simple cases along the y-axis ( $\eta = 0$ ) and the x-axis ( $c = 0$ ), respectively. Notice that a line with  $\Omega = 1$  went through the contour plot, indicating the tipping point where the dominating damping went from the beam to the foundation and vice versa.

As mentioned, the behaviour of  $S'$ , in the case where two types of damping was present simultaneously, was dictated by the term  $(-Iv\eta k_x^5 - cvk_x)$ . An illustration of the behaviour of  $S'$  for different combinations of damping is shown in figure 22.6. When both types of damping was present, the relative size of  $\eta$  and  $c$  determined what was the dominating power of  $k_x$  in  $(IE''k_x^4 - cvk_x)$ . From figure 22.6, we concluded that increasing  $c$  moved the peak to lower  $k_x$ , and thus shifts the value of  $G(x_1)$  in a positive direction. The opposite was seen for increased  $\eta$  which moved the peak to higher  $k_x$ , resulting in  $G(x_1)$  going towards a negative value.

In conclusion, there exists a correlation between the the dominating power of  $k_x$  in the term  $(IE''k_x^4 - cvk_x)$ , which was present in both numerator and denominator, and the pavement response observed through  $\Omega$ . This explained why increased beam and foundation damping had different influences on the pavement response.

### Huet-Sayegh model for $E^*(-vk_x)$

The above analysis was made with the simple Kelvin-Voight model representing the beam behaviour. We will now do the same, but with a more realistic complex modulus model (for more information, see the discussion in section 13.3). In the literature, the Huet-Sayegh model is often mentioned as a good model for the asphalt behaviour over a wide range of frequencies, and thus this will be used in the following analysis (Pronk, 2006; Nilsson et al., 2002; Xu and Solaimanian, 2009).

The complex modulus for the Huet-Sayegh model is given by:

$$E^*(-vk_x) = E_0 + \frac{E_\infty - E_0}{1 + \delta(-ivk_x\tau)^{-k} + (-ivk_x\tau)^{-h}} \quad (22.35)$$

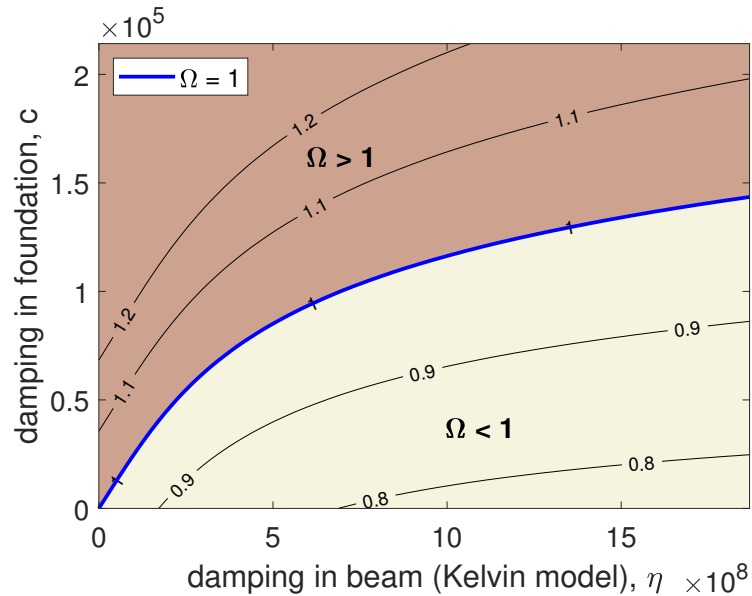


FIGURE 22.5: Contour plot showing the value of  $\Omega$  for different combinations of beam and foundation damping. On the x axis is damping in the beam and on the y axis is damping in the foundation. Increasing beam damping always result in a decrease in  $\Omega$  and increasing foundation damping always result in increase  $\Omega$ .

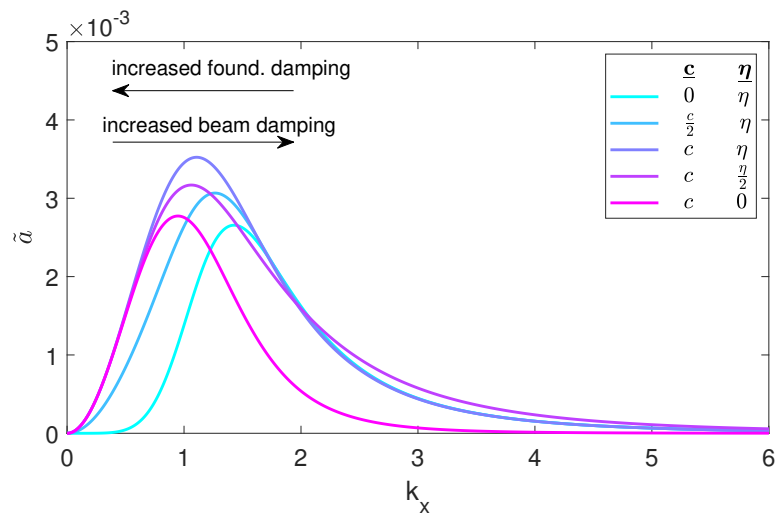


FIGURE 22.6: Behaviour of  $\tilde{a}$  for different combinations of damping, going from viscoelastic beam on elastic foundation to an elastic beam on viscoelastic foundation. When  $c$  is increased the peak is shifted to a lower wave number and as a result the value of  $G(x_1)$ , and thus  $\Omega$ , is increased.

The parameter values used are  $\eta = 8 \cdot 10^8 \frac{\text{Ns}}{\text{m}}$  and  $c = 1.5 \cdot 10^5 \frac{\text{Ns}}{\text{m}^2}$ .

In the Huet-Sayegh model, and similar models, there is a nonlinear relationship between stiffness and damping parameters. In particular when equation (22.35) is divided into storage ( $E'$ ) and loss ( $E''$ ) modulus, these will contain both stiffness and damping related parameters. In addition, they are both functions of  $k_x$ . This is fundamentally different from the Kelvin-Model, where  $E'$  was constant, and it complicates the behaviour of  $S'$  even more.

In figure 22.7, a plot of the complex modulus for the Huet-Sayegh model using the parameter values from section 16.2 is seen. As discussed in chapter 17, due to the moving load we had a frequency dependent pavement response. Only the behaviour of  $E^*(-vk_x)$  within a certain range of frequencies has an influence on the pavement response, the sensitivity interval. Consequently, the parts of  $E'$  and  $E''$  which had an influence on the behaviour of  $S'$  and  $G(x_1)$  is the part within the sensitivity interval.

This gave rise to the question of how to control the beam damping. The *damping expressed by the beam* was given by the value of the storage and loss modulus within the sensitivity interval which depended on various parameters. We chose to change the beam damping by changing the value of  $\tau$ . Increasing  $\tau$  shifted the complex modulus curve to lower wave numbers and as a result, the sensitivity interval covered different parts of the  $E^*(-vk_x)$  curve. On a normalized x-axis, this corresponded to shifting the sensitivity interval and thereby covering different parts of the complex modulus, resulting in different amount of beam damping. This is illustrated on figure 22.7 with three different  $\tau$  values. Note that due to the shape of  $E''$ , there existed a value of  $\tau$  at which the beam expressed a maximum amount of damping. As a result, damping could be increasing by either increasing  $\tau$  from the elastic plateau at low frequency (increasing "from the left") or decreasing  $\tau$  from the elastic plateau at high frequency (increasing "from the right"). Since  $E''$  was not symmetric the two approaches did not give the same results.

In figure 22.8, a contour plot of  $\Omega$  as a function of beam and foundation damping is shown. On the y-axis we have the amount of foundation damping and on the x-axis is the value of  $\tau$ . Below the x-axis, the values of  $E^*(-vk_x)$  within the sensitivity interval at a given  $\tau$  value is plotted. Overall figure 22.8 showed that any given value for  $\tau$ , if the foundation damping  $c$  was increased,  $\Omega$  would increase. Likewise, it showed that if we began at any foundation damping  $c$  and increased the beam damping, either from the left or the right,  $\Omega$  was decreased. The increase/decrease rate of  $\Omega$  depended on the specific combination of parameters, and we found that there in fact was a difference in  $\Omega$  whether we were at high or low  $\tau$ .

The blue line indicates  $\Omega = 1$ . This provides the limits of a closed area in which  $\Omega < 1$ . Within this area the beam damping was the "dominating" damping and thus  $\Omega < 1$ . Likewise outside of the  $\Omega = 1$  line, we had an area where the foundation damping is dominating and thus  $\Omega > 1$ .

As previously, there was a correlation between  $G(x_1)$  and  $\Omega$ . On figure 22.9,  $G(x_1)$  and  $\Omega$  for the simple case with  $c = 0$  an increased  $\tau$  was observed. As before, we found that  $G(x_1)$  always was below or equal to zero. In the extremes for high or low  $\tau$ , we have

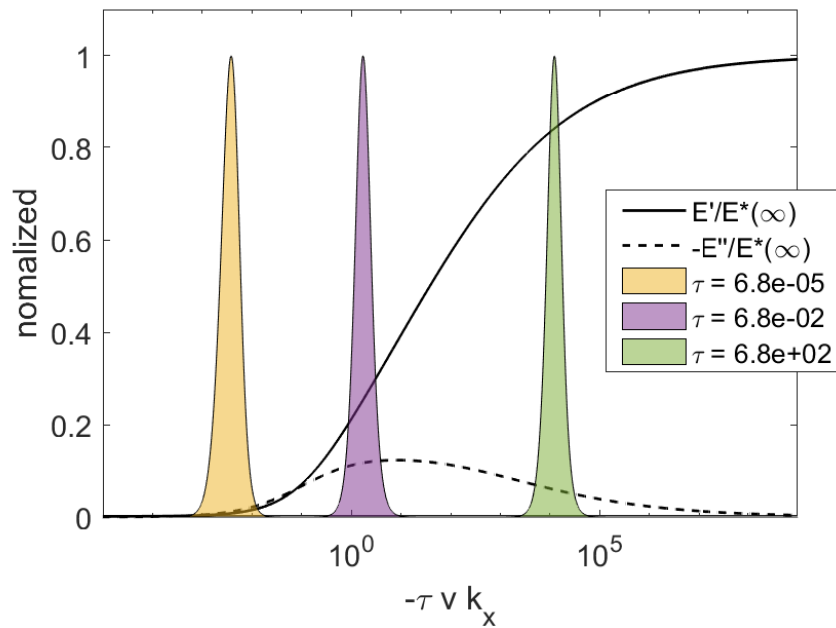


FIGURE 22.7: The complex modulus using the Huet-Sayegh model on normalized axis is showed in black. Due to the moving load, the pavement response is frequency dependent and thus only a particular range of frequencies influence the pavement response. This range can be found by evaluating where the sensitivity function is nonzero. The sensitivity function for different  $\tau$  values is marked with area curves, illustrating how changing  $\tau$  results in different parts of  $E'$  and  $E''$  being covered by the sensitivity interval. Consequently the beam will exhibit different amount of damping and stiffness.



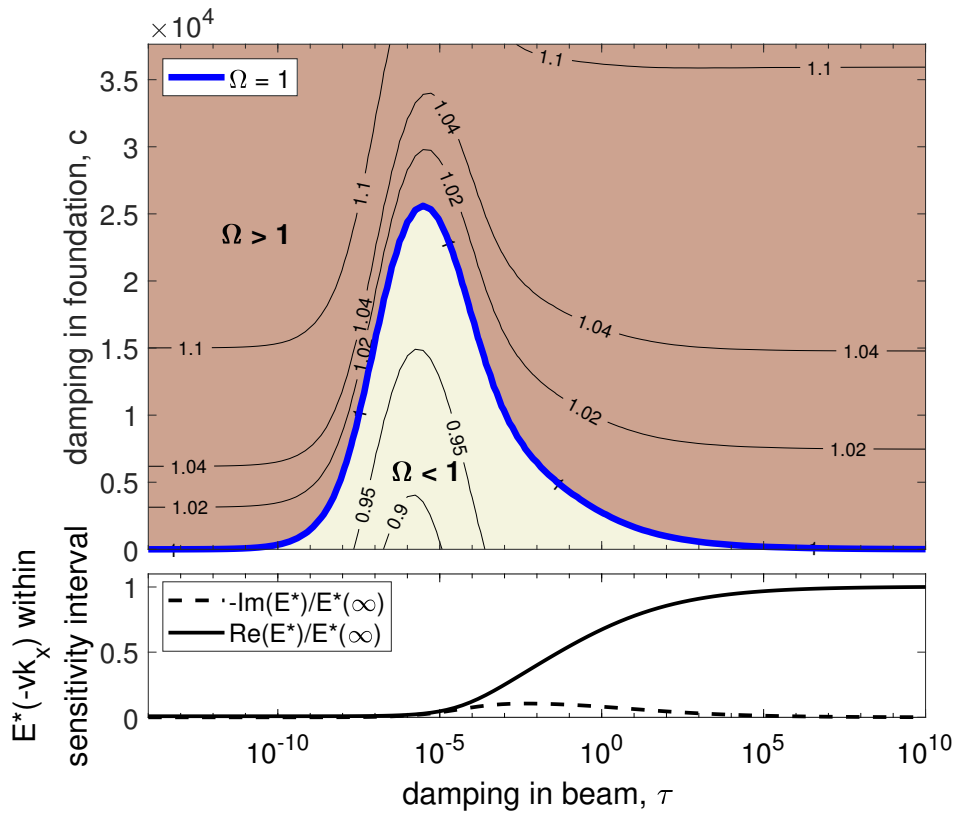


FIGURE 22.8: Contour plot of  $\Omega$  for different combinations of beam and foundation damping. On the y-axis we have the amount of foundation damping  $c$  and on the x-axis the beam damping described by  $\tau$ . Below the x-axis, the values of  $E^*(-vk_x)$  within the sensitivity interval for a given  $\tau$  value is plotted. Parameter values for the Huet-Sayegh model is adopted from (Pronk, 2006). The plot illustrates how increased damping in the beam decreases the value of  $\Omega$ , whereas increased damping in the foundation increases the  $\Omega$  value.

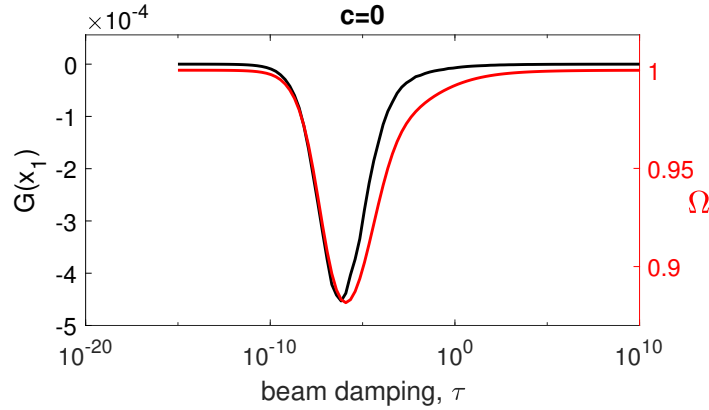


FIGURE 22.9:  $G(x_1)$  and  $\Omega$  for increased  $\tau$  using the Huet-Sayegh model with default parameters (sec. 16.2). A clear correlation between  $G(x_1)$  and  $\Omega$  is found, with the shape of the curves following the shape of the loss modulus  $E''$  for the beam.

an elastic case and  $G(x_1) = 0$ . In-between,  $G(x_1)$  had a negative slope for  $\tau < 1 \cdot 10^6$  and a positive slope for  $\tau > 1 \cdot 10^6$ . A similar behaviour was seen for  $\Omega$ .

An explanation for this change was to be found in the behaviour of  $E''$  within the sensitivity interval for different  $\tau$ . In figure 22.7, we could see how the behaviour of  $E''$  within the three plotted sensitivity intervals was quite different. The behaviour of  $E''$  had the form  $E'' \sim k_x^n$ , where  $n$  was a real number controlling how steep the slope was. If the sensitivity interval was located to the left of  $E''_{max}$ ,  $E''$  had a positive slope and thus  $0 < n$ . If the sensitivity interval on the other hand, was located on the right hand side of  $E''_{max}$ ,  $n < 0$  and thus the slope was negative.

As seen previously, the behaviour of  $S'$  was influenced by the term  $(IE''k_x^4 - cvk_x)$ . In the simple case with  $c=0$ , we have that

$$(IE''k_x^4 - cvk_x) = IE''k_x^4 \quad (22.36)$$

As a result, due to the changing behaviour of  $E''$  the total power to which the wave number was raised will be less than 4 when the sensitivity interval was on the right hand side of the loss modulus peak. This meant that  $S'$  was moved to lower  $k_x$  and that  $G(x_1)$  likewise would be moved in a positive direction. A behaviour we connected previously with foundation damping. The power of  $n$  would determine at which  $k_x$  the peak in  $S'$  was placed, and thus the value of  $G(x_1)$ . In the simulation in figure 22.8,  $E''$  was rather flat on the right side corresponding to a low  $n$ . As a result,  $G(x_1) \leq 0$  when there was no foundation damping present and therefore  $\Omega \leq 1$ .

In the case of both beam and foundation damping, the behaviour of  $S'$  became increasingly complicated to understand as both kinds of damping contributed to  $(IE''k_x^4 - cvk_x)$ . However, in figure 22.8 we found that the area with  $\Omega < 1$  was a connected area and that this area was shaped after the imaginary part of  $E^*(-vk_x)$ . Thus, the hypothesis that the origin of the most dominating source of damping could be found by evaluating  $\Omega$  was

true in this case.

### Exceptions from general trend

As discussed above, the slope of  $E''$  within the sensitivity interval determines the behaviour of  $S'$  which affects  $G(x_1)$  and in the end  $\Omega$ . The slope on the right hand side of  $E''_{max}$  is on the form  $E'' \sim k_x^n$  with  $n < 0$ . This result in  $S'$  being moved to lower  $k_x$  and as a result,  $G(x_1)$  shifts towards a positive value. The higher the value of  $|n|$ , the lower total power of the wave numbers in  $IE''k_x^4$ . For the situation above,  $|n|$  was small enough such that  $G(x_1) \leq 0$ . However, there exist some limit where the total power of the wave numbers in  $IE''k_x^4$  gets so small that the resulting  $G(x_1) > 0$ , and thus  $\Omega > 1$ . This is the case even though there is no foundation damping present, which contradict our hypothesis.

In figure 22.10a, a plot of  $\Omega$  for the case of an elastic foundation is shown for two parametersets. The first was the default parameters which had the parabolic dashpot coefficient  $h = 0.22$ . Here the value of  $\Omega$  was always below 1, in agreement with the hypothesis. The second plot showed a parameterset where  $h$  was changed to  $h = 0.5$  and as a result, there existed an area where  $\Omega > 1$ , even through no foundation damping was present. Thus the pavement response simulated with this particular parameterset did not obey the hypothesis.

The behaviour of the right hand side of  $E''$  for the Huet-Sayegh model was determined by some combination of the parabolic coefficients  $h$  and  $k$ . In figure 22.10b, a double logarithmic plot of  $E''$  was shown, illustrating a clear difference in  $n$  for the two cases in figure 22.10a. Through numerical analysis the value of  $n$  in the limit where the hypothesis stopped being true, was found to be  $n_{lim} = -0.37$  (illustrated in figure 22.10b using  $h=0.37$ ). This meant that for  $|n| < |n_{lim}|$  the hypothesis held and for  $|n| > |n_{lim}|$  the hypothesis did not hold. It must be emphasized that the particular value of  $n_{lim}$  depended on the given choice of parameter values and thus was not a general value. Nonetheless, this showed that there existed some limit for which the behaviour of  $E''$  on the right hand side of the loss peak became so steep that the resulting behaviour of  $S'$ , and thus  $G(x_1)$ , influenced the pavement response in a similar way as foundation damping did. Thus, if we were within this range of parameter values, it was not possible to estimate the origin of dominating damping based on the value of  $\Omega$ .

It is worth noting that for the simple Maxwell model often used in this thesis,  $n=-1$  (fig. 22.10b). Thus, pavement simulations using this, will have an range of  $\tau$  values where the hypothesis is not valid.

#### 22.2.1 Conclusion on model study

By use of a model study, we have showed how the pavement deflection slope can be divided into a symmetric ( $H(x)$ ) and non-symmetric ( $G(x)$ ) contribution. Viscoelastic effects from both the beam and foundation was included in the non-symmetric term, but in different ways. Consequently, they influenced the pavement response differently.  $G(x)$  was evaluated in the point  $x = x_1$ , which is the location of the maximum and minimum

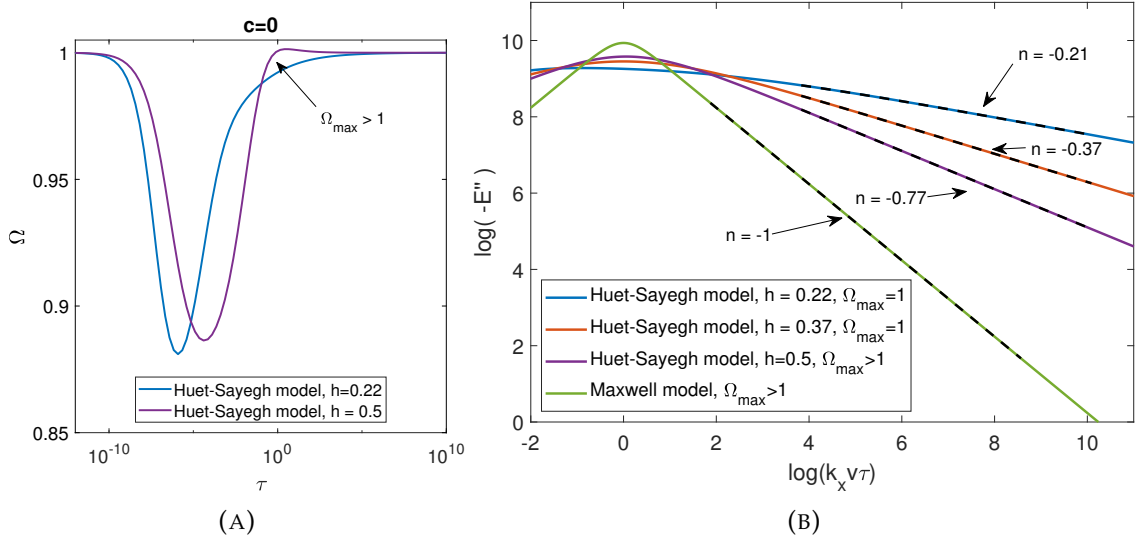


FIGURE 22.10: A)  $\Omega$  as a function of  $\tau$  for the Huet-Sayegh model with parabolic dashpot coefficient  $h=0.22$  and  $h=0.5$  respectively. B) log-log plot of  $E''$  using the Huet-Sayegh model with different values of  $h$  and the Maxwell model. If not otherwise specified, the used parameter values are the default values listed in section 16.2.

of  $H(x)$ . For small perturbations in the symmetric solution ( $G(x_1) \ll 1$ ), a correlation between  $\Omega$  and  $G(x_1)$  was found where  $G(x_1) > 0 \Rightarrow \Omega > 1$  and  $G(x_1) < 0 \Rightarrow \Omega < 1$ .

The different types of damping was found to affect  $G(x_1)$  through  $S'$ ,

$$S' = \frac{-Fk_x(IE''k_x^4 - cvk_x)}{(IE'k_x^4 + Gk_x^2 + k)^2 + (IE''k_x^4 - cvk_x)^2}. \quad (22.37)$$

It was found that the crucial factor that distinguish the two types of damping was the power to which  $k_x$  was raised in the term  $(IE''k_x^4 - cvk_x)$ . This determined whether  $G(x_1)$  was positive or negative, and thus if  $\Omega$  was above or below 1. In general, we found that increasing foundation damping resulted in an increasing  $\Omega$ , whereas increasing beam damping resulted in a decrease in  $\Omega$ . Thus validating the hypothesis. However, it was found that there existed situations where the behaviour of  $E''$  made  $G(x_1) > 0$ , even though only beam damping was present, and in these cases the hypothesis was not true. Such situations arose when  $E''$  within the sensitivity interval had a negative slope which was "too steep", resulting in the overall power of  $k_x$  in  $IE''k_x^4$  being below some threshold. The exact limit for how low the power of  $k_x$  can get before the hypothesis breaks down depended on the used parameter values and was not investigated here. However, we found that  $E''$  described by the Maxwell model would always have this feature.

Reported empirical values in the literature for the loss modulus showed that the Maxwell model was a bad fit for the  $E''$  behaviour (Xu and Solaimanian, 2009). One reason was its

simple nature resulting in a steep a slope of  $E''$  both in front and behind the loss peak. In general, the slope on the right hand side of the loss modulus for real asphalt mixes was often reported to have a low slope and thus not believed to be within the parameter value range where the hypothesis did not hold.

## 22.3 Study of hypothesis using Viscowave II-M

The model used in the analysis above was a fairly simple one-dimensional foundation model. We now aimed to investigate if the overall conclusions made above (increased viscoelastic behaviour in the asphalt layer resulted in a decrease in  $\Omega$ ) could be reproduced using a more complex pavement response model. For this purpose, the pavement response to a moving load of three different pavements were simulated using the time-domain based viscoelastic solver ViscoWave II-M, developed at Michigan State University (Lee, 2013; Balzarini et al., 2017b). This program was previous used and described in section 10.4.1 and is explained in more detail in appendix B.

For the following analysis, two different pavements were simulated. Both pavements consisted of three layers, representing an asphalt layer, a base layer, and a subgrade layer. The parameters for the structure (height, elastic moduli, Poisson's ratio and density) were chosen to be typical values for these kinds of pavement layers, and they are listed in table 22.2 (Nielsen et al., 2020b). The base and subgrade was assumed semi-elastic as some damping was needed in order to stabilise the numerical solution. The asphalt layer was assumed viscoelastic and its viscoelastic properties were described by the relaxation modulus  $E(t)$ .

We chose to simulate pavements with the same mechanical characteristics in the base and subgrade layer, and different viscoelastic properties of the asphalt layer. The viscoelastic properties were described through  $E(t)$ , given by

$$\log(E(t)) = c_1 + \frac{c_2}{1 + e^{(-c_3 - c_4 \log(t_R))}}, \quad (22.38)$$

$$\log(t_R) = \log(t) - \log(a_T), \quad (22.39)$$

where  $c_1, \dots, c_4$  are the sigmoid coefficients,  $t_R$  is the reduced time and  $a_T$  is the shift factor (Balzarini et al., 2019).

In order to ensure realistic  $E(t)$  curves, the parameters for the relaxation modulus were taken from back-calculated falling weight deflectometer tests on road segments located in California (Balzarini et al., 2019). On figure 22.11, a plot of  $E(t)$  for the two asphalt layers used in this analysis is seen (parameter values listed in table 22.3). These were chosen as they had approximately the same  $E_\infty$  value, but different  $E_0$  and thus also a different slope within the two plateaus. In general, the value of  $E_0$  was an indication on the stiffness of the asphalt layer. Thus we expected PAV2 to behave stiffer than PAV1. Likewise, will the slope of the curve provides an indication on the viscous behaviour of the asphalt layer. The smaller a difference between  $E_0$  and  $E_\infty$  (hence a small slope), the more elastic

TABLE 22.2: Mechanical characteristics for the simulated pavement. All pavement structures are made of three layers, each characterized by their Poisson's ratio ( $\nu$ ), mass density ( $\rho$ ), average thickness ( $h$ ) and the relaxation modulus ( $E$ ). The relaxation modulus for the asphalt layer is given by equation (22.38).

Asphalt
$E(t)$ $\nu = 0.35$ $\rho = 2322.7 \frac{\text{kg}}{\text{m}^3}$ $h = 0.15 \text{ m}$
Base
$E_2 = 124.3 \text{ MPa}$ $\nu = 0.35$ $\rho = 2082.4 \frac{\text{kg}}{\text{m}^3}$ $h = 0.3 \text{ m}$
Subgrade
$E_3 = 65.4 \text{ MPa}$ $\nu = 0.45$ $\rho = 1762 \frac{\text{kg}}{\text{m}^3}$ $h = \infty$

a behaviour is seen in the pavement. Based on these criteria, we would expect PAV1 to have a more soft and elastic behaviour than PAV2.

In figure 22.12, a plot of the deflection basin and slope is shown for the simulated pavements. As expected, we found that PAV2 had a stiffer behaviour than PAV1, seen by the magnitude of the maximum deflection. Furthermore, the maximum deflection for PAV2 ( $x = -0.12\text{m}$ ) was located further away from the load ( $x=0$ ) than for PAV1 ( $x = -0.07\text{m}$ ). This, combined with having maximum and minimum deflection slope located far from the load, indicated increased asphalt damping.

As a consequence, if the hypothesis about increased asphalt damping being expressed in the  $\Omega$  value was true, then

$$\Omega_{PAV2} < \Omega_{PAV1}. \quad (22.40)$$

In table 22.3, the calculated values of  $\Omega$  are listed, and the relation above was found to hold.

It should be emphasized that for this kind of multi-layered models where the viscous behaviour of the asphalt layer were controlled by  $E(t)$ , it was not trivial to only increase damping of the asphalt layer and hold all other parameters fixed. As the top layer stiffness was correlated with the damping and controlled by  $E(t)$  as well, the relative stiffness between the layers would change when damping changed and consequently affect the pavement response. Nonetheless, the analysis above illustrated that using the ratio between maximum and minimum pavement deflection slope ( $\Omega$ ) as an indicator of the

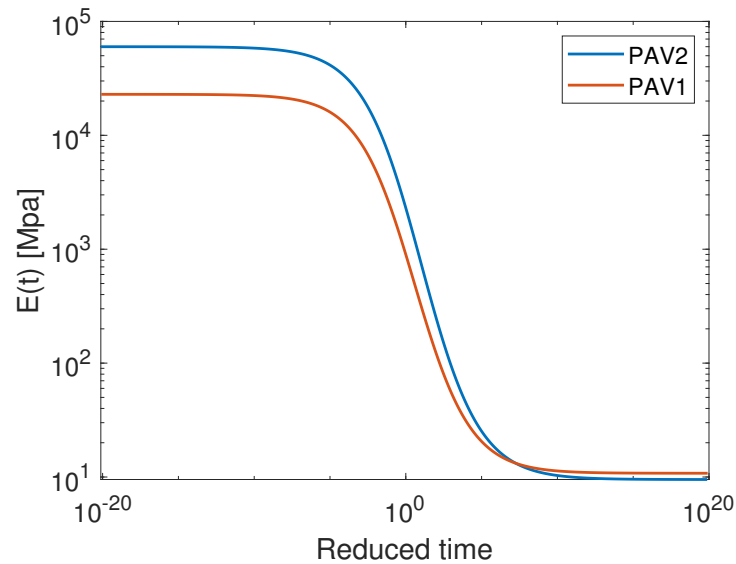


FIGURE 22.11: Relaxation modulus  $E(t)$  for the two pavements PAV1 and PAV2. The parameters for the relaxation moduli are chosen among back-calculated falling weight deflectometer tests on road segments located in California (Balzarini et al., 2019). They are chosen such that  $E_\infty$  is approximately the same, but  $E_0$  varies resulting in different behaviour with respect to stiffness and elasticity.

origin of damping was valid also for a complex layered halfspace model, and thus was not just an artifact of the simple two layered beam model.

It is worth noticing that  $\Omega$  for the simulated pavement structures here was always above 1. The same was true when evaluating TSD data, as seen in the following section.

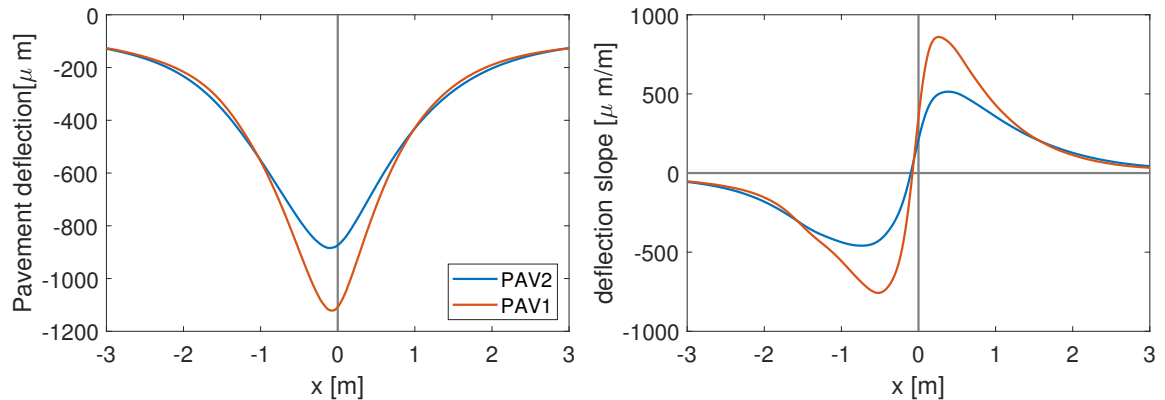


FIGURE 22.12: Pavement response to a moving load for the three simulated pavement structures. Parameter values for the structures are listed in table 22.2 and 22.3. The maximum deflection was located at  $x = -0.07\text{m}$  for PAV1 and  $x = -0.12\text{m}$  for PAV2.

TABLE 22.3: Sigmoidal parameter values used in  $E(t)$  to simulate the four different pavement structures. In addition, characteristic for the different simulated pavements responses in figure 22.12 and the calculated  $\Omega$ .

	Pavements	
	PAV1	PAV2
<u>Sigmoid coefficients</u>		
$c_1$	1.033	0.978
$c_2$	3.327	3.8
$c_3$	0.311	0.521
$c_4$	-0.54	-0.519
Shift factor $\log(a_T)$	0.09	0.12
<u>E(t) characteristics</u>		
$E_0$ [Mpa]	22,906	59,970
$E_0 - E_\infty$ [Mpa]	22,895	59,960
<u>Pavement response characteristics</u>		
Asphalt stiffness	—————>	
Amount of asphalt damping	—————>	
Amplitude ratio $\Omega$	1.14	1.12



## 22.4 $\Omega$ in TSD data

It was shown that evaluating  $\Omega$  could be used as a qualitative method to examine from which layer the dominating damping was coming. We here use this result on the TSD data presented in section 9.

In section 20, the TSD data measured in Måløv at 18°C was analysed by use of the two layered pavement response model. One of the conclusions from the analysis was that damping from the foundation was the most significant source of damping for this particular road segment. Accordingly, we would expect  $\Omega > 1$  for this data set.

On figure 22.13, a plot of  $\Omega$  calculated based on the model fit was shown for all measurements at 18°C. A clear trend in  $\Omega$  was seen with a mean value of  $\Omega = 1.4$ . The area between 0.5-1 km. had a significantly different behaviour than the rest of the road segment as  $\Omega$  dropped to around 1. Earlier investigations of this area (section 20.6) had shown that the top layer parameters were more dominating here which was reflected in the value of  $\Omega$ .

The effect of temperature was also studied as  $\Omega$  was calculated based on the model fit to data measured at 35°C. Overall, we found that the average value of  $\Omega$  decreased, thus damping in the top layer became increasingly dominant. When temperature of the asphalt layer increased, it causes a shift in the sensitivity interval to lower frequencies. Whether this result in more or less damping expressed in the top layer, depended on the exact location of the sensitivity interval with respect to the loss modulus peak. Analysis in section 20 indicated that the sensitivity interval was located on the left side of the loss peak, and consequently, we would expect an increase in the amount of damping expressed by the top layer. However, when fitting the model to data at 35°C, we found a large decrease in the estimated value of the foundation damping. Thus the results in figure 22.13 indicated that the foundation damping was decreased more than the top layer damping when temperature increased, and as a result  $\Omega$  decreased.

Common for both data series was that the value of  $\Omega$  does not change a lot during the 10 km road segment measured on. This was consistent with the theory that the foundation damping was controlling the value of  $\Omega$ , as this was estimated to be almost constant over the road segment.

In conclusion, analysing the value of  $\Omega$  agreed with results obtained through other analyses made previously on the same data set. This supported the conclusion that evaluating  $\Omega$  can be used as a qualitatively measure of where the origin of the most dominating pavement damping was located. Using the method with  $\Omega$  had the advantage that it was a fairly easy method compared to the comprehensive analyses made in section 20.

When evaluating  $\Omega$  above, we used a model to fit to data. Ideally,  $\Omega$  could be evaluated without any modelling involved, as this would remove any underlying modelling assumptions. However, as the minimum and maximum deflection slopes often were not fully captured in data, calculating  $\Omega$  based on the data-points could result in incorrectly values. This might result in a wrong conclusion about the origin of damping. An example

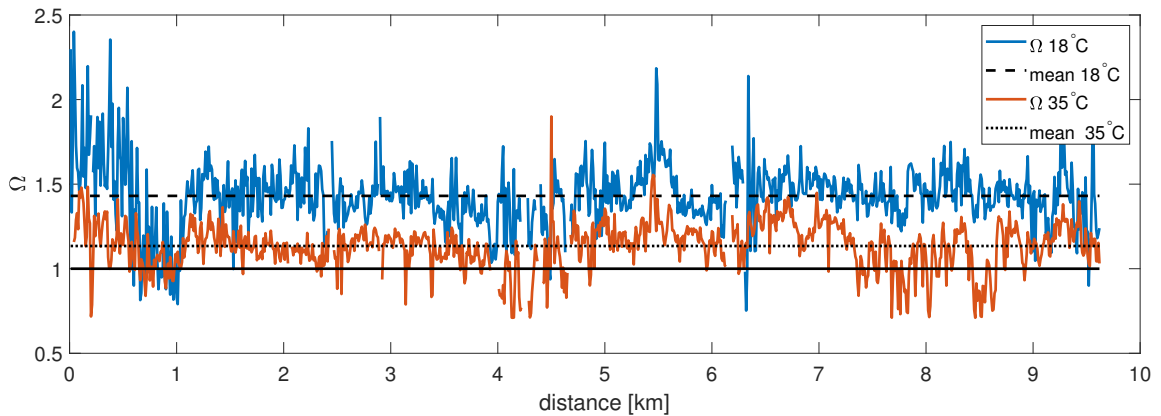


FIGURE 22.13: Calculated  $\Omega$  values based on model fit to all Måløv data at 18°C and 35°C. The mean value for each data series is indicated with dotted lines. An overall decrease in  $\Omega$  is found when the road surface temperature increases, indicating that the dominating viscoelastic effects is affiliated with the top layer.

where this was the case is shown in figure 22.14. Here the maximum was fully captured by the sensors, but the minimum was not. As a result, the calculated  $\Omega$  based on data and model fit was very different.  $\Omega_{data} > 1$  and hence we would conclude that the damping originated from the foundation, whereas  $\Omega_{model} < 1$  indicated that the dominating damping in fact originated from the asphalt layer. Consequently, some modelling of data was recommended in most cases if the consistent  $\Omega$  value was to be obtained.

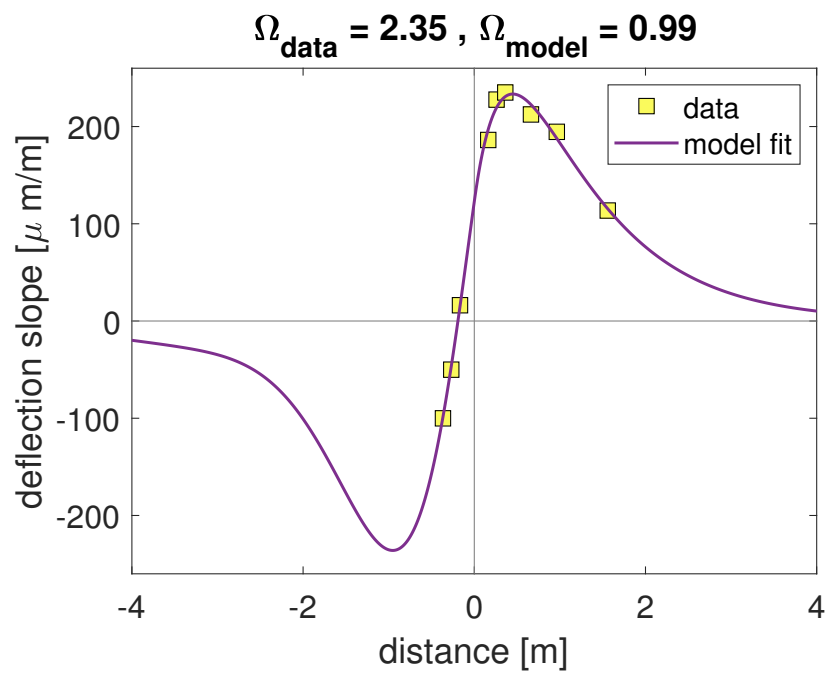


FIGURE 22.14: Example of data set where calculating  $\Omega$  based on the data-points and the best fitted model yielded two different results. This is due to the minimum and maximum deflection slope often is not fully captured in data. Thus, calculating  $\Omega$  based on the data-points can result in incorrectly values.



**Part VI**  
**Summary**



## Chapter 23

# Summarising discussion and outlook

### 23.1 Measuring total and structural rolling resistance

The starting point of this PhD project, was to develop a method for measuring the total and structural rolling resistance simultaneously. Based on this, we aimed to evaluate, not just the total rolling resistance of a given pavement section, but also how big a contribution arises from the structural rolling resistance.

The theoretical principle behind measuring the total rolling resistance of a heavy vehicle was based on the relationship between longitudinal deformation of the rear-end tire axle and the rolling resistance loss. In practice, deformation of the tire-axle in the longitudinal direction was measured using a circuit of strain gauges mounted on the rear-end axle, near the tires. Using the developed measurement setup, a set of preliminary experiments were conducted with the purpose of evaluating the reproducibility of the method. Analysis of data revealed a systematic error in the measurements caused by temperature effects in the tire axle. A simple temperature compensation of the calibration procedure was developed and tested. However, this was insufficient to compensate, to a high enough degree, for temperature effects.

We speculated that a temperature gradient within the axle was present and thus a setup including multiple temperature sensors should be developed to study the problem. Consequently, we concluded that a proper understanding of temperature effects in the axle should be obtained before reliable and reproducible measurements can be made. As a result, no useful measurements of the total rolling resistance was obtained.

Concurrent while working on the method for measuring the total rolling resistance, a simple method for measuring the structural rolling resistance (SRR) was developed. This method was based on the relation between SRR and the slope of the deflection basin under a moving load. For measuring the pavement deflection underneath a moving tire, we used the Traffic Speed Deflectometer (TSD) technology, which provided high resolution measurements of the pavement deflection slope. The method was proven to obtain highly reproducible measurements of SRR (standard deviations from three repeated measurements of 4-10%) with a high spatial resolution. Using a simple pavement response model to estimate the pavement deflection slope underneath the load, the method was tested on an approximately 10 km long road segment. The same section was measured

with road surface temperature 18°C and 35°C. The measured structural rolling resistance coefficient ( $C_{SRR}$ ) varied considerably over the traveled distance, with average values in the range 0.01% – 0.03% of the load for 18°C and 0.01% – 0.05% of the load for 35°C. However, these variations were found to be highly reproducible with low standard deviations, even in regions where the  $C_{SRR}$  changed rapidly with distance. This demonstrated that the method was robust and could measure the  $C_{SRR}$  values of the road precisely, with high spatial resolution even under changing pavement conditions.

The influence of temperature on SRR was studied both in Måløv data with an increase in road surface temperature from 18°C to 35°C, and in Finland data with an increase from 14°C to 22°C. For both studies, an increase in SRR was seen when temperature increased. For Måløv data, the increase was on average 59%, with a few places showing a 400% increase. Based on findings in literature, an increase in SRR with temperature was expected (Sandberg et al., 2012). However, evaluating the individual data sets revealed a large difference in how SRR increased with temperature. We found that structural characteristics for the given pavement section determined how big an increase with temperature was seen. In the Måløv data, a section of the road was found to have a stiffer foundation behaviour than the rest, and here temperature had less of an effect on the measured SRR.

The effect of driving velocity on SRR was studied by analysing Finland data. Through this, velocity was found to have significant influence on the measured  $C_{SRR}$ . This was an unexpected result, as asphalt is a viscoelastic material and thus the driving velocity was expected to affect the stiffness expressed by the top layer. A potential explanation for the observed behaviour was that the sensitivity interval with respect to the complex modulus curve was located at the lower elastic plateau. Consequently, a change in velocity had little effect on the resulting storage and loss modulus. However, when fitting the model to Finland data, we did indeed find a change in both storage and loss modulus. Another potential explanation, was that the structural rolling resistance was primarily determined by the foundation damping, and if this was independent of driving velocity, so was SRR. Having the foundation damping as the primary source of damping was established for the Måløv data, and thus could be a possible explanation. Either way, we concluded that even with large driving velocity changes from 5 to 80 km/h the calculated SRR remained unaffected.

The effect of velocity on the overall pavement deflection was found to be localized around the load, where an increased velocity reduced the magnitude of the measured slopes. A consequence of this was that if the influence of velocity on the pavement deflection was evaluated by looking at a single point far away from the load, e.g. sensor 7 located 450mm away from the load, no changes was seen. In contrast, a change with velocity was observed if evaluated close to the load.

The found values of SRR had a magnitude which indicated a small contribution to the overall rolling resistance. As we were not able to obtain reproducible results of the total rolling resistance, a direct comparison could not be made. However, using values found by Sandberg et al. (2011b), the average rolling resistance of a truck is estimated to be 3.8% of the load. If this value is used, the found SRR values were 0.3%-1.3% of the total



rolling resistance. Even though this only provided a rough estimate of a realistic value, it indicated that the contribution from structural effects is very small. For future work, measurements of SRR on several different road sections are desired. Using these, a more general conclusion about the magnitude of SRR and structural effects contribution to the overall rolling resistance could be determined.

Comparison of the measured values of SRR with values found in literature was difficult, as no direct measurements of SRR had been conducted before. Investigations of the structural effects on the driving resistance have been conducted by comparing fuel consumption measurements on flexible (asphalt) and rigid (concrete) pavements. Results from these kind of studies spans between finding no significant effect and finding up to 4% increase in fuel consumption (Bienvenu et al., 2013; Balzarini et al., 2018; Zaabar and Chatti, 2014; Akbarian et al., 2012). All in all, in agreement with our findings of a small effect.

The structural rolling resistance was also investigated through simulation studies in the literature. However, a direct comparison with our work was not suitable as SRR was highly dependent of the structural characteristics of the simulated pavement.

### 23.1.1 Discussion of the simple approach

A key principle behind the our approach to calculating SRR was that it should be easy to apply with TSD data. As a result, the first simple approach presented included no model fit to data. Instead, the deflection slope underneath the tire was assumed linear and, as a result, could be found by a linear interpolation between the sensor points closes to the load. The strength of this method was that it required no knowledge about the structure or mechanical properties of the pavement measured on. Furthermore, the use of the TSD vehicle made data collection both fast and very precise. However, assuming that the deflection slope underneath the load was linear was not always valid, and as a consequence, the calculated SRR values were not always accurate.

The validity of using a linear interpolation was investigated first through a numerical study using the sophisticated three layered pavement response model Viscowave II-M. From this, we concluded that using a linear interpolation in some cases underestimates the structural rolling resistance by as much as 50%. Subsequently, the use of linear interpolation was investigated by fitting the developed simple one-dimensional pavement response model to data and comparing the calculated  $C_{SRR}$ . Based on this, we developed a set of general guidelines, describing when the linear interpolation method was valid. These were based on the qualitative behaviour of the maximum and minimum deflection slope. In general, we found that when the minimum was closer to the load than the nearest sensor point behind the load, the method tended to overestimate the SRR. The opposite was seen in the case where the maximum was closer to the load than the nearest data point, and the minimum simultaneously was well resolved in the data points behind the load. In this case, the simple approach tended to underestimate SRR. Lastly, in the

case where both the maximum and minimum were located far away from the load (compared to the sensor location), and thus were fully resolved in the data points, the linear interpolation method provided a good estimate of the SRR. For the data series presented in this thesis, most of the data sets belonged to the second case, and as a result the simple approach provided a lower limit of the SRR.

By analysing the result of fitting the simple pavement response model to data, a correlation between the x-location of the maximum and the relative stiffness between the asphalt layer and the foundation was found. Consequently, data sets where the maximum deflection was located far away from the load corresponded to having a relatively stiff top layer compared to the foundation. In these situations, the corresponding deflection basin was broad and shallow, and using linear interpolation to estimate the deflection slope underneath the tire was valid. In a similar fashion, when the deflection basin became narrow and deep, the method was found to give increasingly inaccurate estimates of SRR.

In conclusion, we showed that using linear interpolation to estimate the deflection slope underneath the tire was valid when the asphalt layer behaved stiff compared to the underlying foundation. The softer a behaviour in the top layer, the more inaccurate estimates the simple approach gave. In these situations, we recommended using a simple pavement response model to obtain the pavement deflection slope underneath the load. However, it should be noted that SRR values obtained using a model fit provided values within the same order of magnitude as results obtained using the linear interpolation method. Consequently, the simple approach could be used as a fast method for easily calculating the SRR for large quantities of TSD data. If more accurate results were desired the more sophisticated method using a pavement response model should be used.

## 23.2 Characterising structural properties based on model fit to TSD data

The developed pavement response model was based on physical elements and, as a consequence, it could be used to analyse the measured pavement deflection slopes and provide information about the structural characteristic of the pavement. This was done by fitting the model to data and using the resulting estimated parameter values. Overall, the model was found to provide a good fit to data, even for warm road temperatures.

We investigated if the division of data based on empirical observations could be related to structural changes of the pavement. The deflection slope curve was characterised by having a maximum in front of the load and a minimum behind the load. Based on the x-position and the amplitude of the maximum deflection, TSD data measured in Målöv were divided into six data groups. Using the estimated parameter values obtained in the fitting procedure, a simulated pavement response curve was created for each data set and, as a result, more detailed information about the maximum and minimum were obtained. Comparing the characteristics of the maximum and minimum seen across groups, with

the estimated parameter values showed a correlation between the relative stiffness of the top and underlying layers ( $\frac{k}{IE}$ ) and the movement of the maximum closer to the load. From the estimated parameters, the foundation stiffness  $k$  was found to be approximately constant along the measured pavement section, and thus we concluded that the changes in maximum position observed in data was due to a change in stiffness of the top layer. An increase in top layer stiffness was manifested in the pavement deflection by a broad and shallow deflection basin. In addition, by analysing the amplitudes of the maximum deflection we concluded that there where a shift in the underlying foundation structure after around 2.5 km, resulting in a significantly higher maximum amplitude in data sets located after the shift.

For increased road temperature, a similar change in the minimum deflection slope was also observed, where the  $x$ -position are moved closer to the load. When a data set contains a minimum close to the load (with respect to the sensor location), this was often accompanied by a maximum close to the load (data group 1). The corresponding pavement deflection basing for this behaviour was characterised by being narrow and steep. A physical interpretation of this behaviour was that the top layer became increasingly soft and, as a consequence, deformed underneath the load. We hypothesised that the validity of assuming a stiff in-compressible top layer broke down in these cases, and proposed that a deformable top layer should be considered in order to obtain a better fit to data.

### 23.2.1 Characterising damping based on deflection slope features

An important result about the correlation between the relative amplitudes of the maximum and minimum deflection slope ( $\Omega$ ) and the origin of damping was derived in chapter 22. The motivation for this analysis arose from observing that adding damping to the top layer and the foundation in the simple response model affected the resulting pavement deflection slope curve differently. When damping was included in the beam, the maximum and minimum slope peaks were shifted downwards compared to a purely elastic case. Conversely, when damping was included in the foundation they were shifted upwards.

This phenomenon was studied primarily using the simple one-dimensional pavement response model, as this had an analytical expression in the wave number domain. As a result, an understanding of the mechanisms behind the different sources of damping, and how they affected the deflection slope curve, was obtained. Using Fourier analysis, we found that the asymmetric behaviour in the deflection slope curve was caused by the real part of the Fourier transformed deflection slope. Analysis of this revealed that the fundamental difference between the two types of damping are the power to which  $k_x$  is raised in the term  $IE''k_x^4 - cvk_x$ . As a result, when foundation damping (represented by  $c$ ) was increased,  $\Omega$  was increased, and vice versa for beam damping.

Results obtained through the simple pavement response model were attempted verified using the more sophisticated multi-layered model Viscowave II-M. However, using a more complicated model made it hard to change the different layers specific damping

without changing other characteristics as well. As a consequence, it was difficult to recreate the extreme cases tested by the simple model. Nonetheless, the underlying correlation between the origin of damping and  $\Omega$  was demonstrated, suggesting that this was not just a feature of the simple model.

The correlation between the source of dominating damping and  $\Omega$  was an easy qualitative way to examine pavement damping behaviour based on TSD data behaviour. However, it required a simple model fit to data in order to provide information about the minimum and maximum peak. Ideally, a measure which required no modelling at all would be desirable.

The method was tested on Måløv data and showed that the main damping contribution originated in the foundation. This result was also obtained using a different analysis, in which different simplified models were fitted to Måløv data and compared. The result of this analysis showed that foundation damping was the most dominating source of damping for this particular road segment. In fact, the top layer acted almost elastic in a majority of data. The results emphasised that foundation damping had a significant influence on the pavement response and that it should not be neglected when modelling the pavement response. Furthermore, the results indicated that potential improvement of the pavement with respect to minimizing the energy dissipation should include the underlying layers, as we hypothesised that improvement of the asphalt layer alone would not reduce all pavement damping.

The presented results were based on measurement of a single road segment, and for future work we recommend conducting similar analysis for other road segments in order to evaluate if this is a general trend.

### 23.2.2 Creating asphalt master curves based on TSD data

With the Finland data, we had a unique set of deflection slope measurements made at several driving velocities and temperatures, enabling us to characterise the top layer damping. A pilot study was presented in section 21.2 where this specific data was used to create a complex modulus master curve, characterising the viscoelastic behaviour of the asphalt layer. Such master curves are traditionally made based on laboratory test, where a sample of the asphalt mix is required. Consequently, it was advantageous if these could be made based on TSD measurements, as this is a nondestructive measurement technique easily applicable to large road segments.

In order to create the master curves, we extracted information about the behaviour of the storage and loss modulus of the asphalt mix. This was done using the notion of a sensitivity interval developed through the theoretical sensitivity analysis of the model. It was derived that, due to the model being in a moving reference frame, only the behavior of the asphalt complex modulus within some range of wave numbers influenced the modelled pavement response. As a result, we could extract a characteristic value for the loss and storage modulus for each velocity-temperature configuration. This was done using two different models; the Maxwell model and the simple nonphysical hysteretic model. The two approaches provided comparable results, with the Maxwell model proving slightly

better. The Time-Temperature Superposition principle was applied to the obtained loss and storage modulus values, using a reference temperature of 24°C .

Overall, the proposed procedure for creating asphalt complex modulus master curves based on TSD measurements was successful. However, the method was highly dependent on the behaviour of the complex modulus behaving approximately constant within the sensitivity interval. If this was not the case, the estimated characteristic values may not be representable. As this was a pilot study, only a small range of frequencies were covered. For future work, a more comprehensive master curve should be created using measurements at several temperatures. This would ensure a better basis for comparison with literature studies.

### 23.2.3 Model validity

In this thesis, a simple pavement response model used for fitting the measured TSD data was developed. The model consisted of a viscoelastic Euler-Bernoulli beam on top of a damped Pasternak foundation. A fundamental assumption behind an Euler-Bernoulli beam was that the cross section did not deform when the beam bends. This assumption was complied with by assuming a stiff top layer compared to underlying layers for the pavements measured. Consequently, we assumed that all deformation took place in the foundation. However, analysis of the deflection slope data indicated that for some data sets, increased road temperature resulted in a soft behaviour of the top layer and consequently, a deformation of this layer. In these situations, the validity of using an Euler-Bernoulli beam model should be reconsidered.

For further development of the model, we proposed a change in how the top layer is modelled such that potential deformations of this are included. One approach could be to consider the top layer as an elastic or viscoelastic half-space. Including this into the model might increase the ability of the model to mimic the very steep and pointy behaviour of the maximum and minimum seen in some data sets. Another approach would be to replace the simple Euler-Bernoulli beam with an Timoshekno beam, which allows for shear deformation of the beam (Saito and Terasawa, 1980; Ding et al., 2014). However, the simple pavement response model used in this thesis overall provided a good fit to data, both at 18°C and 35°C , as indicated by  $R^2$  values close to one.

Based on an analysis of the estimated parameter values obtained by fitting the model to Finland data, an alternative model for modelling foundation damping was proposed. In the original model, foundation damping was modelled as viscous damping by a set of uniformly distributed dashpot elements, described by the viscous damping coefficient  $p$  per unit length  $c$ . Fitting the model to data at different driving velocities revealed a clear dependence of velocity in the estimated values of  $c$ . This contradicted the assumption that the damping coefficient should be constant and as a result, indicating that using the simple Kelvin-Voigt model to describe foundation damping was not appropriate. Instead, a parabolic dashpot was found to characterise damping well. However, this model required information about the damping coefficient over a range of different driving velocities, and thus it was not possible to characterise the viscous behaviour of the parabolic dashpot

based on a single measurement. Consequently, implementing this into the pavement response model would not make a difference when fitting TSD data sets at a single velocity, as in the case of Måløv data. In fact it would introduce a set of insensitive parameters. Instead the simple nonphysical hysteretic model was proposed, and a fit to data using this revealed a higher degree of non systematic behaviour with velocity. As a result, we proposed that the hysteretic damping model should be used to model foundation damping when no detailed information about velocity dependency was available.

### **23.3 Conclusive remarks**

In conclusion, we have demonstrated how measurements of the pavement deflection slope, obtained with the Traffic speed deflectometer (TSD) technology, can be used to analyze the measured pavement. We have presented a novel way to measure the structural rolling resistance directly in an easy and fast way. The method can become a vital tool in the ongoing discussion of the importance of structural effects on the rolling resistance loss. Furthermore, the use of TSD measurements makes it suitable for evaluating large quantities of pavements. In addition, it was illustrated how structural characteristics about the measured pavement could be extracted from the TSD data, by evaluating the deflection slope behaviour. This provided a simple and accessible way to evaluate pavement properties without using a sophisticated model procedure and consequently, changes in damping and relative stiffness of the pavement layers could easily be evaluated.

# Bibliography

- Adams, R. A. (1999). *Calculus: A complete course*. 4th edition.
- Aidara, M. L. C., Ba, M., and Carter, A. (2015). Choice of an Advanced Rheological Model for Modeling the Viscoelastic Behavior of Hot Mixtures Asphalt (HMA) from Senegal (West Africa). *Open Journal of Civil Engineering*, 05(03):289–298.
- Akbarian, M., Moeini-Ardakani, S. S., Ulm, F., and Nazzal, M. (2012). Mechanistic Approach to Pavement-Vehicle Interaction and Its Impact on Life-Cycle Assessment. *Transportation Research Record: Journal of the Transportation Research Board*, 2306:171–179.
- Akbarian, M. and Ulm, F.-J. (2012). Model based pavement-vehicle interaction simulation for life cycle assessment of pavements. Technical report.
- Andersen, L. G., Larsen, J. K., Fraser, E. S., Schmidt, B., and Dyre, J. C. (2014). Rolling Resistance Measurement and Model Development. *Journal of Transportation Engineering*, 141(2):1–10.
- Balzarini, D., Chatti, K., Zaabar, I., Butt, A. A., and Harvey, J. T. (2019). Mechanistic-Based Parametric Model for Predicting Rolling Resistance of Flexible Pavements. *Transportation Research Record: Journal of the Transportation Research Board*, 2673(7):341–350.
- Balzarini, D., Zaabar, I., and Chatti, K. (2017a). Impact of concrete pavement structural response on rolling resistance and vehicle fuel economy. *Transportation Research Record: Journal of the Transportation Research Board*, 2640(1):84–94.
- Balzarini, D., Zaabar, I., and Chatti, K. (2018). Effect of Pavement Structural Response on Rolling Resistance and Fuel Economy using a Mechanistic Approach. *Advances in Materials and Pavement Performance Prediction*, 10:49–51.
- Balzarini, D., Zaabar, I., Chatti, K., and Losa, M. (2017b). Impact of Flexible Pavement Structural Response on Rolling Resistance and Vehicle Fuel Consumption. In *World Conference on Pavement and Asset Management*.
- Bauchau, O. and Craig, J. (2019). *Structural Analysis with Applications to Aerospace Structures*, volume 53. Springer.
- Bazi, G., Hajj, E. Y., Ulloa-Calderon, A., and Ullidtz, P. (2018). Finite element modelling of the rolling resistance due to pavement deformation. *International Journal of Pavement Engineering*, pages 1–11.

- Beskou, N. D. and Theodorakopoulos, D. D. (2011). Dynamic effects of moving loads on road pavements: A review. *Soil Dynamics and Earthquake Engineering*, 31(4):547–567.
- Bienvenu, M., Jiao, X., and Assistant, G. R. (2013). COMPARISON OF FUEL CONSUMPTION ON RIGID VERSUS FLEXIBLE PAVEMENTS ALONG I-95 IN FLORIDA. Technical report.
- Bolton, M. and Wilson, J. (1990). Soil Stiffness and Damping. In *International Conference on Structural Dynamics*, pages 209–216.
- Chatti, K., Kutay, M. E., Lajnef, N., Zaabar, I., Varma, S., and Lee, H. S. (2017). Enhanced Analysis of Falling Weight Deflectometer Data for Use With Mechanistic-Empirical Flexible Pavement Design and Analysis and Recommendations for Improvements to Falling Weight Deflectometers. Technical report, Michigan State University.
- Cheneler, D. (2016). *Viscoelasticity of Polymers: Theory and Numerical Algorithms*, volume 26.
- Chupin, O., Piau, J.-M., and Chabot, A. (2010). Effect of Bituminous Pavement Structures on the Rolling Resistance. In *11th International Conference On Asphalt Pavements*, pages pp.1287–1296.
- Chupin, O., Piau, J. M., and Chabot, A. (2013). Evaluation of the structure-induced rolling resistance (SRR) for pavements including viscoelastic material layers. *Materials and Structures/Materiaux et Constructions*, 46(4):683–696.
- Coleri, E. and Harvey, J. T. (2017). Impact of Pavement Structural Response on Vehicle Fuel Consumption. *Journal of Transportation Engineering, part B: pavements*, 143(1).
- Craig Jr., R. R. (2000). *Mechanics of Materials*. John Wiley & Sons, Inc, second edition.
- Di Graziano, A., Marchetta, V., and Cafiso, S. (2020). Structural health monitoring of asphalt pavements using smart sensor networks: A comprehensive review. *Journal of Traffic and Transportation Engineering (English Edition)*, 7(5):639–651.
- Di Paola, M., Heuer, R., and Pirrotta, A. (2013). Fractional visco-elastic Euler-Bernoulli beam. *International Journal of Solids and Structures*, 50(22-23):3505–3510.
- Ding, H., Yang, Y., Chen, L. Q., and Yang, S. P. (2014). Vibration of vehicle-pavement coupled system based on a Timoshenko beam on a nonlinear foundation. *Journal of Sound and Vibration*, 333(24):6623–6636.
- Elnashar, G., Bhat, R. B., and Sedaghati, R. (2019). Modeling and dynamic analysis of a vehicle-flexible pavement coupled system subjected to road surface excitation. *Journal of Mechanical Science and Technology*, 33(7):3115–3125.
- Engineering, G. (2020). <https://greenwood.dk/road/tsd/references/>. Greenwood Engineering homepage, accessed 20-10-2020.



- European Environment Agency (2018). Greenhouse gas emissions from transport in Europe. Technical report.
- Eurostat (2016). Energy , transport and environment indicators 2016 edition. Technical report.
- Ferne, B. W., Langdale, P., Round, N., and Fairclough, R. (2009). Development of a Calibration Procedure for the U.K. Highways Agency Traffic-Speed Deflectometer. *Transportation Research Record: Journal of the Transportation Research Board*, 2093(1):111–117.
- Flügge, W. (1975). *Viscoelasticity*. Springer, Berlin, Heidelberg.
- Frederiksen, S. L., Jacobsen, K. W., Brown, K. S., and Sethna, J. P. (2004). Bayesian ensemble approach to error estimation of interatomic potentials. *Physical Review Letters*, 93(16):1–4.
- Froio, D., Rizzi, E., Simões, F. M., and Costa, A. P. D. (2018). Universal analytical solution of the steady-state response of an infinite beam on a Pasternak elastic foundation under moving load. *International Journal of Solids and Structures*, 132-133:245–263.
- Gopalakrishnam, K., Kim, S., Ceylan, H., and Kaya, O. (2014). Development of Asphalt Dynamic Modulus Master Curve Using Falling Weight Deflectometer Measurements. Technical Report June, Iowa State University, Institute for Transportation.
- Gould, P. L. and Feng, Y. (2018). *Introduction to linear elasticity*.
- Haider, M., Conter, M., and Glaeser, K.-P. (2011). Discussion paper - What are rolling resistance and other influencing parameters on energy consumption in road transport. *Models for Rolling Resistance in Road Infrastructure Asset Management Systems (MIRIAM)*, AIT, Austria.
- Hall, D. E. and Moreland, J. C. (2001). Fundamentals of rolling resistance. *Rubber Chemistry and Technology*, 74(3):525–539.
- Han, M. S., Benaroya, H., and Wei, T. (1999). Dynamics of transversely vibrating beams using four engineering theories. *Journal of Sound and Vibration*, 5(225):935–988.
- Harvey, J. T., Lea, J. D., Kim, C., Coleri, E., Zaabar, I., Louhghalam, A., Chatti, K., Buscheck, J., and Butt, A. (2016). Simulation of Cumulative Annual Impact of Pavement Structural Response on Vehicle Fuel Economy. Technical Report May, Univ. of California Pavement Research Center, Davis, CA.
- Hoffmann, K. (2017). *An Introduction to Stress Analysis and Transducer Design using Strain Gauges*. HBM UK Ltd.
- Kellermann, W. (2009). *Springer Topics in Signal Processing*, volume 2.
- Lakes, R. (2009). Introduction: Phenomena. In *Viscoelastic Materials*, chapter 1, pages 1–13. Cambridge University Press, Cambridge.

- Lautrup, B. (2011). *Physics of continuous matter*. Second edi edition.
- Lédée, F. A. (2016). Experimental validation of the rolling resistance measurement method including updated draft standard. *Experimental validation of the rolling resistance measurement method including updated draft standard (ROSANNE)*, (August 2016).
- Lee, H. S. (2013). *Development of a New Solution for Viscoelastic Wave Propagation of pavements structures and its use in dynamic backcalculations*. PhD thesis, Michigan State University.
- Lee, H. S. (2014). Viscowave - A new solution for viscoelastic wave propagation of layered structures subjected to an impact load. *International Journal of Pavement Engineering*, 15(6):542–557.
- Lee, H. S., Quintus, H. V., and Steel, D. (2018). Effect of moving dynamic loads on pavement deflections and backcalculated modulus. In *Proceedings of the TRB 97th Annual Meeting*.
- Lee, S., Arim Chatti, D., and Zaabar, I. (2009). Development of a Simple Diagnosis Tool for Detecting Localized Roughness Features. *Michigan State University Project RC-1505*.
- Louhghalam, A., Akbarian, M., and Ulm, F.-J. (2013). Flügge’s Conjecture: Dissipation-versus Deflection-Induced Pavement-Vehicle Interactions. *Journal of Engineering Mechanics*, 140(8):04014053.
- Louhghalam, A., Akbarian, M., and Ulm, F.-J. (2014). Scaling Relationships of Dissipation-Induced Pavement-Vehicle Interactions. *Transportation Research Record: Journal of the Transportation Research Board*, 2457:95–104.
- Lv, P., Tian, R., and Liu, X. (2010). Dynamic Response Solution in Transient State of Viscoelastic Road under Moving Load and Its Application. *Journal of Engineering Mechanics*, 136(2).
- Mallik, A. K., Chandra, S., and Singh, A. B. (2006). Steady-state response of an elastically supported infinite beam to a moving load. *Journal of Sound and Vibration*, 291(3-5):1148–1169.
- Mazurek, G. and Iwański, M. (2017). Modelling of Asphalt Concrete Stiffness in the Linear Viscoelastic Region. *IOP Conference Series: Materials Science and Engineering*, 245(3).
- Michaels, P. (1998). In Situ Determination of Soil Stiffness and Damping. *Journal of Geotechnical and Geoenvironmental Engineering*, 124(8):709–719.
- Nasimifar, M., Chaudhari, S., Thyagarajan, S., and Sivaneswaran, N. (2020). Temperature adjustment of Surface Curvature Index from Traffic Speed Deflectometer measurements. *International Journal of Pavement Engineering*, 21(11):1408–1418.
- Nielsen, C. P. (2019). Visco-Elastic Back-Calculation of Traffic Speed Deflectometer Measurements. *Transportation Research Record: Journal of the Transportation Research Board*, 2673(12):439–448.

- Nielsen, N., Hecksher, T., Nielsen, C., and Hjorth, P. (2020a). Measurement of structural rolling resistance at two temperatures. In *Advances in Materials and Pavement Performance Prediction II*, pages 220–223.
- Nielsen, N. R., Chatti, K., Nielsen, C. P., Zaabar, I., Hjorth, P. G., and Hecksher, T. (2020b). Method for Direct Measurement of Structural Rolling Resistance for Heavy Vehicles. *Transportation Research Record: Journal of the Transportation Research Board*, 2674(5):371–380.
- Nilsson, R. N., Isacsson, U., and Hopman, P. C. (2002). Influence of Different Rheological Models on Predicted Pavement Responses in Flexible Pavements. *Road Materials and Pavement Design*, 3(2):117–149.
- Pham, N. H., Sauzéat, C., Di Benedetto, H., González-León, J. A., Barreto, G., Nicolai, A., and Jakubowski, M. (2015). Analysis and modeling of 3D complex modulus tests on hot and warm bituminous mixtures. *Mechanics of Time-Dependent Materials*, 19(2):167–186.
- Pouget, S., Sauzéat, C., Benedetto, H. D., and Olard, F. (2012). Viscous Energy Dissipation in Asphalt Pavement Structures and Implication for Vehicle Fuel Consumption. *Journal of Materials in Civil Engineering*, 24(5):568–576.
- Pouget, S., Sauzéat, C., Di Benedetto, H., and Olard, F. (2014). Calculation of viscous energy dissipation in asphalt pavements. *The Baltic Journal of Road and Bridge Engineering*, 9(2):123–130.
- Pronk, A. C. (2006). The huet-sayegh model: A simple and excellent rheological model for master curves of asphaltic mixes. *Geotechnical Special Publication*, (146):73–82.
- Saito, H. and Terasawa, T. (1980). Steady-State Vibrations of a Beam on a Pasternak Foundation for Moving Loads. *Journal of Applied Mechanics*, 47(4):879–883.
- Saltelli, A., Chan, K., and Scott, E. M. (2000). *Sensitivity Analysis*. John Wiley & Sons, Ltd.
- Sandberg, U., Bergiers, A., Ejsmont, J. a., Goubert, L., Karlsson, R., and Zöller, M. (2011a). Road surface influence on tyre/road rolling resistance. *Models for rolling resistance In Road Infrastructure Asset Management systems (MIRIAM project)*.
- Sandberg, U., Bergiers, A., Ejsmont, J. A., Goubert, L., and Zoller, M. (2012). Rolling Resistance Measurement Methods for Studies of Road Surface Effects. *Models for rolling resistance In Road Infrastructure Asset Management systems (MIRIAM)*, Deliverabl.
- Sandberg, U., Haider, M., Conter, M., Goubert, L., Bergiers, A., Glaeser, K.-P., Schwalbe, G., Zöller, M., Boujard, O., Hammarström, U., Karlsson, R., Ejsmont, J. A., Harvey, J., and Wang, T. (2011b). Rolling resistance-Basic information and State-of-the-Art on measurement methods. *Models for rolling resistance In Road Infrastructure Asset Management systems (MIRIAM project)*.

- Seong-Min Kim and Roesset, J. M. (2003). Dynamic response of a beam on a frequency-independent damped elastic foundation to moving load. *Canadian Journal of Civil Engineering*, 30(2):460–468.
- Shakiba, M., Hasan Ozer, Ziyadi, M., and Al-Qadi, I. L. (2016). Mechanics based model for predicting structure-induced rolling resistance (SRR) of the tire-pavement system. *Mech Time-Depend Mater*, 20:579–600.
- Sharpe, B. R., Clark, N., and Lowell, D. (2014). Trailer Technologies for Increased Heavy-Duty Vehicle Efficiency: Technical, Market, and Policy Considerations. *SAE International Journal of Commercial Vehicles*.
- Snehasagar, G., Krishnanunni, C. G., and Rao, B. N. (2019). Dynamics of vehicle-pavement system based on a viscoelastic Euler-Bernoulli beam model. *International Journal of Pavement Engineering*, 8436.
- Solatifar, N., Kavussi, A., Abbasghorbani, M., and Katicha, S. W. (2019). Development of dynamic modulus master curves of in-service asphalt layers using MEPDG models. *Road Materials and Pavement Design*, 20(1):225–243.
- Solatifar, N., Kavussi, A., Abbasghorbani, M., and Sivilevičius, H. (2017). Application of FWD data in developing dynamic modulus master curves of in-service asphalt layers. *Journal of Civil Engineering and Management*, 23(5):661–671.
- Sun, L. (2001). Dynamic displacement response of beam-type structures to moving line loads. *International Journal of Solids and Structures*, 38(48-49):8869–8878.
- Tanahashi, H. (2004). Formulas for an infinitely long Bernoulli-Euler beam on the Pasternak model. *Soils and Foundations*, 44(5):109–118.
- Tofteskov, J., Tørngren, M. A., Bailey, N. P., and Hansen, J. S. (2019). Modelling headspace dynamics in modified atmosphere packaged meat. *Journal of Food Engineering*, 248:46–52.
- USDOT (2010). Transportation's Role in Reducing U.S. Greenhouse Gas Emissions Volume 1: Synthesis Report. Technical report, Center for Climate Change and Environmental Forecasting Cambridge Systematics Inc.
- Uzzal, R. U. A., Bhat, R. B., and Ahmed, W. (2012). Dynamic response of a beam subjected to moving load and moving mass supported by Pasternak foundation. *Shock and Vibration*, 19(2):201–216.
- Verruijt, A. (2010). An Introduction to Soil Dynamics. In *Springer, Dordrecht*. Springer.
- Wang, Y. H., Tham, L. G., and Cheung, Y. K. (2005). Beams and plates on elastic foundations: A review. *Progress in Structural Engineering and Materials*, 7(4):174–182.
- Wineman, A. S. and Rajagopal, K. R. (2000). Discussion of response of a viscoelastic material. In *Mechanical Response of Polymers : an Introduction*, pages 1–27.

- Xu, Q. and Solaimanian, M. (2009). Modelling linear viscoelastic properties of asphalt concrete by the Huet-Sayegh model. *International Journal of Pavement Engineering*, 10(6):401–422.
- Yu, H., Cai, C., Yuan, Y., and Jia, M. (2017). Analytical solutions for Euler-Bernoulli Beam on Pasternak foundation subjected to arbitrary dynamic loads. *International Journal for Numerical and Analytical Methods in Geomechanics*, 41(8):1125–1137.
- Zaabar, I. and Chatti, K. (2014). A field investigation of the effect of pavement type on fuel consumption. In *T and Di Congress 2011 : Integrated Transportation and Development for a Better Tomorrow*,, pages 772–781.
- Zaabar, I., Chatti, K., Lee, H. S., and Lajnef, N. (2014). Backcalculation of asphalt concrete modulus master curve from field-measured falling weight deflectometer data: Using a new time domain viscoelastic dynamic solution and genetic algorithm. *Transportation Research Record*, 2457(2457):80–92.
- Zhao, Y., Cao, D., and Chen, P. (2015). Dynamic backcalculation of asphalt pavement layer properties using spectral element method. *Road Materials and Pavement Design*, 16(4):870–888.
- Zhao, Y. and Kim, Y. R. (2003). Time–Temperature Superposition for Asphalt Mixtures with Growing Damage and Permanent Deformation in Compression. *Transportation Research Record*, 1832(1):161–172.
- Zoller, M. (2014). State of the art on rolling resistance measurement devices. *Rolling resistance, Skid resistance, AND Noise Emission measurement standards for road surfaces (ROSANNE)*, 43(0):1–122.



**Part VII**  
**Appendix**





## Appendix A

# Reprints of articles

### **A.1 Method for Direct Measurement of Structural Rolling Resistance for Heavy Vehicles**

Published in Transportation Research Record: Journal of the Transportation Research Board.

## Method for Direct Measurement of Structural Rolling Resistance for Heavy Vehicles

Natasja R. Nielsen<sup>1</sup>, Karim Chatti<sup>2</sup>, Christoffer P. Nielsen<sup>3</sup>, Imen Zaabar<sup>4</sup>, Poul G. Hjorth<sup>5</sup>, and Tina Hecksher<sup>1</sup>

Transportation Research Record  
1–10

© National Academy of Sciences:  
Transportation Research Board 2020

Article reuse guidelines:  
sagepub.com/journals-permissions

DOI: 10.1177/0361198120915699  
journals.sagepub.com/home/trr



### Abstract

In this paper, a new in situ method for determining the structural rolling resistance (SRR), defined as the dissipated energy caused by deformation of the pavement when subjected to a moving load, is presented. The method is based on the relation between SRR and the slope of the deflection basin under a moving load. Using the Traffic Speed Deflectometer, the deflection slope is measured at several positions behind and in front of the right rear-end tire pair of a full-size truck trailer while driving under realistic conditions. The deflection slope directly under the tire is estimated from a linear interpolation between the two nearest sensors. A set of data from a test road segment located in Denmark is analyzed and the SRR coefficients are found to be in the range 0.005% to 0.05%. The deflection slope measurements have a high reproducibility (repeated measurements agree within standard deviations of 4% to 10%) with high spatial resolution, and the method for calculating SRR from these measurements has the clear advantage that it requires no knowledge or model of the pavement structure or viscoelastic properties. Numerical simulations of pavement response show that the proposed interpolation method tends to underestimate the actual SRR, and better estimates can be obtained by other interpolation schemes.

When driving at constant speed, the fuel consumption goes into overcoming driving resistance. Many different factors contribute to the driving resistance in a vehicle; among the most prominent are uphill driving, air drag, internal friction, and rolling resistance ( $I$ ). It is estimated that for heavy trucks, 15% to 30% of the fossil fuel input is used to overcome the rolling resistance (2). Rolling resistance losses arise from two main sources: 1) viscoelastic effects in the tires and 2) effects of the pavement, including unevenness, texture, and viscoelastic deformation of the pavement (3–5). The focus in this paper is on the latter.

An elastic or viscoelastic pavement subject to a moving vehicle will deform underneath the tires. If the pavement is viscoelastic, this deformation will result in energy dissipating into the pavement structure. The lost energy has to be compensated through additional work from the vehicle engine, to maintain a constant driving speed (6). The amount of additional energy needed depends on the structure of the pavement and this will be referred to as structural rolling resistance (SRR) throughout the paper.

The deflection basin under a moving tire ( $z(x)$ ) is asymmetric because of the viscoelastic properties of the pavement causing a time delay in the deflection of a

viscoelastic pavement. This time delay makes the maximum deflection appear behind the center of the tire, as seen on Figure 1a. This means that the tire always will be on an uphill slope ( $\frac{\partial z(x=0)}{\partial x} > 0$ ), (see Figure 1b) and thus has to do work in order to maintain a constant driving speed (7). Using this uphill slope notion, the SRR can be calculated directly from the asymmetric deflection basin (1, 8, 9). Deflection of a structure subject to a moving load has been reported in the literature since the 1960s; for example, in (7), the viscoelastic response of a Kelvin beam is analyzed, and the viscoelastic effects reported to manifest themselves through an asymmetric deflection basin.

<sup>1</sup>Department of Science and Environment, Roskilde University, Roskilde, Denmark

<sup>2</sup>Department of Civil and Environmental Engineering, Michigan State University, East Lansing, MI

<sup>3</sup>Greenwood Engineering A/S, Brøndby, Denmark

<sup>4</sup>Department of Computer Science and Engineering, Michigan State University, East Lansing, MI

<sup>5</sup>DTU Compute, Technical University of Denmark, Lyngby, Denmark

### Corresponding Author:

Natasja R. Nielsen: narini@ruc.dk

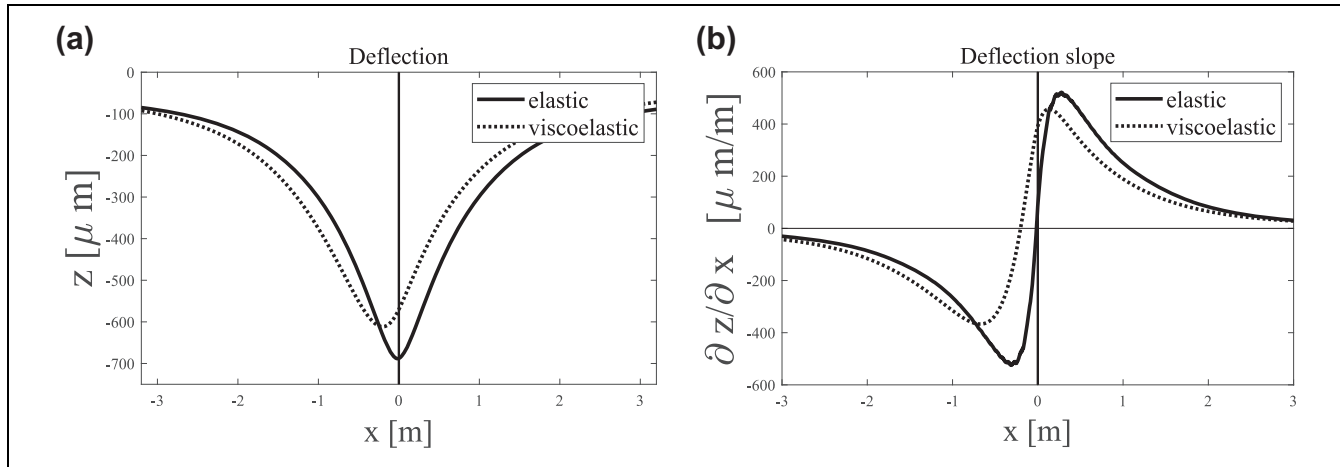


**Figure 1.** (a) Simulated deflection basin underneath a moving load for an elastic (solid line) and viscoelastic (dotted line) pavement, and (b) associated deflection slope for the elastic and viscoelastic pavement. The basin is obtained using a numerical simulation explained at a later point in this paper.

Although SRR has been studied for decades, it has proven difficult to devise accurate and robust ways of measuring it (10). As a consequence, little is known about the absolute magnitude of SRR or its relative contribution to the overall rolling resistance. Indirect measurements of the influence of the dissipative effects in bituminous layers have been estimated by comparing fuel consumption measurements on flexible and rigid pavements. These studies rely on the assumption that rigid pavements have little or no viscous losses and thus the difference in fuel consumption between these types of pavements can be ascribed to the viscous behavior of the asphalt (8, 11, 12). However, it can be difficult to isolate the effects that relate to the pavement structure from other effects caused by, for example, texture or unevenness (9). In addition, unlike texture and unevenness, the effect from pavement structure is found to be highly dependent on external parameters such as temperature, pavement conditions, and so forth (13). It is therefore difficult to say anything conclusive on SRR influence on fuel consumption based on these types of experiments.

Direct estimates of SRR typically come from simulations of pavement deflections with pavement parameters obtained either from backcalculations using falling weight deflectometer tests or other rheological measurements of the bituminous layer. An often used method is to simulate the pavement response in a finite pavement section, as a moving load is passing with constant speed (14). From the response, one can obtain the displacement field of the pavement surface and calculate the dissipated energy in the pavement (3, 10, 12, 15, 16). On the basis of such calculations, it is believed that the SRR loss is smaller than the energy loss caused by pavement texture and unevenness (15), but whether it is negligible or

significant enough that it should be included in pavement planning is not clear.

Development of methods for reliable measurement of the pavement's influence on the vehicle fuel consumption is thus highly desirable when making lifecycle assessment studies of pavements and should be included in the development of sustainable pavement designs (3, 6).

This paper presents a novel method for determining the SRR under realistic driving conditions using the Traffic Speed Deflectometer technology developed by Greenwood Engineering. The technique measures the slope of the deflection basin between the right pair of rear-end tires of a full-size truck trailer, as it moves at realistic driving speeds. Thus, the uphill slope seen by the tire, which is caused by the deformation of the pavement, is directly measured and, from this, the associated SRR loss can be calculated. The estimated SRR is thus obtained under conditions directly comparable to what normal traffic experiences. The method gives spatially resolved (10-m resolution), reproducible, and robust estimates of SRR, even in road segments where the value fluctuates considerably, making it a reliable and model-free method to measure SRR.

## Aim

The aim of the paper is to present a new concept for measuring SRR using Traffic Speed Deflectometer (TSD) technology. The TSD measures the slope of the deflection basin under the tires of a truck trailer during driving. The concept and its robustness are demonstrated by pilot measurements of a test road segment of 9 km, and the underlying assumptions are discussed in the light of numerical pavement simulations.

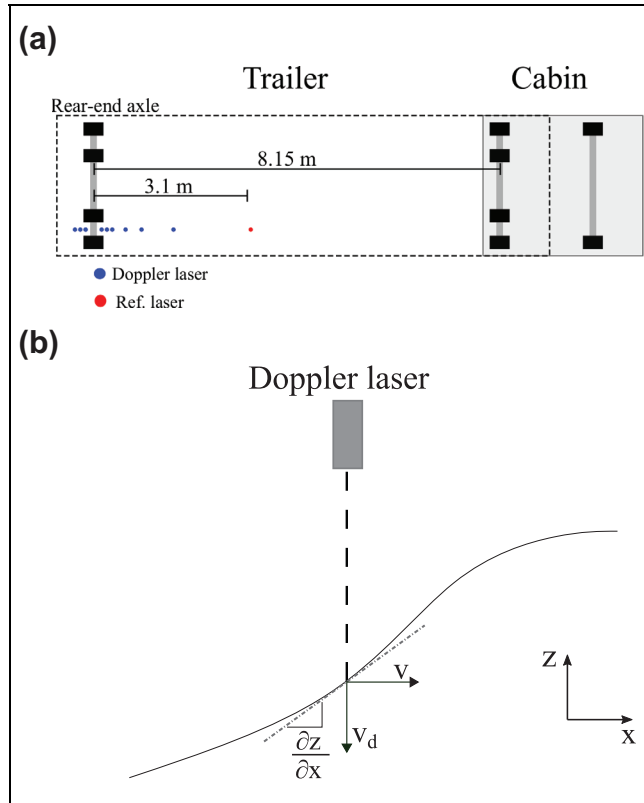


**Figure 2.** (a) Top view sketch of the Traffic Speed Deflectometer. Nine Doppler lasers are located in between the right rear-end tire pair, as indicated with blue dots. Note that the drawing is not to scale, and the tires in the tire-pair are only separated by 64 mm. (b) Vertical pavement velocity ( $v_d$ ) at a given point measured using a Doppler laser. See text for further details.

## The TSD Concept

The TSD is conventionally used for continuous bearing capacity measurements by evaluating the slope of the pavement deflection basin. It has the advantage that it makes continuous measurements of the deflection slope and that the TSD trailer is a normal truck trailer and thus can measure under normal driving speed and load as well as measuring directly in the wheel path. In this study a full axle load of 10 tonnes was used.

The TSD device measures the deflection velocity of the pavement as it is subjected to a moving load. This is done by use of Doppler lasers that measure the vertical velocity of the pavement (see Figure 2b). The TSD truck is equipped with nine Doppler lasers (sensors): three sensors located behind and six in front of the rear-end axle, as shown in Figure 2a. Their exact positions relative to the center of the axle (in meters) are

$$\text{Sensor position} = [-0.366, -0.269, -0.167, 0.163, 0.260, 0.362, 0.662, 0.964, 1.559]. \quad (1)$$

The measured pavement velocity is adjusted such that effects caused by vertical movements of the truck are subtracted. This is done by using a reference laser mounted 3.1 m from the rear-end axle, where the deflection of the pavement is assumed zero (red sensor on Figure 2a). The technique is explained in more detail in (17–20).

Figure 2b shows how the vertical pavement velocity ( $v_d$ ) is measured in a given point using a Doppler laser. The deflection slope at that point ( $\frac{\partial z}{\partial x}$ ) corresponds to the slope of the tangent going through the point (gray dotted line) and can be found by dividing  $v_d$  by the horizontal driving speed ( $v$ ),

$$\frac{\partial z}{\partial x} = \frac{\frac{\partial z}{\partial t}}{\frac{\partial x}{\partial t}} = \frac{v_d}{v} \quad (2)$$

The driving speed,  $v$ , is measured using an odometer located behind the right rear-end tire pair.

## Deflection Slope Data

For this study, three repeated measurements were made with the TSD, on a 9.7-km road section near Copenhagen, Denmark. The measurements were conducted in the spring of 2018 with almost constant air temperature ( $\sim 14^\circ\text{C}$ ) and road temperature ( $\sim 18^\circ\text{C}$ ) throughout all three measurements. The driving speed was between 50 km/h and 60 km/h; the exact driving speed was recorded continuously during all measurements. The measured deflection slopes for each sensor were collected at a sampling frequency of 1,000 samples per second and subsequently averaged over 10 m. A plot of the mean value for the three subsequent measurements of each sensor as a function of the driven distance is seen on Figure 3. The measured deflection slope for each sensor varies significantly throughout the measured distance. This variation is however highly reproducible, with average standard deviations between 12  $\mu\text{m}/\text{m}$  and 26  $\mu\text{m}/\text{m}$  (corresponding to 4–10%) between the three measurement runs.

The inset in Figure 3 shows the measured deflection slope as a function of the sensor position measured at 4.5 km (marked in gray in the main image). The center of the axle in this plot is at  $x = 0$ , indicated with a black dotted line. As mentioned in the introduction, the deflection slope curve is characterized by the minimum deflection slope occurring behind and the maximum deflection slope in front of the tire. The asymmetry in minimum and maximum peak magnitudes is believed to be caused by damping in the pavement. Thus, the location and magnitude of the maximum and minimum carries information about the viscoelastic properties of the pavement.

For analysis of the data, it is necessary to estimate the deflection slope at the axle location, that is, around

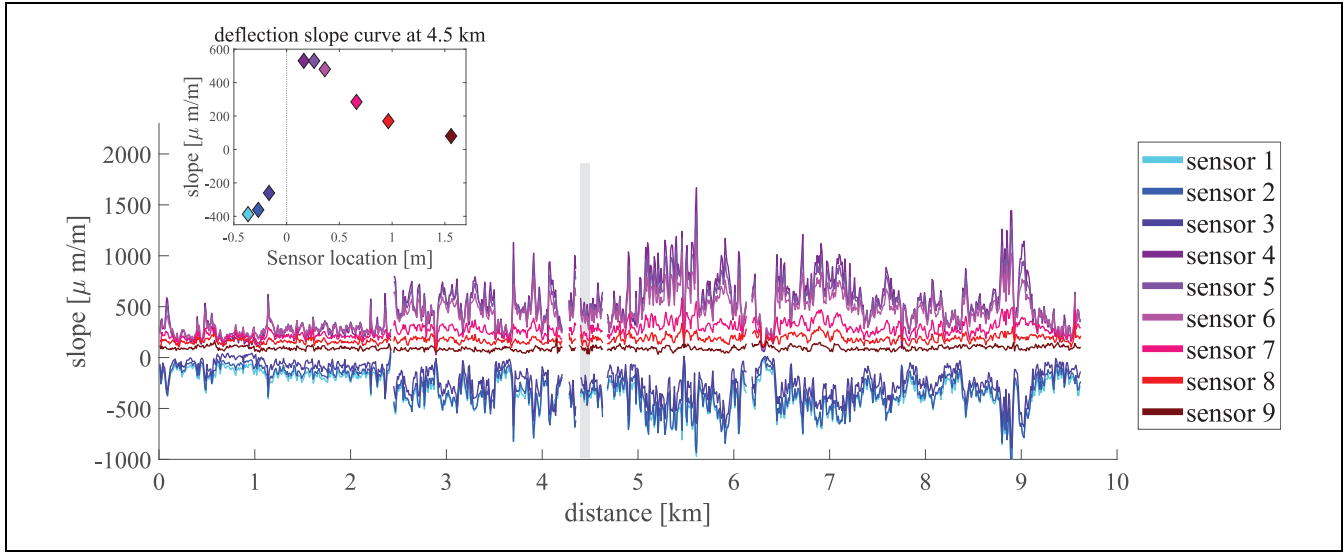


**Figure 3.** Measured deflection slope for each sensor as a function of the distance, with inset showing a plot of the deflection slopes measured at 4.5 km as a function of sensor location.

**Table 1.** Partitioning of the Traffic Speed Deflectometer Measurements into Groups

Group	Behavior of signal in Sensors 4, 5, and 6	Location of maximum
Group 1	Monotonic decrease	Closer to center of axle than Sensor 4
Group 2	Increasing or equal from Sensors 4 to 5 and then decreasing in Sensor 6	Partly captured by Sensors 4 and 5
Group 3	Monotonic increase	Fully captured by the sensors

Note: The division is made based on the behavior of the measured deflection slope in Sensors 4, 5, and 6. In total this gives three groups, illustrated in Figure 4a.

$x = 0$ , where a measurement cannot be taken because of the presence of the axle. Instead, the slope must be inferred from the measured locations in front of and behind the center position. This task is easier when the features of the deflection slope are fully captured by the sensors, which is not the case for all traces. Accordingly, the measurements were partitioned into three groups based on the behavior of the signal in Sensors 4, 5, and 6 (Table 1), which gives an indication of where the maximum is located: Group 1 was used for measurements for which the maximum was not captured by the sensors and therefore had to be located closer to the center of the axle than Sensor 4; Group 2 was used for measurements for which the maximum was partly captured by the sensors; and Group 3 was used for measurements for which the maximum was fully captured by the sensors (see Table 1). Examples of measurements from each group are shown in Figure 4a. Here the symbols are the average values of the three repeated measurements and the errorbars represent the standard deviations, showing a high degree of reproducibility. Within Groups 1 and 2, a big variation was found in the magnitude of the

maximum and the minimum, whereas for measurements belonging to Group 3 this variation was not observed.

### Calculating the SRR

This section shows how the SRR loss can be calculated directly from the measured deflection slope data. In the following it is assumed that the applied load is a point load at the center of the tire, corresponding to  $x = 0$  and with the magnitude  $F_L$ . The dissipated power caused by SRR,  $P_{SRR}$ , can be found from the applied load and the pavement velocity at this point,

$$P_{SRR} = F_L v_d(x=0) = F_L v \frac{\partial z}{\partial x}(x=0) \quad (3)$$

where the last equality sign comes from Equation 2.

In the case of a perfectly elastic pavement, the maximum deflection will occur directly under the load, making the deflection slope at this point zero and thus  $P_{SRR} = 0$ . For a viscoelastic pavement, however, the maximum deflection occurs behind the load and there is an uphill slope underneath the load, thus  $P_{SRR} > 0$ , as

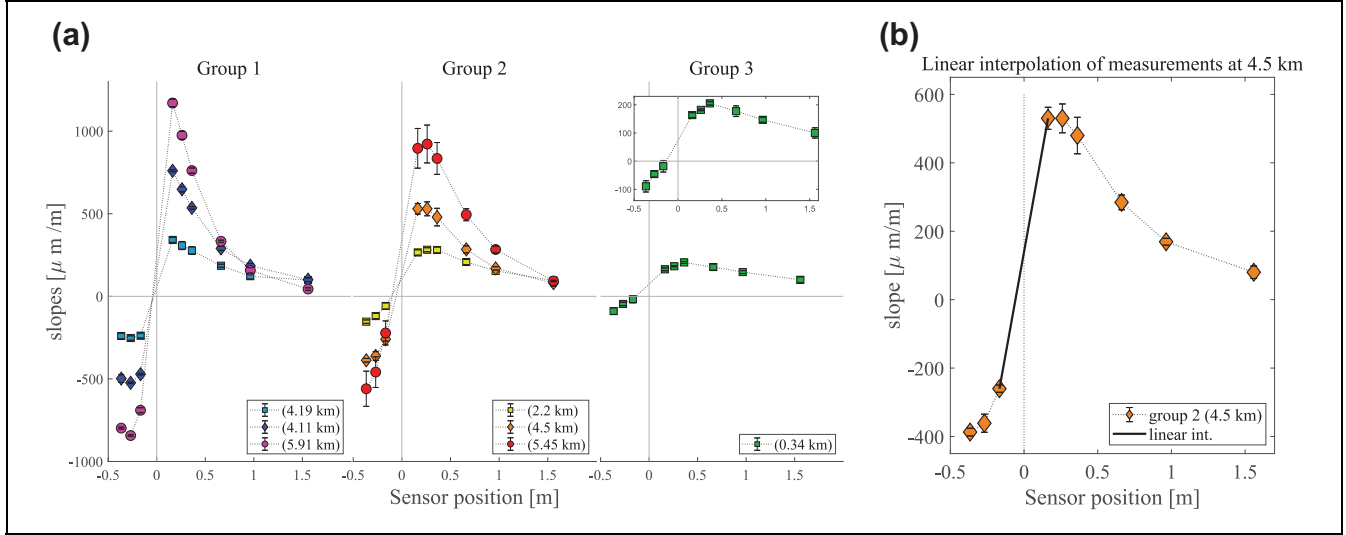


**Figure 4.** (a) Representative examples of deflection slope plotted as a function of sensor location for the different measurement groups (see Table 1), and (b) linear interpolation between the measured values in the two sensors closest to the axle for data measured at 4.5 km belonging to Group 2.

already illustrated in Figure 1. Note that, the deflection maximum occurs behind the center of the load, whether a point load or a finite contact area is considered. Thus, the tire also experiences an uphill slope if considered a finite contact area, and thereby has  $P_{SRR} > 0$  whenever there is damping in the pavement.

To estimate the deflection slope directly under the tire, a linear interpolation is used between the measured deflection slope in the two sensors located closest to the center (Sensors 3 and 4), located at  $x = -0.167$  m and  $x = 0.163$  m respectively, as shown in Figure 4b. Therefore the dissipated energy can be written as

$$P_{SRR} = F_L v b \quad (4)$$

where  $b$  is the intersection of the linear interpolation  $\frac{\partial z}{\partial x}(x) = ax + b$  with the  $z$ -axis,  $\frac{\partial z}{\partial x}(x = 0)$ . From the dissipated power, the rolling resistance force can be defined as  $F_{SRR} = \frac{P_{SRR}}{v} = F_L b$ . Using the standard definition of rolling resistance coefficient as the ratio between rolling resistance force and load, this leads to the following simple relation between deflection slope at  $x = 0$  and the SRR coefficient:

$$C_{SRR} = \frac{F_{SRR}}{F_L} = b \quad (5)$$

Using these relations on the data trace presented in Figure 4b, we find an SRR power of  $49 \text{ W} \pm 6 \text{ W}$ , an SRR force of  $6.8 \text{ N} \pm 0.8 \text{ N}$ , and  $C_{SRR} = 1.4 \cdot 10^{-4} \pm 1.6 \cdot 10^{-5}$  or  $0.014\% \pm 0.0016\%$ .

The  $C_{SRR}$  values for all measurement sets were found following this procedure, and the results are presented in Figure 5. Here, the different groups are marked with

different colors, the symbols represent the mean values of the three repeated measurements, and the error bars are found as the standard deviation of the three measurements. We see that the  $C_{SRR}$  value varies considerably over the traveled distance, from 0.005% to 0.05%, with most data points in the region from 0.01% to 0.02%. The method shows a good reproducibility with low standard deviations, even in regions where the  $C_{SRR}$  changes rapidly with distance. This demonstrates that the method is robust and can measure the  $C_{SRR}$  values of the road precisely, with high spatial resolution even under changing pavement conditions.

The different data groups are indicated with red, green, and blue on Figure 5. Average values of  $P_{SRR}$ ,  $F_{SRR}$  and  $C_{SRR}$  for each group are shown in Table 2. The groups were divided based on the location of the maximum, captured by Sensors 4, 5, and 6, and it is possible to see a clear difference in the SRR values within the different groups. Furthermore, the variations in  $C_{SRR}$ , with distance seen in Figure 5 follow the trends seen in the measured deflection slopes in Figure 3. This is because a large deflection slope signal in the sensors closest to the axle (Sensors 3 and 4) generally results in a high intersection value with the  $y$ -axis, and thus a high calculated  $C_{SRR}$  (Equation 5).

The magnitude and the location of the peaks in the deflection slope curves are determined by the shape of the deflection basin, which mainly is controlled by the relative stiffness of the top asphalt layer compared with the lower layers. For situations with a relatively stiff top layer, the deflection basin will be broad and have a small amplitude, resulting in curves like those of Group 3 and a small SRR. A relatively soft top layer, on the

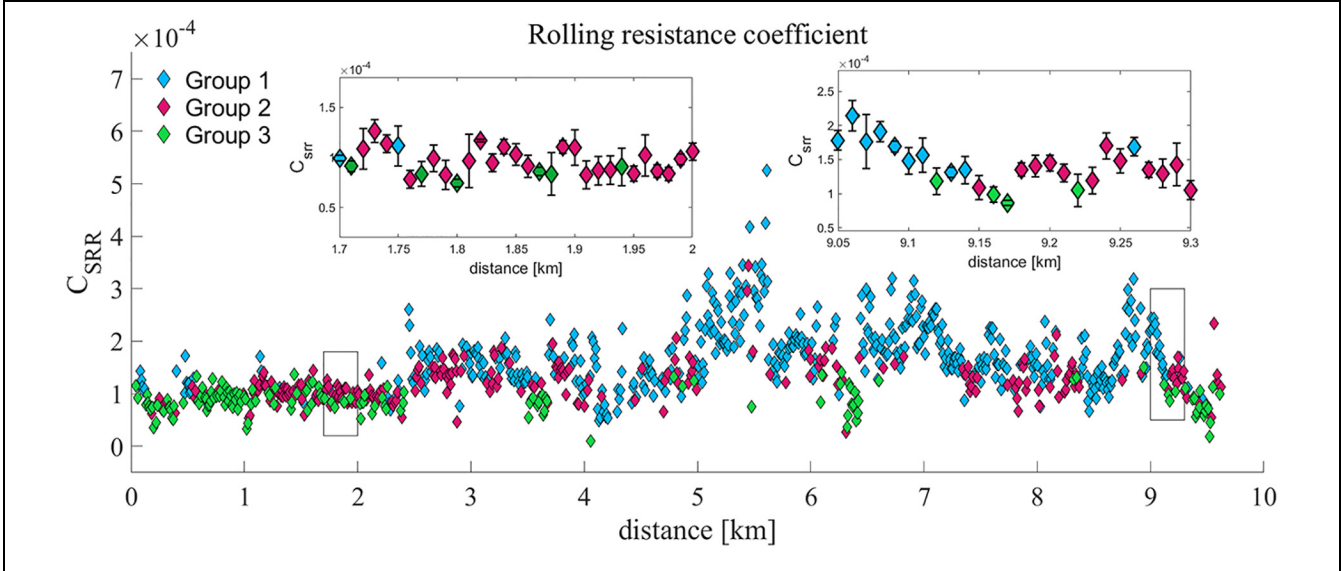


**Figure 5.** Calculated  $C_{SRR}$  values plotted versus distance, with insets showing a steady and a varying section with standard deviations illustrated by error bars. The different colors represent the three different Groups (see Table 1).

Note:  $C_{SRR}$  = structural rolling resistance coefficient.

**Table 2.** Average  $C_{SRR}$ ,  $F_{SRR}$ , and  $P_{SRR}$  for the Three Groups of Traffic Speed Deflectometer Data

Group	$C_{SRR}$ [-]	$P_{SRR}$ (W)	$F_{SRR}$ (N)	# in group
Group 1	$1.7 \cdot 10^{-4} \pm 6 \cdot 10^{-5}$	$124.2 \pm 57$	$8.6 \pm 3.0$	506
Group 2	$1.2 \cdot 10^{-4} \pm 4 \cdot 10^{-5}$	$84.9 \pm 30$	$5.9 \pm 1.8$	272
Group 3	$0.9 \cdot 10^{-4} \pm 3 \cdot 10^{-5}$	$61.7 \pm 21$	$4.2 \pm 1.3$	159

Note: It can be seen that SRR for data in Group 1 is largest, followed by Group 2, and then Group 3. The number of measurements within the dataset belonging to each group is listed in the last column.  $C_{SRR}$  = SRR coefficient;  $F_{SRR}$  = rolling resistance force;  $P_{SRR}$  = dissipated power due to SRR; SRR = structural rolling resistance.

other hand, will give a deep and narrow basin, giving deflection curves like those of Group 1 and a higher SRR. This is consistent with what is visible in the measurements.

### Impact of a Finite Contact Surface

For the calculations of the dissipated power and  $C_{SRR}$  above, it is assumed that the interaction between tire and road can be described as a point load. This is a simplification of the real interaction between the tire and the pavement where the contact surface has a finite area. To investigate whether this approximation has a significant influence on the calculated SRR loss, an expression is adopted for the power dissipation derived by (9). The expression is based on a moving reference frame with constant velocity, which is consistent with the TSD setup. Furthermore, it is assumed that the tire is elastic and therefore does not dissipate energy and that the tire provides a uniform applied stress to the surface,

$$P_{SRR}^{\text{contact area}} = pv \int_S \frac{\partial z(X, y, z)}{\partial X} dS \quad (6)$$

where

$p$  is the tire pressure,

$v$  is the driving speed,

$Z$  is the vertical component of the displacement field of the pavement surface, and

$\frac{\partial z(X, y, z)}{\partial X}$  is the deflection slope.

The integral is taken over the contact surface,  $S$ , which is the area where the tire is in contact with the pavement. Plugging in a linearly varying deflection slope and assuming a circular contact area obtains

$$\begin{aligned} P_{SRR}^{\text{contact area}} &= pv \int_S \frac{\partial z(X, y, z)}{\partial X} dS \\ &= pv \int_{-r}^r \int_{-\sqrt{r^2-X^2}}^{\sqrt{r^2-X^2}} (aX + b) dy dX \\ &= pvb\pi r^2 = Fvb = P_{SRR}^{\text{point load}} \end{aligned} \quad (7)$$

Thus, for a linearly varying deflection slope the power dissipated over a finite contact area is equal to the power dissipated at a point load.

### Model Calculation of Pavement Response

So far, it has been assumed that the deflection slope underneath the tire is linear and can be found by interpolation between the two sensors nearest to the axle. The validity of this assumption will now be investigated by use of simulated deflection slopes. The purpose of this is solely to generate curves with similar behaviors to those observed in the measurements, and to investigate how well the assumption of a linear deflection slope performs for the simulated curves. In particular, this is not an attempt to model the exact pavement response measured, but rather a theoretical exploration of the interpolation approach.

For simulating the pavement response, the investigation uses the time-domain based viscoelastic solver ViscoWave II-M, developed at Michigan State University (21, 22). ViscoWave II-M employs the so-called spectral element method to solve the wave propagation problem in the pavement structure and calculate the pavement response to an arbitrary loading. The model can simulate the time-dependent responses and allows each pavement layer to be either elastic or viscoelastic (23).

The program was modified slightly for this study such that the simulated conditions are similar to the TSD setup and therefore can be used for comparison. The original solver calculates the pavement deflection under the tire in a steady reference frame. The modified version calculates the response between the two tires in the tire reference frame, that is, a moving reference frame. From the simulated deflection curve the corresponding slope is calculated and filtered to remove numerical noise.

The pavement structure used for the simulation consists of three layers, representing an asphalt layer, a base layer, and a subgrade layer. Four different pavement models with identical construction are simulated, only changing viscoelastic parameters for the asphalt (top) layer. The parameters for the structure (height, elastic moduli, Poisson's ratio and density) are chosen to be typical values for these kinds of pavement layers and they are listed in Table 3. The viscoelastic properties of the asphalt layer are described by the relaxation modulus  $E(t)$ , given by

$$\log(E(t)) = c_1 + \frac{c_2}{1 + e^{(-c_3 - c_4 \log(t_R))}} \quad (8)$$

$$\log(t_R) = \log(t) - \log(a_T) \quad (9)$$

where

**Table 3.** Mechanical Characteristics for the Simulated Pavement

Asphalt	Base	Subgrade
$E(t)$	$E_2 = 124.3 \text{ MPa}$	$E_3 = 65.4 \text{ MPa}$
$\nu = 0.35$	$\nu = 0.35$	$\nu = 0.45$
$\rho = 2,322.7 \frac{\text{kg}}{\text{m}^3}$	$\rho = 2,082.4 \frac{\text{kg}}{\text{m}^3}$	$\rho = 1,762 \frac{\text{kg}}{\text{m}^3}$
$h = 0.15 \text{ m}$	$h = 0.3 \text{ m}$	$h = \infty$

Note: All pavement structures are made of three layers, each characterized by their Poisson's Ratio ( $\nu$ ), mass density ( $\rho$ ), average thickness ( $h$ ) and the relaxation modulus ( $E$ ). The relaxation modulus for the asphalt layer is given by Equation 8.

**Table 4.** Properties of the Four Different  $E(t)$  Used for the Study

Properties	Pavements			
	PAV1	PAV2	PAV3	PAV4
<u>Sigmoid coefficients</u>				
$c_1$	1.4	1.054	0.978	1.67
$c_2$	2.04	2.986	3.8	3.39
$c_3$	0.944	0.335	0.521	0.981
$c_4$	-0.417	-0.436	-0.519	-0.767
Shift factor $\log(a_T)$	0.37	0.32	0.49	0.34
<u><math>E(t)</math> characteristics</u>				
$E_0$ [MPa]	2,753	10,956	59,970	114,820
$E_0 - E_\infty$ [MPa]	2,728	10,945	59,960	114,770
Stiffness	→			
Amount of damping	→			

$c_1, \dots, c_4$  are the sigmoid coefficients,

$t_R$  is the reduced time, and

$a_T$  is the shift factor (16).

The parameters for the relaxation moduli are taken from backcalculated falling weight deflectometer tests on road segments located in California, to have realistic  $E(t)$  curves (16). The characteristics of these moduli range from very stiff with high damping to very soft with little damping (see Table 4). These sets of parameters generated deflection slope curves with a similar variation to that seen in the data groups as shown in Figure 6a. In the simulated deflection curves, the stiff pavement with large damping (PAV4) shows a small deflection and deflection slope peaks far apart, whereas the soft pavement with little damping (PAV1) has the opposite behavior. Probably, other choices of pavement parameters could result in similar deflection basins. However, for the present purpose the detailed input parameters of the model are not so important, as long as they are reasonably realistic.

In Figure 6b a zoom of the contact region for each of the simulated deflection slope curves is shown. The contact area between the tire and pavement is assumed circular with radius ( $r$ ) and the interval  $[-r; r]$  is marked with gray color. The idea is to determine how much the *actual* SRR in the simulated deflection slope curve deviates from



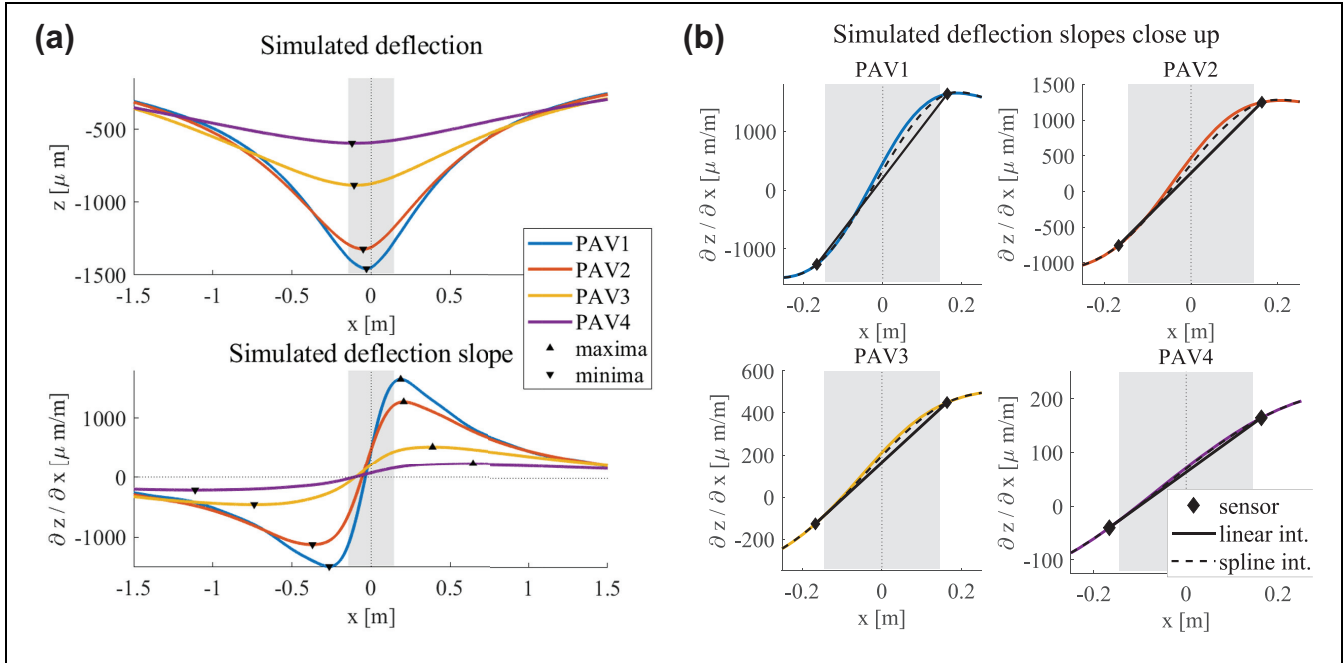


**Figure 6.** (a) Simulated deflection and deflection slope curves for four pavements with different  $E(t)$  of the asphalt layer, and (b) close up of the simulated deflection slope curves with a linear and a cubic spline interpolation. The contact area interval is marked with gray color.

the SRR obtained by assuming a linear interpolation between coordinates of the two sensors closest to the axle in the measurement. The linear interpolation is marked on Figure 6b by a black line and the SRR is found as the intersection of this linear interpolation with the  $z$ -axis.

Calculating the SRR for the simulations involves integrating the deflection slope over the contact area as described above in Equation 6, again assuming a circular contact area with origin in  $x = 0$  and radius  $r$ . A value of  $r = 14.5$  cm, found from the tire pressure and axle load of the TSD, is used.

In addition to the linear interpolation, a cubic spline interpolation was also created. In this, a 3rd order polynomial is used to find the values in between the two interpolation points instead of a linear function, thus giving a smoother interpolation curve. As this method has more unknown parameters to fit than the linear, nine simulation points are used, corresponding with the coordinates of the TSD sensors, to make the interpolation. The spline interpolation is marked on Figure 6b with a dotted line. The spline interpolation is included in an attempt to approximate the actual deflection slope in the contact area better.

The relative difference between the interpolations and the simulation curves is found by the relative difference in the dissipated energy over the contact area,

$$\frac{\Delta P^{\text{int.}}}{P} = \frac{\int_S \frac{\partial z^{\text{sim}}}{\partial x} dS - \int_S \frac{\partial z^{\text{int.}}}{\partial x} dS}{\int_S \frac{\partial z^{\text{sim}}}{\partial x} dS} \quad (10)$$

**Table 5.** Calculated Change in  $P_{\text{SRR}}$  of the Simulated Deflection Slope and the Linear and Cubic Spline Interpolations for Different Pavements, Also Showing Values for the Calculated  $P_{\text{SRR}}$  of Both the Simulation and the Interpolations for Each Pavement

Pavement	PAV1	PAV2	PAV3	PAV4
$P_{\text{SRR}}^{\text{sim}}$	335 W	356 W	170 W	59 W
$P_{\text{SRR}}^{\text{linear}}$	172 W	220 W	134 W	54 W
$P_{\text{SRR}}^{\text{spline}}$	257 W	297 W	159 W	58 W
$\frac{\Delta P^{\text{linear}}}{P}$	49%	38%	17%	9%
$\frac{\Delta P^{\text{spline}}}{P}$	23%	17%	6%	2%

The calculated  $P_{\text{SRR}}$  values for the different deflection slope curves and the two interpolated curves are listed in Table 5 along with their relative differences.

The analysis shows that the difference between the simulated deflection slope and the linear interpolation is small for PAV4,  $\frac{\Delta P^{\text{linear}}}{P} = 9\%$ , where the deflection maximum and minimum are far apart. With decreasing stiffness, and thus smaller distance between maximum and minimum, the error increases, with the largest deviation found in PAV1, where  $\frac{\Delta P^{\text{linear}}}{P} = 49\%$ .

The spline interpolation shows the same trend, but it gives a better estimate of SRR. Thus, for the PAV1 the difference is only  $\frac{\Delta P^{\text{spline}}}{P} = 23\%$ , whereas for PAV4 it gives practically the same value as the model curve.

It can be concluded that the linear assumption is valid when the deflection slope peaks are far apart, whereas it

underestimates SRR when the peaks are too close to the origin to be resolved. The spline interpolation in all cases gives a slightly better estimate of SRR, especially for pavements for which the peaks are close together.

Lastly, the numerical calculations were employed to estimate the difference in the deflection slope obtained underneath the tires and at the location of the TSD sensors. In the TSD setup, the sensors are located between the tire pair (see Figure 2a) and therefore the deflection slopes reported in this paper are measured in between the tire pair. This deviates from the analysis assumptions about the contact area in Equation 6, where it is assumed to be circular with origin in  $x = 0$ . By simulating the pavement deflection for pavement PAV1 directly underneath the tires and in between the tire pair, respectively, it was found that the difference in  $P_{SRR}$  is 3.6%. Consequently, this does not have a significant impact on the final SRR results.

## Summary and Outlook

This paper has presented a model-free way to estimate SRR from pavement deflection slope measurements obtained with the TSD. In the simplest approach, it was assumed that the contact between tire and road is point-like (i.e., a “moving point load”). In that case, the SRR coefficient,  $C_{SRR}$ , is simply given as the value of the deflection slope curve at the position of the point load. Because it is not possible to measure exactly at that position because of the presence of the axle, the deflection slope was estimated from a linear interpolation of nearby measurement points behind and in front of that location. The point load assumption is shown to be equivalent to calculations based on a finite contact area, if the deflection slope varies linearly within the contact region.

A set of data from a test road was investigated and the values of  $C_{SRR}$  found by this method span from 0.005 % to 0.05 %, which are modest values compared with typical tire rolling resistance coefficients that are in the range 0.5% to 1%. The values are slightly lower than those found in empirical and numerical studies on the subject (9–11, 15). The data were divided into three groups based on how much of the deflection slope maximum was resolved by the TSD sensors. This was based on the hypothesis that this criterion is critical for the linear interpolation to be a good estimate of the deflection slope under the tire. It was found that for measurements in Group 1 with maximum located closest to the load, the SRR was highest, and for Group 3 with maximum located the furthest away, the SRR was lowest. Through simulated deflection slope curves obtained using the program ViscoWave II-M the linear interpolation was found to underestimate the actual SRR by up to  $\sim 50\%$  in the worst case. Using a cubic spline interpolation between nine positions corresponding to the TSD sensor positions improved the SRR estimate considerably, confirming

that the resolution of the maximum is critical for the linear interpolation approach to give accurate results. Further development of the interpolation method will improve the method and improve the accuracy of the estimated SRR values. By use of numerical studies the authors aim to develop a simple functional expression that will allow the deflection slope values underneath the axle to be estimated with greater accuracy.

The strength of the method is that it requires no knowledge about the pavement structure or pavement properties. Furthermore, the use of the TSD vehicle makes data collection relatively fast and easy and the deflection slope measurements are very precise. This leads to reproducible values of  $C_{SRR}$  determined with low standard deviation, even in areas of the road where the values vary considerably.

The measurements included in this study were made on a test road with the purpose of illustrating the new method and this was chosen for purely practical reasons. They were carried out in relatively cold conditions (pavement temp.  $\sim 18^\circ\text{C}$ ) and a future study with higher pavement and air temperature is expected to provide higher SRR values. In the study, it was found that the magnitude and location of the maximum deflection slope is correlated with the SRR. It is expected that these quantities are mainly dependent on the relative stiffness of the top layer compared with the underlying layers and that the location of the maximum deflection depends on the amount of damping in the pavement (damping in top layer, foundation, or a combination). The relationship between these pavement characteristics and the behavior of the deflection slope curve should be explored further by use of simple physical models.

Through this new, easy method for measuring SRR, it will be feasible to conduct a series of tests on roads with different pavement structures and thus investigate the relationship between pavement structure and SRR. Furthermore, the impact of road temperature or driving speed could also be investigated. Such large-scale systematic surveys could provide much needed clarity in the study of SRR, and establish under which circumstances SRR is important for overall fuel consumption as well as how it is affected by various parameters.

## Author Contributions

The authors confirm contribution to the paper as follows: study conception and design: Natasja R. Nielsen, Christoffer P. Nielsen, Tina Hecksher, Poul G. Hjorth; data collection: Christoffer P. Nielsen; analysis and interpretation of results: Natasja R. Nielsen, Christoffer P. Nielsen, Imen Zaabar, Karim Chatti; draft manuscript preparation: Natasja R. Nielsen, Christoffer P. Nielsen, Tina Hecksher, Poul G. Hjorth, Karim Chatti, Imen Zaabar. All authors reviewed the results and approved the final version of the manuscript.

### Declaration of Conflicting Interests

The authors declared no potential conflicts of interest with respect to the research, authorship, and/or publication of this article.

### Funding

The authors received no financial support for the research, authorship, and/or publication of this article.

### References

- Chupin, O., J. M. Piau, and A. Chabot. Effect of Bituminous Pavement Structures on the Rolling Resistance. *Proc., 11th International Conference on Asphalt Pavements*, Nagoya, Japan, 2010, pp. 1287–1296.
- Hall, D. E., and J. C. Moreland. Fundamentals of Rolling Resistance. *Rubber Chemistry and Technology*, Vol. 74, No. 3, 2001, pp. 525–539.
- Coleri, E., and J. T. Harvey. Impact of Pavement Structural Response on Vehicle Fuel Consumption. *Journal of Transportation Engineering, Part B: Pavements*, Vol. 143, No. 1, 2017, p. 04017002. <https://doi.org/10.1061/JPEODX.0000004>.
- Louhghalam, A., M. Akbarian, and F. J. Ulm. Scaling Relationships of Dissipation-Induced Pavement-Vehicle Interactions. *Transportation Research Record: Journal of the Transportation Research Board*, 2014. 2457: 95–104.
- Bazi, G., E. Y. Hajj, A. Ulloa-Calderon, and P. Ullidtz. Finite Element Modelling of the Rolling Resistance Due to Pavement Deformation. *International Journal of Pavement Engineering*, 2018, pp.1–11. <https://doi.org/10.1080/10298436.2018.1480778>.
- Louhghalam, A., M. Akbarian, and F. J. Ulm. Scaling Relationships of Dissipation-Induced Pavement-Vehicle Interactions. *Transportation Research Record: Journal of the Transportation Research Board*, 2015. 2457: 95–104.
- Flügge, W. *Viscoelasticity*. Springer, Berlin, Heidelberg, 1975.
- Balzarini, D., I. Zaabar, and K. Chatti. Effect of Pavement Structural Response on Rolling Resistance and Fuel Economy using a Mechanistic Approach. *Advances in Materials and Pavement Performance Prediction*, Vol. 10, 2018, pp. 49–51.
- Chupin, O., J. M. Piau, and A. Chabot. Evaluation of the Structure-Induced Rolling Resistance (SRR) for Pavements Including Viscoelastic Material Layers. *Materials and Structures/Materiaux et Constructions*, Vol. 46, No. 4, 2013, pp. 683–696. <https://doi.org/10.1617/s11527-012-9925-z>.
- Akbarian, M., S. S. Moeini-Ardakani, F. Ulm, and M. Nazzal. Mechanistic Approach to Pavement-Vehicle Interaction and Its Impact on Life-Cycle Assessment. *Transportation Research Record: Journal of the Transportation Research Board*, 2012. 2306: 171–179.
- Zaabar, I., and K. Chatti. A Field Investigation of the Effect of Pavement Type on Fuel Consumption. *Proc., T&DI Congress 2011: Integrated Transportation and Development for a Better Tomorrow*, Chicago, IL, 2011, pp. 772–781.
- Balzarini, D., I. Zaabar, and K. Chatti. Impact of Concrete Pavement Structural Response on Rolling Resistance and Vehicle Fuel Economy. *Transportation Research Record: Journal of the Transportation Research Board*, 2017. 2640: 84–94.
- Harvey, J. T., J. D. Lea, C. Kim, E. Coleri, I. Zaabar, A. Louhghalam, K. Chatti, J. Buscheck, and A. But. *Simulation of Cumulative Annual Impact of Pavement Structural Response on Vehicle Fuel Economy*. Research Report: UCPRC-RR-2015-05. University of California Pavement Research Center, Davis, CA, 2016.
- Louhghalam, A., M. Akbarian, and F. J. Ulm. Flügge's Conjecture: Dissipation-Versus Deflection-Induced Pavement-Vehicle Interactions. *Journal of Engineering Mechanics*, Vol. 140, No. 8, 2013, p. 04014053. [https://doi.org/10.1061/\(asce\)em.1943-7889.0000754](https://doi.org/10.1061/(asce)em.1943-7889.0000754).
- Pouget, S., C. Sauzéat, H. D. Benedetto, and F. Olard. Viscous Energy Dissipation in Asphalt Pavement Structures and Implication for Vehicle Fuel Consumption. *Journal of Materials in Civil Engineering*, Vol. 24, No. 5, 2012, pp. 568–576. [https://doi.org/10.1061/\(ASCE\)MT.1943-5533.0000414](https://doi.org/10.1061/(ASCE)MT.1943-5533.0000414).
- Balzarini, D., K. Chatti, I. Zaabar, A. A. Butt, and J. T. Harvey. Mechanistic-Based Parametric Model for Predicting Rolling Resistance of Flexible Pavements. *Transportation Research Record: Journal of the Transportation Research Board*, 2019. 2673: 341–350.
- Hildebrand, G., and S. Rasmussen. *Development of a High Speed Deflectograph*. Technical Report 117. Road Directorate, Danish Road Institute, 2002.
- Krupar, J., S. Rasmussen, L. Aagaard, and P. G. Hjorth. Output from the Greenwood Traffic Speed Deflectometer. *Proc., 22nd ARRB Conference: Research into Practice*, South Vermont, Australia, 2006.
- Chai, G., S. Manoharan, A. Golding, G. Kelly, and S. Chowdhury. Evaluation of the Traffic Speed Deflectometer Data using Simplified Deflection Model. *Transportation Research Procedia*, Vol. 14, 2016, pp. 3031–3039. <https://doi.org/10.1016/j.trpro.2016.05.444>.
- Nielsen, C. P. Visco-Elastic Back-Calculation of Traffic Speed Deflectometer Measurements. *Transportation Research Record: Journal of the Transportation Research Board*, 2019. 2673: 439–448.
- Lee, H. S. *Development of a New Solution for Viscoelastic Wave Propagation of Pavements Structures and Its Use in Dynamic Backcalculations*. PhD thesis. Michigan State University, 2013.
- Balzarini, D., I. Zaabar, K. Chatti, and M. Losa. Impact of Flexible Pavement Structural Response on Rolling Resistance and Vehicle Fuel Consumption. *Proc., World Conference on Pavement and Asset Management*, Baveno, Italy, 2017.
- Lee, H. S., H. V. Quintus, and D. Steel. Effect of Moving Dynamic Loads on Pavement Deflections and Backcalculated Modulus. Presented at 97th Annual Meeting of the Transportation Research Board, Washington, D.C., 2018.

## **A.2 Measurement of structural rolling resistance at two temperatures**

Published in Proceedings for Advances in Material and Pavement Performance Prediction II, December 14, 2020.

## Measurement of structural rolling resistance at two temperatures

N.R. Nielsen & T. Hecksher  
Roskilde University, Roskilde, Denmark

C.P. Nielsen  
Greenwood Engineering A/S, Brøndby, Denmark

P.G. Hjorth  
DTU Compute, Lyngby, Denmark

**ABSTRACT:** In this study, we investigate how an increase in road temperature influences the structural rolling resistance of a heavy vehicle. The structural rolling resistance (SRR) is defined as the dissipated energy due to pavement deflection under a moving load. It is measured using a newly proposed method, which is based on the relationship between SRR and the slope of the deflection basin underneath the load. Using the Traffic Speed Deflectometer technology, we measured SRR on the same road under two different road temperatures, 18°C and 35°C respectively. On average, an increase in SRR of 59% was observed, with some areas of the road having up to 400% increase. This indicates that under warm road conditions SRR might have a significant effect on the overall rolling resistance of a heavy vehicle.

### 1 INTRODUCTION

When a pavement is subject to a moving load, it will deform underneath it. If the pavement is viscoelastic, the time delay in the deflection makes the maximum deflection appear behind the load. This results in an asymmetric deflection basin, as illustrated on Figure 1a. Consequently, the load experiences an uphill deflection slope (Fig. 1b) and has to do work in order to maintain a constant speed (Flügge, 1975). The excess energy consumption due to deflection of the pavement is dependent on the pavement structure, and we will refer to it as structural rolling resistance (SRR). SRR can be calculated directly from the asymmetric deflection basin (Balzarini et al. 2018, Chupin et al. 2013).

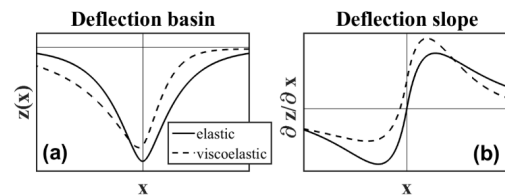


Figure 1. Pavement deflection (a) and associated deflection slope (b) of an elastic and viscoelastic pavement. Viscous properties make the deflection basin asymmetric, which results in a positive deflection slope underneath the load ( $x=0$ ).

Estimates of SRR are often derived by simulating the pavement response to a moving load with constant speed. The pavement parameters used in these simulations are obtained from either back-calculated falling weight deflectometer measurements or laboratory measurements on the pavement materials (Pouget et al. 2012, Akbarian et al. 2012, Balzarini et al. 2017). Moreover, indirect measurements of SRR have been conducted (Zaabar & Chatti 2014). However, it has been proven difficult to develop accurate and robust methods for measuring SRR directly.

In Nielsen et al. (accepted) we presented a new method for direct measurements of SRR, using the Traffic Speed Deflectometer (TSD) technology. The method is based on the relation between SRR and the slope of the deflection basin underneath a moving load. Using the TSD has the advantage that it mimics a full-size trailer and thus it measures the pavement deflection slope under realistic driving conditions. The method proved to be robust and measure SRR with high accuracy when repeated measurements were compared. Furthermore, it has the clear advantage that it does not require a model or prior knowledge about the pavement in order to calculate SRR.

The influence of temperature on SRR has been investigated in literature, by use of numerical simulations (Pouget et al. 2012, Shakiba et al. 2016). The magnitude of the found temperature effect differs between the studies is dependent on the applied pavement models. To the authors knowledge no direct measurements of the temperatures influence on SRR for heavy vehicles exist.

In this paper, we investigate the effect of road temperature on SRR. We expect that a higher road temperature will lead to a softer asphalt layer and an increased pavement response to the moving load. In addition, within the investigated temperature range we expect the viscoelastic damping of the asphalt to increase with increasing temperature (Pouget et al. 2012, Shakiba et al. 2016). Consequently, we expect that an increase in road temperature will lead to a higher SRR.

## 2 TRAFFIC SPEED DEFLECTOMETER DATA

### 2.1 TSD principle

The Traffic Speed Deflectometer (TSD) continuously measures the vertical velocity ( $v_d$ ) of the pavement underneath the right rear-end trailer tires, while the truck is moving. This is done by means of Doppler lasers positioned between the tire set both in front and behind the axle. From this, the pavement deflection slope ( $dz(x_n)/dx$ ) for each position ( $x_n$ ) is obtained by dividing with the driving speed ( $v$ ),

$$\frac{dz(x_n)}{dx} = \frac{v_d(x_n)}{v}. \quad (1)$$

The principle is explained in more depth in Nielsen (2019).

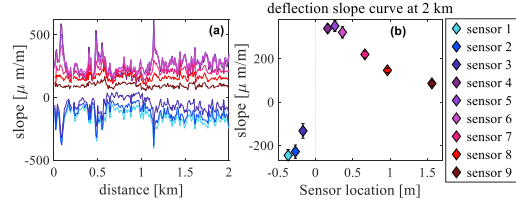
Having measurements on both sides of the load enable us to determine the asymmetry in the deflection basin arising from viscoelastic properties in the pavement.

### 2.2 Raw data

For this study, two sets of measurements were made at a road section near Copenhagen, Denmark. The measurements were made on two days (15 months apart), where the pavement temperature was 18°C and 35°C respectively. Each set of measurements were repeated three times and a good reproducibility was seen with median standard deviations of 9% (18°C) and 5.5% (35°C). The TSD truck was at maximum axle load (10 tonnes) and driving speed was between 50-60 km/h, with the exact driving speed recorded continuously during the measurement rounds.

In Figure 2a, a plot of the measured deflection slope data in the beginning of the ~10 km measured road section is shown. The measured deflection slope for each sensor is an average over 10 m. An example

of the deflection slopes at 2 km, as a function of distance from the load, is seen in Figure 2b. The center of the axle is at  $x=0$ . The deflection slope curve is characterized by a minimum located behind the load and a maximum in front of the load. The standard de-



viations are illustrated with error bars in Figure 2b. In some cases, the error bars are smaller than the markers and thus not visible.

Figure 2. Example of raw data at 18°C. (a) Measured deflection slope for all sensors in the beginning of the measured road. (b) deflection slopes as a function of distance from the load. Standard deviations are shown with error bars.

## 3 SIMPLE METHOD FOR ESTIMATING THE STRUCTURAL ROLLING RESISTANCE

This method was presented for the first time in Nielsen et al. (accepted). In the simplest approach, we assume that the applied load is a point load, located at the center of the tire ( $x=0$ ) with magnitude  $F_L$ . The dissipated energy in the pavement ( $P_{SRR}$ ), can be calculated from the vertical pavement velocity underneath the load and the applied load,

$$P_{SRR} = F_L v_d(x=0) = F_L v \frac{dz}{dx}(x=0), \quad (2)$$

where the last expression comes from Equation 1. In the case of a perfectly elastic pavement the deflection slope under the load is zero, and therefore the dissipated energy is also zero,  $P_{SRR} = 0$ . On the other hand, if there is some damping in the pavement, the slope underneath the load will be larger than zero. In this case, energy is dissipated in the pavement i.e.  $P_{SRR} > 0$ . Equation 2 requires knowledge of the deflection slope exactly underneath the load ( $x=0$ ). However, due to the presence of the axle, it is not possible to measure in that point. Therefore, we have to estimate the slope at  $x=0$  based on the surrounding data points. The simplest approach is to make a linear interpolation between the two sensor points closest to the load (sensor 3 and 4). Doing this we have that

$$P_{SRR} = F_L b v, \quad (3)$$

where  $b$  is the intersection at  $x=0$  for the linear interpolation. From this, we obtain the expression for the structural rolling resistance force,  $F_{SRR} = P_{SRR}/v$ . We can also derive the structural rolling resistance coefficient, defined as the ratio between the rolling resistance force and the applied load,

$$C_{SRR} = \frac{F_{SRR}}{F_L} = b. \quad (4)$$

## 4 RESULTS

### 4.1 The influence of temperature on the structural rolling resistance coefficient

Using two sets of deflection slope data measured at the road temperatures 18°C and 35°C, we study the influence of road temperature on SRR. The temperatures were measured at the surface using an infrared temperature sensor through all measurements. In Figure 3  $C_{SRR}$  is plotted versus distance on the ~10 km measured road segment. In this plot, the mean  $C_{SRR}$  values after three repeated measurements are shown. There is a systematic increase in  $C_{SRR}$  as the road temperature increases. The median of the standard deviations in  $C_{SRR}$  are  $0.13 \cdot 10^{-4}$  (9%) for 18°C and  $0.2 \cdot 10^{-4}$  (5.5%) for 35°C. Thus, the calculated  $C_{SRR}$  values have a good precision.

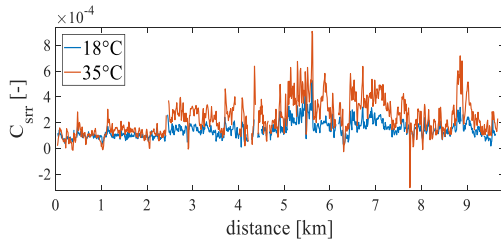


Figure 3. Calculated  $C_{SRR}$  at warm (35°C) and cold (18°C) road temperature. The median of the standard deviations are  $0.13 \cdot 10^{-4}$  (9%) for 18°C and  $0.2 \cdot 10^{-4}$  (5.5%) for 35°C. Note that the  $C_{SRR}$  values are negative in some points at 35°C, which is unphysical. This behavior is commented on in section 4.2.

In Figure 4, a histogram of the measured  $C_{SRR}$  values is shown. Here, we see that the mean  $C_{SRR}$  over the entire road increases from  $1.4 \cdot 10^{-4}$  to  $2.3 \cdot 10^{-4}$  when the temperature is increased. Furthermore, the distribution of  $C_{SRR}$  becomes broader with higher temperature. This means that the calculated  $C_{SRR}$  for 35°C varies more along the road. The total rolling resistance of a truck is typically on the order of 1% of the load. Based on this, the mean  $C_{SRR}$  found in this study are 1.4% (cold) and 2.3% (warm) of the typical total rolling resistance.

$C_{SRR}$  varies considerably throughout the measured distance (from 0.01% of the load to 0.06%). This variation is completely reproducible within the three repeated measurement runs, and we see that spatial variations are similar for the two temperatures. A notable increase in  $C_{SRR}$  is seen around 2.5 km. There is no visible change in the asphalt in this area, and thus the change is due to a structural change in the underlying layers. The varying  $C_{SRR}$  values reflect the fact that the road measured on is not a homogeneous road, but

a real road with varying pavement structure. Most likely the thickness of the asphalt layer and possibly also the type of asphalt differs along the road. As a result, SRR and its temperature dependence will also differ along the road. The method shows a good ability to reproducibly capture these changes in  $C_{SRR}$ , even in areas where  $C_{SRR}$  changes dramatically.

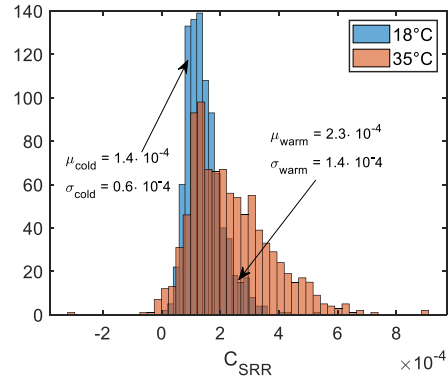


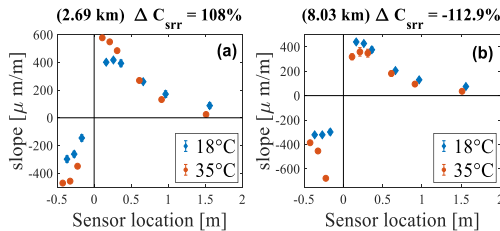
Figure 4. Histogram of measured structural rolling resistance coefficients for cold (18°C) and warm (35°C) road conditions. We see an increase in the mean ( $\mu$ )  $C_{SRR}$  value, when the road temperature is increased. Furthermore, the distribution of measured values is broader under warm conditions (increased  $\sigma$ ).

### 4.2 Influence of temperature on the deflection slope curves

By looking into some representative sets of deflection slopes, we can qualitatively investigate the change caused by increased road temperature. Figure 5a illustrates the most commonly encountered influence that the increased road temperature has on the deflection slope curves. Either the maximum deflection slope increases, the minimum deflection slope decreases or both effects occur at the same time (as seen in Figure 5a). An increase in maximum deflection slope value means that the deflection basin gets steeper in front of the load. This often leads to the deflection slope value underneath the load being increased (thus higher  $P_{SRR}$ ). A decrease in the minimum deflection slope value means that the deflection basin becomes steeper behind the load. Furthermore, we often see that the minimum deflection slope is moved to the left (away from the load) in the warm data. This corresponds to the maximum deflection moving further behind the load, something which is associated with an increased effect of viscous damping.

In Figure 3, the calculated  $C_{SRR}$  is negative in a few places, which is unphysical. In Figure 5b, an example of such a deflection slope curve in a place with negative  $C_{SRR}$  is plotted. Here, a plot of the deflection slope values at 8.03 km is shown for both temperatures. The relative change in  $C_{SRR}$  from cold to warm

data is -112.9%, as in the warm situation, we calculate a negative  $C_{SRR}$  when using linear interpolation. Note that the shape of the deflection slope curve changes dramatically around the minimum, when temperature is increased. Furthermore, for the warm data we see that the magnitude of the deflection slope is higher



behind the load than in front of the load. This behavior indicates that using linear interpolation to find the deflection slope underneath the load, in some cases is too simple to capture the actual slope assess.

Figure 5. Representative sets of deflection slope curves. The relative change in  $C_{SRR}$  is listed for each plot as  $\Delta C_{SRR}$ . Standard deviations are indicated with error bars (not visible when these are smaller than the markers). It should be noted that in between the two sets of measurements the sensor locations have been changed slightly. We only expect this to have a minor effect on the results of the analysis.

## 5 SUMMARY AND CONCLUSION

In this study, we have presented measurements of structural rolling resistance of a  $\sim 10$  km road section, measured at two different road temperatures (18°C and 35°C). The method shows good reproducibility between the repeated measurements, with small standard deviations. Furthermore, it was also able to capture the spatial changes in  $C_{SRR}$ , which occur in data at 18°C and 35°C.

The found SRR values have a magnitude which is comparable with results found in empirical and numerical studies on the subject (Akbarian et al. 2012, Chupin et al. 2013, Zaabar & Chatti 2014, Pouget et al. 2012). On average,  $C_{SRR}$  increased with 59% over the measured distance when temperature increased, in some areas even up to 400% increase, showing that for warm weather conditions SRR have an effect on the overall energy consumption for heavy vehicles.

An increase in SRR with temperature was expected based on studies in the literature and our physical intuition. We observed a difference in the degree of which temperature influenced SRR, depending on which area of the measured road we looked at. This result in a broadening of the distribution of  $C_{SRR}$  for increasing road conditions. The general trend is, that the magnitude of the deflection slope maximum and minimum increases (separately or together) which shows that the deflection basin gets steeper and deeper. This is consistent with our expectation, that

the asphalt layer becomes softer at higher temperatures. Furthermore, the maximum deflection moves further behind the load, indicating that the role of viscous damping in the pavement becomes greater.

Some unexpected behavior in the deflection slope curves was also observed. In some areas, the magnitude of the slope becomes bigger behind the load than in front of the load, when the temperature is increased. This odd behavior was fully reproducible within the three repeated measurements. We speculate that this behavior is due to a situation where the asphalt layer becomes much softer than usual. In this case, there will be a compression of the top layer in addition to the usual bending of the top layer. This leads to a non-intuitive behavior of the overall deflection basin, and thus an odd signal in the deformation slope. A better understanding of the temperature influence on the pavement response requires a model study, giving a more detailed insight into road temperatures effect on the structural behavior.

## 6 REFERENCES

- Akbarian, M., Moeini-Ardakani, S. S., Ulm, F. & Nazzal, M. 2012. Mechanistic Approach to Pavement-Vehicle Interaction and Its Impact on Life-Cycle Assessment. *Transport Res Rec.* No. 2306:171-179.
- Balzarini, D., Zaabar, I. & Chatti, K. 2018. Effect of Pavement-structural response on rolling resistance and fuel economy using a mechanistic approach. *Advances in Material and Pavement Performance Predictions.* Vol. 10:49-51.
- Balzarini, D., Zaabar, I., & Chatti, K. 2017. Impact of Concrete Pavement Structural Response on Rolling Resistance and Vehicle Fuel Economy. *Transport Res Rec.* Vol. 2640(1): 84-94.
- Chupin, O., Piau, J. & Chabot, A. 2013. Evaluation of the Structure-induced Rolling Resistance (SRR) for pavements including viscoelastic material layers. *Materials and Structures, Springer Verlag.* Vol. 46 (4):683-696.
- Flügger, W. (second ed.) 1975. *Viscoelasticity.* Springer-Verlag Berlin Heidelberg
- Nielsen, N. R., Chatti, K., Nielsen, C. P., Zaabar, I., Hjorth, P. G. & Hecksher T. Method for Direct Measurement of Structural Rolling Resistance for Heavy Vehicles. *Accepted for publication in Transport Res Rec.* (Feb. 28, 2020).
- Nielsen C. P. 2019. Visco-Elastic Back-Calculation of Traffic Speed Deflectometer Measurements. *Transport Res Rec.* Vol. 2673 (12): 439-448
- Pouget, S., Sauzéat, C., Benedetto, H.D. & Olard, F. 2012. Viscous Energy Dissipation in Asphalt Pavement Structures and Implication for Vehicle Fuel Consumption. *Journal of materials in civil engineering.* Vol. 24 (5):568-576.
- Shakiba, M., Ozer, H., Ziyadi, M. & Al-Qadi. 2016. Mechanics based model for predicting structure-induced rolling resistance (SRR) of the tire-pavement system. *Mech Time-depend Matter.* Vol. 20:579-600
- Zaabar, I. & Chatti, K. 2014. A field investigation of the effect of pavement type on fuel consumption. *T and Di Congress 2011.* Pp. 772-781.



### **A.3 Impact of viscous damping in asphalt and foundation - part 1: Theoretical investigation of a viscoelastic beam on a damped Pasternak foundation**

This paper draft is a part of a series consistent of two papers. Part 1 concerns the theoretical derivation of the pavement response model and a numerical analysis of this. Part 2 describes the result from the model fitting procedure to Måløv data (presented in chapter 20). An initial draft for part 2 has been developed, but this was not deemed finished enough to be included as a draft in the thesis.

# *Impact of viscous damping in asphalt and foundation - part 1: Theoretical investigation of a viscoelastic beam on a damped Pasternak foundation*

*Natasja R. Nielsen<sup>a</sup>, Christoffer P. Nielsen<sup>b</sup>, Poul G. Hjorth<sup>c</sup>, Tina Hecksher<sup>a</sup>*

<sup>a</sup>*Roskilde University, Universitetsvej 1, 4000 Roskilde, Denmark*

<sup>b</sup>*Greenwood Engineering A/S, H. J. Holst Vej 3-5C, 2605 Brøndby, Denmark*

<sup>c</sup>*DTU Compute, Richard Petersens Plads, Bygning 324, 2800 Kgs. Lyngby, Denmark*

**Abstract:** ...

## **1. Introduction**

The dynamic response of a pavement subject to a moving load has been studied throughout the last decades. There exist a variety of different approaches towards simulating a pavement system, going from complex numerical methods to simple models where closed-form solutions can be obtained. Two good reviews in the area are [1] and [2]. The different modelling approaches all have advantages and disadvantages and is suited for different purposes. Thus, the end goal of the modelling process should guide the choice of modelling approach applied. In order to model the entire pavement structure, a multi layered model is needed, often with different mechanical properties of each layer. However, these types of models easily gets complicated and often contain insensitive parameters that can not be fitted to any data and thus, are not very useful in practise. Therefore it is often convenient to use a more simple, but still physical model of the pavement structure [2]. This approach will be used in this paper.

The simplest kind of pavement response models either consist of an elastic beam on a (damped) foundation, called a Winkler-foundation, or an elastic half space, a Boussinesq type problem [3, 4]. This types of models have been studied extensively in the literature [5, 4, 6, 2]. The interest into these simple 1D models are growing, since they can be used both with respect to the railway industry and the highway industry [5, 7]. The advantage of a simple model is that the parameters influence on the dynamic response easily can be evaluated. They does, however, comes with some limitations as they often are used without a damping component, even though soil is known to posses damping [8]. Furthermore, the Winkler foundation uses an idealization of the soil medium, and thus does not accurately represent the continuous behaviour of real foundations [7, 9].

The simple beam model can be extended in different ways. E.g. a more realistic 2D situation can be considered by having a plate on a foundation, the foundation can be extended to multiple layers or one can model the soil as a three-dimensional continuous medium [10, 2, 1].

Asphalt consists of bituminous materials, which are known to have viscoelastic behaviour that affect the dynamic response of the pavement. This is especially true under warm conditions [6]. The viscous effect of the bituminous material can be investigated experimentally through complex modulus tests and from this, the linear viscoelastic behaviour can be characterized. The viscoelastic properties of the asphalt can be modelled using mechanical models containing springs and dashpot elements. In [11], a comparison between the Huet-Sayegh's and Burgers' viscoelastic models and Hooke's elastic model is presented. Several other studies has been made in this area, investigating which viscoelastic model that determine the behaviour of asphalt the best [12, 13, 14, 15, 16]. Generally, models like the Huet-Sayegh, the Burgers and the 2S2P1D model are good candidates, all containing several spring and dashpot elements (both linear and parabolic) [17, 16].

The viscoelastic properties of asphalt can be incorporated into the simple models by introducing viscoelastic behaviour in the beam. In [18] they have made a comparison study of a model with viscoelastic effects in the asphalt layer and a model with elastic top layer. They conclude that a difference in the pavement response can be seen between the two situations at slow driving conditions and/or high temperatures. And that, in these cases, the viscoelastic effects of the pavement top layer should not be neglected. In [18] both viscoelastic effects of the top layer and the foundation is considered. However, this is often not the case as the underlying layers are assumed elastic and thus the dissipated energy due to viscous effects are only coming from the top layer [12, 11].

This paper is a part of a two-parted study on the impact of viscous behaviour in asphalt and foundation on the pavement response. In this paper we will extend the well known Pasternak foundation model to include viscoelasticity in the beam. Furthermore, the model is shifted to a moving reference frame such that the results are comparable with pavement deflection slope data measured using a Traffic Speed Deflectometer (TSD). A theoretical and numerical study of the model and how its physical parameters influence the pavement deflection is made in this paper. These theoretical considerations are used to analyse TSD data in [data paper kilde](#), where the model is fitted to data in order to simulate the behaviour of the pavement deflection underneath the load. Using this, we are able to calculate the dissipated energy due to the pavement deflection (structural rolling resistance) of a test road segment, using the method presented in [19].

Finally we derive an important correlation between the pavement deflection slope behaviour and the origin of pavement damping. Using this we are able to deduce if the dominating pavement damping origins from the top or underlying layers directly by looking at pavement deflection slope measurements.

Since the purpose of this model is to fit to TSD data, the number of model parameters are limited by the number of data points as overparameterization is to be avoided. In our case this number is 9 data points. Thus we aim to develop the simplest possible model that still accurately capture the desired pavement characteristics, such as viscous properties and pavement stiffness, and is founded in physical elements. Newer developed TSD's might be equipped with more sensors and thus allow more model parameters.

## 2. Developing an extended version of the elastic Pasternak model

### 2.1. Model presentation and introduction of damping

The model developed in this paper is an extended version of the simple elastic Pasternak model for pavement response under a moving load [7]. The model is extended by introducing viscous damping in both the beam and foundation.

The elastic Pasternak model is a two layered model, consisting of an elastic Euler-Bernoulli beam resting on a two parameter foundation model [2]. The beam is assumed to extend to infinity, be made from a homogeneous and isotropic material and is characterised by its elastic modulus  $E$  [ $\frac{N}{m}$ ] and the second moment of area pr. unit length,  $I$  [ $m^3$ ]. Note that the units of  $E$  and  $I$  is different than the classical use, since we are in a 1D situation. The flexural rigidity,  $EI$ , of the beam is as normal in units [ $Nm^2$ ]. A sketch of the model can be seen on figure 1. In the model, the soil is represented by a set of continuously-distributed springs with spring constant per unit length  $k$  [ $\frac{N}{m^2}$ ]. In order to take into account the cohesive bonds between the soil particles, a shear interaction parameter  $G$  [ $N$ ] is included. This accounts for the shear forces in the foundation by connecting the spring elements at the top with an in-compressible layer [2, 9, 20]. Physically, this can be thought of as a set of horizontal springs in between the soil elements (as illustrated on figure 1). Beside coping with the shear interactions, the layer also ensures that the applied load is distributed over multiple foundation elements, instead of just a few. Thereby the foundation will act more like a continuous medium [9, 20].

The govern equation for vertical pavement deflection,  $w(x', t)$  [m], of the purely elastic Pasternak model is given by equation (1).

$$EI \frac{\partial^4 w(x', t)}{\partial x'^4} + \tilde{\rho} \frac{\partial^2 w(x', t)}{\partial t^2} - G \frac{\partial^2 w(x', t)}{\partial x'^2} + kw(x', t) = q(x', t), \quad (1)$$

where  $\tilde{\rho}$  is the mass per unit length of the beam (found by the density of the beam times the cross section area, and assumed constant) [ $kg/m$ ] and  $q(x', t)$  is a distributed load function with units [ $\frac{N}{m}$ ].

Damping is introduced into the model in two ways. Firstly, we introduce damping in the soil by adding a set of uniformly-distributed dashpots with viscous damping coefficient per unit length  $c$  [ $\frac{Ns}{m^2}$ ]. This will add an extra term  $c \frac{\partial w(x', t)}{\partial t}$  to equation (1). Damped Pasternak models like this has been studied in literature before, see [7, 9, 21, 20].

Secondly, we include viscoelastic effects of the asphalt into the model by considering a viscoelastic beam.

#### 2.1.1. Governing equation for deflection of a viscoelastic beam

Consider an isotropic and homogeneous visco-elastic Euler-Bernoulli beam. For describing the beam we have an internal and outer coordinate system. The inner coordinate system is defined for each element on the neutral axis (axis going through the center of mass of the cross section area) with the  $z$  coordinate perpendicular to the

neutral axis, pointing downwards. The outer coordinate system is defined with  $x'$  aligned with the neutral axis of the straight beam and  $w(x')$  denoting the vertical displacement of the neutral axis compared to the straight beam. Thus  $w(x') = 0$  for a straight beam.

The constitutive equations for a linear viscoelastic material which dictates the relationship between stress and strain, are not the one of Hook's law but explained through the relaxation function  $E(t)$ . As the beam only experience uni-axial stresses, the constitutive equations is a single relation between stress and strain given by the general expression in equation (2).

$$\sigma(t) = E_0\varepsilon(t) - \int_0^t \varepsilon(t') \frac{dE(t-t')}{d(t')} dt', \quad (2)$$

where  $E_0$  is the instantaneous elastic modulus and  $E(t-t')$  is the relaxation function convoluted over all previous strain experienced by the material, starting at  $t = 0$ . Equation (2) shows that a viscoelastic material has memory and that the stress response of an applied strain depends on the strain history experimented by the material.

The relation between the bending moment of the beam  $M(x', t)$ , shear forces in the beam  $T(x', t)$  and vertical load  $q(x', t)$  in an dynamical beam problem is described through the equations of motion.

$$\text{dynamic conservation of momentum: } \frac{\partial T(x', t)}{\partial x'} = \tilde{\rho} \frac{\partial^2 w(x', t)}{\partial t^2} - q(x', t), \quad (3)$$

$$\text{dynamic moment of momentum: } \frac{\partial M(x', t)}{\partial x'} = T(x', t), \quad (4)$$

where  $\tilde{\rho}$  is the mass per unit length of the beam [kg/m] and the bending moment is given by

$$M(x', t) = \int_A z \sigma(x', z, t) dA. \quad (5)$$

Here  $A$  is the cross section of the beam which is assumed constant.

Furthermore, we have the kinematic relation which relates the displacement  $w(x', t)$  and the strain  $\varepsilon(x', z, t)$  for small deformations.

$$\text{Kinematic equation: } \varepsilon(x', z, t) = -z \frac{\partial^2 w(x', t)}{\partial x'^2}. \quad (6)$$

The equations of motion and the kinematic equations is true for both elastic and viscoelastic materials, and thus only the constitutive equation is different in the two cases.

Inserting equation (6) into equation (2) and then inserting this into equation (5) gives

$$M(x', t) = -I \frac{\partial^2 w(x', t)}{\partial x'^2} E_0 + I \int_0^t \frac{dE(t-t')}{dt'} \left( \frac{\partial^2 w(x', t')}{\partial x'^2} \right) dt'. \quad (7)$$

Taking the second-order derivative with respect to  $x'$  on both sides and then inserting the expression for  $M(x', t)$ , obtained by combining equation (3) and (4), gives the governing equation for the deflection a viscoelastic beam subject to a vertical load

$$\tilde{\rho} \frac{\partial^2 w(x', t)}{\partial t^2} + \frac{\partial^4 w(x', t)}{\partial x'^4} I E_0 - I \int_0^t \frac{dE(t-t')}{dt'} \frac{\partial^4 w(x', t')}{\partial x'^4} dt' = q(x', t). \quad (8)$$

Including the two types of damping (damping in the foundation and in the beam) into equation (1), results in the following equation that govern the pavement response to a moving load for a viscoelastic beam on a damped Pasternak foundation,

$$E_0 I \frac{\partial^4 w(x', t)}{\partial x'^4} - I \int_0^t \frac{dE(t-t')}{d(t')} \frac{\partial^4 w(x', t)}{\partial x'^4} dt' + \tilde{\rho} \frac{\partial^2 w(x', t)}{\partial t^2} - G \frac{\partial^2 w(x', t)}{\partial x'^2} + c \frac{\partial w(x', t)}{\partial t} + kw(x', t) = q(x', t). \quad (9)$$

A solution for the pavement deflection  $w(x', t)$  can be found using an semi-analytical approach. Here an analytical solution is found in the Fourier domain and the the inverse Fast Fourier Algorithm (iFFT) is used to find the pavement deflection in spacial domain numerically.

Using the convolution theorem, the Fourier transformed of equation (9) with respect to time and space is derived (equation (10)). We use  $\omega$  and  $k_x$  as the transform variable with respect to time and space respectively.

$$(E_0 - \tilde{E}(\omega)i\omega)Ik_x^4\hat{w}(k_x, \omega) - \tilde{\rho}\omega^2\hat{w}(k_x, \omega) + Gk_x^2\hat{w}(k_x, \omega) + ci\omega\hat{w}(k_x, \omega) + k\hat{w}(k_x, \omega) = \hat{q}(k_x, \omega) \quad (10)$$

We then solve for the pavement deflection,  $\hat{w}(k_x, \omega)$ .

$$\hat{w}(k_x, \omega) = \frac{\hat{q}(k_x, \omega)}{IE^*(\omega)k_x^4 - \tilde{\rho}\omega^2 + Gk_x^2 + ci\omega + k} \quad (11)$$

Here the term  $E^*(\omega) = (E_0 - \tilde{E}(\omega)i\omega)$  is the complex modulus of the beam.  $E^*(\omega)$  is a general term, and specific viscoelastic models to describe the beams behaviour can be inserted as required.

## 2.2. Change of reference frame to moving coordinate system

Equation (9) account for the vertical deflection of the pavement in a fixed coordinate. However, in this paper we are interested in the pavement deflection underneath a moving tire and therefore equation (9) has to be changed into a moving reference frame. This is done by assuming a steady state situation, where the driving velocity ( $v$ ) is constant. In this case we can make the coordinate shift  $x = x' - vt$ , where  $x$  is our new time dependent  $x$  coordinate. Applying a coordinate shift in equation (9) is not trivial, due to the presence of a convolution integral, and thus this is done in the Fourier domain. This means that we have to find the corresponding coordinate shift in the frequency domain and apply it to equation (11).

We start of by showing how this is done for a general system on the form  $Lw(x', t) = q(x', t)$ , where  $L$  is a linear differential operator, and afterwards it is applied to our particular system (equation (9)).

The solution to a system on the form  $Lw(x', t) = q(x', t)$  can be found using the Green's function. The Greens function ( $w_\delta(x', t)$ ) to a linear differential operator  $L$ , is the solution to a system subject to an impulse load,

$$Lw_\delta(x', t) = \delta(x')\delta(t)$$

The Green's function has the property that the solution to a system  $Lw(x', t) = q(x', t)$  can be found using the convolution  $w(x', t) = w_\delta(x', t) * q(x', t)$ . A property that in the Fourier domain becomes  $\hat{w}(k_x, \omega) = \hat{w}_\delta(k_x, \omega) \cdot \hat{q}(k_x, \omega)$ .

Using this relation, we can write up the general expression for the inverse Fourier transformed pavement deflection in a fixed frame.

$$w(x', t) = \frac{1}{(2\pi)^2} \int_{-\infty}^{\infty} \int_{-\infty}^{\infty} \hat{w}(k_x, \omega) e^{ik_x x'} e^{i\omega t} dk_x d\omega \quad (12)$$

$$= \frac{1}{(2\pi)^2} \int_{-\infty}^{\infty} \int_{-\infty}^{\infty} \hat{w}_\delta(k_x, \omega) \hat{q}(k_x, \omega) e^{ik_x x'} e^{i\omega t} dk_x d\omega \quad (13)$$

We start by evaluating the loading function term  $\hat{q}(k_x, \omega)$  in equation (13). From the definition of the Fourier transform we have that

$$\hat{q}(k_x, \omega) = \int_{-\infty}^{\infty} \int_{-\infty}^{\infty} q(x', t) e^{-ik_x x'} e^{-it\omega} dx' dt \quad (14)$$

A moving load is described by a impulse load in the time domain and thus the loading function can be rewritten

$$q(x', t) = Q(x' - vt). \quad (15)$$

Including this into equation (14) gives

$$\hat{q}(k_x, \omega) = \int_{-\infty}^{\infty} \int_{-\infty}^{\infty} Q(x' - vt) e^{-ik_x x'} e^{-it\omega} dx' dt \quad (16)$$

Now we include the coordinate shift  $x = x' - vt$  and that  $\frac{dx}{dx'} = \frac{d(x' - vt)}{dx'} = 1$ . Since the limits is from minus infinity to infinity, changing the coordinate do not affect these.

$$\hat{q}(k_x, \omega) = \int_{-\infty}^{\infty} \int_{-\infty}^{\infty} Q(x) e^{-ik_x(x+vt)} e^{-it\omega} dx dt \quad (17)$$

$$= \int_{-\infty}^{\infty} Q(x) e^{-ik_x x} dx \int_{-\infty}^{\infty} e^{-it(vk_x + \omega)} dt \quad (18)$$

Using that  $\int_{-\infty}^{\infty} e^{it(x-a)} dt = 2\pi\delta(x-a)$  we get the expression for the loading function in a moving reference frame:

$$\hat{q}(k_x, \omega) = 2\pi \int_{-\infty}^{\infty} Q(x) e^{-ik_x x} dx \delta(vk_x + \omega) = 2\pi \hat{Q}(k_x) \delta(vk_x + \omega). \quad (19)$$

We now return to the Fourier transform of the pavement deflection in equation (13).

$$w(x', t) = \frac{1}{(2\pi)^2} \int_{-\infty}^{\infty} \int_{-\infty}^{\infty} \hat{w}_\delta(k_x, \omega) \hat{q}(k_x, \omega) e^{ik_x x'} e^{i\omega t} dk_x d\omega \quad (20)$$

$$= \frac{1}{2\pi} \int_{-\infty}^{\infty} \int_{-\infty}^{\infty} \hat{w}_\delta(k_x, \omega) \hat{Q}(k_x) \delta(vk_x + \omega) e^{ik_x x'} e^{i\omega t} dk_x d\omega \quad (21)$$

$$= \frac{1}{2\pi} \int_{-\infty}^{\infty} \hat{Q}(k_x) e^{ik_x x'} \int_{-\infty}^{\infty} \hat{w}_\delta(k_x, \omega) \delta(vk_x + \omega) e^{i\omega t} d\omega dk_x \quad (22)$$

In order to solve the integral over  $\omega$  we use the fact that a delta function  $\delta(x-a)$  is zero all other places than in  $a$ . Hence if we have a function  $\int_{-\infty}^{\infty} f(t)\delta(t-t_0)dt = f(t_0)$ . Thus we get

$$w(x', t) = \frac{1}{2\pi} \int_{-\infty}^{\infty} \hat{Q}(k_x) e^{ik_x x'} \hat{w}_\delta(k_x, -vk_x) e^{-ivk_x t} dk_x \quad (23)$$

$$= \frac{1}{2\pi} \int_{-\infty}^{\infty} \hat{Q}(k_x) \hat{w}_\delta(k_x, -vk_x) e^{ik_x(x'-vt)} dk_x \quad (24)$$

$$= \frac{1}{2\pi} \int_{-\infty}^{\infty} \hat{Q}(k_x) \hat{w}_\delta(k_x, -vk_x) e^{+ik_x x} dk_x \quad (25)$$

This shows that making a coordinate shift in the Fourier domain correspond to the substitution  $\omega = -vk_x$ . Thus a general expression for the the Fourier transformed pavement deflection in a moving frame is

$$\hat{w}(k_x, -vk_x) = \hat{w}_\delta(k_x, -vk_x) \hat{Q}(k_x). \quad (26)$$

As for the loading function, the pavement deflection can be rewritten in terms of the new moving reference coordinate

$$w(x', t) = W(x - vt) = w(x). \quad (27)$$

For the system in equation (9), the Fourier transformed Green's function in a moving reference frame is

$$\hat{w}_\delta(k_x, -vk_x) = \frac{1}{IE^*(-vk_x)k_x^4 - \tilde{\rho}v^2k_x^2 + Gk_x^2 - cik_x v + k}$$

We will in this paper assume a point load (described by the Dirac delta function) with constant amplitude  $F$  [N]. Thus we have  $Q(x' - vt) = F\delta(x' - vt)$  and  $\hat{Q}(k_x) = F$ . Since we are working with an beam model, where the assumption is that the beam only deflect and not deform this will contribute to distributing the load and thus assuming a point load and not a distributed load is reasonable assumption.

Using this, we obtain the expression for the Fourier transformed pavement deflection,  $\hat{w}(k_x, -vk_x)$ . The pavement deflection of the beam,  $w(x)$  can then be found using the inverse Fast Fourier Algorithm (iFFT) for numerical inversion of equation (28).

$$\hat{w}(k_x, -vk_x) = \frac{F}{IE^*(-vk_x)k_x^4 - \tilde{\rho}v^2k_x^2 + Gk_x^2 - vck_x + k} \quad (28)$$

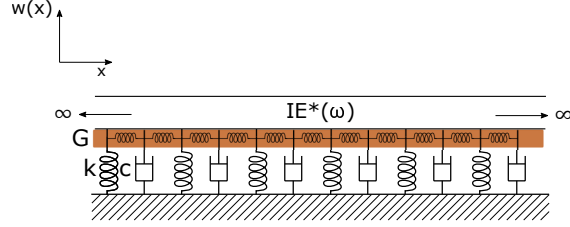


Figure 1: Sketch of a viscoelastic beam resting on a damped Pasternak-Winkler foundation. Here  $E^*(\omega)$  is the complex modulus of the beam,  $I$  is the beams second moment of area,  $k$  is the foundation spring constant,  $c$  is the viscous damping constant and  $G$  is the shear interaction parameter. The elastic Winkler-Pasternak model is obtained by setting  $c = 0$  and  $E^*(\omega) = E$ .

Equation (28) contains a general expression for the complex modulus of the beam where different viscoelastic models for the beam can be inserted. If we assume that  $q(x', t)$  varies slowly with time, the vertical acceleration term  $\tilde{\rho} \frac{\partial^2 w(x', t)}{\partial t^2}$  in of (9) can be neglected for simplicity [22].

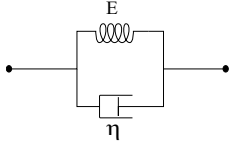
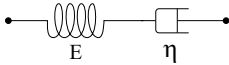
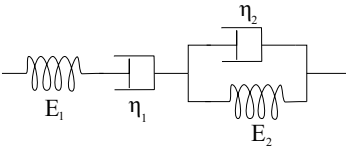
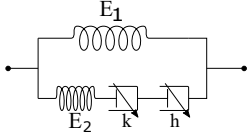
### 3. Choice of viscoelastic model for the beam

There exist two different ways to model the complex modulus: empirical models or mechanistic models where a mechanical analog of the viscous response of the material is made from spring and dashpot elements [13]. In this study we will consider mechanistically models where physically elements is used to describe the viscoelastic behaviour. Studies like [13] and [17] have investigated the mechanical properties of bitumen mixes and their complex modulus. They have proposed that models consistent of several springs, dashpots and parabolic dashpot elements is needed in order to reasonable describe the viscoelastic behaviour of bituminous mixes.

In table 1, three mechanistic models are listed; the Maxwell model, the Burgers model and the Huet-Sayegh model. The last two is often mentioned as models that satisfactorily describes the viscoelastic behaviour over a wide range of temperatures and frequencies, where the simple Maxwell model is the simplest mechanistic model with the qualitatively correct behaviour of the complex modulus curve (an sigmoidal real part and a bell curved imaginary part) [15]. As seen, the number of parameters needed to describe the complex modulus curves increase from 2 in the simple case to 9 for the Huet-Sayegh model. Later in this paper we investigate how the different models influence the model output, but in the following we will go with the simplest model that has the correct  $E^*(\omega)$  behaviour, namely the Maxwell model. The complex modulus for the Maxwell model can be written in terms of elastic modulus  $E$  and characteristic time  $\tau$ ,

$$E^*(\omega) = E \frac{i\omega\tau}{1 + i\omega\tau} \quad (29)$$

Table 1: Tabel over mechanistic models to describing the viscoelastic behaviour of bituminous mixes.

Model name	Schematic representation	Complex modulus	Numbers of parameters
Kelvin-Voigt model		$E^*(\omega) = E + \eta i\omega$	2
Maxwell model		$E^*(\omega) = E \frac{\tau i\omega}{1 + \tau i\omega}, \tau = \frac{\eta}{E}$	2
Burger's model		$E^* = \frac{1}{\frac{1}{E_1} (1 + \frac{1}{i\omega\tau_1}) + \frac{1}{E_2} \frac{1}{(1 + i\omega\tau_2)}}, \tau_i = \frac{\eta_i}{E_i}$	4
Huet-Sayegh model		$E^*(\omega) = E_1 + \frac{E_2}{1 + \delta(i\omega\tau)^{-k} + (i\omega\tau)^{-h}}$ $\ln(\tau) = a + bT + cT^2, \delta = \frac{E_2\tau}{\eta_1}$	9

#### 4. Numerical analysis of the model

By use of inverse FFT algorithm, equation (28) can be solved. From this we can make a numerically study of the pavement deflection.

To do the numerical study we use the parameter values listed in table 2. Parameter values for the stiffness (k) and shear parameter (G) for the foundation are adopted from [23]. The foundation stiffness value is also used in [21, 7] and is referred to as a medium stiff soil. Assuming the foundation is isotropic, the parameters k and G can be converted to a measure of elastic modulus E and shear modulus  $\tilde{G}$  of the soil layer respectively.

$$k = E \frac{A}{H}, \quad G = B \frac{EH}{6(1 + \nu)} = B\tilde{G} \frac{H}{3}, \quad (30)$$

where A is the area over which the force is applied (as k is spring constant per unit length  $A = 1$  m), H is the height of the soil layer, B is the width of the beam and foundation layer and  $\nu$  is the Poisson's ratio of the soil [24, 25]. Assuming  $H = 3$  m gives  $E_{soil} = 12$  MPa, which is relative low for soil. Thus we expect the foundation to behave rather soft. Assuming  $B=1$  m (as done in [24]), the shear modulus corresponding to G is found as  $\tilde{G} = 0.6$  MPa. this exact value for G is used in a lot of numerical studies about the Pasternak foundation and thus we choose to use this here [21, 18, 7, 23].

The foundations damping (c) is determined based on the damping ratio,  $\zeta$ . We assume a damping ratio  $\zeta = 0.3$ , as we aim to study a system with significant damping in the foundation.

Parameters for the viscoelastic model for the beam (equation (29)) is based on rheological experiments made in [14]. Here the Huet-Sayegh model is fitted to data and parameter values listed. Using this as a reference, we have fitted equation (29) and obtained parameters in table 2. Compared with studies of bituminous mix found in the literature, the chosen value of E is in the lower end wheres the characteristic time  $\tau$  is in the middle [15, 18, 16] Beside the parameters from the complex modulus, the beam is also described by its second moment of area per unit length, I. The beam is assumed a rectangle and I is given by  $I = \frac{1}{12} h^3$ . We assume that the beam is 10 cm thick.

To enable a comparison between elastic and viscoelastic beams, we chose an value for the elastic module,  $E_{elastic}$ ,



which gives a similar maximum deflection for the elastic repose as the viscoelastic case. Thus the two solution has the same effective stiffness and only the amount of damping is different (as seen on figure 2a).

Table 2: Parameter values used for numerical study.

Simulation parameters				
Description	symbol	value	unit	based on
Moving load	F	49000	N	
Vehicle velocity	v	16.67	m/s	
<b>Foundation</b>				
foundation stiffness per unit length	k	$40.8 \cdot 10^5$	N/m <sup>2</sup>	[23]
shear interaction parameter	G	$66.7 \cdot 10^4$	N	[23]
damping ratio	$\zeta$	0.3		
foundation damping per unit length	c	$8.5 \cdot 10^4$	$\frac{Ns}{m^2}$	
<b>Beam</b>				
Elastic modulus per unit length	$E_{visco}$	$1.7 \cdot 10^{10}$	$\frac{N}{m}$	[14]
Second moment of area per unit length	I	$8.3 \cdot 10^{-5}$	$m^3$	
Characteristic time	$\tau$	$5.4 \cdot 10^{-4}$	s	[14]
Elastic modulus per unit length	$E_{elastic}$	$4.2 \cdot 10^8$	$\frac{N}{m}$	
Temperature	T	25	$^{\circ}C$	[14]

Using the parameters in table 2, a plot of the pavement deflection underneath the load and the corresponding pavement deflection slope is obtained for the model with various degrees of viscoelasticity (fig. 2).

On figure 2a, the deflection basing is plotted with the center of the load at  $x = 0$ . The model is plotted for a full viscoelastic pavement, an elastic beam on viscoelastic foundation (using  $E^*(-vk_x) = E_{elastic}$ ), a viscoelastic beam on an elastic foundation ( using  $c=0$ ) and a purely elastic pavement.

The pavement deflection basin for the viscoelastic models is characterised by having the maximum deflection located behind the load. This is due to the viscoelastic effects of the pavement causing a time delay in the pavement repose as it is subject to a moving load. For the elastic model on the other hand, the maximum deflection occur directly underneath the load. It is seen that the different viscoelastic solutions gives different amount of time lag in the maximum deflection. This can be seen in the x-position of the maximum in figure 2a and in the intersection with the x-axis in figure 2b.

For the viscoelastic beam on a elastic foundation, an uplift behind the load is seen, where the deflection is positive. The phenomenon is also seen in [23] and [7].

On figure 2b, a plot of the pavement deflection slopes is seen. The deflection slope curves are characterised by having a minimum behind behind the load and a maximum in front of the load. For the elastic beam case these two peaks behave anti-symmetric around (0,0). For the viscoelastic solutions however, there are a change in both the x-location and amplitude resulting in a highly non-symmetrical signal. In section 9, a correlation between the the non-symmetric deflection slope signal and the origin of damping is explored.

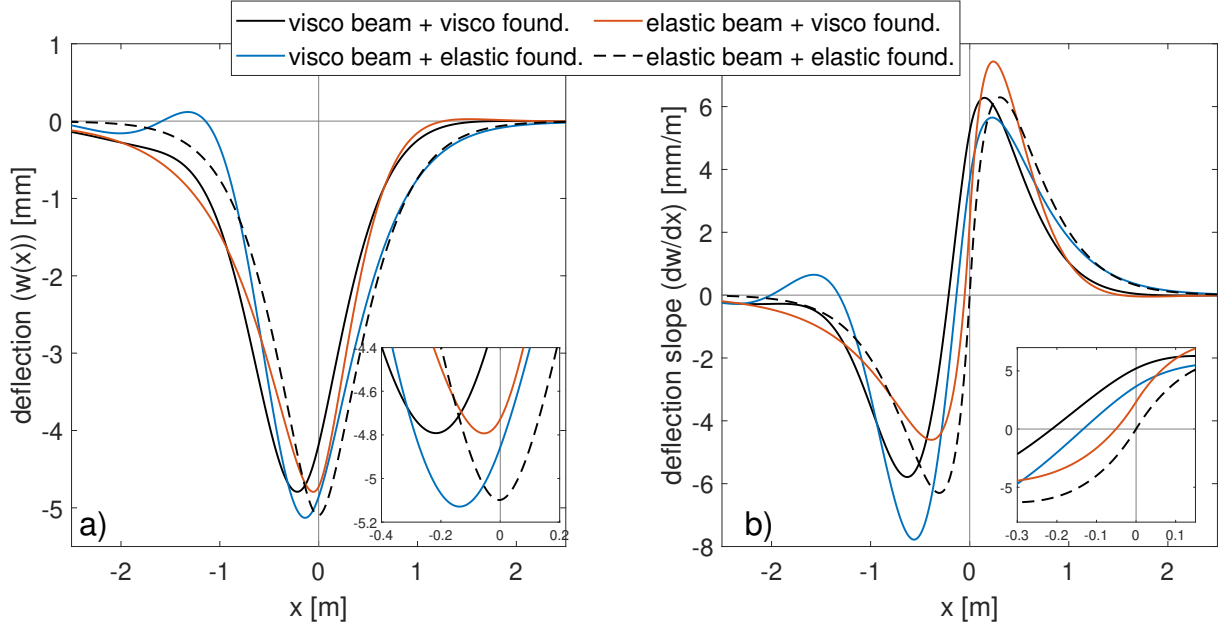


Figure 2: Pavement deflection underneath a moving load for the model with various degrees of viscoelasticity using the parameters in table 2. The model is plotted for a full viscoelastic pavement (damping in beam and foundation), an elastic beam on viscoelastic foundation ( $E^*(-vk_x) = E_{elastic}$ ), a viscoelastic beam on an elastic foundation ( $c=0$ ) and a purely elastic pavement ( $E^*(-vk_x) = E_{elastic}$  and  $c=0$ ).

## 5. Influence of the physical parameters on the pavement response

The influence of various physical parameters on the dynamical pavement response is studied. We want to look at the impact on both the pavement deflection basin and the deflection slope. This is done since the Traffic Speed Deflectometer technology provides direct measurements of the pavement deflection slope, and thus the influence of various physical parameters on this quantity is interesting.

The parameters influence will be evaluated with respect to their impact on the maximum deflection and the maximum and minimum deflection slope. We are looking at both the magnitude and x-location, as these gives separate information. In the deflection basin, the time delay in the pavement response due to viscous effects in the pavement is manifested by the maximum deflection occurring behind the load. The bigger a time delay experienced, the further away from the center of the load ( $x=0$ ) the maximum deflection occurs. Thus we would expect this quantity to say something about the amount of damping in the pavement. Similarly, the magnitude of the maximum deflection, reflect how stiff or soft the pavement behaves. The behaviour of the pavement deflection slope is more complicated to interpret.

On figure 3, a combined plot of the influence of the parameters  $k, G, \zeta, \tau$  and  $E$  is seen. The individual parameter values are changed while all others are held constant and the resulting pavement response plotted. This gives information about how the pavement response is influenced by a particular parameter. Note that all parameter values are decreased with a factor 0.01 and increased with 1000 times. This gives some unrealistic parameter values for some parameters, and will also result in some unnatural deflection basins. However these plots can be used to get a general idea about how each parameter influence the model output and to which parameter the model output is most sensitive.

On figure 3a-b, the behaviour of the amplitude and x-position of the maximum deflection is shown and some interesting features is found. First of all, we find that the foundation stiffness  $k$  has the biggest influence on the amplitude of the maximum deflection among all the parameters. This is particularly evident when  $k$  gets small and the foundation gets soft, and the result is a deep and narrow deflection basin.

Secondly, a peak in the x-position curves for both the foundation and beam damping is found. This quantity is often correlated with the amount of damping in the pavement and thus this indicates that there exist a value for both  $\tau$  and  $\zeta$  which gives an maximum amount of damping. This behaviour is not surprising for  $\tau$ , as it was also seen in figure ?? . It reflect that the loss modulus in equation (29) is bell shaped and thus has a maximum.

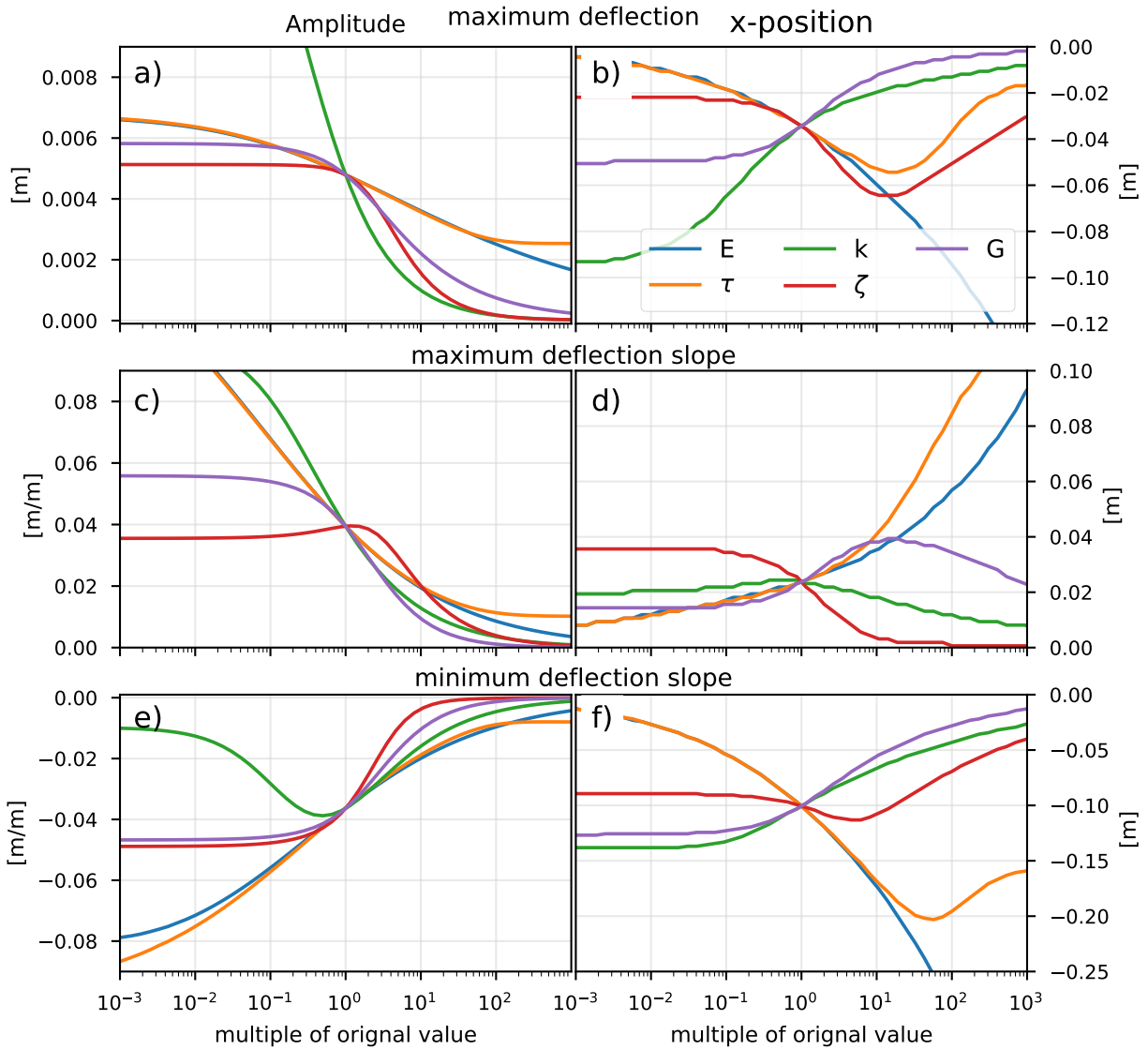


Figure 3: The influence of the physical parameters in the model on the pavement response. The parameters influence will be evaluated with respect to their impact on the maximum deflection, and the maximum and minimum deflection slope. We are looking at both the magnitude and x-location, as these gives separate information.

A similar behaviour is not seen for the E curve, as this acts as a scaling in eq. (29) and thus just amplifies the value of the loss modulus. More surprising is it to see this behaviour for the foundation damping  $\zeta$  as this is expected to influence the damping in the model in a linear way. The explanation is that the values at which the maximum damping behaviour is seen, is so large that the dash-pot becomes increasingly difficult to compress and thus begin to act stiff.

The third thing worth noticing about the deflection basin is that increasing foundation stiffness in form of  $k$  or  $G$  can counteract an increase in foundation damping. Thus the "actual damping" experienced by the pavement from the foundation is not just determined by the damping parameter  $\zeta$ , but a function of all foundation parameters.

On figure 3c-f the parameters influence on the deflection slope is plotted. A common trend is observed, that for increased parameter values the magnitude of both the minimum (3e) and maximum (3c) goes towards zero. On the other hand, the behaviour of the x-position of the two peaks is behaving different with respect to the different parameters. This makes us capable of distinguish between changes in the different parameter values based on the pavement deflection slope signals. E.g. it is possible to distinguish between increased (or decreased) stiffness in the top layer and the foundation. Where an increase in  $k$ , and in some extend  $G$ , makes the peaks moves closer to  $x=0$ , an increase in  $\eta$  and  $E$  moves the peaks away from  $x=0$ .

The influence of driving velocity  $v$  was also investigated and it was found that for a big range, it has the same influence on the pavement response at  $\tau$ . This is due to  $v$  being multiplied on  $\tau$  in the used viscoelastic model and thus these are correlated. However  $v$  is also correlated with the foundation damping  $\zeta$ , and thus deviates from the behaviour of the beam parameters when it is large.

### 5.1. Sensitivity analysis using Metropolis Monte-Carlo method

Above we have conducted a local sensitivity analysis on the different physical parameters included in the model. An analysis of this kind takes its starting point in the given parameter values and explores the parameter space in the neighbourhood of these. However, it is highly dependent on the chosen starting point and it gives only a local interpretation of the parameters influence on the model output. Furthermore it does not give any information about correlated parameters. In order to get a more comprehensive analysis, a global sensitivity analysis using the Metropolis Monte-Carlo (MMC) method has been made. Using this, we can obtain information about the sloppiness and degree of correlation within the parameters.

The MMC method investigate how changes in the parameter set  $\theta$  influence the model output. This is done in an iterative way, where the parameters are changed by  $\theta_{new} = \theta_{old} + \delta\theta_0$ , where  $\delta\theta_0$  is a uniformly distributed random number with mean 0. The variance of  $\delta\theta_0$  determines how big steps the algorithm takes in the parameter space. For each new parameter set  $\theta_{new}$ , the cost function  $C(\theta)$  is calculated and evaluated. In this study we use the following cost function

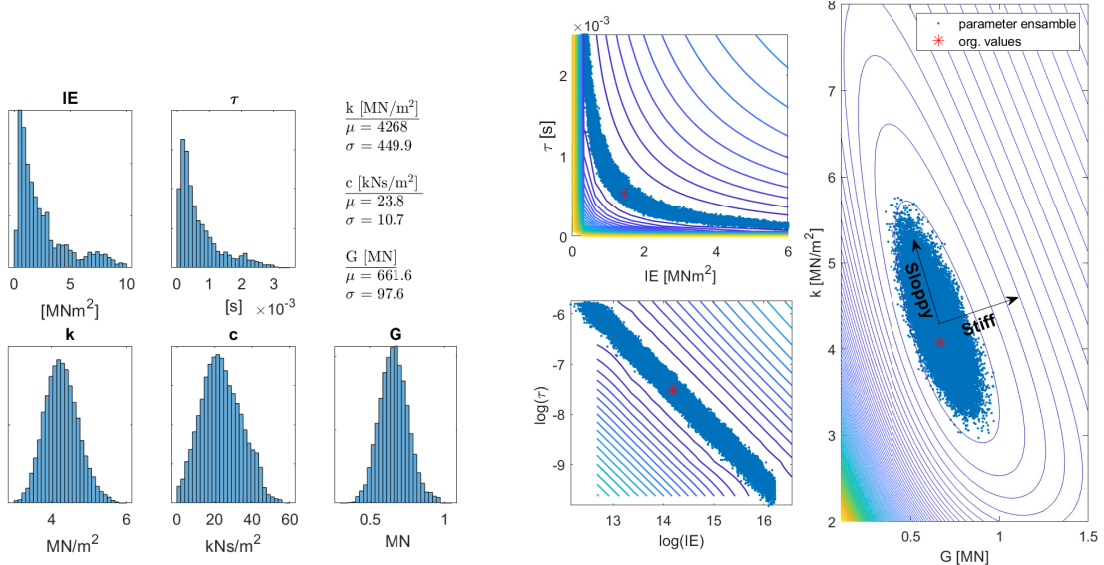
$$C(\theta_{new}) = \sum_{i=1}^m \left( (w(x_i, \theta_0) - w(x_i, \theta_{new}))^2 \right), \quad (31)$$

where  $m$  is the number of data points and  $\theta_0$  is original parameter set. If  $C(\theta_{new}) < C(\theta_{old})$  the parameter set is accepted and the iteration is repeated. If  $C(\theta_{new}) \geq C(\theta_{old})$  the set is only accepted if

$$R < \exp\left(-\frac{C(\theta_{new}) - C(\theta_{old})}{T_s}\right), \quad (32)$$

where  $R$  is a random number taken from a uniform distribution between  $[0;1]$  and  $T_s$  is the sampling temperature. We choose to use  $T_s = \frac{2C(\theta_0)}{N}$ , where  $N$  is the number of parameters in  $\theta$  as suggested in [26, 27].  $\delta\theta_0$  is chosen such that the acceptance ratio is around 0.5 [tjek!!](#). The analysis was made with  $\theta = \{IE, \tau, k, c, G\}$ , as  $I$  and  $E$  is directly correlated and thus can be considered one parameter. A synthetic set of  $m$  data points  $(w(x, \theta_0))$  is generated using the model with initial parameter values values listed in table 2 plus some white noise. This is done to avoid the algorithm to get stuck in a minimum corresponding to  $\theta_0$ .

The main findings from the analysis is that all foundation parameters ( $k$ ,  $c$  and  $G$ ) was found to be well defined, illustrated by a normal distribution of the parameter ensemble in figure 4a. On the other hand the beam parameters  $IE$  and  $\tau$  are found to be sloppy, indicated by a skewed distribution of their parameter ensemble (fig. 4a). Furthermore it was found that  $IE$  and  $\tau$  is correlated, which is seen by the contour plot on figure 4b. This means that an increase in  $IE$  can be compensated by an decrease in  $\tau$ .  $IE$  and  $\tau$  is found to



(a) histogram over parameter ensemble accepted in the Metropolis Monte-Carlo algorithm. (b) contour plot over the cost function for the parameter sets IE- $\tau$  and G-k. The original parameter values are indicated with a red star.

Figure 4

be log-log linear correlated, with the sloppy direction where  $\log(\tau)$  is increased and  $\log(\text{IE})$  decreased (and vice versa). This means that there exist a power law on the form

$$\tau = \text{IE}^{-\alpha} e^{\beta}, \quad (33)$$

which describes the relation between the two and that the model output is sensitive to changes in this function and not the individual parameters. If we replace  $\tau = \text{IE}^{-\alpha} e^{\beta}$  in the model, we would not have gained any new information, as we just have introduced two new nonlinear parameters  $\alpha$  and  $\beta$ . Consequently, this shows us that we can not estimate  $\tau$  and IE based on one set of pavement deflection measurement.

The parameters k and G was also found to correlate, with stiff and sloppy direction indicated on figure 4b. Here it is found that increasing G while simultaneously decreasing k has a little effect on the model output (Sloppy direction) whereas decreasing (or increasing) G and k simultaneously has a big effect on the model output. Thus a reduced stiffness in the foundation can be compensated for by an increased shear interaction and vice versa. But a decrease/increase in both parameters will affect the pavement response significantly. Furthermore this is found to be a well defined minimum (closed contour lines).

## 6. limitations to the beam model

To model the asphalt layer an Euler-Bernoulli beam is used. The Euler-Bernoulli beam theory is widely used within engineering as it is simple, and in many cases provides reasonable approximations to the desired solution [28]. However, as this is a simple model it has its limitations and one should be careful not to use the model to predict pavement response behaviour outside of the models validity domain.

A fundamental assumption in the beam model is that one dimension has to be much larger than the other, meaning that the length of the beam has to be much larger than the height,  $L \gg h$ . When investigating the beam thickness influence on the pavement response, this assumption should always be fulfilled in order to obtain trustworthy results. Likewise, there are restrictions for decreasing the beam thickness, as this will influence the flexural rigidity (IE) of the beam. As mentioned in section 5, the height of the beam h is associated with the second moment of area I by

$$I = \frac{1}{12} h^3. \quad (34)$$

Thus this influence the flexural rigidity by

$$IE = \frac{1}{12}h^3E. \quad (35)$$

Thus if  $h$  is decreased,  $IE$  is decreased. As  $IE$  is a measure of how much moment that is required to bend the beam with a given curvature, an to small value of this will result in some nonphysical behaviour of the deflection basin. This can be seen by evaluating the model for  $I$  going to zero. In this case, equation (9) will be reduced to a second order linear partial differential equation. The solution to this is an exponential function ??? and thus if we predict the pavement response from this model, we will obtain a deflection basin that is constructed by two exponential functions. This is clearly an nonphysical behaviour.

Provided that we are within the limits of the models validity domain, the influence of  $h$  can be investigated. The beam thickness is a desired physical property to investigate as the asphalt thickness often changes in real life situations. On figure 5, a plot of the pavement response simulated for different beam thicknesses are seen. The thickness is changed within 5-15 cm, as these are realistic thicknesses for an asphalt layer. The flexural rigidity is also listed for each height. We find that when  $h$  (and  $IE$ ) is increased, the maximum deflection is decreased and the deflection basin gets increasingly narrow. Furthermore the maximum deflection moves away from the center of the load as  $IE$  acts as a scaling of the beam damping. The decrease in maximum deflection is not linearly correlated with the decrease in  $h$ , as predicted based on equation (35).

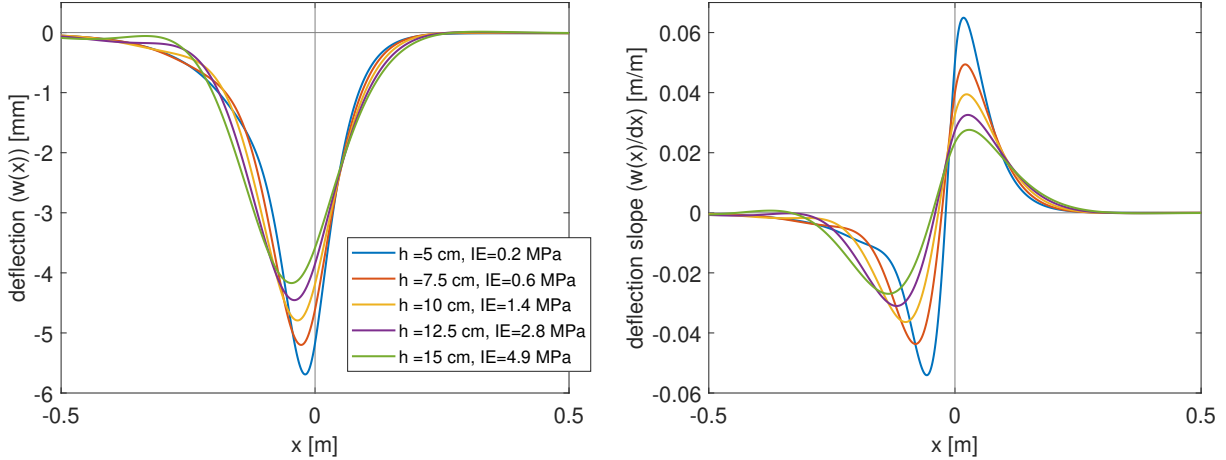


Figure 5: simulated pavement response at different height of the top layer.

## 7. The impact of beam complex modulus $E^*(\omega)$ on pavement response

The viscoelastic behaviour of the beam is determined by the chosen viscoelastic model. In this study we have chosen to use the Maxwell model, whose complex modulus in a moving reference frame is:

$$E^*(-vk_x) = E \frac{-ivk_x\tau}{1 - ivk_x\tau}$$

Due to the present of a moving load characterised by its driving velocity  $v$ , the viscoelastic behaviour of the beam is frequency dependent. This means that the pavement deformation is dependent on the specific loading time determined by the driving velocity. This is opposite to the elastic case, where the deformation is independent on the driving velocity. Having a frequency dependent pavement response, correspond to saying that only the behaviour of  $E^*(-vk_x)$  in a certain range of frequencies has an influence on the pavement response. This range of frequencies (or equivalent in a moving reference frame, the range of wave numbers), at which the pavement response is sensitive to the  $E^*(-vk_x)$  curve behaviour, will hereafter be referd to as the sensitivity interval. The sensitivity interval can be found either in the terms of frequency  $\omega$  or wave number  $k_x$ , as  $\omega = vk_x$ .

Changing the physical parameters related to the beam in the model, such as driving speed  $v$ , the stiffness

modulus  $E$  or the characteristic time  $\tau$ , will shift the the sensitivity interval and  $E^*(-vk_x)$  curve respectively. Resulting in a different amount of storage and loss modulus within the sensitivity interval, and thus different amount of damping expressed in the simulated pavement response.

The sensitivity of the pavement response with respect to  $E^*(-vk_x)$  can be found by looking at the partial derivative  $\frac{\partial \hat{w}(k_x, -vk_x)}{\partial E^*(-vk_x)}$  (eq. (36)). this is called the sensitivity function with respect to  $E^*(-vk_x)$ . The sensitivity interval is then the interval of wave numbers where  $\frac{\partial \hat{w}(k_x, -vk_x)}{\partial E^*(-vk_x)} \neq 0$ .

$$\frac{\partial \hat{w}(k_x, -vk_x)}{\partial E^*(-vk_x)} = - \frac{FIk_x^4}{(E^*(-vk_x)Ik_x^4 + Gk_x^2 - icvk_x + k)^2} \quad (36)$$

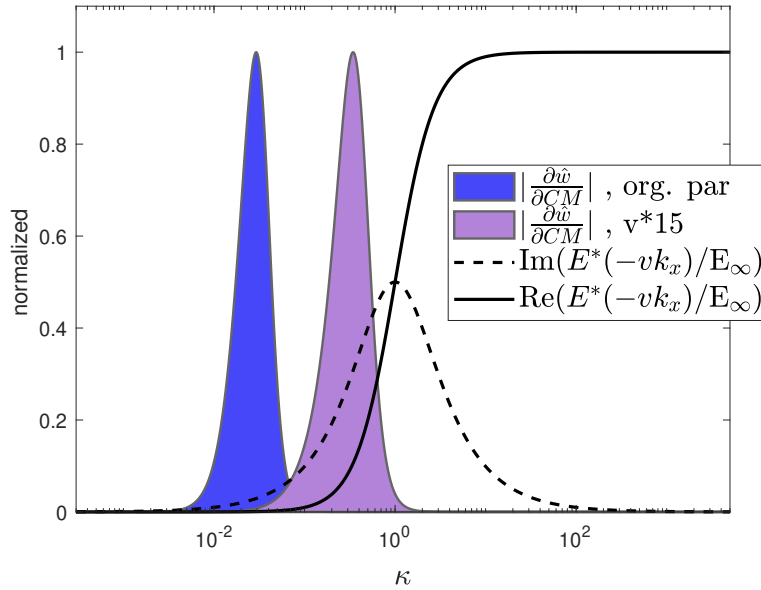


Figure 6:  $E^*(-vk_x)$  curve and the sensitivity function  $\frac{\partial \hat{w}(k_x, -vk_x)}{\partial E^*(-vk_x)}$  plotted on normalized axis. Normalized wave number  $\kappa = -v\tau k_x$

On figure 6, a plot of  $E^*(-vk_x)$  is shown using a normalized x and y axis. The use of normalized wave numbers ( $\kappa$ ) ensures that that the complex modulus curve is fixed and only the sensitivity function will shift up or down when parameter values are changed. This makes a comparison of different parameter sets possible.  $E^*(-vk_x)$  is characterised by the storage modulus (real part) and the loss modulus (imaginary part). The storage modulus accounts for the amount of elastic response in the beam and the loss modulus accounts for the amount of damping in the beam.

The sensitivity function using the default parameters (table 2) is also plotted as the absolute value of equation (36). This is used since (36) is a complex function. The sensitivity function indicates which parts of the complex modulus that has an influence on the pavement response. It is found to be located at low normalized wave numbers on the left side of the loss modulus peak. In this area, only a small amount of viscous damping is present and the elastic part behaves rather soft.

Increasing the driving velocity  $v$  shifts the sensitivity function to a higher normalized wave number, as seen on figure 6, purple area. This result in a pavement response with a higher degree of viscous damping and a slightly higher stiffness. If  $v$  is increased further the sensitivity interval will pass the loss modulus top and the behaviour will be like an elastic beam with  $E^*(\infty)$  as an elastic modulus, thus experience no damping from the beam.

### Impact of temperature

Changing the temperature of the viscoelastic beam correspond to changing the parameter values of  $\tau$  and  $E$ . Thus this is effectively just a shift of the complex modulus curve. In order to investigate the effect of

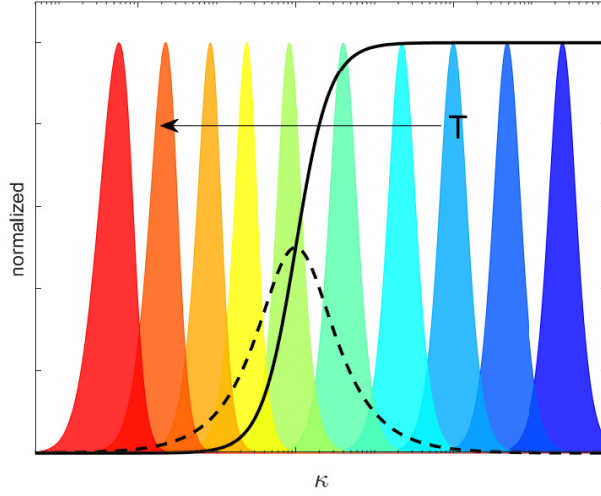


Figure 7: Plot of the sensitivity interval and the  $E^*(-vk_x)$  curve on normalized axis. Changing the temperature of the asphalt layer changes the parameter values for  $E$  and  $\tau$ , which correspond to shifting the  $E^*(-vk_x)$  curve. On normalized axis, this is like moving the sensitivity function downwards with respect to the  $E^*(-vk_x)$  curve.

temperature on the pavement response, we use the relation between asphalt temperature and viscoelastic model parameter values found from rheological measurements in [14].

On figure 7 we see the sensitivity intervals and  $E^*(-vk_x)$  in normalized axis for different temperatures, using the given parameter values in table 2 and the relation between  $E^*(-vk_x)$  parameters and temperature from [14]. Here we see that increasing the temperature of the beam result in the sensitivity interval being shifted from high to low normalized wave numbers. Thus when having a low temperature road result in a stiff road and having a warm road result in a softer road. The amount of  $\tau$  of damping expressed by the pavement depends on the specific location of the sensitivity interval.

## 8. Choice of $E^*(\omega)$

For the model presented in this paper (eq. (28)) it holds that

$$\lim_{k_x \rightarrow 0} \hat{w}(k_x, -vk_x) = \frac{F}{k} \quad (37)$$

$$\lim_{k_x \rightarrow \infty} \hat{W}(k_x, -vk_x) = 0 \quad (\approx \frac{F}{IE^*(-vk_x)k_x^4}) \quad (38)$$

In equation (37) it is seen that the behaviour of the pavement response at big wavelengths (small wave numbers) is dominated by the elastic springs in the foundation. On the other had, the behaviour of the pavement response at low wavelengths (large wave numbers) is dominated by the viscoelastic beam term (eq. (38)). This means that for pavement behaviour close to the load, the beam properties is important and for pavement behaviour far away from the load the elastic part of the foundation is the most dominant.

The pavement deflection model (eq. (28)) allows for any viscoelastic model to be inserted. In the previous analyses, the model used for describing the viscoelastic behaviour of the beam is the simple Maxwell model. However, this model is known to be to simple to proper characterise the behaviour of a bituminous mix over all temperatures and frequencies [13], as previous shown in figure ??.

The influence on the pavement response when choosing different rheological models is determined by the behaviour of  $E^*(-vk_x)$  in the relevant frequency range. On figure 8a, a plot of the complex modulus for the three mechanistic models; Maxwell, Burger's and Huet-Sayegh (see table 1) is shown. This is plotted with normalized axis for comparison. How a change in  $E^*(-vk_x)$  will influence the pavement response, depends on their individual behaviour within the sensitivity interval determined by the sensitivity function.



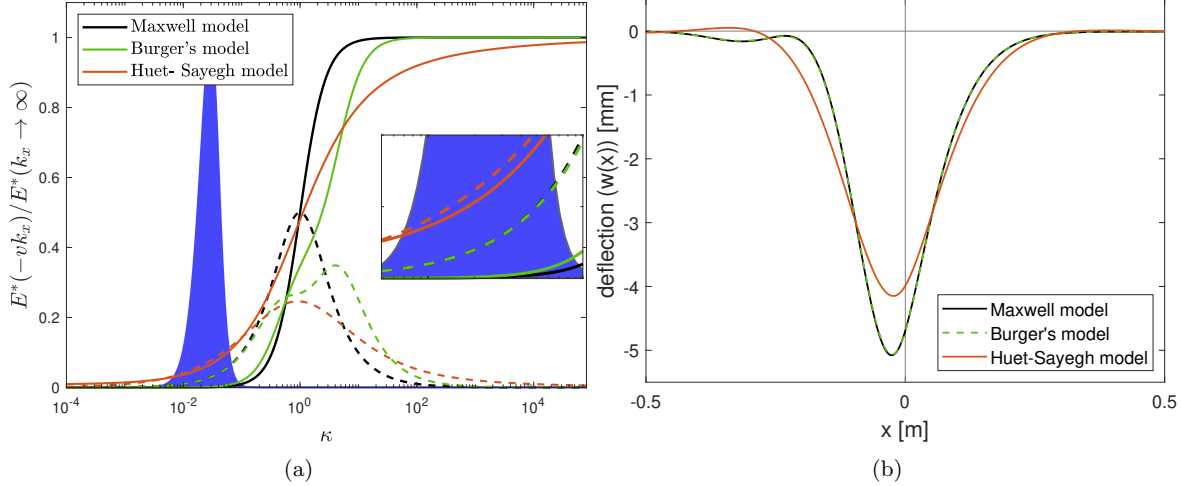


Figure 8: a) complex modulus for the three mechanistic models; Maxwell, Burger's and Huet-Sayegh. For details see table 1. The sensitivity function is marked with blue, indicating the range of wave numbers that influence the pavement response. It is found that the Maxwell and burger's model behaves the same within the sensitivity interval, whereas the Huet-Sayegh model behaves differently. b) simulated pavement response using the three complex modulus models. The simulations is made using parameters from table 2 and 3.

The complex modulus curve for the different models has the same trends, with a peak in the loss modulus and a elastic regime at low and high frequencies. If we look at the complex modulus for the models at high frequencies, we find that they all goes towards some plateau value, determined by the spring constants (eq. (39) ). However, if we look at their behaviour at low frequencies (eq. 40) the Maxwell and Burger model goes to zero whereas the Huet-Sayegh model goes to a nonzero plateau value.

$$\lim_{k_x \rightarrow \infty} E_{Maxwell}^* = E, \quad \lim_{k_x \rightarrow \infty} E_{Burger}^* = E_1, \quad \lim_{k_x \rightarrow \infty} E_{Huet-Sayegh}^* = E_2 + E_1 \quad (39)$$

$$\lim_{k_x \rightarrow 0} E_{Maxwell}^* = 0, \quad \lim_{k_x \rightarrow 0} E_{Burger}^* = 0, \quad \lim_{k_x \rightarrow 0} E_{Huet-Sayegh}^* = E_1 \quad (40)$$

The sensitivity function on figure 8a is located left of the loss modulus peak, where there is a big difference between the behaviour of the Maxwell and Burger model and the Huet-Sayegh model. This is reflected in the simulated pavement response in figure 8b. In figure ??, we found that the Maxwell model has a nonphysical behaviour at low frequencies due to the storage modulus going to zero faster than the loss modulus. Thus this model will no be advantageous to use for lower driving velocities or higher temperatures with the given parameter set, as this shifts the sensitivity function to lower frequencies.

The Burger model is found to behave similar to the Maxwell model within the sensitivity interval. From figure 8a we conclude that of the three tested models, the Huet-Sayegh model is preferable when the used parameter values result in a sensitivity function located at low frequencies. It is also found that if sensitivity interval for the pavement response is located at high frequencies where all models has a constant elastic modulus and no damping, there will be no different in the contribution to the pavement response within the models. Above it was showed how such a shift can be made by changing the driving velocity or temperature. Furthermore it should be noted that both beam and foundation parameters influence the sensitivity function and thus can influence a potential shift.

## 9. Manifestation of viscoelastic effects through the pavement deflection slope

In figure 2 the viscoelastic effects of either the beam or foundation was found to manifests itself in the pavement deflection slope through a change in both the x-location and amplitude resulting in a highly non-symmetrical signal. However, a different behaviour was found depending on where the damping originated. It

Table 3: Parameters used for simulation in figure 10, 8a and 8b. The parameter values is chosen such that the complex modulus curves, explained in table 1, is comparable.

Simulation parameters for $E^*(\omega)$ models											
Kelvin-Voigt model			Maxwell model			Burger's model			Huet-Sayegh model		
E	$1.7 \cdot 10^{10}$	$\frac{\text{N}}{\text{m}}$	E	$1.7 \cdot 10^{10}$	$\frac{\text{N}}{\text{m}}$	$E_1$	$1.7 \cdot 10^{10}$	$\frac{\text{N}}{\text{m}}$	$E_1$	$150 \cdot 10^6$	$\frac{\text{N}}{\text{m}}$
$\eta$	$9.3 \cdot 10^6$	$\frac{\text{Ns}}{\text{m}}$	$\tau$	$5.4 \cdot 10^{-4}$	s	$\tau_1$	$5.4 \cdot 10^{-4}$	s	$\tau$	$1.3 \cdot 10^{-5}$	s
						$E_2$	$1.7 \cdot 10^{10}$	$\frac{\text{N}}{\text{m}}$	$E_2$	$1.8 \cdot 10^{10}$	$\frac{\text{N}}{\text{m}}$
						$\tau_2$	$2.7 \cdot 10^{-4}$	s	k	0.7	-
									h	0.2	-
									$\delta$	0.08	-

appears that damping originating from the top layer and damping originating from underlying layers affect the deflection slope curve in different ways. As a result, the origin of damping is reflected in the relative difference between the amplitudes of the maximum and minimum deflection slope.

The asymmetry in the deflection slope curve can be quantified by looking at the ratio between the minimum and maximum peak amplitude. This will be denoted  $\Omega$  in the following,

$$\Omega = \left| \frac{\max\left(\frac{dw(x)}{dx}\right)}{\min\left(\frac{dw(x)}{dx}\right)} \right|. \quad (41)$$

For the simulated pavement responses in figure 2,  $\Omega = 1$  for the elastic pavement,  $\Omega = 0.72$  for the viscoelastic beam on an elastic foundation and  $\Omega = 1.61$  for the elastic beam on viscoelastic foundation. This indicates that the origin of damping is reflected in the ratio  $\Omega$ .

We hypothesise, that the viscoelastic effects in the pavement affect the pavement deflection slope differently depending on their origin, and by evaluating  $\Omega$  the origin of the most dominating form of damping can be found. For  $\Omega > 1$ , the most dominating viscoelastic effects is affiliated with the foundation. Conversely, for  $\Omega < 1$  the most dominating viscoelastic effects is affiliated with the top layer. The special case of  $\Omega = 1$  occurs for either a perfectly elastic pavement, or when the viscoelastic contributions from the different layers are equal. This hypothesis is investigated using the model derived in equation (28).

The pavement deflection slope of the deflection basin can be written in the form of an the inverse Fourier transform,

$$\frac{d(-w(x))}{dx} = \frac{1}{2\pi} \int_{-\infty}^{\infty} \hat{S}(k_x, -vk_x) e^{ixk_x} dk_x. \quad (42)$$

Note that as  $w(x)$  is a measure of how much the beam deflect compared to a straight beam,  $w(x)$  is a positive value when the beam is deflected. In order to get a depiction of the deflection basin (as on figure 2) we have to plot  $-w(x)$  and as a result the associated deflection slope is  $\frac{d(-w(x))}{dx}$ .

Equation (42) can be rewritten as

$$\frac{d(-w(x))}{dx} = \frac{1}{2\pi} \int_{-\infty}^{\infty} S' \cos(xk_x) - S'' \sin(xk_x) dk_x + i \frac{1}{2\pi} \int_{-\infty}^{\infty} S' \sin(xk_x) + S'' \cos(xk_x) dk_x \quad (43)$$

$$= \frac{1}{2\pi} \int_{-\infty}^{\infty} S' \cos(xk_x) - S'' \sin(xk_x) dk_x \quad (44)$$

Where  $S'$  and  $S''$  is the real and imaginary part of  $\hat{S}$ . The last equal sign is due to the fact that the imaginary part of a Fourier transform of a real function,  $\mathcal{F}\{f(x)\} = \hat{f}(k_x)$ , must become zero when inverse transformed, as the resulting function  $\mathcal{F}^{-1}\{\hat{f}(k_x)\} = f(x)$  is real. The step is proven more detailed in supplementary.

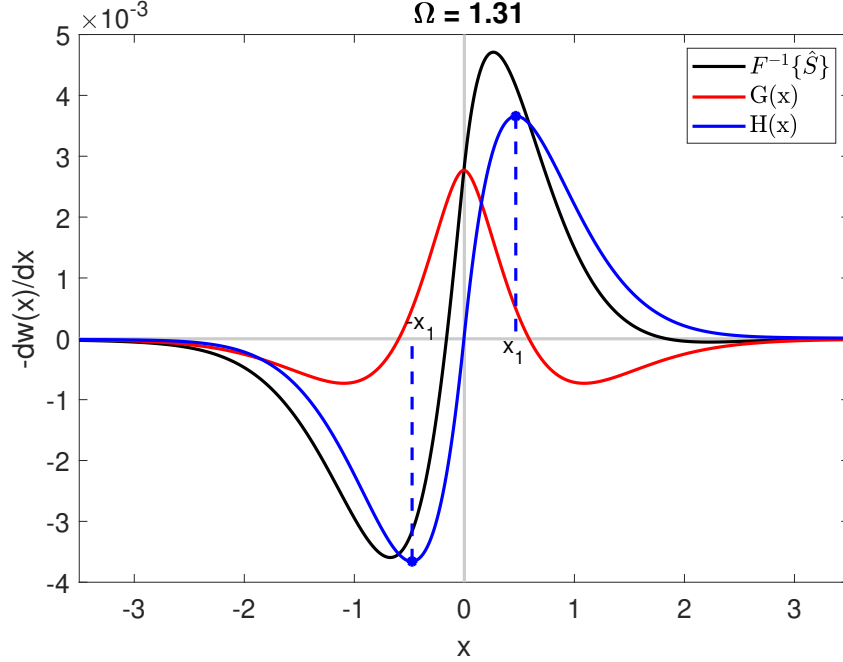


Figure 9: Pavement deflection slope found by inverse Fourier transform  $F^{-1}\{\hat{S}\}$  together with the anti-symmetric contribution  $H(x)$  and the asymmetric contribution  $G(x)$ .

Define the functions  $G(x)$  and  $H(x)$  as

$$G(x) = \frac{1}{2\pi} \int_{-\infty}^{\infty} S' \cos(xk_x) dk_x = F^{-1}\{S'\} \quad (45)$$

$$H(x) = \frac{1}{2\pi} \int_{-\infty}^{\infty} -S'' \sin(xk_x) dk_x = F^{-1}\{iS''\} \quad (46)$$

$G(x)$  corresponds to taking the inverse Fourier transform of  $S'$  and  $H(x)$  corresponds to taking the inverse Fourier transform of  $iS''$ . On figure 9, a plot of  $G(x)$ ,  $H(x)$  and the inverse Fourier transform of  $\hat{S}$  is seen.  $H(x)$  represent the elastic contribution to the total deflection slope curve and is an even function, thus anti-symmetric around the y-axis. The maximum of  $H(x)$  is indicated to be at  $x = x_1$ . As  $H(x)$  is anti-symmetric, the minimum is located at  $x = -x_1$ .  $G(x)$ , on the other hand, is an odd function, and contribute to the asymmetric behaviour in the total deflection slope.

In the case of a perfectly elastic solution,  $\frac{d(-w(x))}{dx} = H(x)$ . For small perturbations to the elastic solutions ( $|G(x)| \ll 1$ ), the maximum and minimum of  $\frac{d(-w(x))}{dx}$  is assumed to be located in the same place as maximum and minimum of  $H(x)$ . This assumption breaks down in the case of substantial amount of damping where the viscoelastic effects will shift the  $\frac{d(-w(x))}{dx}$  signal to the left, thus affecting the x-position of the maximum and minimum. As we are interested in understanding the fundamental characteristics of the problem, we will conduct the analysis in the simple framework of a small perturbation and study the behaviour of  $H(x)$  and  $G(x)$  in  $x = x_1$ .

$G(x)$  introduces the asymmetric behaviour in the pavement deflection slope, and thus in order to understand the asymmetry seen in the deflection slope we have to investigate this.

$G(x)$  is described by the function  $S'$ , which is the real part of  $\hat{S}(k_x, -vk_x)$ . Using the pavement response model derived in equation (28),  $S'$  can be found as

$$S' = \frac{-Fk_x(IE''k_x^4 - cvk_x)}{(IE'k_x^4 + Gk_x^2 + k)^2 + (IE''k_x^4 - cvk_x)^2} \quad (47)$$

Equation (47) reveals that when damping in the pavement structure is changed, the term  $f(k_x) = (IE''k_x^4 - cvk_x)$  changes. In  $f(k_x)$ , the main difference between the two types of damping is the power in which  $k_x$  is

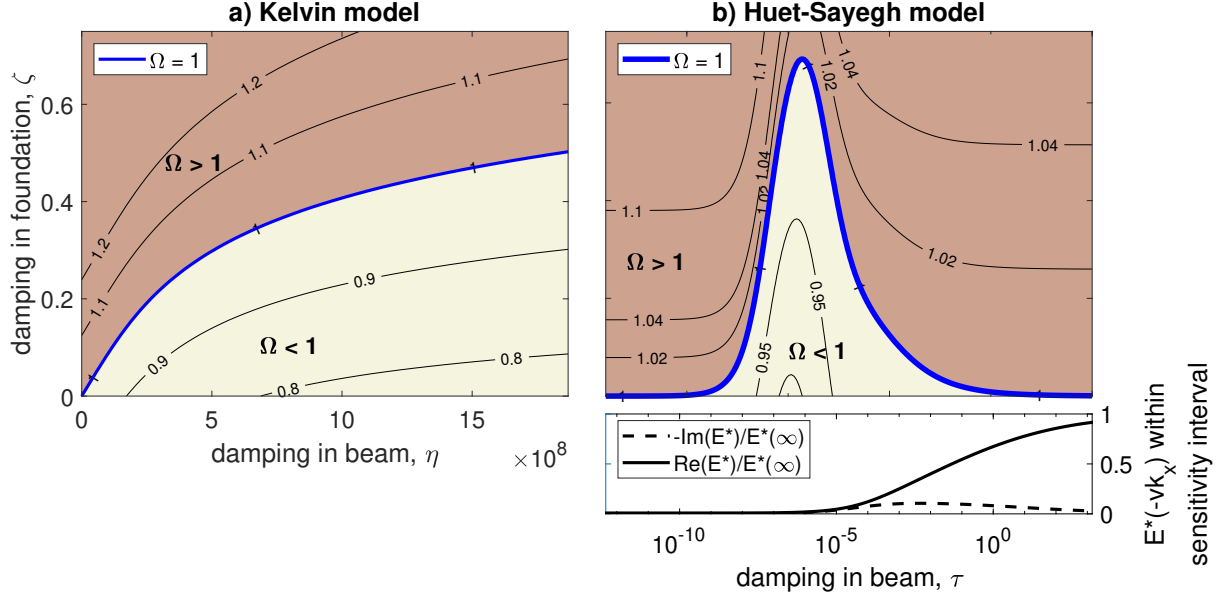


Figure 10: Contour plot of  $\Omega$  as a function of damping in the foundation on the y-axis and beam on the x-axis. Damping in the foundation is controlled by  $\zeta$ , whereas damping in the beam is controlled by three different  $E^*(-vk_x)$  models. The storage and loss modulus ( $Re(E^*)$  and  $Im(E^*)$  respectively) that characterise the beam response for each  $\tau$  value is plotted underneath the x-axis for figure b. The plot shows a clear trend that when damping in the foundation is increased  $\Omega$  is increased and when damping in the beam is increased,  $\Omega$  is decreased. The line  $\Omega = 1$  illustrate the tipping point between the two damping forms. Parameters used for the simulations is listed in table 2 and 3.

raised. For pure foundation damping  $f(k_x)$  is raised to the power of one, whereas for pure beam damping it is raised to a power higher than one, depending on the expression for  $E''$ . In the case where damping is present in both the beam and foundation, the situation becomes more complicated and the resulting power determines the final behaviour of the pavement response.

On figure 10a the value of  $\Omega$  is shown in the form of a contour plot, for the simple case with beam damping modelled by the Kelvin-Voigt model (see table 1 for description). The Kelvin-Voigt model do not describe the asphalt behaviour correctly, but is used due to its simplicity and linear relationship between stiffness ( $E$ ) and damping ( $\eta$ ).

$$E^*(-vk_x) = E - ivk_x\eta \quad (48)$$

This makes it perfect for preliminary analysis, as the beam damping is controlled by one single parameter which can be adjusted. On figure 10a we find that increasing beam damping always result in a decrease in  $\Omega$  and vice versa for foundation damping, which always result in increase  $\Omega$ .

The same analysis is now preformed using a more realistic complex modulus model to describe the viscoelastic behaviour of the beam, namely the Huet-Sayegh model. The complex modulus for the Huet-Sayegh model is given by:

$$E^*(-vk_x) = E_0 + \frac{E_\infty - E_0}{1 + \delta(-ivk_x\tau)^{-k} + (-ivk_x\tau)^{-h}} \quad (49)$$

In the Huet-Sayegh model, and similar models, there are a nonlinear relationship between stiffness and damping parameters. This means that when equation (49) is divided into storage ( $E'$ ) and loss ( $E''$ ) modulus, these will contain both stiffness and damping related parameters. In addition, they are both functions of  $k_x$ . This is fundamentally different from the Kelvin-Model, where  $E'$  was constant, and it means that adjusting the beam damping is not trivial.

We chose to change the beam damping by changing the value of  $\tau$ . Increasing  $\tau$  shifts the complex modulus curve to lower wave numbers and as a result, the sensitivity interval will cover different parts of the  $E^*(-vk_x)$

curve. On a normalized x-axis, this correspond to shifting the sensitivity interval and thereby covering different parts of the complex modulus, resulting in different amount of beam damping. Note that due to the shape of  $E^*$  there exist a value of  $\tau$  at which the beam express a maximum amount of damping. As a result, damping can be increasing by either increasing  $\tau$  from the elastic plateau at low frequency (increasing "from the left") or decreasing  $\tau$  from the elastic plateau at high frequency (increasing "from the right"). Since  $E^*$  is not symmetric the two approaches will not give the same result.

Using this notion of beam damping, we obtain the contour plot of  $\Omega$  seen in figure 10b. On the y-axis we have the amount of foundation damping and on the x-axis is the value of  $\tau$ . Below the x-axis, the values of  $E^*(-vk_x)$  within the sensitivity interval at a given  $\tau$  value is plotted. Overall figure 10b shows that at any given value for  $\tau$ , if we increase the foundation damping  $c$ ,  $\Omega$  will increase. The stiffness of the beam (given by  $E'$  within the sensitivity interval) affects how much foundation damping increases  $\Omega$ . This is seen when comparing the elastic regimes (left vs right side of figure 10b). Furthermore we find that if we begin at any foundation damping  $c$  and increase the beam damping, either from the left or the right,  $\Omega$  is decreased.

Thus we can conclude that different kinds of damping affects  $G(x)$  differently, and thus in the end affect the pavement deflection slope differently. The crucial factor that distinguish beam and foundation damping is the power to which  $k_x$  is raised in  $f(k_x)$ . This determines whether  $G(x_1)$  is positive or negative, and thus if  $\Omega$  is above or below 1. In general, we found that increasing foundation damping result in an increasing  $\Omega$ , whereas increasing beam damping result in a decrease in  $\Omega$ . Thus validating the hypothesis. The result is found to hold for "realistic" beam complex modulus models, while it do not hold for all  $\tau$  in the simple Maxwell model. In this case, we find that the behaviour of  $E^*$  within the sensitivity interval for some  $\tau$  becomes to steep, and as a result the behaviour in  $f(k_x)$  mimics that seen for foundation damping. However, the Maxwell model is known to be to simple to describe the complex behaviour of asphalt mixed accurately [13]. Consequently, the results found here is believed to hold for real pavement structures.

From the analysis, we can conclude that by evaluating the ratio of amplitudes between the maximum and minimum deflection slope, the location of the dominating damping can be found. On figure 10, the line of  $\Omega = 1$  is marked with blue. In the left corner this is due to the purely elastic nature of the pavement, but in the rest of the plot damping is in-fact present in the pavement. Thus we can see that  $\Omega = 1$  can happen when the right ratio of foundation and beam damping is present. This illustrated the turning point where the dominating damping goes from one layer to the other.

Being able to evaluate if the main damping is occurring from the foundation or beam directly from the pavement deflection slope is use full when combined with Traffic Speed Deflection measurements, as this measures the deflection slope directly.

## 10. Summary

In this study, we have presented and analysed a pavement response model consistent of a viscoelastic beam on top of a damped Pasternak foundation. The pavement response is found in a moving reference frame such that it is comparable with the measuring set-up in a Traffic Speed Deflectometer. The full viscoelastic beam model was compared with models containing damping in only the beam or foundation and a purely elastic model. The viscoelastic properties in the beam is seen to manifest itself with an increased time delay in the response compared to both the elastic beam model and purely elastic model. Thus, the deflection basin for the viscoelastic solution is highly asymmetric around the maximum load. The viscous effects was also studied in terms of the deflection slope curve, as this is the direct output of the TSD method. The deflection slope curve is characterised by having a minimum behind the load and a maximum in front of the load. In a purely elastic case, these are perfectly anti-symmetric. Adding damping into the pavement result in a non-symmetric behaviour of the peaks by changing both the amplitude and location of the maximum and minimum. The ratio between the magnitudes of the maximum and minimum deflection slope,  $\Omega$ , is studied in detail in figure 10. Here it was fund that damping in the beam result in  $\Omega < 1$  whereas damping in the foundation result in  $\Omega > 1$ . When both damping type are present the vale of  $\Omega$  reveals what is the most dominating source of damping. Relating this result with Traffic Speed Deflectometer measurements will be a powerful tool to evaluate the origin of the pavement damping, as it can be extracted directly from the measurements.

The proposed model was analysed with two different sensitivity methods; a local and a global method. Here the impact of the various physical parameters on the model output was investigated. This was done using a set of parameter values based on findings in the literature. The main findings was that

- (i) The foundation stiffness  $k$  has the biggest impact on the pavement deflection basin of all the parameters. This is particularly evident for increased stiffness where the resulting deflection basin is deep and narrow.
- (ii) Increasing the foundation stiffness or the shear interaction parameter can counteract an increase in foundation damping. Thus the "actual" foundation damping experienced by the pavement is not determined by the damping parameter  $\zeta$  alone, but through a function of all foundation parameters.
- (iii) Through analysis of the pavement deflection slope signals, it was possible to distinguish between a change in stiffness of the top layer and in the foundation.
- (v) The flexural rigidity  $IE$  and the characteristic time  $\tau$  of the viscoelastic beam, was found to be sloppy. This means that a change in the sloppy direction for the individual parameter will not affect the model output significantly. Furthermore,  $IE$  and  $\tau$  was found to correlate in such a way that increasing  $IE$  can be counterbalanced by an decrease in  $\tau$ . Thus there exist a function of these to which the model output is sensitive.
- (vi) All foundation parameters ( $k$ ,  $c$  and  $G$ ) was found to be well defined. Furthermore  $k$  and  $G$  was found to correlate, with the sloppy direction such that a decrease in  $k$  is counterbalanced by an simultaneously increase in  $G$ . The stiff direction indicates that a simultaneously decrease or increase in  $k$  and  $G$  affects the pavement response significantly. This harmonize with our physically intuition of the system, as both  $G$  and  $k$  characterize stiffness in the foundation.

The results found from the theoretical sensitivity analysis of the pavement deflection slope signal can be applied in combination with Traffic Speed Deflectometer measurements to obtain easy accessible information about the pavement without complicated modelling work. Especially using the fact that we can distinguish between increased foundation stiffness and top layer stiffness is useful. This is done in [data paper kilde](#).

The influence of driving velocity and temperature on the pavement response using the proposed model was also studied. In the numerical study presented here, increasing the driving velocity resulted in a more viscous behaviour of the beam. Opposite, increasing temperature resulted in a less viscous behaviour. The relationship between the viscoelastic properties of a beam and velocity and temperature dependence, was also studied in [18], using a more complicated viscoelastic beam model where the Burger's model is used for the viscoelastic response and the vehicles is modelled as a spring-mass system. Here it was found that increased  $v$  leads to a decrease of viscous effects of the top layer and an increase in temperature result in a more viscous beam. Thus opposite conclusions as found in this study.

Whether an increase in driving velocity or temperature will lead to more or less viscous behaviour of the beam, depends on where the sensitivity function of the complex modulus is located relative to the loss modulus peak in  $E^*(-vk_x)$ . The location of the sensitivity function, and thus the relevant wave numbers within the sensitivity interval, is dependent on both the beam parameters (temperature dependent), foundation parameters and the driving velocity of the wheel. Thus these parameters has an influence on whether increased driving velocity is seen to increase or decrease the pavement damping, and should be kept in mind when comparing studies.

In the literature, it is often noted that decreasing the driving speed result in a more viscous behaviour, indicating that under these measurement or simulation conditions the frequency range is located on the right side of the peak [11, 18]. This indicates that the chosen parameter values for the viscoelastic beam used in this study is not representative. the parameter values where based on rheological experiments from the literature and are similar other reported values in the litterature obtained through rheological measurements [11, 14, 15, 16, 18]. This could indicate that values obtained through rheological measurements is not well suited for numerical simulations with simple beam models. And that relevant parameter values for such simplified models should be obtained in another way.

The parameter values used for the foundation stiffness  $k$  and shear interaction parameter  $G$  was chosen based on often used values in the literature. In figure 2 the width of the deflection basin was found to be smaller than seen in measured deflection basins, indicating that the used parameter values are to soft. In [data paper](#) the model was fitted to a set of TSD data and estimated parameter values obtained. The estimated foundation spring constant  $k$  was found to be in the same order of magnitude as the theoretical value used in this study, indicating that this is a reasonable choise. The estimated shear interaction parameter however was found to be three orders or magnitude larger than the one listed in table 2. Indicating that a much higher  $G$  value should be used when making numerically studies with a Pasternak foundation model.

Lastly, the impact of diffident viscoelastic response models for the top layer was studied. The impact on the pavement response when choosing different  $E^*$  models depends on the location of the sensitivity function ,

as seen on figure 8a. In the literature it has been found that when increasing the temperature or lowering the driving velocity, the choice of  $E^*(-vk_x)$  is of importance [11]. As mentioned before the influence of changing velocity or temperature depends on the specific location of the sensitivity function, and thus is specific to the individual study conditions. In general it holds that if the sensitivity interval is located at high or low frequency, thus in the elastic regime of the complex modulus there are no difference in choosing various  $E^*$  models, whereas if it is located around the peak this can have a significant influence. A similar conclusion is found in [15], where the Burger and Huet-Sayegh model is compared.

## References

- [1] Niki D. Beskou and Dimitrios D. Theodorakopoulos. Dynamic effects of moving loads on road pavements: A review. *Soil Dynamics and Earthquake Engineering*, 31(4):547–567, 2011.
- [2] Y. H. Wang, L. G. Tham, and Y. K. Cheung. Beams and plates on elastic foundations: A review. *Progress in Structural Engineering and Materials*, 7(4):174–182, 2005.
- [3] Arnold Verruijt. An Introduction to Soil Dynamics. In *Springer, Dordrecht*. Springer, 2010.
- [4] Seong-Min Kim and Jose M. Roesset. Dynamic response of a beam on a frequency-independent damped elastic foundation to moving load. *Canadian Journal of Civil Engineering*, 30(2):460–468, 2003.
- [5] Lu Sun. A closed-form solution of beam on viscoelastic subgrade subjected to moving loads. *Computers and Structures*, 80:1–8, 2002.
- [6] Pengmin Lv, Runli Tian, and Xiaoyun Liu. Dynamic Response Solution in Transient State of Viscoelastic Road under Moving Load and Its Application. *Journal of Engineering Mechanics*, 136(2), 2010.
- [7] Rajib Ul Alam Uzzal, Rama B. Bhat, and Waiz Ahmed. Dynamic response of a beam subjected to moving load and moving mass supported by Pasternak foundation. *Shock and Vibration*, 19(2):201–216, 2012.
- [8] Paul Michaels. In situ determination of soil stiffness and damping, 1998.
- [9] Diego Froio, Egidio Rizzi, Fernando M.F. Simões, and António Pinto Da Costa. Universal analytical solution of the steady-state response of an infinite beam on a Pasternak elastic foundation under moving load. *International Journal of Solids and Structures*, 132-133:245–263, 2018.
- [10] Mehdi Akbarian and Franz-Josef Ulm. Model based pavement-vehicle interaction simulation for life cycle assessment of pavements. *CSHub at Massachusetts Institute of Technology (MIT)ets Institute of Technology (MIT) - Report*, (April), 2012.
- [11] Lukasz Mejlun, Józef Judycki, and Bohdan Dolzycki. Comparison of Elastic and Viscoelastic Analysis of Asphalt Pavement at High Temperature, 2017.
- [12] Simon Pouget, Cédric Sauzéat, Hervé Di Benedetto, and François Olard. Calculation of viscous energy dissipation in asphalt pavements. *The Baltic Journal of Road and Bridge Engineering*, 9(2):123–130, 2014.
- [13] Qinwu Xu and Mansour Solaimanian. Modelling linear viscoelastic properties of asphalt concrete by the Huet-Sayegh model. *International Journal of Pavement Engineering*, 10(6):401–422, 2009.
- [14] Adriaan C. Pronk. The huet-sayegh model: A simple and excellent rheological model for master curves of asphaltic mixes. *Geotechnical Special Publication*, (146):73–82, 2006.
- [15] Roger N. Nilsson, Ulf Isacsson, and Piet C. Hopman. Influence of Different Rheological Models on Predicted Pavement Responses in Flexible Pavements. *Road Materials and Pavement Design*, 3(2):117–149, 2002.
- [16] Mouhamed Lamine Chérif Aidara, Makhaly Ba, and Alan Carter. Choice of an Advanced Rheological Model for Modeling the Viscoelastic Behavior of Hot Mixtures Asphalt (HMA) from S&eacute;n&eacute;gal (West Africa). *Open Journal of Civil Engineering*, 05(03):289–298, 2015.
- [17] Nguyen Hoang Pham, Cédric Sauzéat, Hervé Di Benedetto, Juan A. González-León, Gilles Barreto, Aurélia Nicolai, and Marc Jakubowski. Analysis and modeling of 3D complex modulus tests on hot and warm bituminous mixtures. *Mechanics of Time-Dependent Materials*, 19(2):167–186, 2015.
- [18] G. Snehasagar, C. G. Krishnanunni, and B. N. Rao. Dynamics of vehicle–pavement system based on a viscoelastic Euler–Bernoulli beam model. *International Journal of Pavement Engineering*, 8436, 2019.
- [19] Natasja R Nielsen, Karim Chatti, Christoffer P Nielsen, Imen Zaabar, Poul G Hjorth, and Tina Hecksher. Method for Direct Measurement of Structural Rolling Resistance for Heavy Vehicles. *Transportation Research Record: Journal of the Transportation Research Board*, 2674(5):371–380, 2020.
- [20] H. Yu, C. Cai, Y. Yuan, and M. Jia. Analytical solutions for Euler-Bernoulli Beam on Pasternak foundation subjected to arbitrary dynamic loads. *International Journal for Numerical and Analytical Methods in Geomechanics*, 41(8):1125–1137, 2017.
- [21] Gamaledine Elnashar, Rama B. Bhat, and Ramin Sedaghati. Modeling and dynamic analysis of a vehicle-flexible pavement coupled system subjected to road surface excitation. *Journal of Mechanical Science and Technology*, 33(7):3115–3125, 2019.
- [22] M. Di Paola, R. Heuer, and A. Pirrotta. Fractional visco-elastic Euler-Bernoulli beam. *International Journal of Solids and Structures*, 50(22-23):3505–3510, 2013.
- [23] A. K. Mallik, Sarvesh Chandra, and Avinash B. Singh. Steady-state response of an elastically supported infinite beam to a moving load. *Journal of Sound and Vibration*, 291(3-5):1148–1169, 2006.
- [24] Hideaki Tanahashi. Formulas for an infinitely long Bernoulli-Euler beam on the Pasternak model. *Soils and Foundations*, 44(5):109–118, 2004.
- [25] B Lautrup. *Physics of continuous matter*. Second edi edition, 2011.
- [26] Søren L. Frederiksen, Karsten W. Jacobsen, Kevin S. Brown, and James P. Sethna. Bayesian ensemble approach to error estimation of interatomic potentials. *Physical Review Letters*, 93(16):1–4, 2004.
- [27] Jon Tofteskov, Mari Ann Tørngren, Nicholas P. Bailey, and Jesper Schmidt Hansen. Modelling headspace dynamics in modified atmosphere packaged meat. *Journal of Food Engineering*, 248(June 2018):46–52, 2019.
- [28] M. Seon Han, Haym Benaroya, and Timothy Wei. Dynamics of transversely vibrating beams using four engineering theories. *Journal of Sound and Vibration*, 5(225):935–988, 1999.



## Appendix B

# Viscowave

The sophisticated pavement response model ViscoWave II-M was used at several occasions to simulate pavement responses to a moving load. Viscowave II-M is developed at Michigan State University, and the theoretical framework behind the solution is described in Chatti et al. (2017) appendix C and Lee (2013). In this appendix, we will give an overview of the solution and the modifications made by the author such that the model output matches a TSD framework.

### B.1 Overview over the solution

Viscowave II-M employs the so-called spectral element method to solve the wave propagation problem in the pavement structure and subsequently calculate the pavement response to an arbitrary loading. The model can simulate the time-dependent responses while allowing the pavement materials to be either elastic or viscoelastic (Lee et al., 2018). Overall, the program employs a cylindrical axisymmetric coordinate system and uses the spectral element method to get the pavement response, where each element is defined as a layer in the pavement (Balzarini et al., 2019). This is done by solving the wave equation that govern the axisymmetric wave motion in a continuous, linear viscoelastic medium. From this, the pavement response to an arbitrary loading is calculated.

The program uses a continuous integral transformation, the Laplace and Hankel transform. These are used as they are appropriate for transient, nonperiodic signals in the time domain (Chatti et al., 2017). To obtain these integrals numerically, an elaborate numerical integration scheme is required which will not be described here. For more information see Chatti et al. (2017) appendix C.

Viscowave II-M calculates the pavement response due to a moving load of an observation point (Lee et al., 2018). This is done by first obtaining the pavement response to a stationary load at a number of observation points along the driving direction  $x$ . Subsequently, the superposition principle is used to shift the pavement responses by the time it would take the load to reach the point and the all the deflection is summed. The result is the pavement response in one point (the observation point) as a load is moving past it at a constant speed.

## B.2 Modifications of the program to match TSD setup

The output of the program was slightly modified in order to be comparable with the TSD setup. The modifications are listed here.

- i The original solution calculates the pavement deflection under the tire in a steady reference frame. It has been modified such that the response is calculated in-between a dual tire and furthermore, is obtained in a moving reference frame.
- ii The model provides the vertical pavement deflection and subsequently the deflection slope was calculated.
- iii The signal was filtered in order to remove low frequency noise. Here a moving average filter and a 6-pole Butterworth filter was used. Two passes have been performed (forward and backward) to remove the phase lag.

Details about the different modifications is described below.

First of all (i), the simulation output was changed such that the simulated conditions are similar to the TSD setup. The original solution calculates the pavement deflection under a tire in a steady reference frame. This has been modified such that the response is calculated in between two dual tires with 6.4 cm spacing (matching the distance at the TSD). Furthermore a coordinate shift is made such that the model output is in a moving reference frame.

Secondly (ii), numerical differentiation is used to obtain the deflection slope as *ViscoWave* provides the pavement deflection. As a consequence, some numerical noise is introduced into the signal. In our case, we experience both high frequency and low frequency noise, which is expressed in the signal through small and bigger oscillations respectively (see fig. B.1, raw signal). These artifacts is removed using a filtering procedure (iii).

The high frequency noise is a typical artifact related to numerical differentiation and is removed by use of a moving average filter. After visual inspection we choose the cut off at  $30 \text{ m}^{-1}$  and the result is shown on figure B.1.

The low frequency noise seen in the model output (bigger oscillations) was unexpected, and we have investigated whether this was due to a bad choice of parameter values making the solution numerical unstable. In the solver, the solution to the wave equations is found in the Laplace-Hankel domain and therefore an inverse Hankel and Laplace transform is needed in order to get a solution the physical domain (Chatti et al., 2017, p. 269). Both the inverse Laplace transform and the inverse Hankel transformation is obtained numerically through an elaborate integration scheme. The different steps in this integration scheme was inspected in order to evaluate if these where the basis of the oscillations seen in the model output. However they where ruled out, as the solution provided stable results when key parameter values where perturbed and thus it was concluded that the low frequency oscillations seen in the model output is computational

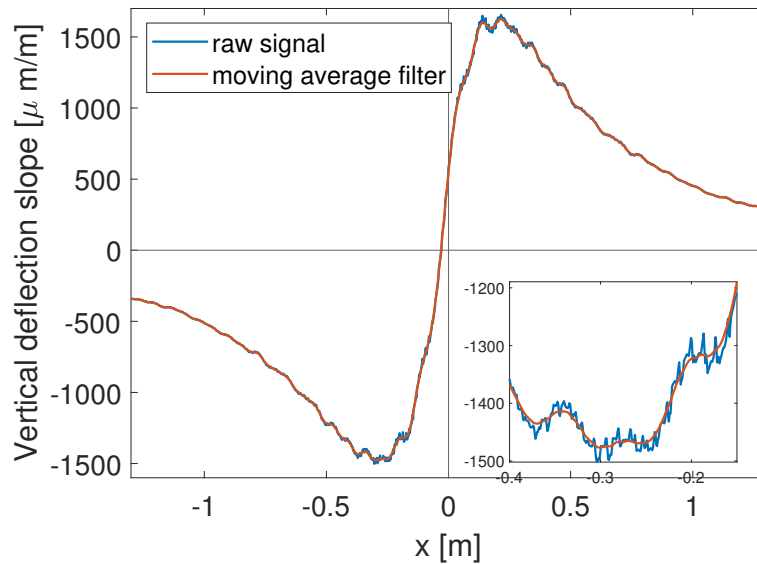


FIGURE B.1: Example on pavement deflection slope simulated using ViscoWave II-M. The raw signal (blue line) has both high and low frequency noise, seen as fast and more slow oscillations in the signal. The high frequency noise is a typical artifact related to numerical differentiation and is removed by use of a moving average filter (red line).

noise.

A 6-pole Butterworth filter was used to remove the low frequency noise from the slope. The Butterworth low-pass filter is a band filter, meaning that one can define a passband which is the range of frequencies passing through the filter. In our case we chose a cut-off frequency  $f_c$  and then the passband is the range  $f = [0 - f_c]$ . When applying the filter is important not to remove any of the physical characteristics of the signal, as these are used in the following analysis.

When choosing a filter there are two important things to consider; the flatness of the magnitude within the passband and the amount of shift introduced in the output signal, given by the phase. The strength of the Butterworth filter is that it is very flat in the passband, meaning that the same magnitude of these frequencies are going through the filter (Lee et al., 2009). This prevents that the filter removes some of the frequencies that one wants to have in the signal.

In figure B.2a the frequency response of a Butterworth filter with varying orders is seen. The sharpness of the curves around the cut off frequency  $f_c$  is determined by the filter order, with a sharper cut off when order increase. On the other hand, a high order filter introduce a large amount of phase shift on the output signal.

In our case we want as sharp a cut of as possible and do not really care about the phase shift since we do a reverse filter as well. consequently we choose a 6'th order filter. By visual inspection the cut off frequency is chosen to be  $7 \text{ m}^{-1}$ , which removes most of the numerical noise but not physical features about the deflection slope curve.

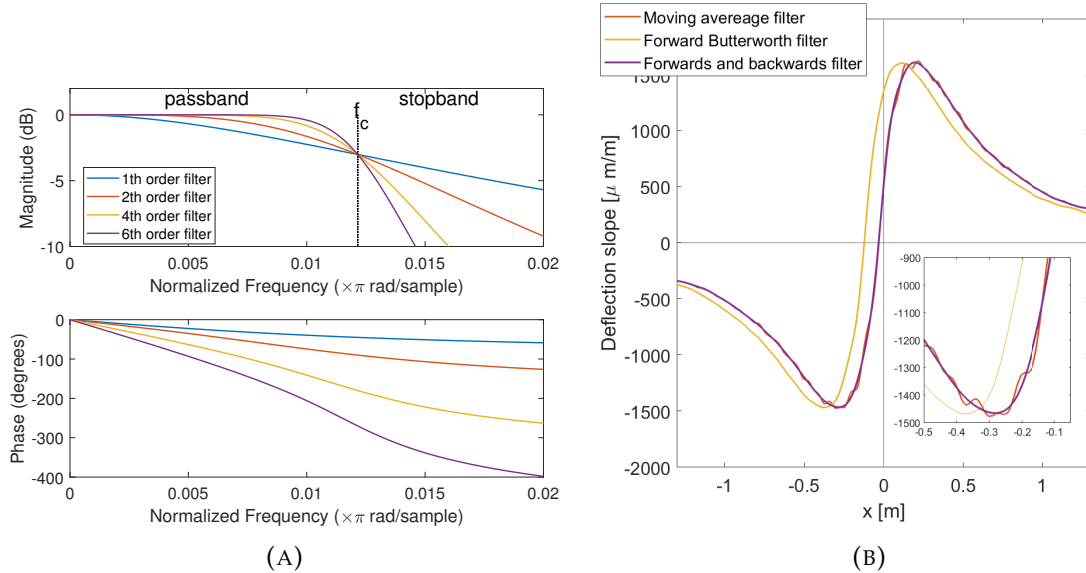


FIGURE B.2: A) Frequency response of a Butterworth filter with varying orders. A high order implies a sharp cut of behaviour, but also introduce an increased phase shift in the output signal. B) The model output subject to a moving average filter is shown in red. Two passes of a 6-pole Butterworth filter has been applied to this signal in the forward and reverse direction (yellow and purple line respectively).

Two passes have been performed (forward and backward) to remove the phase lag. The result of applying a 6-pole Butterworth filter (after a moving average filter has been applied to the raw signal) in the forward direction and subsequently in the reverse direction is seen in figure B.2b. As we are interested in the location of the maximum and minimum in the deflection slope the last reverse step is crucial for the filtering process.

## Appendix C

# Metropolis Monte Carlo algorithm

In chapter 18, a Global sensitivity analysis was made using the Metropolis Monte Carlo method. In the MMC method, the parameter values  $\theta$  is varied in an iterative way and then the given cost function,  $cost(\theta)$ , is evaluated. The new parameter set is then either accepted and saved or rejected based on some criteria. This procedure is repeated until a certain amount of parameter sets has been accepted. The iterative process performed in the MMC algorithm can be described in the following three steps:

### 1) Creating $\theta_{new}$

A new parameter set  $\theta_{new}$  is found from the old one by

$$\theta_{new} = |\theta_{old} + \delta\theta_0| \quad (C.1)$$

Since we deal with only positive parameter values we chose to have  $\theta_{new} = |\theta_{old} + \delta\theta_0|$ .  $\delta\theta$  determines how big a jump in the parameter space there is made and is found as  $\delta\theta_0 = \theta_0\sigma_{\delta\theta}r$ , where  $r$  is a random number between -1 and 1 and  $\sigma_{\delta\theta}$  determines the step size in the parameter space. Consequently, if  $\sigma_{\delta\theta}$  is too big the algorithm will jump around a lot in the parameter space and if it is too small one risks to get trapped in a local minimum.

### 2) Calculate $cost(\theta_{new})$

Using the given cost function, we now calculate  $cost(\theta_{new})$ . This can have two outcomes

i)  $cost(\theta_{new}) < cost(\theta_{old})$ ,  
in the case that the new cost function is smaller than the old, the step is accepted and the parameter set  $\theta_{new}$  is saved and the iteration is repeated.

ii)  $cost(\theta_{new}) \geq cost(\theta_{old})$ ,  
In the case the cost function for the new parameter set is bigger or equal to the old one, the parameter set is only accepted if

$$R < e^{-\frac{cost(\theta_{new}) - cost(\theta_{old})}{T_s}} \quad (C.2)$$

where  $R$  is a random number taken from a uniform distribution between  $[0;1]$  and  $T_s$  is the sampling temperature.

3) Sampling

Only every tenth parameter set that gets accepted is sampled to the parameter sample that is the output of the MMC algorithm. This is done in order to avoid spurious correlations, which is when a correlation appears to be causal but is not.